

Pathways for solar wind plasma and energy transfer to the earth's magnetosphere

Wing, S.

Published: 21/09/2016

Document Version

Publisher's PDF, also known as Version of Record (includes final page, issue and volume numbers)

Please check the document version of this publication:

- A submitted manuscript is the author's version of the article upon submission and before peer-review. There can be important differences between the submitted version and the official published version of record. People interested in the research are advised to contact the author for the final version of the publication, or visit the DOI to the publisher's website.
- The final author version and the galley proof are versions of the publication after peer review.
- The final published version features the final layout of the paper including the volume, issue and page numbers.

[Link to publication](#)

Citation for published version (APA):

Wing, S. (2016). Pathways for solar wind plasma and energy transfer to the earth's magnetosphere Eindhoven: Technische Universiteit Eindhoven

General rights

Copyright and moral rights for the publications made accessible in the public portal are retained by the authors and/or other copyright owners and it is a condition of accessing publications that users recognise and abide by the legal requirements associated with these rights.

- Users may download and print one copy of any publication from the public portal for the purpose of private study or research.
- You may not further distribute the material or use it for any profit-making activity or commercial gain
- You may freely distribute the URL identifying the publication in the public portal ?

Take down policy

If you believe that this document breaches copyright please contact us providing details, and we will remove access to the work immediately and investigate your claim.

Pathways for solar wind plasma and energy transfer to the Earth's magnetosphere

PROEFSCHRIFT

ter verkrijging van de graad van doctor aan de Technische Universiteit Eindhoven, op gezag van de rector magnificus prof.dr.ir. F.P.T. Baaijens, voor een commissie aangewezen door het College voor Promoties, in het openbaar te verdedigen op woensdag 21 september 2016 om 16:00 uur

door

Simon Wing

geboren te Makassar, Indonesië

Dit proefschrift is goedgekeurd door de promotoren en de samenstelling van de promotiecommissie is als volgt:

voorzitter:	prof.dr. H.J.H. Clercx
1 ^e promotor:	prof.dr. U.M. Ebert
copromotor(en):	dr. E. Camporeale (CWI) dr.ir. S. Nijdam
leden:	prof.dr. G. Lapenta (KU Leuven) prof.dr. A. Fazakerley (University College London) prof.dr. N.J. Lopes Cardozo
adviseur(s):	dr. P. Escoubet (ESA/ESTEC)
reserve:	prof.dr.ir. G.M.W. Kroesen

Het onderzoek of ontwerp dat in dit proefschrift wordt beschreven is uitgevoerd in overeenstemming met de TU/e Gedragscode Wetenschapsbeoefening.

Copyright © 2016 Simon Wing

Printed by IPSKAMP Printing, The Netherlands

Front cover: Background is an image of a legion of galaxies from NASA Hubble Space Telescope and foreground is a sketch of the Earth's magnetosphere, images of the Sun and aurora (from NASA).

Back cover: A composite image of an auroral image from NASA IMAGE satellite and an image of a legion of galaxies from NASA Hubble Space Telescope (from NASA).

A catalogue record is available from the Eindhoven University of Technology Library

ISBN: 978-90-386-4119-5

Contents

1	Introduction	1
1.1	Solar wind	2
1.2	Magnetosphere	4
1.3	Ionosphere	5
1.4	Magnetospheric currents	6
1.5	Space weather	7
1.6	Outline of this thesis: organization and statement of work	8
1.7	Summary of science questions to be addressed by this thesis	13
1.7	References	14
2	Review of some quantitative aspects of magnetospheric physics	17
2.1	Coordinate systems	17
2.1.1	Geomagnetic coordinate system (MAG)	17
2.1.2	Geocentric solar magnetospheric system (GSM)	18
2.2	Space plasma properties	19
2.3	Particle motion	20
2.4	Guiding center motion	23
2.5	Signature of dayside reconnection in the ionosphere	24
2.6	APL open field line particle precipitation model (APL–OPM)	28
2.6.1	Case 1: strongly southward IMF cusp	31
2.6.2	Case 2: weakly southward IMF cusp	34
2.6.3	Case 3: cusp for large IMF B_y and small IMF B_z	36
2.7	Summary	39
2.8	References	40
3	Solar wind plasma and energy entry through dayside reconnection into the polar cap	45
3.1	Solar wind plasma and energy entry in the dayside	

polar cap	46
3.1.1 Downward and upward field-aligned electric fields in the polar cap	48
3.1.2 A morphology of the low-latitude polar rain electrons in the upward FAC region	53
3.1.3 The occurrence of the upward field-aligned electric fields in the polar cap	56
3.2 Solar wind electrons in the nightside polar cap	59
3.2.1 Modeling the polar rain energy-latitude dispersion	61
3.2.2 Estimation of electron path length	65
3.2.3 Where is the nightside magnetic field line open-closed boundary?	69
3.2.4 The electron overhang	71
3.3 Summary and conclusion	72
3.3.1 Dayside polar cap	72
3.3.2 Nightside polar cap	73
3.4 References	74
4 Solar wind energy transfer to the magnetosphere through low-latitude boundary layer	79
4.1 Introduction	79
4.2 Analytical theory for upward FAC	81
4.2.1 Analytical model	81
4.2.2 Maximum current	85
4.2.3 Width of the field-aligned current layer	88
4.3 Data and method	90
4.3.1 Data	90
4.3.2 Method for obtaining field-aligned currents	91
4.3.3 Method for determining the source regions and particle precipitation morphology	92
4.3.4 Summary of data and method (putting it all together)	95
4.4 Theory-data comparisons	95
4.4.1 Field-aligned current density	95
4.4.2 FAC latitudinal width	105
4.4.3 Thickness of the boundary layer	108

4.4.4	Sources of uncertainties	110
4.5	Summary and conclusion	112
4.6	References	114
5	Auroral particle precipitation characterized by the substorm cycle	121
5.1	Introduction	121
5.2	Review of the solar wind entries into the plasma sheet	122
5.3	Substorm and auroral particle precipitation	129
5.4	DMSP particle data set	132
5.5	The substorm database	132
5.6	Methodology	133
5.6.1	Electron aurorae	134
5.6.2	Ion aurora	135
5.6.3	Model construction	135
5.7	Auroral particle precipitation characterized by substorm phases	136
5.7.1	Particle precipitation maps throughout the substorm cycle	136
5.7.2	The nightside particle precipitation powers throughout the substorm cycle	143
5.7.3	The electron auroral dawn-dusk asymmetry	149
5.8	Comparisons of DMSP observations and RCM simulation	150
5.8.1	The RCM–Dungey simulation	150
5.8.2	RCM precipitating ion energy flux	153
5.9	Discussion and summary	155
5.9.1	Summary of key observations	155
5.9.2	Electron and ion aurora substorm cycles	156
5.9.3	Diffuse electron aurora	158
5.9.4	Broadband electron aurora	159
5.9.5	Monoenergetic electron aurora	161
5.9.6	Is there any link between broadband and mono- energetic electrons	162
5.10	References	164

6	Information theoretical approach to discovering solar wind drivers of the outer radiation belt	177
6.1	Introduction	177
6.2	Dataset	181
6.3	Mutual information, conditional mutual information, and transfer entropy	182
6.4	Applying information theory to radiation belt MeV electron data	185
6.4.1	Radiation belt MeV electron flux vs. V_{sw}	185
6.4.2	Radiation belt MeV electron flux vs n_{sw}	187
6.4.3	Anticorrelation of V_{sw} and n_{sw} and its effect on radiation belt	190
6.4.4	Ranking of solar wind parameters based on information transfer to radiation belt electrons	193
6.4.5	Detecting changes in the system dynamics	197
6.5	Discussion	198
6.5.1	Solar wind velocity driving geosynchronous MeV electron flux	198
6.5.2	n_{sw} and V_{sw} anticorrelation	199
6.5.3	Solar wind density driving geosynchronous MeV electron flux	200
6.5.4	Revisiting the triangle distribution	201
6.5.5	Improving models with information theory	206
6.6	Summary	207
6.7	References	208
7	Summary and conclusion	217
7.1	Overview	217
7.2	Chapter 2: Quantitative aspects of magnetospheric physics	218
7.3	Chapter 3: Solar wind plasma and energy entry into the polar cap	219
7.3.1	The dayside polar cap	220
7.3.2	The nightside polar cap	221
7.4	Chapter 4: Solar wind energy transfer at the low-latitude boundary layer	222

7.5	Chapter 5: Auroral particle precipitation	223
7.6	Chapter 6: Solar wind drivers of the outer radiation belt	225
7.7	Practical applications: space weather	227
	Dankwoord	229
	Summary	231
	Curriculum Vitae	235

Chapter 1

Introduction

Although Mars and Earth are neighbors in our solar system, the two planets are quite different in many aspects. One of the most striking differences between the two planets is how barren Mars is compared to Earth, which is apparent even with just a cursory examination of images like the one shown in Figure 1.1. Unlike Earth, Mars has little atmosphere, which is needed to trap moisture and facilitate a water or hydrological cycle, a process that is largely responsible for redistributing water and for sustaining life on Earth. An atmosphere could also trap greenhouse gasses, which would help moderate Mars' surface temperature. Mars' thin atmosphere has been attributed to its weak or non-existent magnetic field. It is believed that a long time ago, in its infancy, Mars had a magnetic field and an atmosphere, but after its dynamo stopped, over time, the solar wind stripped its atmosphere away.

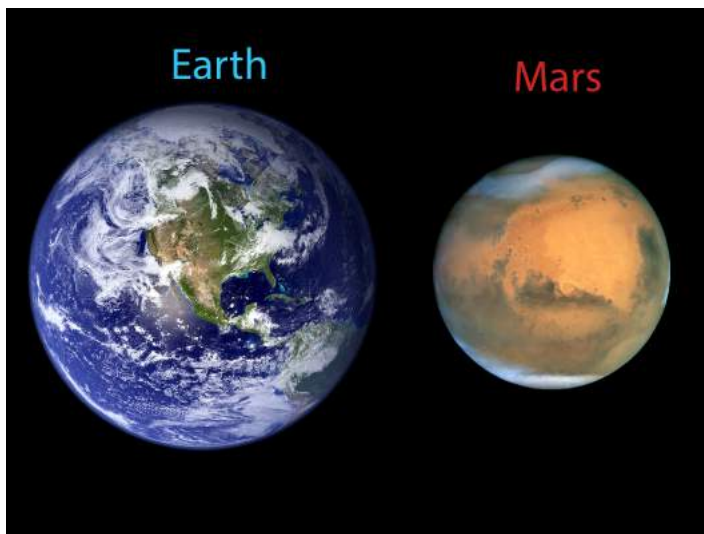


Figure 1.1. Images of Earth and Mars showing Mars is barren compared to Earth (Earth and Mars images are from <http://visibleearth.nasa.gov> and <http://apod.nasa.gov/apod>, respectively.)

At Earth, the magnetic field has been credited for shielding much of its atmosphere and inhabitants from solar wind. However, this magnetic shielding is not perfect – a small fraction of the solar wind plasma enters into the Earth’s magnetosphere and some precipitates into the ionosphere. The transport of plasma and energy from the solar wind to the dayside magnetosphere, to the magnetotail, and finally to the inner magnetosphere is the main focus of this dissertation. The investigation is carried out with theory, modeling, and observations.

Figure 1.2 shows a schematic of the Earth’s magnetosphere. The Sun is located to the left of the figure. Here, we briefly introduce several prominent features in the figure, which will be referred frequently throughout the thesis.

1.1 Solar wind

The Sun emits hot plasma at supersonic speed resulting from the expansion of solar corona. This hot plasma, which consists mainly of protons and electrons and a small fraction of helium and other heavy ions, is called the solar wind. The solar wind streams down toward the Earth (from the left of Figure 1.2), reaching a nominal speed of about 400 km s^{-1} , density of about $5\text{--}10 \text{ cm}^{-3}$, ion temperature of $\sim 1 \times 10^5 \text{ K}$, and electron temperature of $\sim 1.4 \times 10^5 \text{ K}$ at 1 astronomical unit (AU = the distance between the Sun and the Earth). The solar wind also has a high speed component (fast solar wind) with a mean speed of $\sim 700 \text{ km s}^{-1}$, density of $\sim 2 \text{ cm}^{-3}$, ion temperature of $\sim 2.3 \times 10^5 \text{ K}$, and electron temperature of $\sim 1 \times 10^5 \text{ K}$ (all properties obtained at 1 AU). Because the solar wind plasma is highly conducting, the solar magnetic field is “frozen in” the plasma. Thus, the solar wind carries with it solar magnetic field, which is known as interplanetary magnetic field (IMF) and which has a magnitude of $\sim 6 \text{ nT}$ at 1 AU. In a reference frame that does not move with the solar wind, e.g., Earth’s reference frame, the motion of the solar wind (and the IMF) induces an electric field called the convective electric field or solar wind electric field.

Contribution statement:

S. Wing: contributed main ideas, wrote the chapter.

E. Camporeale: contributed useful comments and discussions.

U. Ebert: contributed useful comments and discussions.

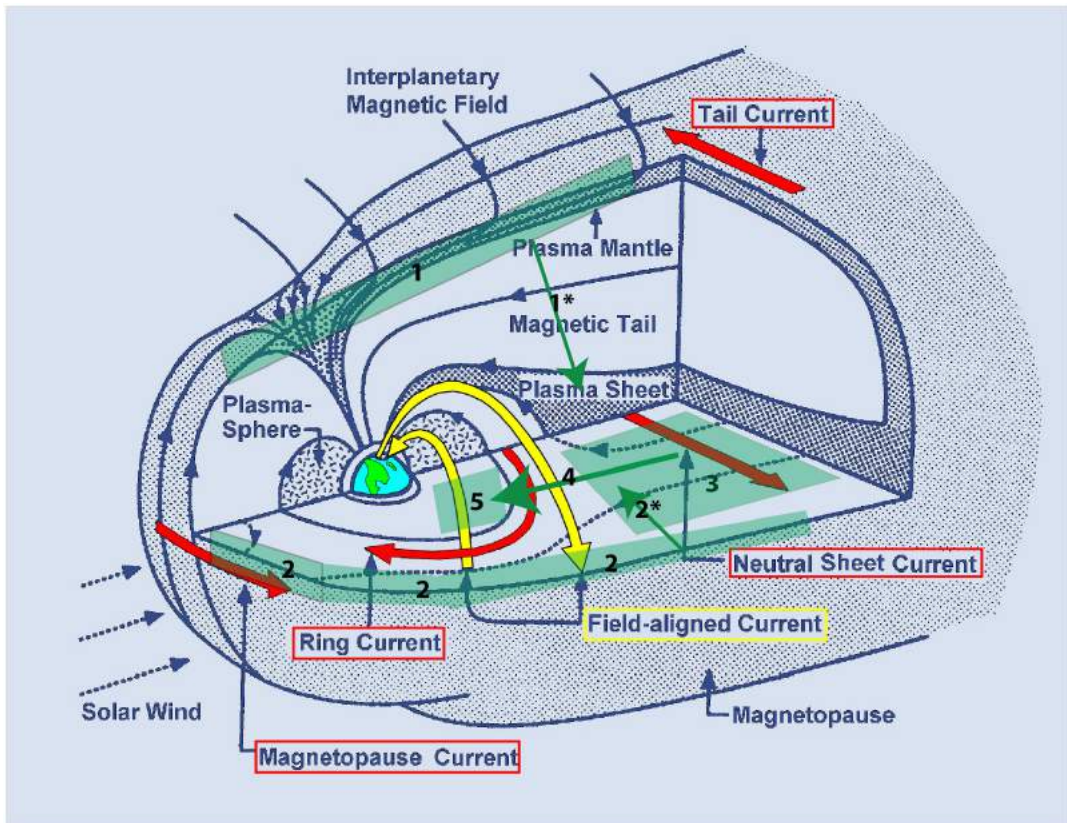


Figure 1.2. Schematic of the Earth's magnetosphere showing currents and plasma regions. This dissertation covers the processes in the green shaded regions and green arrows. Except for 1 and 2, which can occur without any preferential order, the numbers give the **rough** sequence for solar wind plasma and energy transport from the dayside magnetopause to the plasma sheet and finally to the inner magnetosphere. The green arrows indicate plasma transport directions. (originally from Kivelson and Russell [1995]).

As the solar wind approaches the Earth, it encounters the Earth's magnetic field, which acts as an obstacle, and it slows down. The Earth's magnetic field deflects the solar wind around it. Because the solar wind is supersonic when it encounters the obstacle, a shock wave is generated. The outermost boundary of this shock is called the bow shock (not shown in Figure 1.2). Once the solar wind crosses the bow shock, its speed changes from supersonic to subsonic and much of its kinetic energy is converted to thermal energy. The shocked solar wind in this region, which is called the magnetosheath, is denser and hotter than the solar wind. The magnetosheath region spans from the bow shock to the magnetopause, which is the outermost region of the obstacle created by the Earth's magnetic field.

1.2 Magnetosphere

The magnetosheath particles, ions and electrons, cannot easily cross to the Earth's magnetic field line because these particles cannot easily leave the solar wind magnetic field line due to the "frozen in" properties (but, this magnetic shielding is not perfect, which is the topic of this thesis). This magnetic shielding creates a "cavity", which is called the magnetosphere, and is shown in Figure 1.2. The outermost boundary of the magnetosphere is the magnetopause where the Earth's magnetic field and the magnetosphere end and the domain of the solar wind (heliosphere) begins. The location of the magnetopause, which is nominally located at $\sim 10 R_E$ ($R_E =$ radius of the earth ~ 6372 km) at the subsolar point, can be roughly obtained by balancing the solar wind dynamic (kinetic) pressure with Earth's magnetic pressure. The magnetopause is sketched in Figure 1.2. The magnetosphere consists mainly of particles of solar wind and ionospheric origins. The characteristics of these particles vary greatly, depending on the region. Figure 1.2 shows some of the main regions in the magnetosphere such as the plasmasphere, magnetotail, plasma sheet, and plasma mantle.

The subsolar point of the magnetopause is often called the stagnation point because here the solar wind speed reaches its lowest value. The solar wind density and temperature increase as kinetic energy is converted to thermal energy. From the stagnation point, the solar wind flows radially away, going around the obstacle. As it does so, it gains speed as it flows toward dawn and dusk flanks and then on to the nightside. The nightside magnetosphere stretches out like a tail, as shown in Figure 1.2, and so it is called the magnetotail. The plasma sheet is the equatorial region of the magnetotail of about $10 R_E$ thickness where plasma β (ratio of plasma pressure over magnetic pressure) is high ($> \sim 1$). Plasma pressure is the pressure exerted by the particles in the plasma ($= n k_b T$) and magnetic pressure is the energy density of the magnetic field ($B^2/[2\mu_0]$), where $n =$ plasma number density, $k_b =$ Boltzman constant, $T =$ plasma temperature, $B =$ magnitude of magnetic field and $\mu_0 =$ permeability of free space. The plasma sheet acts as a reservoir of plasma and energy for the magnetosphere. In the magnetosphere, the magnetic field and hot plasma dominate the physical processes.

1.3 Ionosphere

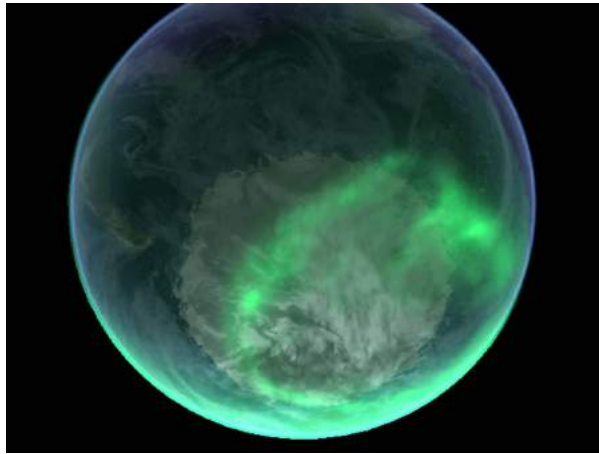


Figure 1.3. An image of auroral oval obtained by an imager on board of the IMAGE satellite. (from NASA Aurora Image Gallery: https://www.nasa.gov/mission_pages/sunearth/aurora-image-gallery/index.html).

The solar extreme ultraviolet (EUV) light ionizes a fraction of the neutral atoms and molecules in the Earth's atmosphere. At low altitude, the ionized ions and electrons can easily recombine to form neutrals because of high plasma density and collisional rates, but at high altitude ($> \sim 60$ km) the ions and electrons remain ionized. This permanently or semi permanently ionized atmospheric population is called ionosphere. Solar EUV is not the only source of ionization. At high-latitudes, plasma sheet electrons can precipitate along magnetic field lines down to the ionosphere, where they collide and ionize the neutrals, e.g., atoms and molecules. These collisions can leave the ions, atoms, and molecules in excited states and when they return to lower energy states, photons are emitted, creating an amazing display of light known as an aurora. Aurorae can also result when ions gain electrons. There is a band of region in the ionosphere known as the auroral oval where aurorae are emitted. However, most of the light from the auroral oval is not visible to the naked eye, but it can be observed by optical imagers operating in various wavelengths from EUV to infrared (IR). An example of an image of auroral oval observed by IMAGE satellite is shown in Figure 1.3. The aurorae commonly observed by humans are emitted at night where (1) the precipitating particles have higher energies and (2) there is less interference from sunlight. This can be seen in Figure 1.3, which shows that the dayside (lower portion) auroral oval is obscured by the sunlight, although the viewing angle is not optimal

for the dayside auroral oval. Because most auroral particle precipitation originates from the magnetosphere, particle precipitation at high-latitude provides a “window” to study the particle population and the processes in the magnetosphere, as discussed in Chapter 5. Poleward of the auroral oval, the magnetic field lines are “open” in the sense that the field lines originating from Earth do not come back to Earth, unlike the field lines in the “closed” region, as discussed in Chapters 2 and 3. This open field line region is called the polar cap.

The ionosphere can extend from 60 to 1000 km in altitude and consists of 3 layers: (1) the D layer (altitude $\sim 60\text{--}90$ km), (2) the E layer (altitude $\sim 90\text{--}150$ km), and (3) the F layer (altitude ~ 150 – upward of 500 km). At night, due to lack of sunlight, the D layer disappears or weakens, effectively lifting the lower boundary of the ionosphere to ~ 90 km. At mid and low latitudes, the outer boundary of the ionosphere is the plasmasphere, which is part of the magnetosphere as shown in Figure 1.2. Together, the magnetosphere, ionosphere, and heliosphere (e.g., solar wind) form a core region that is the main subject of a science discipline called space physics.

1.4 Magnetospheric currents

The plasmas in the magnetosphere rarely remain stationary. Instead, they move under external forces, as discussed in Chapter 2. If the ions and electrons move together, no current is generated. However, sometimes the ions and electrons move in separate ways, creating currents. Figure 1.2 shows several large scale currents in the magnetosphere, namely, neutral sheet (cross tail), ring, magnetopause, tail, and field-aligned currents. The magnetopause current, which resides at the magnetopause, is caused by the interaction of the terrestrial magnetic field with the solar wind. The tail like structure of the magnetosphere on the nightside is associated with the tail and neutral sheet (cross-tail) currents. The tail current is located in the lobe, whereas the cross-tail or neutral sheet current is located in the plasma sheet or neutral sheet. The neutral sheet is part of the plasma sheet that is located typically in the equatorial plane. The ring current, which is located in the inner magnetosphere, flows westward due to the ion and electron drifts, as discussed in Chapter 2. Finally, the field-aligned current flows parallel and anti-parallel to the magnetic field line, which is the topic of Chapter 4.

1.5 Space Weather

Because the shielding of the Earth's atmosphere is not perfect, the magnetosphere and ionosphere are susceptible to disturbances on the Sun and to certain conditions in the solar wind. For example, solar flares and coronal mass ejections (CMEs) produce energetic ions and electrons that can trigger magnetic storms in the magnetosphere. High speed streams in the solar wind have been associated with increased substorm occurrences and higher radiation belt energetic electron fluxes [e.g., *Kissinger et al.*, 2011; *Tanskanen*, 2009; *Reeves et al.*, 2011; *Wing et al.*, 2016]. The radiation belt electrons are known as “killer electrons” to the satellite operators because these electrons pose serious hazards to satellites at the geosynchronous orbit and in the ionosphere, at the magnetic field line footprints of the radiation belts. The radiation belt electrons with energies > 1 MeV can penetrate deep into a spacecraft while those with energies < 1 MeV can lodge on a spacecraft's skin, leading to spacecraft charging. The terms geomagnetic or magnetic storm and substorm are often used to describe disturbances in space that are analogous to the usage of the word storm in describing terrestrial weather disturbances. Storms can affect a large region of space, nearly the entire magnetosphere, over a time scale of several days while substorms refer to magnetic disturbances that occur over a time scale of a few hours over a smaller region, typically on the nightside of the magnetosphere. The plasma and energy that are stored in the plasma sheet are violently released during storms and substorms, which can disrupt life on Earth. The adverse effects of solar wind on our technological systems and lives are topics of the study of a relatively new field called space weather.

Space weather refers to conditions on the sun, in the solar wind, magnetosphere, ionosphere, and thermosphere that can influence the performance and reliability of space-borne and ground-based technological systems and can endanger human life or health [The National Space Weather Program Strategic Plan, FCM-P30-1995, Washington, DC, 1995]. As technology advances and as we continue to rely more on these advancing technologies, space weather will increasingly play significant roles in human activities, approaching those of terrestrial weather. For example, space weather can affect satellite communications, navigation systems, satellite health, power grids, and space travel. Some common space weather adverse effects on satellites include: (1) radiation damage to satellite electronics and solar cells; (2) electrostatic charging on satellite's body surface and instruments; (3) atmospheric drag on the satellite

motion; and (4) attitude control of the satellites [e.g., *Wing*, 2012]. Of these, (1), (2) and (4) can affect satellites at a wide range of altitudes from low Earth orbit (LEO < ~2000 km in altitude) to geosynchronous orbit (GEO ~ 35,786 km in altitude) or higher whereas (3) can affect satellites at LEO where the atmospheric density is still high enough to cause significant friction on the satellite motion. Additionally, geomagnetic storms and substorms can disturb the atmosphere and introduce significant noise to electromagnetic signals traveling to and from satellites. The perturbation in the ionospheric density, so called scintillation, can cause loss of accuracy of location determination, timing, and reduced carrier-to-noise ratio in Global Positioning Satellite (GPS) signals [*Messerotti*, 2009; *Wing*, 2012]. This can severely affect air traffic control, ship navigation, as well as mobile and wireless communication. Space weather prediction is a growing and active research area due to its growing impacts on lives on Earth [e.g., *Wing et al.*, 2005b; *Zhu et al.*, 2006; 2007; *Wei et al.*, 2011]. Chapter 6 describes a study on solar wind driving of radiation belt MeV electrons that can damage spacecraft.

1.6 Outline of this thesis: organization and statement of work

The pathways for plasma and energy transport from the solar wind all the way to the inner magnetosphere that are covered by this dissertation are shaded green in Figure 1.2. Except for 1 and 2, which can occur without any preferential order, the numbers in Figure 1.2 give roughly the sequence for solar wind plasma and energy transport to the dayside magnetopause, to the plasma sheet, and finally to the inner magnetosphere. This is also the sequence that this dissertation is laid out. In this dissertation, except for Chapter 2, which provides some background information on magnetospheric physics, each chapter describes one or more green regions and/or green arrows in Figure 1.2. Below, we provide a quick tour of each chapter and its associated region(s). Except for Chapter 2, the description of each chapter includes a brief statement of motivations, the science objectives or problems, and the approach or methodology to address the science questions.

Chapter 1 provides an introduction, a brief tutorial on the near Earth space, motivation, and identifies the problems to be addressed by the thesis. Chapter 2 provides some quantitative aspects of magnetospheric physics that are needed to understand the materials presented in this thesis. It is not meant to be a comprehensive review of magnetospheric physics, but rather, it is intended to

provide some review materials that can serve as a quick reference for readers.

Chapter 3 discusses solar wind plasma and energy entries in the aftermath of dayside magnetic reconnection (labels 1 and 1* in Figure 1.2). The dayside magnetic field reconnection is a process in which the Earth's magnetic field reconnects with the IMF. As a result, the previously closed magnetic field line becomes open, allowing solar wind particles to enter the magnetosphere. As the open field lines convect from the dayside to the nightside over the polar regions, solar wind continues to enter the magnetosphere, some precipitate into the ionosphere. Finally, on the nightside, these open field lines would once again reconnect in the magnetotail to form a newly closed field line (magnetotail X-line), which would convect back to the dayside to complete the so called Dungey cycle [Dungey, 1961]. Based on the topics, this chapter is naturally divided into two parts: (1) the dayside, and (2) the nightside.

For the dayside, we previously developed an open field line particle precipitation model that models the processes involved in the solar wind particle, ion and electron, entries into the magnetosphere and ionosphere [Wing *et al.*, 1996; 2001; 2005a]. Fairfield *et al.* [2008] shows that the model's downward field-aligned electric field resulting from maintaining charge quasi-neutrality qualitatively agrees with observations, but the study also found an occasional anomaly: the field-aligned electric field is upward. Herein, field-aligned refers to aligned or parallel with magnetic field. What is the cause of this anomaly? How frequently does it occur? These are the questions that we address in this study. We investigate this anomaly using Defense Meteorological Satellite Program (DMSP) satellite particle and magnetometer observations. The DMSP particle data can give some information about the field-aligned electron acceleration and electric field while the magnetometer data can give some information about the field-aligned currents. We perform a statistical study to investigate how often this anomaly occurs. The findings are reported in Chapter 3 (Section 3.1).

For the nightside, an algorithm that estimates the magnetotail X-line distance based on the polar rain electron energy-latitude dispersion was developed. How accurate is this algorithm? This has never been investigated. In order to address this question observationally, one would have to be really lucky to find events in which magnetospheric and ionospheric satellites observe a magnetic reconnection of the same magnetic field line simultaneously. Because of the difficulty of finding such satellite conjunctions, such study has never been done. However, here we propose to investigate this with a model. First, we need to

extend the *Wing et al.* [1996; 2001; 2005a] open-field line particle precipitation model to the nightside. Then, using this model we estimate the error of the algorithm. One of the questions that we would like to address is that under what conditions would the algorithm be optimal? An important parameter that is related to the magnetotail reconnection is the nightside magnetic field line open-closed boundary (the open magnetic field line is the magnetic field line that has one end connected to the Earth and the other connected to the solar wind; in contrast, the closed magnetic field line is the field line that has both ends connected to the Earth.) Studies have proposed methodologies to obtain the open-closed boundary, but unfortunately, some of these methodologies produce conflicting results. So, another question that we would like to address is: where is the nightside magnetic field line open-closed boundary? The open-closed boundary is investigated using *Wing et al.* [1996; 2001; 2005a] model and DMSP particle observations. The findings are reported in Chapter 3 (Section 3.2).

As the solar wind streams down toward the Earth, it first encounters the subsolar region of the magnetopause near noon where it slows down and stagnates at the stagnation point. From the stagnation point, the solar wind speeds up as it moves radially away toward dawn and dusk, and then on to the nightside. The plasma flow in the magnetosphere just inside the magnetopause is generally small and sunward. The velocity shears at the low-latitude boundary layer (LLBL) resulting from the sunward flow of the magnetospheric plasma and the anti-sunward flow of solar wind provide another path for the solar wind to transfer energy and plasma to the magnetosphere. LLBL is labeled 2 in Figure 1.2. There are two interesting consequences.

First, the velocity shear generates a field-aligned electric potential drop across the boundary, which couples to the ionosphere to generate upward region-1 field-aligned currents in the afternoon. This was first proposed a few decades ago, but recently *Echim et al.* [2008] examined this topic more quantitatively with a field-aligned current model. However, it is hard to compare observations with *Echim et al.* [2008] model quantitatively because to do so would require a separate run for each solar wind and ionospheric conditions. On the other hand, an analytical theory that explicitly expresses the dependences of the upward field-aligned current on solar wind and ionospheric parameters can be more useful for analysis and forecast. Such analytical theory is developed precisely with this in mind. How does this theory compare with the *Echim et al.* [2008] model? How accurately can this theory predict field-aligned currents at the magnetopause

boundary layer? Can the theory predict the width of the boundary layer accurately? How do the field-aligned currents depend on the magnetopause boundary layer thickness, ionospheric conductivity, solar wind velocity, and solar wind density (theoretically and observationally)? In Chapter 4, we present an analytical theory of the field-aligned current generation at the magnetopause boundary layer. We then use DMSP particle and magnetometer data to verify the accuracy of the analytical theory and address these questions. The magnetometer data are used to obtain the field-aligned currents. The particle data are used to determine the magnetospheric origin of the field-aligned currents.

Second, the velocity shear can lead to Kelvin-Helmholtz Instability (KHI) that can in turn lead to massive solar wind particle entries (label 2* in Figure 1.2) into the plasma sheet (label 3 in Figure 1.2) [e.g., *Wing et al.*, 2014; *Johnson et al.*, 2014; *Wing and Johnson*, 2015]. Once in the plasma sheet, these particles can be injected and energized into the inner magnetosphere through a process such as a substorm (label 4 in Figure 1.2). Once in the inner magnetosphere, these injected electrons can attain energies up to tens of MeV or even higher. These relativistic electrons encircle the Earth in a region known as the radiation belt (label 5 in Figure 1.2). Some of these particles are pitch-angle scattered into the loss cone, the lower energy of which can be observed by DMSP satellites in the auroral oval in the ionosphere. Wave-particle interaction has been identified as a major source for both particle energization and pitch-angle scattering [e.g., *Reeves*, 2007; *Kellerman and Shprits*, 2012]. Thus, the precipitating ions and electrons in the auroral oval can serve as a window for the particle populations and processes in the magnetosphere, including both in the plasma sheet and the outer inner magnetosphere, which are labeled 3 and 5, respectively, in Figure 1.2.

Substorm is one of the most important processes in the magnetosphere. The substorm cycle has three distinct phases: growth, expansion, and recovery. Based on their spectral characteristics, we classify the auroral electrons as diffuse, monoenergetic, and broadband. *Newell et al.* [2010] describes how substorms modify these electrons and ions at the time scale of tens of minutes before and after substorm onsets, but it does not address the question: How do substorms modulate the auroral electrons and ions throughout the substorm cycle? This can help shed light on the question how much energy is released by substorms and how much of that energy is absorbed by the precipitating ions and electrons. In order to investigate this we first need to know: How long is the substorm cycle? The duration of the substorm cycle has been estimated using some magnetospheric

parameters, but this has never been done with particle precipitation data. As it turns out, monoenergetic and broadband electrons exhibit some of the same behaviors throughout the substorm cycle. This raises the question if there is any link between monoenergetic and broadband electrons. Finally, we address the question: How do the dawn-dusk asymmetries in diffuse, monoenergetic, and broad electrons change throughout the substorm cycle? The answers to the questions raised in this study can help us better understand the substorm process and provide observational constraints to substorm theories. In Chapter 5, using DMSP electron and ion precipitation observations in the ionosphere from 1996 to 2007, we attempt to address these questions.

There have been studies that investigate the solar wind driving of the radiation belt MeV electrons (label 5 in Figure 1.2) [e.g., *Reeves, 2007; Kellerman and Shprits, 2012*]. Previous studies used the standard correlational analysis, but the solar wind–radiation belt system is highly nonlinear and hence standard correlational analysis is inadequate or imprecise. Some studies suggested that solar wind velocity is the main driver [e.g., *Reeves, 2007; Kellerman and Shprits, 2012*] while other studies suggested that solar wind density is the main driver [e.g., *Balikhin et al., 2011*]. The interpretation of which of these two solar wind parameters is the main driver is complicated by the anticorrelation between solar wind velocity and density. Additionally, studies have found that the scatter plot of radiation belt electron fluxes vs. solar wind velocity looks like a triangle [*Reeves et al., 2011*]. The mystifying part of the triangle distribution is that high values of radiation belt electron fluxes are observed for all solar wind velocity conditions. For the study described in Chapter 6, we address the following questions: (1) What solar wind parameters drive the radiation belt electrons and at what the time scales?; (2) Given the anticorrelation of solar wind velocity and density, can we disentangle the effects of solar wind velocity from solar wind density and vice versa?; and (3) What is the origin of the triangle distribution? We use information theory to discover the solar wind drivers of MeV electron fluxes in the radiation belt. We consider nine solar wind parameters and determine how much information is transferred from each parameter to radiation belt MeV electrons. We also resolve the ambiguity that results from the anticorrelation between solar wind velocity and density. For example, in order to establish the influence of solar wind density, it is necessary to remove the effects of solar wind velocity and vice versa. This is done with information theory.

Finally, Chapter 7 provides a summary and conclusion of the thesis. It

describes how the research has advanced the state of magnetospheric physics, outlooks, possible practical applications, etc.

1.7 Summary of science questions to be addressed by this thesis

In this thesis, we follow the solar wind particles as they journey from the dayside magnetopause to the dayside magnetosphere, to the plasma sheet, and to the inner magnetosphere and radiation belts. Along the paths that these particles take, we investigate some outstanding problems in the magnetosphere that are of interest. The following summarizes the science questions that we attempt to address in this thesis.

Chapter 3

- What causes the anomalous upward field-aligned electric field in the polar cap?
- How frequently does it occur?
- How accurate is the algorithm that estimates the nightside X-line distance from the polar rain energy-latitude dispersion?
- What are the optimal conditions or requirements for the algorithm to work?
- Where is the nightside magnetic field line open-closed boundary?

Chapter 4

- Can we predict accurately the afternoon upward field-aligned currents generated at the magnetopause boundary layer?
- Can we predict the thickness of the low-latitude boundary layer from the solar and ionospheric observations?
- How do the field-aligned currents depend on the magnetopause boundary layer thickness, ionospheric conductivity, solar wind velocity, and solar wind density (theoretically and observationally)?
- How does the field-aligned current width depend on solar wind density and auroral electrostatic scale length (theoretically and observationally)?

Chapter 5

- How long is the substorm cycle from the particle precipitation perspective?

- How do substorms modify these auroral electrons and ions throughout the substorm cycle? How much of the energy that is released by substorms is absorbed by the precipitating electrons and ions?
- Is there any link between monoenergetic and broadband auroral electrons?
- How do the dawn-dusk asymmetries of the diffuse, monoenergetic, and broadband auroral electrons evolve throughout the substorm cycle?

Chapter 6

- What solar wind parameters drive the radiation belt electrons and at what time scales?
- Given the anticorrelation of solar wind velocity and density, can we disentangle the effects of solar wind velocity from solar wind density and vice versa?
- What is the origin of the triangle distribution in the radiation belt electron flux vs. solar wind velocity plot?

1.8 References

- Balikhin, M. A., R. J. Boynton, S. N. Walker, J. E. Borovsky, S. A. Billings, and H. L. Wei (2011), Using the NARMAX approach to model the evolution of energetic electrons fluxes at geostationary orbit, *Geophys. Res. Lett.*, 38, L18105, doi:10.1029/2011GL048980.
- Echim, M. M., M. Roth, and J. de Keyser (2008), Ionospheric feedback effects on the quasi-stationary coupling between LLBL and postnoon/ evening discrete auroral arcs, *Ann. Geophys.*, 26, 913–928, doi:10.5194/angeo-26-913-2008.
- Fairfield, D. H., S. Wing, P. T. Newell, J. M. Ruohoniemi, J. T. Gosling, and R. M. Skoug (2008), Polar rain gradients and field-aligned polar cap potentials, *J. Geophys. Res.*, 113, A10203, doi:10.1029/2008JA013437.
- Johnson, J. R., S. Wing, and P. A. Delamere (2014), Kelvin Helmholtz Instability in Planetary Magnetospheres, *Space Sci. Rev.*, 184, 1 – 31, doi:10.1007/s11214-014-0085-z.
- Kivelson, M. G., and C. T. Russell (1995), *Introduction to space physics*, Cambridge University Press, Cambridge, U.K.
- Kellerman, A. C., and Y. Y. Shprits (2012), On the influence of solar wind conditions on the outer-electron radiation belt, *J. Geophys. Res.*, 117, A05217, doi:10.1029/2011JA017253.

- Kissinger, J., R. L. McPherron, T.-S. Hsu, and V. Angelopoulos (2011), Steady magnetospheric convection and stream interfaces: Relationship over a solar cycle, *J. Geophys. Res.*, 116, A00119, doi:10.1029/2010JA015763.
- Messerotti, M. (2009), TSRS as a solar radio noise monitor for communication and navigation systems, *Earth moon planet*, 104, 51-54, doi:10.1007/s11038-008-9265-8.
- Newell, P. T., A. R. Lee, K. Liou, S.-I. Ohtani, T. Sotirelis, and S. Wing (2010), Substorm cycle dependence of various types of aurora, *J. Geophys. Res.*, 115, A09226, doi:10.1029/2010JA015331.
- The National Space Weather Program Strategic Plan, FCM-P30-1995. Washington D.C., 1995.
- Reeves, G. D. (2007), Radiation Belt Storm Probes: A New Mission for Space Weather Forecasting. *Space Weather*, 5: n/a. doi:10.1029/2007SW000341
- Reeves, G. D., S. K. Morley, R. H. W. Friedel, M. G. Henderson, T. E. Cayton, G. Cunningham, J. B. Blake, R. A. Christensen, and D. Thomsen (2011), On the relationship between relativistic electron flux and solar wind velocity: Paulikas and Blake revisited, *J. Geophys. Res.*, 116, A02213, doi:10.1029/2010JA015735.
- Tanskanen, E. I. (2009), A comprehensive high-throughput analysis of substorms observed by IMAGE magnetometer network: Years 1993–2003 examined, *J. Geophys. Res.*, 114, A05204, doi:10.1029/2008JA013682.
- Wei, H.-L., S.A. Billings, A. S. Sharma, S. Wing, R. J. Boynton, S. N. Walker (2011), Forecasting relativistic electron flux using dynamic multiple regression models, *Ann. Geophys.*, 29, 415 – 420, doi:10.5194/angeo-29-415-2011.
- Wing, S., P. T. Newell, and T. G. Onsager (1996), Modeling the Entry of the Magnetosheath Electrons into the Dayside Ionosphere, *J. Geophys. Res.*, 101, 13155-13167.
- Wing, S., Patrick T. Newell, and J. Michael Ruohoniemi (2001), Double cusp: Model prediction and Observational Verification, *Journal of Geophysical Research*, 106, 25,571-25,593.
- Wing, S., P. T. Newell, C.-I. Meng (2005a), Cusp Modeling and Observations at Low Altitude, *Surveys in Geophysics*, 26: 341-367, doi:10.1007/s10712-005-1886-0 (invited).
- Wing, S., J. R. Johnson, J. Jen, C.-I. Meng, D. G. Sibeck, K. Bechtold, J. Freeman, K. Costello, M. Balikhin, and K. Takahashi (2005b), Kp forecast models, *J. Geophys. Res.*, 110, A04203, doi:10.1029/2004JA10500.

- Wing, Simon (2012), "Mobile and Wireless Communication: Space Weather Threats, Forecasts, and Risk Management," *IT Professional*, vol. 14, no. 5, pp. 40-46, Sept.-Oct. 2012, doi:10.1109/MITP.2012.69.
- Wing, S., J. R. Johnson, C. C. Chaston, M. Echim, C. P. Escoubet, B. Lavraud, C. Lemon, K. Nykyri, A. Otto, J. Raeder, and C.-P. Wang (2014), Review of solar wind entry into and transport within the plasma sheet, *Space Science Reviews*, 184, 33 – 86, doi:10.1007/s11214-014-0108-9.
- Wing, S. and Johnson, J. R. (2015), Solar Wind Entry Into and Transport Within Planetary Magnetotails, in *Magnetotails in the Solar System* (eds A. Keiling, C. M. Jackman and P. A. Delamere), John Wiley & Sons, Inc, Hoboken, NJ. doi: 10.1002/9781118842324.ch14.
- Wing, S., J. R. Johnson, E. Camporeale, and G. D. Reeves (2016), Information theoretical approach to discovering solar wind drivers of the outer radiation belt, submitted to *J. Geophys. Res.*
- Zhu, D., S. A. Billings, M. Balikhin, S. Wing, and D. Coca (2006), Data derived continuous time model for the Dst dynamics, *Geophys. Res. Lett.*, 33, L04101, doi:10.1029/2005GL025022.
- Zhu, D., S. A. Billings, M. A. Balikhin, S. Wing, and H. Alleyne (2007), Multi-input data derived Dst model, *J. Geophys. Res.*, 112, A06205, doi:10.1029/2006JA012079

Chapter 2

Review of some quantitative aspects of magnetospheric physics

In this chapter, we review some of the basic principles that are fundamental in understanding the materials presented in this thesis. The magnetosphere is inhabited by tenuous plasma, a gas of hot ions and electrons. These particles exhibit properties from their collective behaviors as well as those that arise from individual particle's interactions with its environment. This chapter introduces some of the basic properties and physical processes that are commonly found in space plasma. It does not explore all the properties and physical processes in space plasma, but only those that are deemed relevant for the understanding of this thesis. These principles are used throughout this thesis. Additionally, these principles are used in the construction of the open field line particle precipitation model presented at the end of this chapter, and used in a study presented in Chapter 3.

2.1 Coordinate systems

In the study of magnetospheric physics, it is often useful to organize observations and phenomena in a magnetic coordinate system rather than in a geographic coordinate system. There are two magnetic coordinate systems that are particularly useful for this thesis.

2.1.1 Geomagnetic coordinate system (MAG)

The geomagnetic coordinate system (MAG) is defined so that the z axis is parallel to the magnetic dipole axis and points northward. The y axis is

perpendicular to geographic poles such that if \mathbf{D} is the dipole position and \mathbf{P} is the South Pole, $\mathbf{y} = \mathbf{D} \times \mathbf{P}/|\mathbf{D} \times \mathbf{P}|$. The x axis completes the right handed orthogonal set ($\mathbf{x} = \mathbf{y} \times \mathbf{z}$).

In this coordinate system, magnetic latitude is measured from the equator in the magnetic meridians, positive is northward and negative is southward [Kivelson and Russell, 1995]. This coordinate system is used frequently in organizing ionospheric observations. The magnetic longitude is measured eastward of the x -axis, but magnetic longitude itself is seldom used. Instead, magnetic longitude is used to calculate magnetic local time (MLT). MLT is defined such that the magnetic longitude that intersects the Sun-Earth line is noon or 12 MLT. In other words, the magnetic longitude of the Sun is noon.

2.1.2 Geocentric solar magnetospheric system (GSM)

The geocentric solar magnetospheric (GSM) coordinate system has its origin at the center of the Earth and its x axis lies along the line connecting the centers of the Earth and the Sun [Kivelson and Russell, 1995]. The y axis is perpendicular to the Earth's magnetic dipole so that x - z plane contains the dipole axis. The z axis is defined such that the northern magnetic pole has positive z coordinate.

This coordinate system is used frequently to organize observations in the magnetosphere, magnetosheath, and bow shock (see Figure 1.2). All the magnetospheric observations, models, and theories discussed Chapters 3, 4, 5, and

Part of this chapter has been published in the following papers:

Wing, S., P. T. Newell, C.-I. Meng (2005), Cusp Modeling and Observations at Low Altitude, *Surveys in Geophysics*, 26: 341-367, doi:10.1007/s10712-005-1886-0.

Wing, S., Patrick T. Newell, and J. Michael Ruohoniemi (2001), Double cusp: Model prediction and Observational Verification, *Journal of Geophysical Research*, 106, 25,571-25,593.

Contribution statement:

S. Wing: contributed main ideas, wrote the code for the open field line particle precipitation model, analyzed DMSP data for comparisons with model, discovered double cusp, performed most of the work, wrote the papers.

P. T. Newell: contributed some ideas, provided useful comments and discussions.

C.-I. Meng: provided some comments.

J. M. Ruohoniemi: provided SuperDarn convection data that S. Wing converted to electric field.

6 are presented in this coordinate system.

2.2 Space plasma properties

Most known visible matter in the universe is plasma. In fact, more than 99% of all known visible matter is in the plasma state. A plasma is a gas of charged particles (ions and electrons) which has roughly equal numbers of free positive and negative carriers within the same volume element and which exhibits a collective behavior. An important collective property of the plasma is charge quasi-neutrality as described next.

The electric Coulomb potential field of a charged particle, q is given by

$$\phi_c = \frac{q}{4 \pi \epsilon_0 r} \quad (2.1)$$

where ϕ_c = Coulomb potential, ϵ_0 = free space permittivity, and r = distance from the charged particle. In quasi-neutral plasma, the particle's Coulomb potential is shielded by other charges in the plasma. As a result, the particle's potential assumes a Debye potential form,

$$\phi_c = \frac{q}{4 \pi \epsilon_0 r} e^{-r/\lambda_d} \quad (2.2)$$

where λ_d = Debye length. Debye length is the characteristic length scale for which a balance is obtained between thermal particle energy, which can perturb electrical neutrality, and the electrostatic potential energy resulting from charge separation. Debye length is a function of electron temperature and plasma density,

$$\lambda_d = \left(\frac{\epsilon_0 k_b T_e}{n_e e^2} \right)^{0.5} \quad (2.3)$$

where k_b = Boltzmann constant, T_e = electron temperature, n_e = electron density, and e = electron charge. The Debye length indicates the shielding distance of an ion charge by the electrons with temperature T_e . Around the ion there is a cloud of electrons with radius λ_d that shields the electrostatic field of the ion from the surrounding plasma. If we were to take into account the effects of ions, we would need to calculate the effective Debye length, which has two terms, one for ions and one for electrons. The ion term looks similar to equation (2.3), except that T_e is replaced with ion temperature (T_i) and n_e is replaced with ion density (n_i) [$n_i \approx n_e$ in quasi-neutral plasma]. For ions having similar density and temperature as the electrons, the effective Debye length deviates slightly (about 30%) from λ_d calculated in equation (2.3).

When the physical dimension of the system L is large compared to λ_d , $L \gg \lambda_d$, the plasma behaves quasi-neutrally in stationary state. That is, on average, the plasma looks electrically neutral to the outside observer because the randomly distributed particle electric charge fields mutually cancel each other out. In each volume element, the microscopic space charge fields of individual particle cancel each other out to provide macroscopic charge quasi-neutrality.

The number of particles in a Debye sphere is given by

$$N_d = \frac{4 \pi n_e \lambda_d^3}{3} \quad (2.4)$$

The plasma parameter, g , is defined as

$$g = N_d^{-1} \quad (2.5)$$

Combining equations (2.3), (2.4), and (2.5), we can write g as

$$g \sim \frac{n_e^{0.5}}{T_e^{1.5}} \quad (2.6)$$

The description of plasma is significant only if $g \ll 1$ because when this condition is satisfied, we have a large enough quantity that Debye shielding is meaningful and statistical collective behavior applies. The plasma parameter, g , holds another importance. The collision frequency of the particles within the plasma increases with increasing density and with decreasing temperature. Thus, smaller g corresponds to less collisions and in the limit $g \rightarrow 0$, the plasma becomes collisionless. In most regions in the magnetosphere, density is low and temperature is high. Hence, $g \ll 1$ and the plasma approaches the collisionless limit (collisionless is a good approximation).

2.3 Particle motion

The role of electric and magnetic forces are critical to understanding of the motions of the space particles, ions and electrons. A charged particle moving in space would experience the Lorentz force

$$\mathbf{F} = q\mathbf{E} + q\mathbf{V} \times \mathbf{B} \quad (2.7)$$

where \mathbf{E} = electric field, \mathbf{B} = magnetic field, q = particle electric charge, and \mathbf{V} = velocity. Note that in the literature, there is no standard notation for the Lorentz force. Sometimes, the first term is referred to as the Coulomb force and only the second term is referred to as the Lorentz force. In this thesis, we adopt the convention that refers the two terms in equation (2.7) as the Lorentz force. If \mathbf{V} is

small such that relativistic effects can be ignored and gravity is negligible, from Newton's law, equation (2.7) can be rewritten as

$$m \, d\mathbf{V}/dt = q\mathbf{E} + q\mathbf{V} \times \mathbf{B} \quad (2.8)$$

where m = mass of the particle. In a uniform magnetic field with $\mathbf{E} = 0$, a charged particle moves in circular motion because the magnetic field acts only perpendicularly to \mathbf{V} . So, if we assume that \mathbf{B} is along \mathbf{z} , equation (2.8) can be rewritten as

$$m \, dV_x/dt = qV_y B; \quad m \, dV_y/dt = -qV_x B \quad (2.9)$$

Equation (2.9) describes a circular motion of the particle in the plane perpendicular to the magnetic field \mathbf{B} . It can be rewritten as

$$\frac{V_{\perp}^2}{\rho} = \frac{qBV_{\perp}}{m} = \omega V_{\perp} \quad (2.10)$$

where V_{\perp} = perpendicular velocity or velocity perpendicular to the magnetic field, ρ = gyroradius or Larmor radius or cyclotron radius, and $\omega = qB/m$ = gyrofrequency or cyclotron frequency. Equation (2.10) describes a circular motion that is in the left hand sense for $q > 0$ and right hand sense for $q < 0$.

However, the electric field \mathbf{E} may not be zero. There are two interesting possible cases that can be considered. First, \mathbf{E} can be parallel to the magnetic field (E_{\parallel}) or has a component that is parallel to the magnetic field. The electric field can exert a force that can accelerate positively charged particles in the direction of E_{\parallel} and negatively charged particles in the opposite direction. The field-aligned currents are carried mostly by electrons. As discussed in Chapters 3, 4, and 5, upward E_{\parallel} sometimes develops in the upward field-aligned current regions to accelerate electrons downward in order to maintain the current [*Knight*, 1973]. In the second case, \mathbf{E} can be perpendicular to the magnetic field (E_{\perp}) or has a component that is perpendicular to the magnetic field. This condition is often seen in the plasma sheet (region 3 in Figure 1.2) where \mathbf{B} is northward and \mathbf{E} is duskward. In the presence of the electric field, the motion of the particle still gyrate, but electrical force accelerates the particle during part of each orbit and decelerates it during the remaining part of the orbit. The orbit becomes a distorted circle with larger radius during half of the orbit and smaller radius during the other half of the orbit. As a result, there is a net displacement in the direction perpendicular to \mathbf{E} . The particle drifts with velocity \mathbf{V}_d that is given by

$$\mathbf{V}_d = \mathbf{E} \times \mathbf{B}/B^2 \quad (2.11)$$

where $B = \text{magnitude of } \mathbf{B}$. \mathbf{V}_d is often referred to as \mathbf{E} cross \mathbf{B} ($\mathbf{E} \times \mathbf{B}$) drift velocity. Note that both positively and negatively charged particles, e.g., ions and electrons, move in the same direction and at the same velocity, independent of the mass. Hence, \mathbf{V}_d does not introduce currents in the magnetosphere. However, in the ionosphere, \mathbf{V}_d introduces currents due to ions having larger collisional cross sections than the electrons. The $\mathbf{E} \times \mathbf{B}$ drift is quite important in the magnetosphere and ionosphere, as discussed in Chapters 3 and 5.

So far, we have described motions in a uniform magnetic field. Although sometimes this can be a good approximation, in the magnetosphere this is typically not the case. Instead, the magnetospheric magnetic field varies approximately inversely to the cube of distance ($B \propto r^{-3}$) due to the magnetic dipole. A gradient in the field strength in the direction perpendicular to \mathbf{B} produces a drift called gradient drift velocity, which is given by

$$\mathbf{u}_g = \frac{1}{2} m V_{\perp}^2 \mathbf{B} \times \frac{\nabla B}{q B^3} \quad (2.12)$$

where $\mathbf{u}_g = \text{gradient drift velocity}$. The gradient drift comes about because as a particle gyrate in a magnetic field whose strength changes from one side of the gyration to the other, its orbit alternately becomes smaller and larger. Over several gyration, the particle will drift perpendicularly to both the magnetic field (\mathbf{B}) and the gradient the magnetic field (∇B).

The curvature of the magnetic field introduces an additional drift called curvature drift. As the particle moves along a curved magnetic field line, it experiences a centrifugal acceleration. The radius of gyration increases away from the center of the curvature of the field line as the particle drifts perpendicularly to \mathbf{B} . The curvature drift velocity is given by

$$\mathbf{u}_c = \frac{m V_{\parallel} \mathbf{B} \times (\hat{\mathbf{b}} \cdot \nabla) \hat{\mathbf{b}}}{q B^2} = \frac{m V_{\parallel}^2 \mathbf{B} \times \hat{\mathbf{n}}}{R_c q B^2} \quad (2.13)$$

where $\mathbf{u}_c = \text{curvature drift velocity}$, $\hat{\mathbf{b}} = \mathbf{B}/B$, $\hat{\mathbf{n}} = \text{unit vector perpendicular to } \mathbf{B}$ that points away from the center of curvature, $R_c = \text{radius of curvature}$, which is defined as

$$\frac{\hat{\mathbf{n}}}{R_c} = -(\hat{\mathbf{b}} \cdot \nabla) \hat{\mathbf{b}} \quad (2.14)$$

Because curvature and gradient drifts have a dependency on the charge q of the particle, these drifts will introduce electric currents. The ring current shown in Figure 1.2 and discussed in Chapter 6 is produced mainly by the curvature and gradient drifts of the electrons and ions in the inner magnetosphere.

In a collisionless plasma ($g \ll 1$), a particle can move for many gyroradii without being influenced by other particles, even though its energy changes. If the magnetic field changes slowly enough (the magnetic field changes encountered by the particle within a single gyration is small compared with the strength of the initial field), the particle's magnetic moment is conserved. The magnetic moment is defined as

$$\mu = \frac{0.5 m v_{\perp}^2}{B} \quad (2.15)$$

where μ = magnetic moment. Equation (2.15) is often referred to as the first adiabatic invariant. The term adiabatic refers to the requirement that μ may remain constant as long the parameters of the system such as magnetic field strength and direction change slowly.

2.4 Guiding center motion

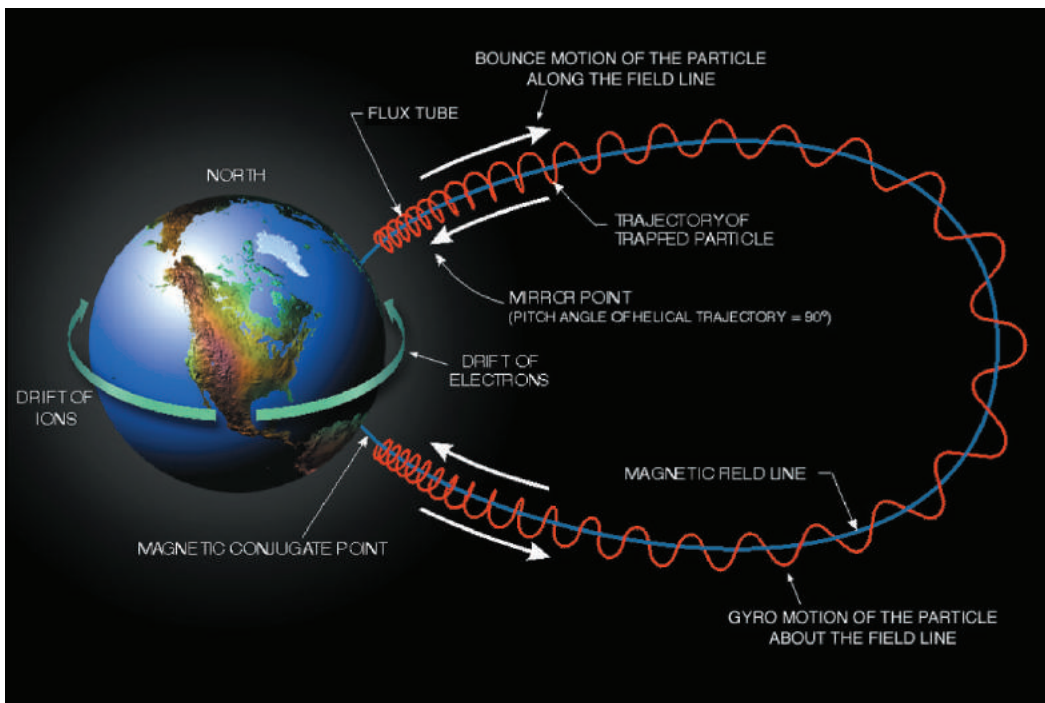


Figure 2.1. The motion of charged particle along the Earth's magnetic field (adapted from *Lyons and Williams*, 1984).

Although the equations of motion for a charged particle in magnetic and electric fields are known (Section 2.3), it is often difficult to derive and

conceptualize the formal solutions of the particles, which often involve complex numerical integrations. In fact, it can be shown that the motion of a charged particle in a dipole magnetic field has no general analytical solution and the particle trajectory must be obtained by a lengthy numerical integration [Stormer, 1955].

However, in many regions in space, the guiding center approximation along with the concepts of adiabatic invariant described in Section 2.3 can be used to track the charged particle motion. In the guiding center approximation, the instantaneous position of a charged particle motion in a magnetic field can be broken down into its circular motion of gyroradius ρ about the magnetic field and the displacement of the center of this circular motion \mathbf{R}_g , which is referred to as the guiding center. We can write the position vector \mathbf{r} as

$$\mathbf{r} = \mathbf{R}_g + \boldsymbol{\rho} \quad (2.16)$$

Combining equations (2.16) and (2.8), ignoring gravity, we get

$$m \frac{d^2 \mathbf{r}}{dt^2} = q\mathbf{E} + q \left(\frac{d\mathbf{r}}{dt} \times \mathbf{B} \right) \quad (2.17)$$

Time averaging over one gyroperiod so that $\langle \rho \rangle = \langle \dot{\rho} \rangle = \langle \ddot{\rho} \rangle = 0$ and expanding \mathbf{B} and \mathbf{E} in a Taylor series about \mathbf{R}_g , we obtain the nonrelativistic guiding center equation

$$m \frac{d^2 \mathbf{R}_g}{dt^2} = q\mathbf{E} - \mu \nabla \mathbf{B} + q \left(\frac{d\mathbf{R}_g}{dt} \times \mathbf{B} \right) + O\left(\frac{\rho}{x}\right) \quad (2.18)$$

where μ = magnetic moment (equation 2.15), x = scale length over which the magnetic field changes appreciably, $O(\rho/x)$ = order of ρ/x .

In the guiding center approximation, the particle's motion in the magnetosphere is broken down into three components: (1) gyration about a magnetic field line, (2) bounce back and forth along the magnetic field line between the reflection (mirror) points, and (3) a slow longitudinal drift around the Earth. This is illustrated in Figure 2.1. However, the vast differences in time scales associated with these three components make it possible to separate each individual component.

2.5 Signature of dayside magnetic reconnection in the ionosphere

A common process in space plasma is magnetic reconnection in which two

oppositely directed magnetic field lines “reconnect” where the plasma on both field lines become demagnetized in a small diffusion region, resulting in an X-line configuration and plasma jets [Eastwood, 2008]. Magnetic reconnection plays an important role in the dayside solar wind-magnetosphere interaction, which is depicted in Figure 2.2. A purely southward interplanetary magnetic field (IMF) and a northward magnetospheric magnetic field near the subsolar magnetopause reconnect, creating two open field lines. Note that reconnection at the dayside magnetopause is sometimes referred to as merging, but in this thesis we use the term reconnection and merging interchangeably to refer to the dayside magnetopause reconnection. The newly open magnetic field lines are carried by the solar wind to the magnetotail on nightside. In the magnetotail, the open field lines reconnect to form a closed field line, which is convected back to the dayside. This process is known as the Dungey cycle and depicted in Figure 2.2 [Dungey, 1961].

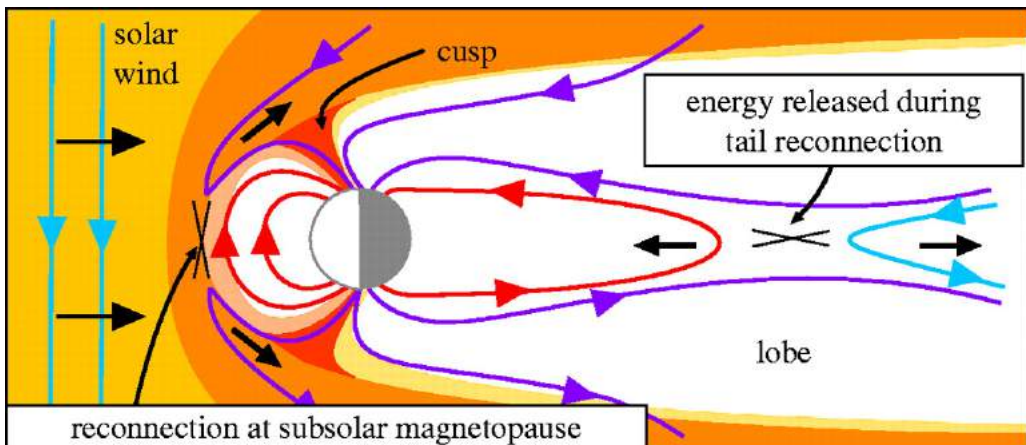


Figure 2.2. Illustrating Dungey cycle. During periods of southward IMF, IMF (blue) and the closed Earth’s magnetic field (red) reconnect near the subsolar magnetopause, creating two open field lines (purple). The newly open magnetic field lines are convected to the nightside magnetosphere by the solar wind flow. In the magnetotail, the open field lines reconnect to form a closed field line (red), which is convected back to the dayside. (from Eastwood, 2008).

As a result of the dayside reconnection, shocked solar wind ions and electrons can and do enter the magnetosphere and some precipitate into the ionosphere. Although these particles originate in the solar wind, once they have entered the magnetosphere and ionosphere they exhibit distinctly different characteristics in energy, density, and temperature at different local times and

latitudes. Observations at low altitude show that the resulting particle precipitation associated with open field lines can generally be classified into four regions (ordered from low to high latitude for a typical southward IMF case): open field line low-latitude boundary layer (LLBL), cusp, mantle, and polar rain [e.g., *Newell et al.*, 1991; *Newell and Meng*, 1995; *Onsager and Lockwood*, 1997].

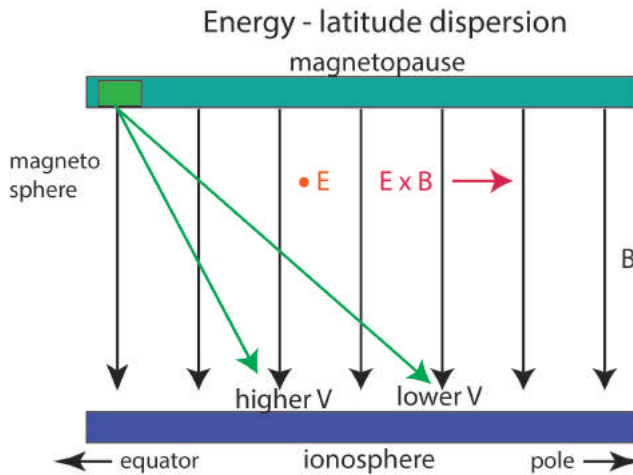


Figure 2.3. Illustrating energy-latitude dispersion in the southward IMF cusp. The geometry is for the northern hemisphere, but using southern hemispheric geometry will give the same result. The equator is to the left and the pole is to the right. The green region at the top is the magnetopause while the blue region at the bottom is the ionosphere. The magnetospheric \mathbf{B} points downward, the magnetospheric \mathbf{E} points out of the page, and hence the convective $\mathbf{E} \times \mathbf{B}$ points to the right. Let the left most magnetic field line be the field line that reconnects with the IMF. The ions on the open field line can enter the magnetosphere and precipitate into the ionosphere. The ions with higher V will arrive first in the ionosphere. Sometime later, the ions with lower V will arrive in the ionosphere. By the time the slower ions reach the ionosphere, they will have spent more time $\mathbf{E} \times \mathbf{B}$ convecting poleward than the faster ions. As a result the ions with lower V will arrive at a more poleward location in the ionosphere than the ions with higher V .

In this section, we describe the characteristics of the particles in each of the four regions. In Section 2.6.1, we explain why these four regions exist with modeling and observations.

The cusp, sometimes known as “cusp proper”, is characterized by very high-fluxes of ions and electrons. Typically, the ions have a spectral peak of $> 10^8 \text{ eV} (\text{cm}^2 \text{ s eV sr})^{-1}$. The typical average electron and ion energies, $\langle E_e \rangle$ and

$\langle E_i \rangle$ are: $\langle E_e \rangle < 200$ eV and 300 eV $< \langle E_i \rangle < 3$ keV. The cusp ions frequently, but not always, exhibit energy-latitude dispersion, especially during periods of southward IMF. The energy-latitude dispersion can be explained as a time of flight effect as illustrated in Figure 2.3. The ions with higher velocity will arrive first in the ionosphere and at lower latitude than those with lower velocity. This is because ions with higher velocity spend less time $\mathbf{E} \times \mathbf{B}/B^2$ (in this thesis herein, written as $\mathbf{E} \times \mathbf{B}$ for short) convecting poleward. The energy-latitude dispersion in a DMSP cusp observation can be seen in Figure 2.4, which presents a DMSP observation of cusp, mantle, and polar rain.

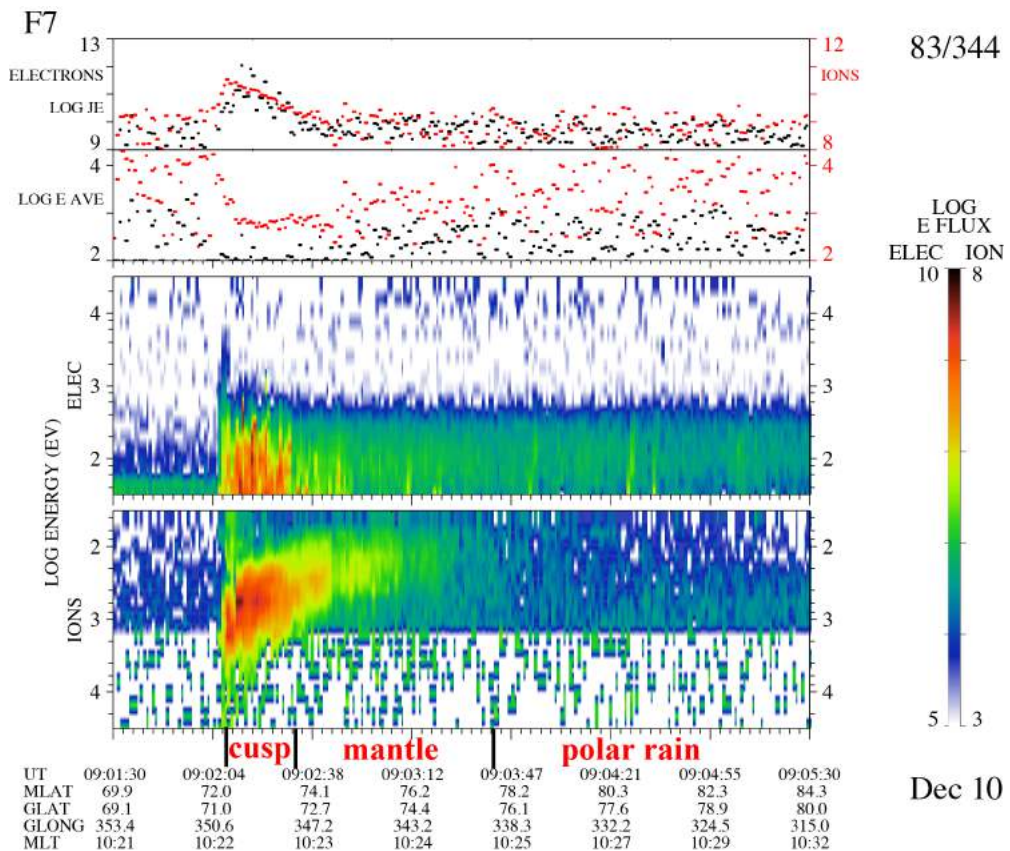


Figure 2.4. The spectrogram of typical Defense Meteorological Satellite Program (DMSP) data. The spectrogram is for December 10, 1983, DMSP F7 observation, which shows a typical cusp, mantle, and polar rain. The cusp, the mantle, and the polar rain regions are labeled in red beneath the X axis. The spectrogram shows log differential energy flux, in units of $\text{eV} (\text{cm}^2 \text{s sr eV})^{-1}$, from 32 eV to 30 keV, with the ion energy scale inverted. The lower of the two line plots shows the average energy in eV for the electrons (black) and ions (orange), and the top line plot is of integral energy flux in units $\text{eV} (\text{cm}^2 \text{s sr})^{-1}$.

The open field line LLBL (open-LLBL) is the region closest to the open-closed field line boundary (see Figure 2.5b). In this region, typically only ions with energies > 1 keV are present. In the mantle, the ions and electrons have lower energies and lower fluxes than those in the cusp. The typical mantle energies range from a few tens to 100 eV, but there are considerable variabilities. The fluxes are lower by a factor of 3–10 from those in the cusp. The mantle ions generally exhibit energy-latitude dispersions. The polar rain electrons have typical energies $<$ a few hundred eVs and have little structures. There is a noticeable absence of ions in the polar rain.

2.6 APL open field line particle precipitation model (APL–OPM)

Using the equations presented in Section 2.3, we construct an open field line particle precipitation model.

Over the three decades since their discoveries, researchers have been able to gather enough evidence to infer some of the main physical processes that give rise to the four particle precipitation regions, namely open-LLBL, cusp, mantle, and polar rain. However, self-consistent global models are not yet advanced enough to permit precise quantitative comparisons with the observations. For example, single-fluid MHD simulations cannot capture parallel electric field arising from the charge quasi-neutrality constraints in the open field lines in the magnetosphere. The suprathermal electrons, which populate much of polar rain, are absent in the MHD simulations.

Efforts to produce a model that can withstand detailed comparisons to low-altitude or mid-altitude cusp data advanced significantly with the work of *Onsager et al.* [1993]. Instead of developing a global model self-consistently for the entire magnetosheath-magnetosphere-ionosphere system, *Onsager et al.* used an assimilative approach that combines good quality empirical models for different regions. However, the original model result and DMSP data comparison shows that the southward IMF cusp can be modeled fairly well but the model electrons have a much more latitudinally extended entry and a much higher temperature in the mantle and polar rain regions [*Onsager et al.*, 1993; *Wing et al.*, 1996]. Other problems include the cusp latitude being several degrees too high (mainly a problem with the magnetic field model) and ionospheric convection velocity (100

m s^{-1}) being several times too low [*Wing et al.*, 1996].

At the Johns Hopkins University Applied Physics Laboratory (APL), we developed an open field line particle precipitation model (APL–OPM) that basically uses the same approach as *Onsager et al.* [1993]. However, we have introduced more realistic processes into the model. We extended the original Onsager model as follows [*Wing et al.*, 1996; *Newell and Wing*, 1998; *Wing et al.*, 2001]: (1) imposed charge quasi-neutrality with a self-adjusting parallel electric field; (2) included suprathermal electrons; (3) used a κ distribution for ions; (4) replaced the *Stern* [1985] magnetic field model with the T96 model [*Tsyganenko and Stern*, 1996]; and (5) used the convective electric field obtained from the statistical APL convection patterns [*Ruohoniemi and Greenwald*, 1996]. The justifications for these improvements are listed below.

Electrons have thermal speeds far exceeding the magnetosheath flow speed and therefore can enter the magnetosphere along the open field lines across the polar cap. In contrast, ions have slower thermal speeds and therefore can only enter the magnetosphere from the regions in the magnetopause where the magnetosheath flow is subsonic [*Reiff et al.*, 1977]. Several researchers have noted that there has to be a mechanism that limits the entry of the electrons to balance the charge carried by the ions, maintaining charge quasi-neutrality in the precipitating particle populations [e.g., *Reiff et al.*, 1977; *Burch*, 1985]. Solar wind electrons have been observed to have thermal and suprathermal components [e.g., *Feldman et al.*, 1978; *Fairfield and Scudder*, 1985]. The original Onsager model mantle ions have much lower flux than in the DMSP data, but ions in the solar wind and the magnetosphere have been observed to have κ distributions [e.g., *Feldman et al.*, 1974; *Christon et al.*, 1989]. A κ distribution resembles a Maxwellian at low energies, but approaches a power law distribution at high energies. For a given characteristic energy, a κ distribution produces a higher total flux in the ionosphere, owing to its high-energy tail. *Christon et al.* [1989] found empirically through spectral fitting that magnetospheric (plasma sheet) ions typically have $\kappa = 4\text{--}8$. Magnetic field models have been steadily improved in the recent years, e.g., with the inclusion of field-aligned currents etc. [e.g., *Tsyganenko and Stern*, 1996]. Finally, in much of the polar cap, the electric field frequently deviates from the dawn-dusk direction, especially when the IMF y -component dominates. Hence, a more realistic electric field from APL convection pattern [*Ruohoniemi and Greenwald*, 1996] is used.

APL–OPM model can now be summarized as follow. For a given IMF,

solar wind temperature and density, ionospheric convection speed, and dipole tilt angle, the model computes the phase space density of the precipitating ions and electrons in three steps.

1. In the first step, which assumes the magnetic moment is conserved, the model traces ionospheric particles back along the guiding center to the magnetopause entry point using T96 magnetic field model [Tsyganenko and Stern, 1996] and electric field derived from APL convection pattern [Ruohoniemi and Greenwald, 1996].
2. The second step is to compute the acceleration ($\mathbf{j} \cdot \mathbf{E} > 0$) or deceleration ($\mathbf{j} \cdot \mathbf{E} < 0$) imparted on the particles when they cross the magnetopause current layers from the magnetosheath to the magnetosphere. This computation is done with the aid of the de Hoffman-Teller reference frame in which $\mathbf{E} = 0$ [e.g., Hill and Reiff, 1977; Cowley and Owen, 1989]. From this calculation, the model obtains the velocity that the particle originally had in the magnetosheath.
3. Finally, it computes the phase space density of particles with that velocity using the gas-dynamics calculations of Spreiter and Stahara [1985] with the assumption that solar wind electrons have a Maxwellian distribution and ions have a κ distribution. Solar wind electrons have thermal and suprathermal components. Charge quasi-neutrality is imposed with a self-adjusting parallel electric field. Assuming conservation of phase space density along particle trajectories, the model can be used to compute the differential energy flux at the location where the particle was “detected” in the ionosphere.

APL–OPM can model not just the cusp, but the entire open field line particle precipitation region, namely open-LLBL, cusp, mantle, and polar rain [Wing *et al.*, 1996 and 2001; Newell and Wing, 1998]. This suggests that all particle precipitation can be governed by the same physical processes. However, although the model generally works well, as shown in the examples given in Sections 2.6.1, 2.6.2, and 2.6.3, it still has deficiencies as outlined below.

Although the APL convection pattern provides an accurate electric field, it is not self-consistent with the T96 magnetic field model. The T96 model itself has its own deficiencies, e.g., it does not take into account the effects of IMF on the magnetopause shape and size, which in turn can affect the cusp footprint [e.g., Shue *et al.*, 1997]. The Spreiter and Stahara [1985] magnetosheath model is a single-fluid gas-dynamic model that does not take into account the magnetic field. In addition, the model has not taken all the particle precipitation processes into

account such as wave-particle interactions, non-adiabatic motions, particle diffusion across the magnetopause, etc.

Next, we show examples of the model runs for three cases: (1) strongly southward IMF, (2) weakly southward IMF, and (3) large IMF B_y and small IMF B_z .

2.6.1 Case 1: strongly southward IMF cusp

The result of the model calculation for the strongly southward IMF case is presented in Figure 2.5a (from Plate 2 in *Wing et al.* [2001]). Note that the y -axis of the ion panel displays the lowest energy at the top, the opposite from the way the electron is displayed. The input parameters to the model are: IMF (B_x, B_y, B_z) = $(-3.4, -0.5, -12.3)$ nT, solar wind thermal (core) component $n = 11 \text{ cm}^{-3}$, $T_i = 1 \times 10^5 \text{ K}$, $T_e = 3 \times 10^4 \text{ K}$, suprathermal (halo) component electron $n_s = 0.2 \text{ cm}^{-3}$, $T_s = 1 \times 10^6 \text{ K}$, $\kappa = 7$, and the altitude of “detected” particle = $1.13 R_E$, which corresponds to the DMSP spacecraft altitude. These IMF and solar wind parameters are chosen to match an event observed by the DMSP spacecraft shown in Figure 2.5b (we use the average values for the solar wind suprathermal electron density and temperature because there was no observation of suprathermal electrons for this event). DMSP are sun-synchronous satellites in a nearly circular polar orbit at an altitude of roughly 835 km and period of approximately 101 minutes per orbit. The SSJ4 instrumental package included on all recent DMSP flights uses curved plate electrostatic analyzers to measure ions and electrons from 32 eV to 30 keV in 19 logarithmically-spaced steps [*Hardy et al.*, 1984]. One complete 19–point electron and ion spectrum is obtained each second. The magnetic coordinates used in our studies are the Altitude Adjusted Corrected Geomagnetic coordinates (AACGM) [*Baker and Wing*, 1989]. For comparisons with DMSP observations, we trace 19 electrons and ions with energies from 32 eV to 30 keV in 19 logarithmically equally spaced steps, the same energies as the 19 electron and ion channels in the DMSP SSJ4 instrument. The solar wind thermal electron temperature is taken to be somewhat lower than that of the ions to compensate for excessive heating in the model magnetosheath. This is because the *Spreiter and Stahara* [1985] model is a single fluid model, which overestimates the amount of electron heating in the magnetosheath. Since the ions carry most of the kinetic energy, upon encountering the magnetopause they are thermalized to a higher temperature than are electrons. Many large-scale features that are seen in

the model can also be seen in a typical DMSP pass such as the one shown in Figure 2.5b.

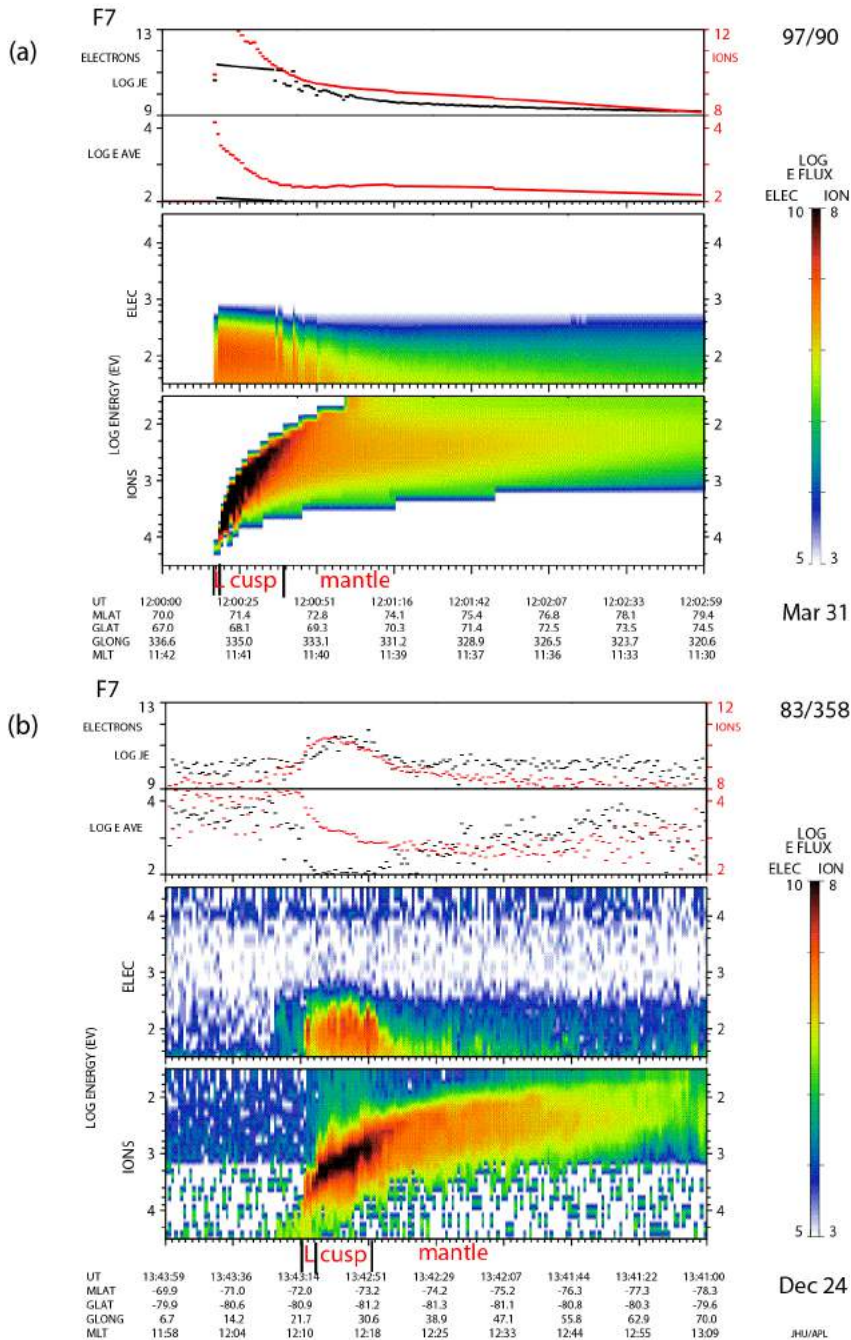


Figure 2.5. (a) The results of the model calculations for strongly southward IMF case and (b) a DMSP observation under similar IMF condition. See caption of Figure 2.4 for the descriptions of the units, scales etc. The red labels beneath the x-axis indicate the region types. L indicates the open-LLBL, which is located equatorward of the cusp.

Figure 2.5 clearly shows that the model can successfully calculate the precipitating ion and electron fluxes for the cusp, mantle, and the open-LLBL, which is located equatorward of the cusp (in order to focus more on the cusp, comparisons with the polar rain are not shown here, but they have been shown to compare well [Wing *et al.* [1996]). The model cusp equatorward boundary is located at 71° invariant magnetic latitude (Λ), which is very close to the statistical cusp boundary for the same IMF condition found in previous studies [e.g., Carbury and Meng, 1986; Newell and Meng, 1989; Zhou *et al.*, 2000; Wing *et al.*, 2001].

The southward IMF cusp exhibits an energy-latitude dispersion, in which the characteristic energy decreases with increasing latitude. The low energy cut off decreases with increasing latitude, which is mainly due to the time of flight effect, as illustrated in Figure 2.3. The higher-energy ions arrive in the ionosphere closer to the point of injection and within each field line, the lower-energy particle comes from a lower latitude [e.g., Onsager *et al.*, 1993]. The high energy cutoff also decreases with increasing latitude in the model results as well as in satellite observations. In the model, this primarily results from the decreasing magnetosheath temperature and decreasing acceleration at the magnetopause crossing at the higher latitude entry points.

The model cusp ions originate from the low latitude magnetopause, within $7 R_E$ from the subsolar point. This result is in agreement with the previous observational cusp studies during the period of southward IMF [e.g., Reiff *et al.*, 1977]. In this thesis, "low latitude magnetopause" refers to the magnetopause locations where $|z| < \sim 5 R_E$, "mid latitude" refers to the region $5 R_E < |z| < 10 R_E$ and "high latitude" refers to regions where $|z| > \sim 10 R_E$.

The success of the open field line particle precipitation model strongly suggests that the same large-scale processes govern all four particle precipitation regions in the open field line domain, namely, open-LLBL, cusp, mantle, and polar rain [Wing *et al.*, 1996]. A question arose in early magnetospheric studies: If all these particles originate from solar wind, why do they look so different at different locations [Tascione, 1994]? Although previous observational studies have offered hints and suggestions, we can address this question more definitively and comprehensively with modeling.

Open field line LLBL is the region closest to the open-closed boundary. When the field line first becomes open, electrons having higher speeds than ions flow into the magnetosphere ahead of the ions. Charge quasi-neutrality and the resulting parallel electric field, however, limit the number of electrons that can

enter. Thus, in this region, few electrons and ions are present. In the cusp, the ions have reached the ionosphere and intense fluxes of ions and electrons are usually observed. In this region, the electrons and ions can enter the magnetosphere relatively freely because the numbers of magnetosheath ions and electrons are already balanced, resulting in little or no parallel electric field. In the mantle region, fewer ions can enter as the magnetosheath flow becomes increasingly tailward and larger, whereas the magnetospheric magnetic field (and hence precipitating particle velocity) becomes more sunward, a condition which is less favorable for particle entries. In this region, $\mathbf{j} \cdot \mathbf{E} < 0$, which means that energy is dissipated leading to plasma deceleration as it crosses the magnetopause [e.g., *Hill and Reiff, 1977; Cowley and Owen, 1989*]. Some of the solar wind thermal or core electron entries are limited by the ensuing parallel electric field that arises to maintain charge quasi-neutrality. Finally, in the polar rain region, no significant amount of ions enter the magnetosphere and the parallel electric field rises to the level where only higher energy tail end of the core electrons and the suprathermal electrons can enter the magnetosphere, by the virtue of having higher energy that can overcome the parallel electric potential. Chapter 3 discusses further the parallel electric potential in the open field line regions.

2.6.2 Case 2: weakly southward IMF cusp

In the second case, the IMF is weakly southward. The input parameters to the model remain the same as before except for the IMF, which has been changed to IMF $(B_x, B_y, B_z) = (-0.5, -0.5, -3)$ nT. The model output and DMSP observations under similar IMF conditions are shown in Figures 2.6a and 2.6b, respectively (from Plate 3 in *Wing et al. [2001]*). Figure 2.6 shows that again the model seems to be able to capture the macro-scale features that are seen in the observations. The location of the cusp equatorward boundary at $76.5^\circ \Lambda$ is very close to the statistical cusp boundary for similar IMF periods [e.g., *Wing et al., 2001; Carbary and Meng, 1986; Newell et al., 1989; Zhou et al., 2000*]. However, these studies also show that the locations of this boundary exhibit large scatters. The DMSP cusp in Figure 2.6b was obtained not under the same exact solar wind and IMF conditions as in Figure 2.6a. (To facilitate comparisons between the model results, the solar wind input parameters are kept the same and only the IMF's change in Figures 2.5a and 2.6a). These two factors contribute the discrepancy of the location of this boundary in the model results and the DMSP example in Figure 2.6.

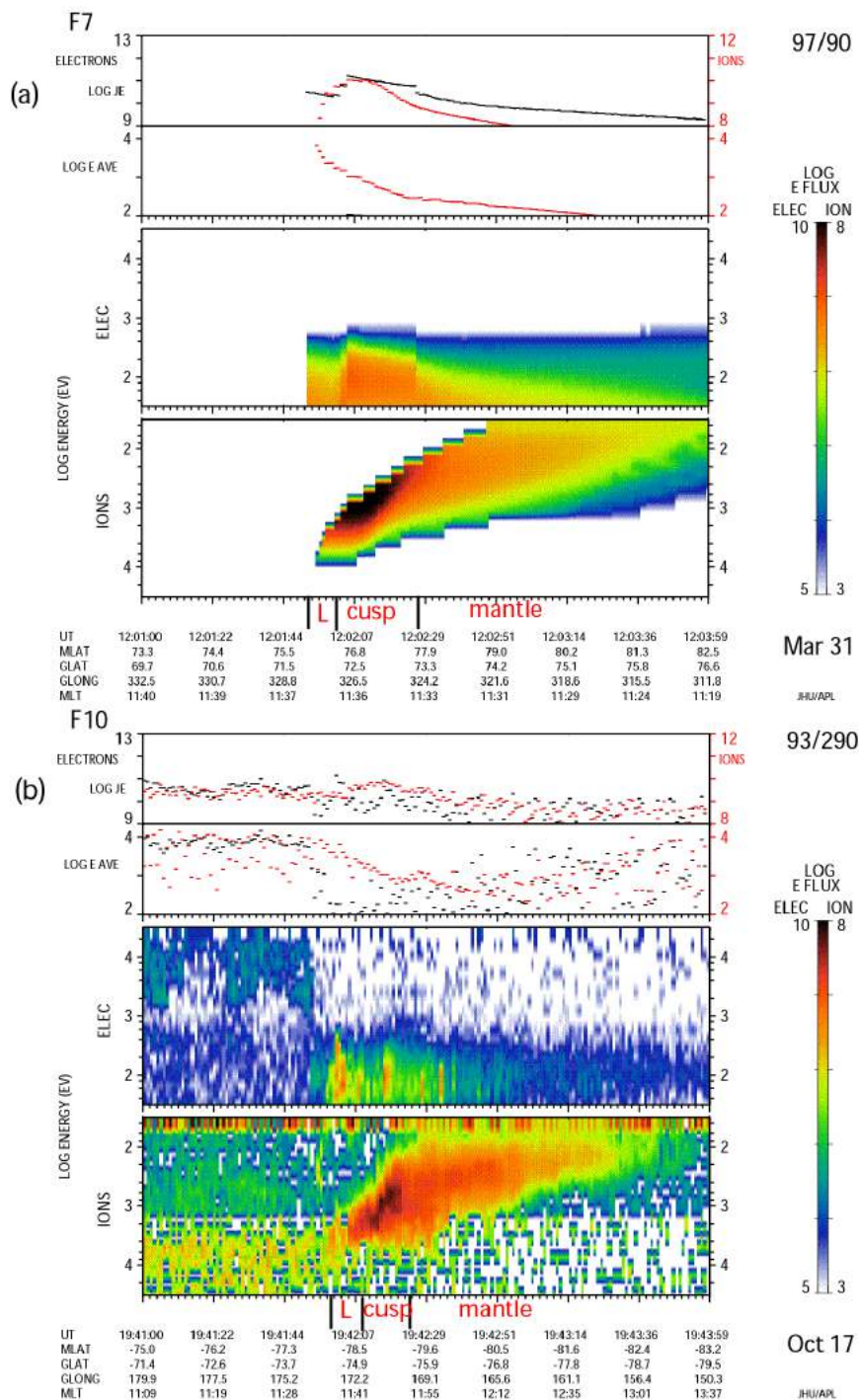


Figure 2.6. The same as Figure 2.4, except for weakly southward IMF case. See caption of Figure 2.4 for the descriptions of the units, scales etc.

One of the main differences between this and the previous IMF case is that the cusp location moves to higher latitude as IMF B_z increases, a well-documented phenomenon in many observational studies [e.g., *Carbary and Meng, 1986; Newell et al., 1989; Zhou et al., 2000*]. The movement of the cusp location has been interpreted in terms of reconnection and the flux erosion on the dayside when IMF B_z turns more southward [e.g., *Zhou et al., 2000*]. Our model does not have explicit reconnection, but most of this effect is captured by the magnetic cusp location in T96 (geometrical effect). In addition, the model magnetopause increases in size with increasing IMF B_z , resulting in longer field lines between the ionosphere and the magnetopause shape [*Roelof and Sibeck, 1993*]. The longer field increases the duration of the particles undergoing $\mathbf{E} \times \mathbf{B}$ drift (time of flight effect). As a result, the particle cusp location is shifted more poleward of the open-closed field line separatrix compared to that in the strongly southward IMF cusp. Thus, the model predicts a wider open-LLBL for weakly southward IMF than that for strongly southward IMF.

The model cusp ions in the weakly southward IMF case originate in the low to mid latitude magnetopause/magnetosheath, $z \sim 2-10 R_E$. The higher energy cusp ions enter from mid-latitude magnetopause, $z \sim 5-10 R_E$. The entry points are at higher latitude compared to those for the strongly southward IMF case.

In both southward IMF cases, the near-noon magnetospheric magnetic field line and the $\mathbf{E} \times \mathbf{B}$ convection have little y -component. So, the precipitating cusp ions at noon originate approximately from the noon magnetopause at low-latitude. Once they enter the magnetosphere, they undergo strong $\mathbf{E} \times \mathbf{B}$ poleward drift, resulting in the classical cusp dispersion in which the ion characteristic energy decreases with increasing latitude, as shown in Figures 2.5 and 2.6.

2.6.3 Case 3: cusp for large IMF B_y and small IMF B_z

For the third case, the IMF B_z is weakly negative and B_y is strongly positive. The input parameters are the same as before, except that now IMF $(B_x, B_y, B_z) = (-3.4, 12.3, -0.5)$ nT. This IMF configuration amounts to -90° rotation in the y - z plane from the strongly southward IMF case while the magnitude remains unchanged. The model result is shown in Figure 2.7 (from Plate 4 in *Wing et al. [2001]*). The model predicts two cusps (double cusp) that are latitudinally separated. The lower latitude cusp has little or no dispersion (stagnant) and the

higher latitude cusp exhibits dispersion that has some resemblance to the classical southward IMF dispersion. The model stops tracing whenever the particle reaches $x < -50 R_E$. This explains the sudden cutoff of the polar rain electrons in Figure 2.7. However, the polar rain in this region is fairly homogeneous and featureless. Had the model continued tracing tailward of $x = -50 R_E$, the resulting polar rain spectra would look just like the ones immediately preceding the cutoff.

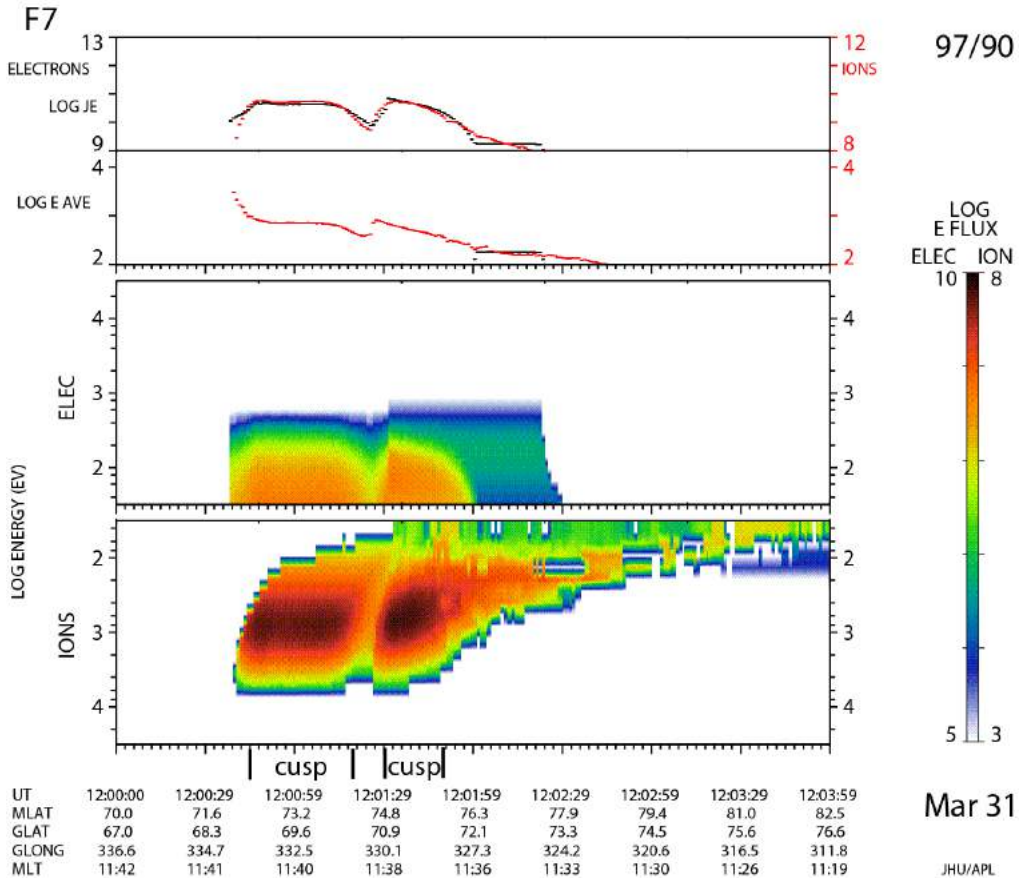


Figure 2.7. The same as Figure 2.4, except for strongly duskward and weakly southward IMF case. The calculation result shows two cusp regions that are latitudinally separated (double cusp). The model stops tracing at $x < -50 R_E$, which explains the sudden cut off of the polar rain electron spectra. See caption of Figure 2.4 for the descriptions of the units, scales etc.

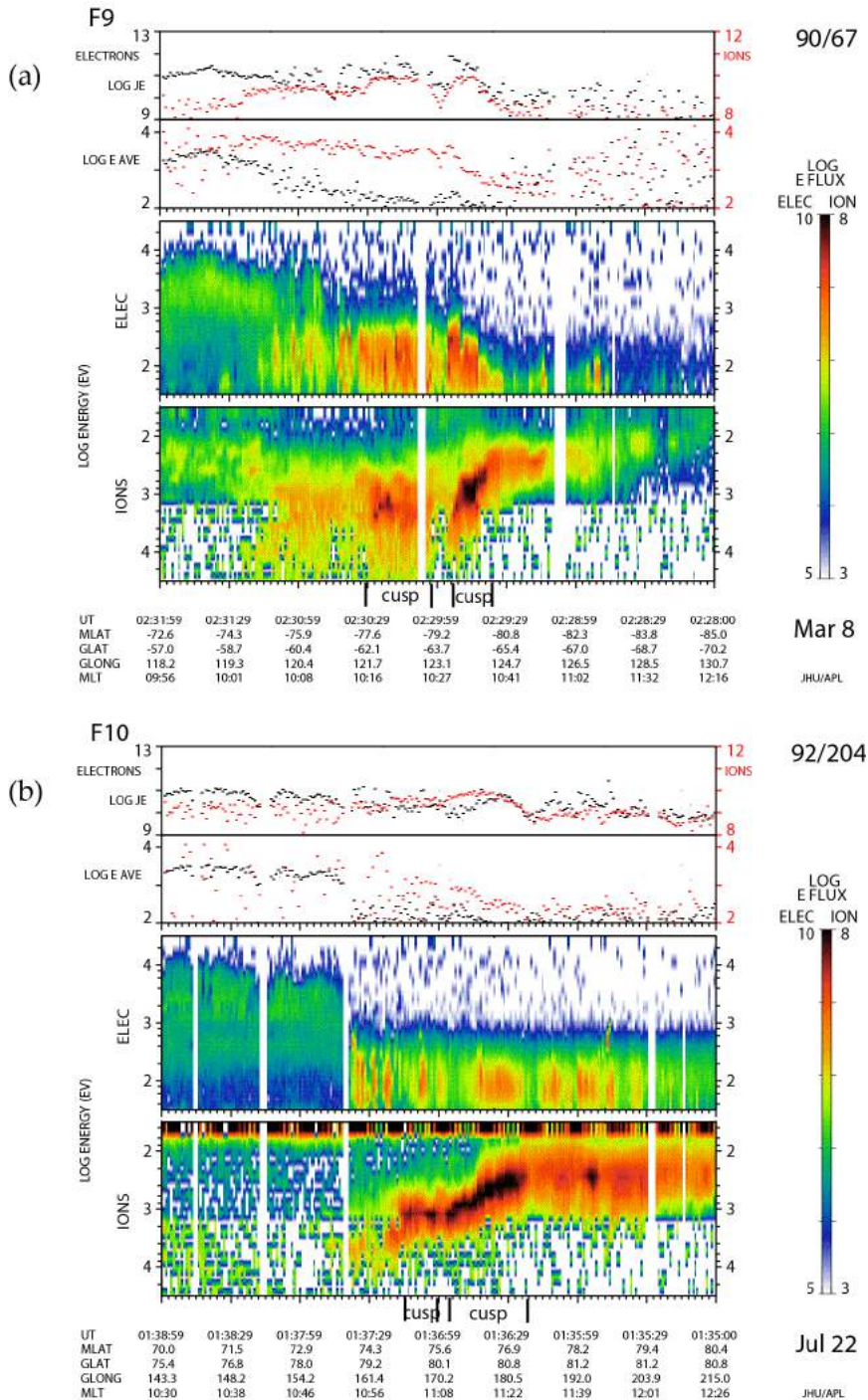


Figure 2.8. DMSF double cusp events (a, b) during periods of strongly duskward IMF. In (b) the lower latitude and the higher latitude cusp appear to form one cusp with extended latitudinal width. See caption of Figure 2.4 for the descriptions of the units, scales etc.

Examples of DMSP observations when IMF B_z is small and B_y is large are shown in Figure 2.8 (from Plate 5 in *Wing et al.* [2001]). In the DMSP observations, sometimes the separation between the two cusps narrow to give the impression of just one cusp with an extended latitudinal width. However, the dispersion signatures remain the same: the lower-latitude cusp has little or no dispersion and the higher-latitude cusp has dispersion that has some resemblance to that of the southward IMF cusp.

In the model, the lower-latitude cusp ions originate from low-latitude magnetopause ($-5 < z < 5 R_E$) and the higher-latitude cusp ions originate from high-latitude magnetopause ($7 < z < 13 R_E$). In the APL convection pattern, the $\mathbf{E} \times \mathbf{B}$ convection in the lower latitude cusp region is weak and directed downward, whereas in the higher latitude cusp region, it is strong and directed downward and poleward (see Figure 2 of *Wing et al.* [2001]). Thus, the model satellite traveling in the meridional direction near noon encounters ions from two magnetosheath sources. The first population is associated with the ions that enter from the low-latitude magnetopause near noon meridian and then undergo little $\mathbf{E} \times \mathbf{B}$ downward convection, nearly perpendicular to the satellite path. This results in the dispersionless ion signature in the lower-latitude cusp in Figures 2.7 and 2.8. The second population is associated with ions that enter at the high-latitude magnetopause eastward of the satellite location. Upon entering the magnetopause, the ions $\mathbf{E} \times \mathbf{B}$ convect strongly westward and poleward. Because of a significant poleward convection, the model satellite "observes" dispersion that is similar to the classical southward IMF dispersion. Our model does not have explicitly reconnection (merging) processes. If all magnetosheath ion entries are the result of reconnection, then the result here suggests that reconnection simultaneously occurs at the high and low latitude magnetopause [*Wing et al.*, 2001; *Weiss et al.* [1995]].

2.7 Summary

We review some of the quantitative aspects of magnetospheric physics. We review the equations for magnetic coordinate systems, plasma properties, particle motion, and guiding center motion. Then, we use some of these equations to construct an open field line particle precipitation model (APL-OPM). We show that the model calculations compare well with DMSP observations. Using the model, we show that all dayside open field line regions, namely, open-

LLBL, cusp, mantle and polar rain, are governed by the same physical processes.

Using modeling, we can more definitively address the question: if all the particles originate from solar wind, then why do they look different at different locations? We show with our modeling work that the answer to this question lies in the complex processes governing the solar wind entries into the magnetosphere and ionosphere: reconnection sites, shocked solar wind evolution along the magnetopause entry points, IMF, magnetopause acceleration/deceleration, $\mathbf{E} \times \mathbf{B}$ drift, field line distance from the magnetopause to the ionosphere (time of flight), observational point (spacecraft trajectory), charge quasi-neutrality, and parallel electric field. Good understanding of how these processes/parameters interact can help unravel the mystery of double cusp and other spatially discontinuous cusps [e.g., *Trattner et al.*, 1999; 2002; *Pitout et al.*, 2002].

In addition to the spatial features, the cusp sometimes exhibits temporal features, including discontinuous cusp structures. The discontinuous cusp ion signature has long been associated with the discontinuity in the IMF, solar wind, and/or reconnection (merging) rate (e.g., flux transfer event (FTE), pulsed or bursty or intermittent injections etc.) [e.g., *Lockwood and Smith*, 1989; 1992; *Smith et al.*, 1992; *Escoubet et al.*, 1992; *Lockwood et al.*, 1995; *Boudouris et al.*, 2001]. Modeling cusp with discontinuous solar wind and IMF is left for future studies.

Not all the features in the DMSP observations match the model results because the model still needs to incorporate a number of processes, as mentioned in Section 2.6. The model does not include the physical processes that generate the micro- and meso-scale features in the cusp. Nonetheless, the model seems to be able to capture the large-scale features in the observations.

2.8 References

- Baker, K. B., and S. Wing (1989), A new magnetic coordinate system for conjugate studies at high latitudes, *J. Geophys. Res.*, 94, 9139-9143.
- Boudouridis, A., H. E. Spence, and T. G. Onsager (2001), Investigation of magnetopause reconnection models using two colocated, low-altitude satellites: A unifying reconnection geometry, *J. Geophys. Res.*, 106, 29,451-29,466.
- Burch, J. L. (1985), Quasi-Neutrality in the polar cusp, *Geophys. Res. Lett.*, 12, 469-472.
- Carbary, J. F., and C.-I. Meng (1986), Relations between the interplanetary

- magnetic field Bz, AE index, and cusp latitude, *J. Geophys. Res.*, 91, 1549-1556.
- Christon, S. P., D. J. Williams, D. G. Mitchell, L. A. Frank, and C. Y. Huang (1989), Spectral characteristics of plasma sheet ion and electron populations during undisturbed geomagnetic conditions, *J. Geophys. Res.*, 94, 13,409-13,424.
- Cowley, S. W. H., and C. J. Owen (1989), A simple illustrative model of open flux tube motion over the dayside magnetopause, *Planet. Space Sci.*, 37, 1461-1475.
- Dungey, J. W. (1961), Interplanetary magnetic field and the auroral zone, *Phys. Rev. Lett.*, 6, 47.
- Eastwood, J. P. (2008), The science of space weather, *Phil. Trans. R. Soc. A*, 4489 – 4500, doi:10.1098/rsta.2008.0161.
- Escoubet, C. P., M. F. Smith, S. F. Fung, P. C. Anderson, R. A. Hoffman, E. M. Baasinska, and J. M. Bosqued (1992), Staircase ion signature on the polar cusp: A case study, *Geophys. Res. Lett.*, 19, 1735.
- Fairfield, D. H., and J. D. Scudder (1985), Polar rain: Solar coronal electrons in the Earth's magnetosphere, *J. Geophys. Res.*, 90, 4055-4068.
- Feldman, W. C., J. R. Asbridge, S. J. Bame, and M. D. Montgomery (1974), Interplanetary solar wind streams, *Rev. Geophys. Space Phys.*, 12, 715.
- Feldman, W. C., J. R. Asbridge, S. J. Bame, J. T. Gosling, and D. S. Lemons (1978), Characteristic electron variations across simple high-speed solar wind streams, *J. Geophys. Res.*, 83, 5285-5295.
- Hardy, D. A., L. K. Schmitt, M. S. Gussenhoven, F. J. Marshall, H. C. Yeh, T. L. Shumaker, A. Hube, and J. Pantazis (1984), Precipitating Electron and Ion Detectors (SSJ/4) for the Block 5D/Flights 6-10 DMSP Satellites: Calibration and Data Presentation, Rep. AFGL-TR-84-0317, Air Force Geophys. Lab., Hanscom Air Force Base, Mass.
- Hill, T. W., and P. H. Reiff (1977), Evidence of magnetospheric cusp proton acceleration by magnetic merging at the dayside magnetopause, *J. Geophys. Res.*, 82, 3623-3628.
- Kivelson, M. G., and C. T. Russell (1995), Introduction to space physics, Cambridge University Press, Cambridge, U.K.
- Knight, L. (1973), Parallel electric fields, *Planet. Space Sci.*, 21, 741 – 750.
- Lockwood, M., and M. F. Smith (1989), Low-altitude signatures of the cusp and flux transfer events, *Geophys. Res. Lett.*, 16m 879.
- Lockwood, M., C. J. Davis, M. F. Smith, T. G. Onsager, and W. F. Denig (1995),

- Location and characteristics of the reconnection X-line deduced from low-altitude satellite and ground observations, Defense Meteorological Satellite Program and European Incoherent Scatter data, *J. Geophys. Res.*, 100, 21,803.
- Lyons, L. R. and D. J. Williams (1984), Quantitative aspects of magnetospheric physics, *Geophysics and Astrophysics Monographs*, pp. 6–7, D. Reidel Publishing Co., Dordrecht, Holland.
- Newell, P. T., C.-I. Meng, D. G. Sibeck, and R. Lepping (1989), Some low-altitude dependencies on the interplanetary magnetic field, *J. Geophys. Res.*, 94, 8921-8927.
- Newell, P. T., and C.-I. Meng (1989), Dipole tilt angle effects on the latitude of the cusp and the cleft/LLBL, *J. Geophys. Res.*, 94, 6949-6953.
- Newell, P. T., S. Wing, C.-I. Meng, and V. Sigilito (1991), The auroral oval position, structure, and intensity of precipitation from 1984 onward: An automated on-line data base, *J. Geophys. Res.*, 96, 5877-5882.
- Newell, P. T., and C.-I. Meng (1995), Magnetopause dynamics as inferred from plasma observations on low-altitude satellites, in *Physics of Magnetopause*, *Geophys. Monogr. Ser.*, vol. 90, edited by P. Song, B. U. Ö. Sonnerup, and M. F. Thomsen, pp. 407-416, AGU, Washington D. C.
- Newell, P. T., and S. Wing (1998), Entry of solar wind plasma into the magnetosphere: Observations encounter simulation, in *Geospace Mass and Energy Flow: Results from the International Solar-Terrestrial Physics Program*, *Geophys. Monogr. Ser.*, vol. 104, edited by J. L. Horwitz, D. L. Gallagher, and W. K. Peterson, 73-84, AGU, Washington D. C.
- Onsager, T. G., C. A. Kletzing, J. B. Austin, and H. MacKiernan (1993), Model of magnetosheath plasma in the magnetosphere: Cusp and mangle particles at low-altitudes, *Geophys. Res., Lett.*, 20, 479-482.
- Onsager, T. G., and M. Lockwood (1997), High-latitude particle precipitation and its relationship to magnetospheric source regions, *Space Sci. Rev.*, 80, 77-107.
- Pitout, F., P. Newell, and S. Buchert (2002), Simultaneous high- and low-latitude reconnection: ESR and DMSP observations, *Ann. Geophys.*, 20, 1311–1320.
- Reiff, P. H., T. W. Hill, and J. L. Burch (1977), Solar wind plasma injection at the dayside magnetospheric cusp, *J. Geophys. Res.*, 82, 479-491.
- Roelof, E. C., and D. G. Sibeck (1993), Magnetopause shape as a bivariate function of interplanetary magnetic field B_z and solar wind dynamic pressure, *J. Geophys. Res.*, 98, 21,421-21,450.
- Ruohoniemi, J. M., and R. A. Greenwald (1996), Statistical patterns of high-

- latitude convection obtained from Goose Bay HF radar observations, *J. Geophys. Res.*, 101, 21,743-21,763.
- Shue, J.-H., J. K. Chao, H. C. Fu, C. T. Russell, P. Song, K. K. Khurana, and H. J. Singer (1997), A new functional form to study the solar wind control of the magnetopause size and shape, *J. Geophys. Res.*, 102, 9497-9511.
- Smith, E. J., M. Lockwood, and S. W. H. Cowley (1992), The statistical cusp: The flux transfer event model, *Planet. Space Sci.*, 40, 1251.
- Spreiter, J. R., and S. S. Stahara (1985), Magnetohydrodynamic and gasdynamic theories for planetary bow waves, in *Collisionless Shocks in the Heliosphere: Reviews of Current Research*, Geophys. Monogr. Ser., Vol. 35, edited by B. T. Tsurutani and R. G. Stone, 85-107., AGU, Washington, D. C.
- Stormer, C. (1955), *The polar aurora*, Oxford Univ. Press, London and New York, p. 403.
- Stern, D. P.(1985), Parabolic harmonics in magnetospheric modeling: The main dipole and the ring current, *J. Geophys. Res.*, 90, 10,851-10,863.
- Tascione, T. F. (1994), *Introduction to the space environment*, p. 67., Krieger Publishing Co., Malabar, Florida.
- Trattner, K. J., S. A. Fuselier, W. K. Peterson, J.-A. Sauvaud, H. Stenuit, and N. Dubouloz (1999), On spatial and temporal structures in the cusp, *J. Geophys. Res.*, 104, 28411.
- Trattner, K. J., S. A. Fuselier, W. K. Peterson, and C. W. Carlson (2002), Spatial features observed in the cusp under steady solar wind conditions, *J. Geophys. Res.*, 107(A0), 10.1029/2001JA000262.
- Tsyganenko, N. A., and D. P. Stern (1996), Modeling the global magnetic field of the large-scale Birkeland current systems, *J. Geophys. Res.*, 101, 27,187.
- Weiss, L. A., P. H. Reiff, E. J. Weber, H. C. Carlson, M. Lockwood, and W. K. Peterson (1995), Flow-aligned jets in the magnetospheric cusp: Results from the Geospace Environment Modeling Pilot program, *J. Geophys. Res.*, 100, 7649-7659.
- Wing, S., P. T. Newell, D. G. Sibeck, and K. B. Baker (1995), A large statistical study of the entry of interplanetary magnetic field Y-component into the magnetosphere, *Geophys. Res. Lett.*, 22, 2083-2086.
- Wing, S. P. T. Newell, and T. G. Onsager (1996), Modeling the entry of magnetosheath electrons into the dayside ionosphere, *J. Geophys. Res.*, 101, 13,155-13,167.
- Wing, S., and D. G. Sibeck (1997), Effects of interplanetary magnetic field z component and the solar wind dynamic pressure on the geosynchronous

magnetic field, *J. Geophys. Lett.*, 102, 7207-7216.

Wing, S., Patrick T. Newell, and J. Michael Ruohoniemi (2001), Double cusp: Model prediction and Observational Verification, *J. Geophys. Res.*, 106, 25,571-25,593.

Zhou, X. W., C. T. Russell, G. Le, S. A. Fuselier, and J. D. Scudder (2000), Solar wind control of the polar cusp at high-altitude, *J. Geophys. Res.*, 105, 245-251.

Chapter 3

Solar wind plasma and energy entry through dayside reconnection into the polar cap

The Earth's magnetic field can reconnect with the interplanetary magnetic field (IMF) on the dayside. The open field lines at both the northern and southern hemispheres are carried by the solar wind to the nightside where they reconnect to form a closed field line in the magnetotail. This process is known as Dungey cycle [*Dungey, 1961*] and is depicted in Figure 3.1, which is adapted from Figure 2.2. From the time of the reconnection on the dayside to the reconnection on the nightside, solar wind particles continuously enter the magnetosphere and a fraction precipitate into the ionosphere. In the ionosphere, the open field line region is called the polar cap. This solar wind entry region is labeled as region 1 in Figure 1.2.

Section 3.1 discusses the solar wind particles that enter the magnetosphere and precipitate in the dayside polar cap. This precipitation region is sketched with a green arc and labeled 1 in Figure 3.1. Section 3.2 discusses the solar wind particles that enter the magnetosphere and precipitate near the open-closed field line boundary in the nightside polar cap. This precipitation region is indicated by a green arc labeled 2 in Figure 3.1. To carry out our investigation, we use satellite observations, the APL-OPM model presented in Chapter 2, and an analytical theory derived in Chapter 4.

3.1 Solar wind plasma and energy entry in the dayside polar cap

Because magnetosheath electrons can enter the magnetosphere more readily than ions, downward field-aligned electric fields must develop to restrict electron entries in order to maintain charge quasi-neutrality. At the Johns Hopkins University Applied Physics Laboratory (JHU/APL), we developed an open field line particle precipitation model (APL–OPM) to model precipitating ions and electrons in the open field line low-latitude boundary layer (open-LLBL), cusp, mantle, and the low-latitude portion of the polar rain [Wing *et al.*, 1996; 2001; 2005]. The APL–OPM is described in Chapter 2. For the southward IMF condition, the model retarding field-aligned potential drop resulting from maintaining charge quasi-neutrality in these four regions is plotted in Figure 3.2a. Immediately after the dayside reconnection, in the open-LLBL, the solar wind ions and electrons can rush into the newly opened field line, but the electrons, having higher speeds, can move ahead of the ions and enter the magnetosphere in a greater proportion than the ions. As a result, retarding potential drop arises to limit some of the electron entries. A short time later, in the cusp, the bulk of the ions and electrons can enter the magnetosphere. So, only a small or no potential drop is needed to maintain charge quasi-neutrality because the electrons and ions already maintain charge quasi-neutrality in the magnetosheath. As the field lines

This chapter has been published in the following papers:

Wing, S. and Zhang, Y. L. (2015), The nightside magnetic field line open–closed boundary and polar rain electron energy-latitude dispersion, *Ann. Geophys.*, 33, 39-46, doi:10.5194/angeo-33-39-2015.

Wing, S., D. H. Fairfield, J. R. Johnson, and S.-I. Ohtani (2015), On the field-aligned electric field in the polar cap, *Geophys. Res. Lett.*, 42, 5090–5099, doi:10.1002/2015GL064229.

Contribution statement:

S. Wing: contributed main ideas, wrote the code for the open field line model, obtained model field-aligned electric field, wrote the code to analyze DMSP data, performed model–data comparisons, interpreted results, performed most of the work, wrote both papers.

Y. L. Zhang: provided some initial motivations and ideas for the work in Section 3.2, provided Figure 3.9, revised Figure 3.8.

D. H. Fairfield: provided Figure 3.2 b–e, contributed useful discussions for Section 3.1

J. R. Johnson: contributed useful discussions for Section 3.1, derived equation (3.1).

S.-I. Ohtani: provided some comments on the journal manuscript.

continue to $\mathbf{E} \times \mathbf{B}$ convect to the nightside, in the mantle, fewer ions can enter the magnetosphere because of increasing tailward speed. Hence, the potential drop slowly rises with increasing latitude to prevent electrons from entering the magnetosphere. Finally, in the polar rain, the entry points are further tailward where few ions can enter and the potential drop increases to a higher level to prevent more electrons from entering the magnetosphere. In fact, the potential drop is so high that only solar wind suprathermal (strahl) electrons, having higher temperatures, can overcome the retarding potential drop to enter the magnetosphere largely unimpeded [Fairfield and Scudder, 1985].

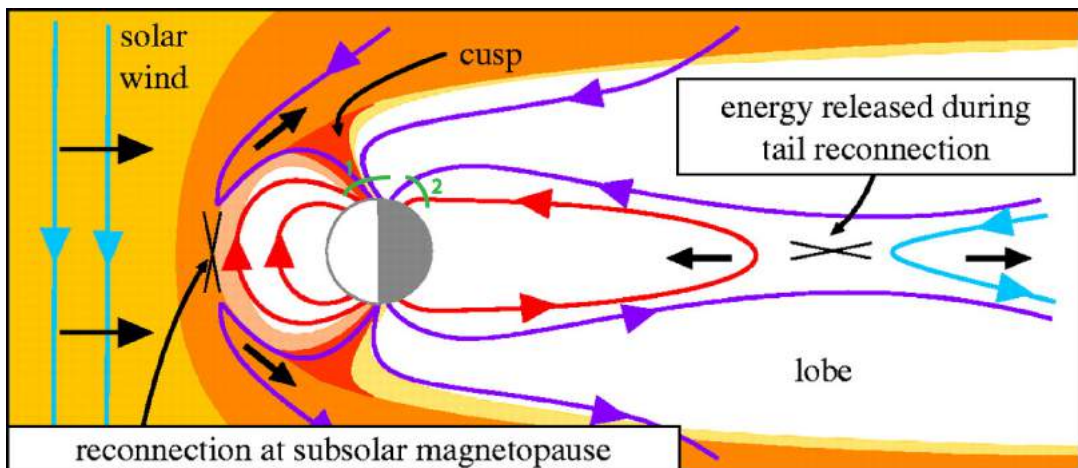


Figure 3.1 A schematic showing the dayside reconnection at the subsolar magnetopause and the nightside reconnection in the magnetotail. After the dayside reconnection, the solar wind particles enter the magnetosphere and some precipitate in the ionosphere. Section 3.1 discusses the solar wind particles that precipitate in the region indicated by the green arc labeled 1. Section 3.2 discusses the solar wind particles that precipitate in the region near the open-closed boundary on the nightside, which is indicated by the green arc labeled 2. (adapted from Eastwood [2008] and Figure 2.2).

Observational studies found retarding potential drops that are consistent qualitatively with the prediction of the APL–OPM model [e.g., Wing *et al.*, 1996; Fairfield *et al.*, 2008]. However, Fairfield *et al.* [2008] found evidence that solar wind electrons occasionally go through an accelerating potential drop before reaching the ionosphere. The present study investigates further field-aligned electric fields in the polar cap that affect the precipitating solar wind electrons.

3.1.1 Downward and upward field-aligned electric fields in the polar cap

In a study of variations in the otherwise uniform precipitation of solar wind electrons over the polar cap, *Fairfield et al.* [2008] plotted the solar wind electron phase space density obtained by ACE along with the corresponding polar rain electrons simultaneously measured at low-altitude by DMSP satellites. They found that the DMSP polar rain spectra would usually match ACE solar wind electron spectra if the DMSP electrons were shifted up in energy. On occasion, however, the shift was in the opposite direction. Examples extracted from *Fairfield et al.* [2008] are shown in Figure 3.2 panels b–e for the 2000 Jul 31 and 2003 Oct 24 events. Panels b and d show the original measurements from ACE (heavy red trace) and DMSP (thinner colored lines). In panels c and e, all traces, excepting the black trace in panel d, have been shifted to the right (up in energy) implying that the solar wind electrons have gone through a net retarding potential drop before reaching DMSP altitudes. This result is consistent qualitatively with the predictions of APL–OPM model. The black trace in Figure 3.2d that is shifted to the left (down in energy) in Figure 3.2e implies a net accelerating potential drop, which is the opposite of that predicted by the APL–OPM model [*Wing et al.*, 1996; 2001; 2005]. An upward field-aligned electric field sometimes arises in the upward field-aligned current (FAC) region when the electron density in the source region is too low to provide enough current carriers to carry the current [e.g., *Knight*, 1973].

To investigate this possibility, we examine the simultaneous observations of the DMSP magnetic field data [*Rich et al.*, 1985] and particle data (SSJ4/5) [*Hardy et al.*, 1984]. The upward pointing particle detectors measure the relevant electrons whose alignment within a few degrees of the magnetic field in the distant magnetosphere allows them to reach low altitude and experience field-aligned electric fields.

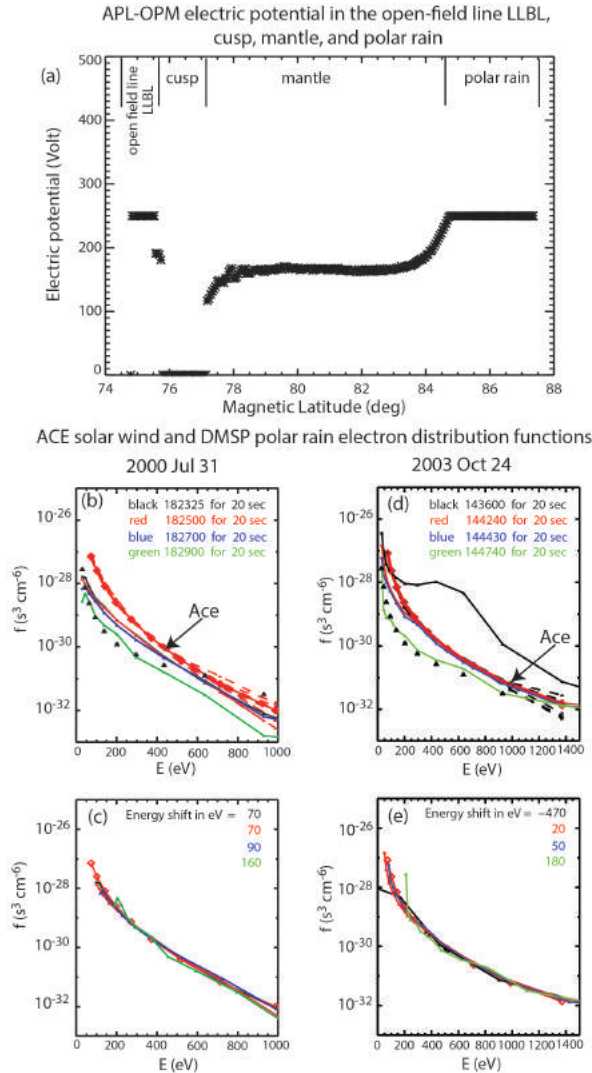


Figure 3.2. (a) Retarding field-aligned potential that arises to keep magnetosheath electrons from entering the magnetosphere in order to maintain charge quasi-neutrality. This potential is obtained from APL-OPM for southward IMF condition [Wing *et al.*, 1996; 2005]. (b) ACE solar wind and DMSP F13 polar rain electron distribution functions plotted versus energy for 2000 Jul 31 event. Field-aligned ACE data are shown by the heavy red trace while DMSP data from four different intervals are shown by the four thinner traces in black, red, blue, and green. Black triangles indicate the one count level for DMSP data. (c) Same as in (b) except that the DMSP data are shifted to the right to best overlay ACE data. The shifts are interpreted as electrons have gone through a net retarding field-aligned potentials (positive values) and their magnitudes are indicated. (d) and (e) are the same as (b) and (c) but for 2003 Oct 24 event. In (d) and (e), the 2003 Oct 24 14:36:00 UT distribution function (black line) is an anomaly because the field-aligned potential is an accelerating potential (negative value). All other distribution functions in the 2000 Jul 31 and 2003 Oct 24 events have positive field-aligned potentials, consistent with Wing *et al.* [1996; 2005] results. [panel (a) is adapted from Wing *et al.* [2005] while panels (b) and (c) are adapted from Fairfield *et al.* [2008].]

Field-aligned electric field in the polar cap

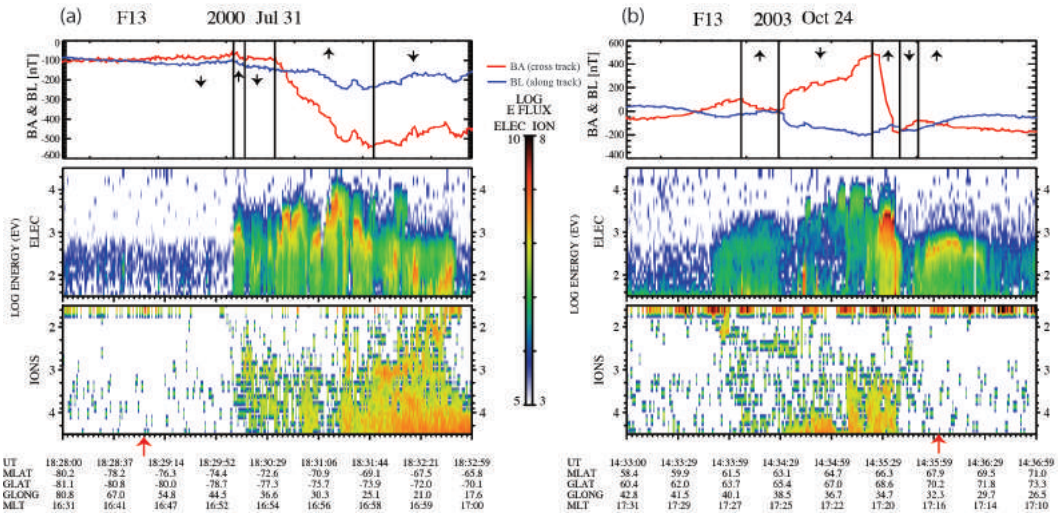


Figure 3.3. DMSP magnetic field and particle precipitation observations for the two events presented in Figure 3.2: (a) 2000 Jul 31 and (b) 2003 Oct 24. The top panel shows the DMSP magnetic field cross-track (BA, red) and along the track (BL, blue) components. The upward and downward field-aligned currents are indicated by the up and down arrows, respectively. The middle and bottom panels show the electron and ion spectrograms showing log differential energy flux, in units of $\text{eV} (\text{cm}^2 \text{s sr eV})^{-1}$, from 32 eV to 30 keV. The ion energy scale is inverted. In (a) the polar rain is located in the weakly downward FAC region and there is no evidence of monoenergetic electron. In fact, at 18:29:00 UT (indicated by the red arrow at the bottom of the third panel, the retarding potential is 160 V (the green curve in Figures 3.2b and 3.2c). In contrast, in (b) there is evidence of monoenergetic electron in the polar rain where FAC is upward. At 14:36:00 UT (indicated by the red arrow at the bottom of the third panel), the electron differential energy flux peak at about 500 eV, consistent with the accelerating potential of 470 V obtained in Figure 3.2e. The magnetic coordinates are obtained from Altitude Adjusted Corrected Geo-Magnetic (AACGM) coordinate [Baker and Wing, 1989].

Figure 3.3a shows the 2000 Jul 31 event (the same event shown in Figures 3.2b and 3.2c) when IMF $(B_x, B_y, B_z) \sim (4, -4, -8)$ nT. The first panel shows up and down arrows indicating the polarities of the field-aligned currents that are derived from the cross track component (red line), assuming infinite current sheet [e.g., Iijima and Potemra, 1976; Wing et al., 2010]. The poleward boundary of the auroral oval is located at about magnetic latitude (MLat) $\sim -73.2^\circ$ (18:30:12

UT). The polar rain, which is located poleward of MLat $\sim -73.2^\circ$, looks like the typical polar rain, showing no evidence of electron acceleration. This is consistent with the magnetic field observations that indicate that FAC is either small or downward.

In Figure 3.2c, the shifted green distribution function for 18:29:00 UT (for the electron spectra marked by the red arrow in Figure 3.3a) indicates that the net retarding potential drop is 160 V. This potential drop is qualitatively consistent with the potential drop needed to maintain charge quasi-neutrality in APL–OPM as shown in Figure 3.2a. In the model, the potential drop has dependencies on the solar wind density and temperature. Ion and electron outflows, which are absent in the model, may affect the charge quasi-neutrality calculation and can complicate model-data comparisons, as discussed next. In any case, the net potential drop in the polar rain has been observed to range from several tens to hundreds of V [Fairfield *et al.*, 2008].

The solar extreme ultraviolet (EUV) radiation can ionize the atmosphere, which leads to up flowing photoelectrons and the development of ambipolar upward electric fields at several hundreds km to a few R_E , which in turn drives ion outflows [e.g., Su *et al.*, 1998]. Upward field-aligned electric fields can also develop in the upward field-aligned current region where the electrons need to overcome the mirror force around 1–3 R_E [Knight, 1973; Block and Fälthammar, 1991]. On the other hand, downward field-aligned electric fields should develop close to the magnetopause boundary to prevent the entry of excess solar wind electrons. Therefore, it is expected that the signatures of acceleration or deceleration may also reflect the differences in the location of the acceleration or deceleration.

Kitamura *et al.* [2012] studied upgoing and reflected photoelectrons and found that a small downward accelerating potential drop of 20 V exists most of the time at altitude above 3800 km. The existence of this accelerating potential drop at intermediate altitudes is not inconsistent with the simultaneous existence of a retarding potential drop at high altitude near the magnetopause. Thus, the retarding potential drop obtained by Fairfield *et al.* [2008] gives a lower bound estimate of the potential drop needed to maintain charge quasi-neutrality near the magnetopause.

Figure 3.3a can be contrasted to Figure 3.3b, which shows the DMSP observations for the 2003 Oct 24 event (the same event shown in Figures 3.2d and 3.2e) when IMF (B_x , B_y , B_z) $\sim (-6, -1, -7)$ nT. In Figure 3.3b, the poleward

boundary of the auroral oval is located at MLat~66.8° (14:35:38 UT). In Figure 3.2e, the shifted black distribution function (14:36:00 UT) suggests that the net accelerating field-aligned potential drop is 470 V. The polar rain electron spectra corresponding to this distribution function are indicated by the red arrow at the bottom of the third panel in Figure 3.3b. The polar rain electrons at MLat~67.7°–69.5° (14:35:55–14:36:30 UT) are monoenergetic electrons or electron acceleration events, which are consistent with the electrons having gone through an upward field-aligned electric field [e.g., *Wing et al.*, 2013]. The magnetometer data indicate that these monoenergetic electrons are located in the upward FAC region. The accelerating potential drop obtained by *Fairfield et al.* [2008] (470 V) gives a lower bound estimate of the potential drop that exists at the acceleration region, 1–3 R_E , because the electrons may have gone through retarding potential drop at the magnetopause.

Moreover, Figure 3.3b shows that at 14:36:00 UT the electron differential energy fluxes peak at about 500 eV, which would not be inconsistent with the net accelerating potential drop of 470 V obtained in Figure 3.2e. The electrons with energies lower than ~500 eV, which have low fluxes, may be attributed to the ionospheric electron outflows that are turned around by the upward electric field. These ionospheric electrons correspond to the electrons having energies below 470 eV on the black curve in Figure 3.2d. In Figure 3.2e, part of the curve representing these electrons (which do not originate from solar wind) does not overlay the solar wind electron curve (the thick red curve), but the rest of the curve does.

Wing et al. [2010; 2011] report that it is not unusual to find upward field-aligned electric fields in the afternoon upward FAC region located within the boundary layer and open field lines. *Lyons* [1980] notes that near the boundary layer on the duskside, the plasma flow is sunward and anti-sunward in the magnetosphere and magnetosheath, respectively, and the magnetic field has a northward component. As a result, the convective electric field converges ($\nabla \cdot \mathbf{E} < 0$), which can lead to large-scale upward field-aligned current. Larger V_{sw} would generate larger upward FAC density (J_{\parallel}) and if the electron density were not large enough, then an accelerating potential drop would develop to draw more electrons downward [e.g., *Wing et al.*, 2011].

3.1.2 A morphology of the low-latitude polar rain electrons in the upward FAC region

In the upward FAC region, the low-latitude polar rain sometimes shows a ramping up of the electron energy with increasing latitude before reaching a plateau. Such structures are typically found slightly poleward of the dayside open-closed boundary. Two examples are presented (more examples can be found in *Wing et al.* [2010]). Unfortunately, solar wind data are not available for these two events.

Figure 3.4a shows the 1985 Mar 27 event in which DMSP F7 observes a double cusp [e.g., *Wing et al.*, 2001] at MLat $\sim -74.7^\circ - -76.4^\circ$, a mantle at MLat $\sim -76.4^\circ - -77.5^\circ$, and polar rain (prior to 01:10:09 UT). Immediately poleward of the mantle, the polar rain electron energies are typical, but at MLat $\sim -77.7^\circ - -78.1^\circ$ (between the two red vertical dashed lines in the middle panel), the electron differential energy flux peak energy increases with increasing latitude before plateauing at just below 1 keV, which is higher than that of the typical of polar rain electrons. The magnetometer data indicate that the polar rain in this interval is located near the poleward edge of the upward FAC region. Poleward of MLat $\sim -78.1^\circ$, the FAC suddenly weakens and the polar rain electron energies and fluxes suddenly drop.

Figure 3.4b shows the DMSP F7 1984 Nov 20 pass that shows the same feature in the polar rain. The DMSP observes cusp at MLat $\sim -77.4^\circ - -80.3^\circ$, mantle at MLat $\sim -80.3^\circ - -83.2^\circ$, and polar rain (prior to 03:27:44 UT). At MLat $\sim -83.2^\circ - -85.1^\circ$ (between the two red vertical dashed lines in the middle panel), the polar rain electron differential energy flux peak energy increases with increasing latitude before reaching a plateau at around 1 keV. The magnetometer data indicate that the polar rain in this interval is located near the poleward edge of the upward FAC region. The FAC changes from upward to slightly downward at MLat $\sim -85.1^\circ$, which is accompanied by a sudden drop in the polar rain electron energies and fluxes. Poleward of MLat $\sim -85.1^\circ$, the polar rain electrons look like the typical polar rain electrons and FAC is small or slightly downward.

Following the reconnection at the magnetopause, the field lines would eventually convect to the nightside while the magnetosheath plasma continuously enters the magnetosphere. The electrons from the higher latitude polar rain originate from the magnetopause region that is further down the tail. Because of the evolution of the magnetosheath density and speed [e.g., *Spreiter and Stahara*,

1985], at progressively higher latitude, polar rain electrons originate from the magnetosheath region that progressively has lower density and higher speed. *Wing et al.*, [2011] and *Echim et al.* [2008] show that higher speed suggests higher velocity shear at the magnetopause boundary, which can increase field-aligned potential drop. The same studies also show that lower density can also increase field-aligned potential drop. These relations can also be seen in equation (3.1), as discussed below. As the magnetosheath speed increases and density decreases, the accelerating potential drop and polar rain electron differential flux peak energy progressively increases. Eventually, the magnetosheath density and velocity asymptotically reach their solar wind values, which may explain the plateauing of the polar rain electron differential flux peak energy.

Polar rain electrons in the upward field-aligned current region

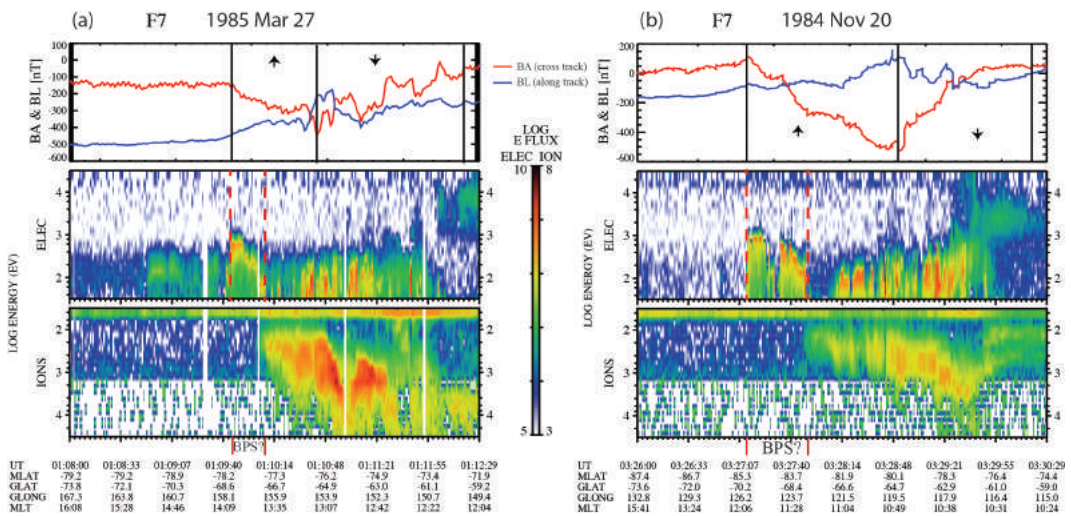


Figure 3.4. Two examples showing polar rain electron energy ramps up with increasing latitude before reaching a plateau. The format is the same as in Figure 3.3. In the top panel, the arrows indicate the polarities of only large-scale field-aligned currents. At the poleward edge of the upward FAC region, between the two red vertical dashed lines, the polar rain electron energy ramps up with increasing latitude before reaching a plateau. Due to the high electron energies, the DMSP automatic algorithm often classifies this region as BPS, which is most likely incorrect (see text). The white vertical bands in (a) indicate data gaps.

In Chapter 4, we present a model for current-voltage relation at the magnetopause boundary layer and open field lines. Chapter 4 shows that in the upward FAC regions the maximum potential drop can be estimated analytically as

$$\Delta\phi_{\parallel,max} = \frac{J_{\parallel}}{\kappa} \approx \frac{V_0 B_m \sqrt{b} L}{2 \left(1 + \frac{\Delta_m}{L \sqrt{b}}\right)} \quad (3.1)$$

where $\Delta\phi_{\parallel}$ = field-aligned potential drop, L = electrostatic auroral scale length = $(\Sigma_p/\kappa)^{0.5}$, Σ_p = Pedersen conductivity, $\kappa = n_e e^2 / (2\pi m_e k_b T_e)^{0.5}$, V_0 = velocity shear at the boundary layer, B_m = magnetic field magnitude at the boundary layer, $b = B_i/B_m$, B_i = ionospheric magnetic field magnitude, Δ_m = thickness of the boundary layer, n_e = electron number density, e = electron charge, m_e = electron mass, T_e = electron temperature, and k_b = Boltzman constant. Equation (3.1) just restates equation (4.19), but included here for convenience. This expression shows that as the magnetosheath flow speed or V_0 increases and n_e decreases, $\Delta\phi_{\parallel}$ increases. Assuming solar wind suprathermal $n_e = 0.4 \text{ cm}^{-3}$, $T_e = 1 \times 10^6 \text{ K}$, $V_0 = 400 \text{ km s}^{-1}$, $B_0 = 3 \text{ nT}$, $B_i = 4 \times 10^{-5} \text{ T}$, $\Delta_m = 6000 \text{ km}$, $\Sigma_p = 2\text{S}$, equation (3.1) predicts field-aligned potential drop of 1.3 kV. Figure 3.4 shows that in the 1985 Mar 27 and 1984 Nov 20 events, the electron differential energy flux peak energy plateau to about 1 keV, which is close to the theoretical prediction.

In Figure 3.4b, the upward FAC region at MLat $\sim -85.1^\circ - -79.9^\circ$ co-locates with mantle and some polar rain regions. In the mantle region, at MLat $\sim -83.2^\circ - -81.8^\circ$, the FAC weakens as evidenced by the reduction of the slope of the red line. This observation underscores a couple of points. First, the smaller FAC corresponds to smaller precipitating electron fluxes. Second, the electron energies in this interval look more similar to those in the polar rain poleward of MLat $\sim -85.1^\circ$ (prior to 03:27:12 UT) than the electron energies that immediately follow, in the interval MLat $\sim -83.2^\circ - -85.1^\circ$ (between the two red vertical dashed lines). This supports our argument that the enhanced electron fluxes and energies in this interval are just the regular polar rain or mantle electrons that have gone through accelerating potential drop associated with upward FAC.

Newell et al. [1991a; 1991b; 1991c] developed an automatic algorithm that classifies the dayside particle precipitation source regions. This algorithm does not take into account the effect of FACs. Often, this algorithm would classify the regions between the two red vertical dashed lines in Figure 3.4 as boundary plasma sheet (BPS), which is a closed field line region. In Figure 3.4b, the algorithm labels the sequence of boundaries from low to high latitude as CPS – BPS – cusp – mantle – BPS – polar rain. If this were correct, then this would suggest a rather unusual scenario where, from low to high latitude, the field lines are closed–open–closed–open. A more likely scenario is that the BPS that is located poleward of the mantle is misclassified because the mantle or polar rain electrons have gone

through upward field-aligned electric field in the upward FAC region and gained enough energy to make their spectra look more similar to those of BPS rather than mantle or polar rain. Thus, taking the upward electric field into account, we would have the expected pattern from low to high latitude as open–closed field lines. (This correction should also apply to the examples presented in Figures 3.2a, 3.2b, and 7 in *Wing et al.* [2010].) Moreover, in the electron acceleration region, there is no significant ion precipitation. In fact, the ions look similar to those in the adjacent polar rain region. Taken together, the present study and *Wing et al.* [2010] suggest that the *Newell et al.* [1991a; 1991b; 1991c] algorithm needs to be modified by taking into account FAC observations.

Without the help of imagers, it is hard to determine whether the electron accelerations in the polar cap in Figure 3.4 are related to polar cap arcs [*Zhu et al.*, 1997; *Shi et al.*, 2013; *Gou et al.*, 2016]. Some polar cap arcs are thought to originate from plasma sheet because they are accompanied by the plasma sheet ion precipitation [*Hoffman et al.*, 1984; *Milan et al.*, 2005; *Fear et al.*, 2014; *Mailyan et al.*, 2015]. In this case, a DMSP traveling poleward across the polar region would indeed observe particle precipitation structure that suggests closed–open–closed–open field lines. However, in Figure 3.4, the electron accelerations in the polar cap are not accompanied by significant precipitating ions – the ions certainly do not look like the typical plasma sheet ions [e.g., *Wing et al.*, 1998]. If the electron accelerations in Figure 3.4 were polar cap arcs, they may be similar to the ones reported in *Burke et al.* [1982], which shows discrete arcs associated with electrons having gone through ~ 1 kV potential drop within upward FAC regions that are located on open field lines.

3.1.3 The occurrence of the upward field-aligned electric fields in the polar cap

The occurrence of the upward field-aligned electric fields in the polar cap in the upward and downward FAC regions from 06 to 18 magnetic local time (MLT) is investigated. The dayside polar cap region includes cusp, mantle, polar rain, and LLBL. About 300 events in each category are randomly chosen from DMSP F7 1984–1987 and DMSP F12 1995–2001 observations. After discarding events with bad data points or events with no simultaneous magnetic field and particle observations, there are 273 and 278 for upward and downward FAC events, respectively. The presence of the electron acceleration is used as evidence for the

presence of upward field-aligned field. Here, the electron accelerations are not necessarily polar cap arcs and the term electron acceleration indicates monoenergetic electrons that occur either alone or in combination with broadband electrons [Wing *et al.*, 2013]. An example of the latter in the closed field line is shown in Figure 3.3b at MLat \sim 66.1 $^{\circ}$ –66.9 $^{\circ}$ (14:35:25–14:35:40 UT) where the electrons may have been heated and accelerated by waves rather than strictly by the upward field-aligned electric field alone [Wing *et al.*, 2013].

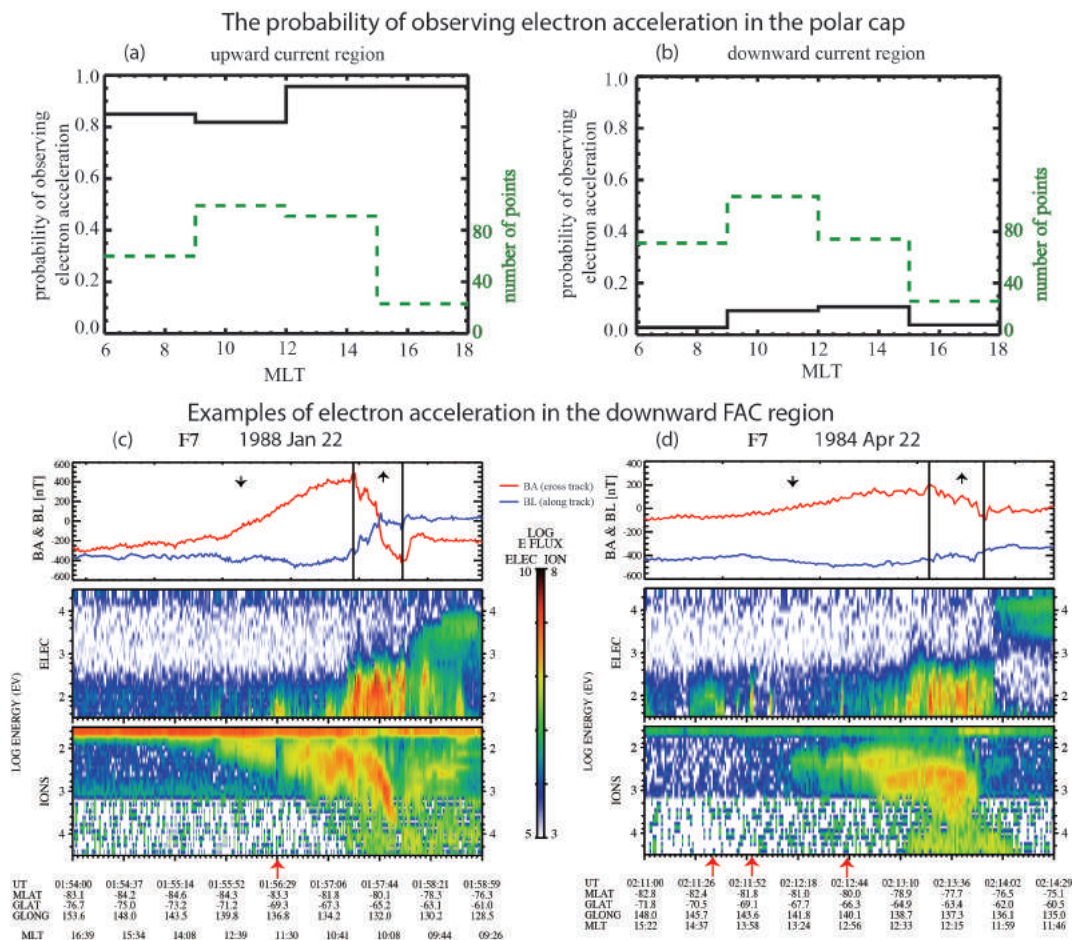


Figure 3.5. The probability of observing electron acceleration in the polar cap plotted as a black solid line in (a) upward current region and (b) in the downward current region. The number of points in each 3 hr bin is plotted as a green dashed line. Two examples of electron acceleration events in the downward FAC regions are presented in (c) and (d) for 1988 Jan 22 and 1984 Apr 22 events, respectively, in the same format as in Figure 3.3. The electron acceleration intervals are indicated by the red arrows at the bottom panel.

Figures 3.5a and 3.5b present the probability of observing any electron acceleration in the upward and downward FAC regions, respectively. Figure 3.5a shows that the probability of observing electron acceleration in the upward FAC region is quite high, 0.82 to 0.96, depending on the MLT. In contrast, the probability of observing electron acceleration in the downward FAC region is much lower, 0.03 to 0.11.

Many data points do not have associated simultaneous IMF observations. For those events that have simultaneous IMF observations, in the upward FAC regions (Figure 3.5a), 92 out of 176 electron acceleration events (52%) are associated with northward IMF. In the downward FAC regions (Figure 3.5b), 7 out of 10 electron acceleration events (70%) are associated with northward IMF. Taking into account the sample sizes, statistically, there is no clear strong preference for north-south orientation of IMF in both distributions. This needs to be investigated further.

Figures 3.5c and 3.5d show two examples of electron acceleration in the downward FAC regions (the solar wind observations are not available). The electron acceleration intervals are indicated by the red arrows at the bottom panel in Figures 3.5c and 3.5d. In Figure 3.5c, the precipitating ion fluxes accompanying the electron accelerations are lower than the surrounding regions, which perhaps can be attributed, at least partly, to the upward field-aligned electric field.

Sometimes, electron acceleration can also be found in weak or no FAC region. An example can be seen in Figure 3.4a, which shows monoenergetic or combination of monoenergetic and broadband electrons (differential energy fluxes peak ~ 150 eV) between 01:08:51 and 01:09:02 UT and broadband electrons between 01:09:05 and 01:09:14 UT.

It is not clear what mechanism(s) can lead to electron acceleration in the downward or no FAC regions. Broadband acceleration in upward, downward, or no FAC regions can be attributed to small-scale dispersive Alfvén waves that create time-varying field-aligned electric field that disperses electron energy [e.g., *Chaston et al.*, 2002; *Watt and Rankin*, 2009; *Wing et al.*, 2013]. On the other hand, monoenergetic electrons are usually attributed to quasi-static potential drops, which are typically associated with upward FAC regions and global magnetic field configuration or low frequency waves [*Damiano and Johnson*, 2012]. However, it is not clear what causes monoenergetic electron in downward or no FAC regions. This topic will be further investigated in the future.

3.2 Solar wind electrons in the nightside polar cap

Magnetic reconnection is an important process in space and plasma physics. On the dayside, magnetic reconnection between the interplanetary magnetic field (IMF) and the magnetospheric magnetic field lines causes the closed magnetospheric field lines to become open. These open field lines at both the northern and southern hemispheres are carried by the solar wind to the nightside, where they reconnect to form a closed field line in the magnetotail [Dungey, 1961].

As a result of the magnetic reconnection on the dayside, the shocked solar wind can enter the magnetosphere and a fraction precipitates into the ionosphere. The solar wind entry points and the processes at the magnetopause lead to four types of particle precipitation regions: open field line low-latitude boundary (LLBL), cusp, mantle, and polar rain [e.g., Newell *et al.*, 1991a; 1991b; 1991c; Wing *et al.*, 1996; 2001]. The polar rain occupies most of the polar cap and consists mainly of precipitating solar wind suprathermal electrons [Fairfield and Scudder, 1985; Wing *et al.*, 1996].

The energy-latitude dispersion in the polar rain electron flux was sometimes observed near the nightside auroral oval by the Akebono satellite and Defense Meteorological Satellite Program (DMSP) satellites [Shirai *et al.*, 1997; Zhang *et al.*, 2011]. The red lines in Figure 3.6 mark the poleward boundary of the energy-latitude dispersion in the DMSP observations. Shirai *et al.* [1997] attributed the energy-latitude dispersion to being a signature of the last injected solar wind suprathermal electrons before the open field lines reconnect in the magnetotail and become closed. Because of the duskward crosstail electric field [e.g., Pedersen *et al.*, 1985], these solar wind electrons from the last open field line would undergo $\mathbf{E} \times \mathbf{B}$ equatorward convection as they move toward the ionosphere, leading to the observed energy-latitude dispersion. The polar rain electron energy dispersion has been used to estimate the electron path length from the X-line to the ionosphere and the X-line location in the magnetotail [Shirai *et al.*, 1997; Alexeev *et al.*, 2006; Zhang *et al.*, 2011]. This dispersion method seems reasonable in principle, but the validation of the method has been difficult because of the lack of coincident *in situ* reconnection measurements in the magnetotail.

DMSP observations of auroral oval and polar cap

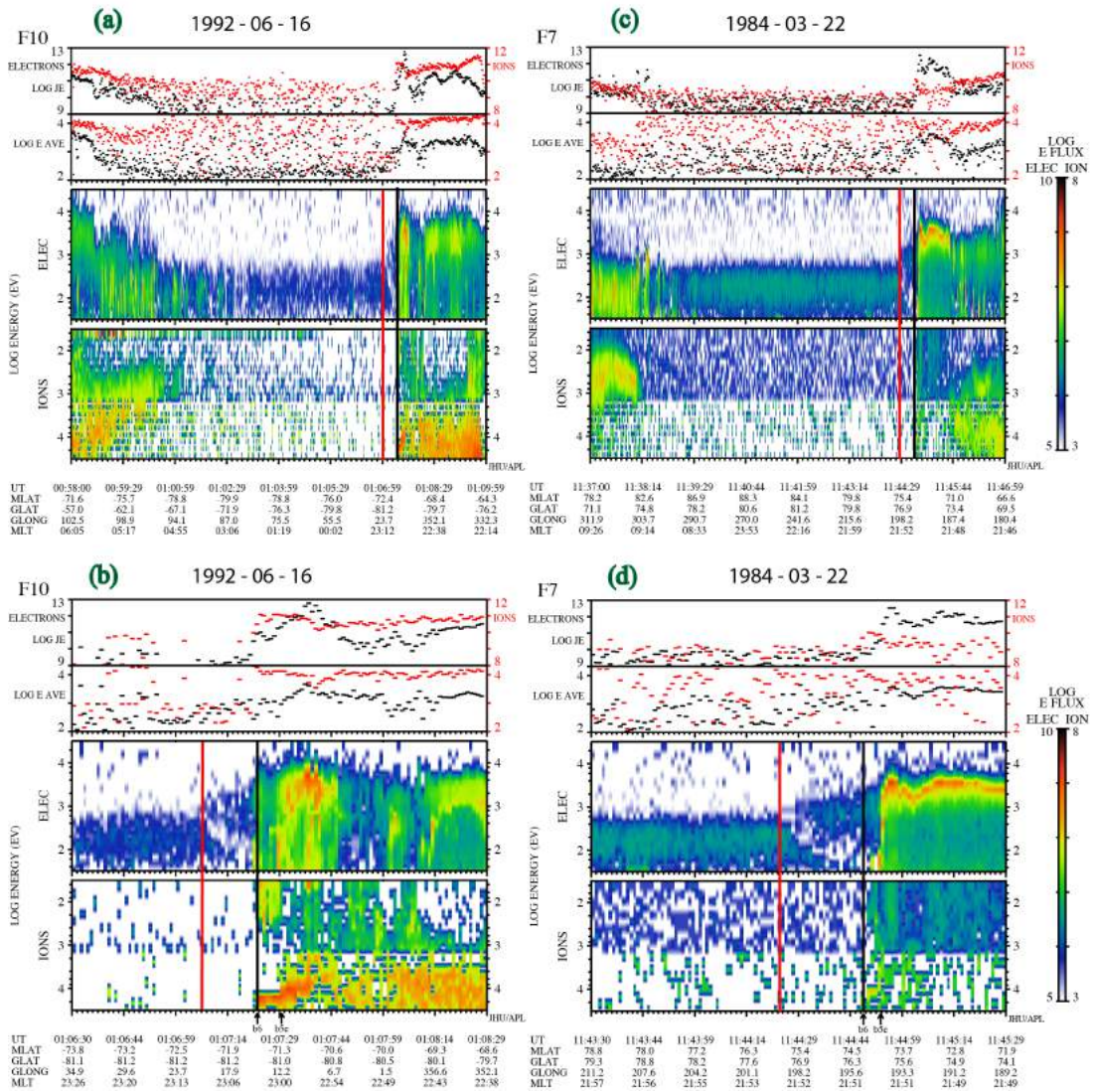


Figure 3.6. (a) and (c) DMSP observations of the auroral oval and polar cap in the same format as in Figure 3.3. (b) and (d) zoom in on the nightside region where the polar rain meets the poleward edge of the auroral oval in (a) and (b), respectively. (b) and (d) show the polar rain energy-latitude dispersion, b_6 , and b_5e . The vertical red lines indicate the location of the highest energy polar rain electrons in the dispersion region while the vertical black lines indicate b_6 .

Newell et al. [1996] identified a few useful boundaries near the poleward edge of the nightside auroral oval, namely b_5e , b_5i , and b_6 . b_5e and b_5i indicate the region near the poleward boundary of the auroral oval where the precipitating electron and ion differential energy flux, respectively, drop off sharply, typically

by an order of magnitude over a short distance ($< 0.2^\circ$). Usually, b5e and b5i are close to each other. b6 is defined as the poleward edge of the subvisual drizzle, which is the region of weak ion and electron precipitation typically poleward of both b5e and b5i. The locations of b6 and b5e in Figures 3.6b and 3.6d are indicated by the labels below the bottom panel. Studies have used b6 [e.g., *Boakes et al.*, 2008; *Longden et al.*, 2010] or a halfway point between b5 (either b5e or b5i) and b6 [*Hubert et al.*, 2006] as the best available proxy for the magnetic field open-closed boundary. These studies also show that in general, there are systematic discrepancies between the open-closed boundary obtained from DMSP and those obtained from optical images, but the exact causes these discrepancies are not entirely clear.

At the Johns Hopkins University Applied Physics Laboratory (JHU/APL), we developed an open field line particle precipitation model (APL–OPM) to model precipitating ions and electrons in the open field line LLBL, cusp, mantle, and polar rain [*Wing et al.*, 1996; 2001]. APL–OPM, which was developed for studying dayside particle precipitation, can be extended to model the nightside electron energy-latitude dispersion. Because the nightside open-closed boundary (magnetotail X-line) is known and can even be arbitrarily set in APL–OPM, the model can be a useful tool to evaluate how well the polar rain dispersion can be used to estimate the X-line location.

In the present study, we model the polar rain electron energy dispersion using a modified APL–OPM [*Wing et al.*, 1996; 2001]. Based on this model, we examine the accuracy of the existing method for using the dispersion to estimate electron path length and X-line distance. Finally, we examine the issue of where the magnetic field line open-closed boundary is located based on our modeling and observational work.

3.2.1 Modeling the polar rain energy-latitude dispersion (APL–OPM extension to the nightside)

APL–OPM has been described in Chapter 2 (Section 2.6) where we show that APL–OPM can model not just the cusp, but also open field line LLBL, mantle, and polar rain particles. In order to study the nightside polar rain near the open-closed boundary, we make the following modifications to APL–OPM.

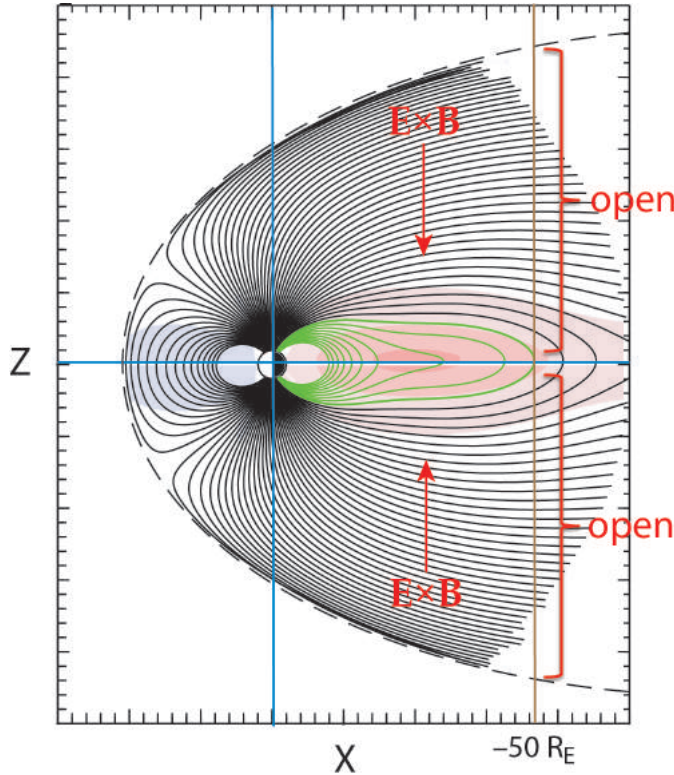


Figure 3.7. A schematic showing a 2D cut in noon–midnight meridional (x – z) plane of the APL–OPM configuration on the nightside. The horizontal and vertical blue lines are x and z axis, respectively. The boundary of the model is set at $x = -50 R_E$, which is indicated by the brown vertical line. The model assumes that the X-line is located at the equatorial plane at $x = -50 R_E$, where the horizontal blue line (x axis) intersects the vertical boundary of the model (vertical brown line). All the field lines above and below equatorial plane are assumed to be open. The nightside closed field lines are colored green. The dashed black line is the magnetopause. The electric field, \mathbf{E} , is duskward and hence $\mathbf{E} \times \mathbf{B}$ is southward (downward in the figure) in the northern hemisphere. The light blue and pink shades indicate the strength of the current density, which should be ignored as they are irrelevant in the present discussion. The scale and magnetic field configuration are just arbitrary and used to illustrate the APL–OPM set up only. (adapted from *Sitnov et al.*, [2008].)

The magnetotail reconnection site (the last open-closed boundary) was arbitrarily set at $x = -50 R_E$, which is the tail boundary of the model. All the field lines that crossed the y – z plane off the equatorial plane at $x = -50 R_E$ are considered open and filled with solar wind suprathermal electrons, which are assumed to enter the magnetosphere at $x < -50 R_E$ and travel to $x = -50 R_E$ unmodified. These assumptions are supported by observations. For example,

Figure 3.6 shows that the nominal polar rain electrons on the nightside have fairly uniform energy fluxes [Newell *et al.*, 1996], suggesting that the magnetosheath and magnetopause properties as well as the processes at the entry point are fairly uniform at the entry points at these locations in the deep tail.

The model geometrical configuration is sketched in Figure 3.7. Note that the choice of the X-line location at $x = -50 R_E$ might not and most likely would not be consistent with the SuperDARN electric field, but it is not the goal of the present study to model a specific observation. We only require that the electric field has a significant duskward component, which it typically does [e.g., Pedersen *et al.*, 1985]. In order to accentuate the polar rain energy-latitude dispersion, the SuperDARN nightside potential is multiplied by an arbitrary factor of 10 (any reasonably large duskward electric field would work for the purpose of the present study). In mapping the electric field from the ionosphere to the magnetosphere, we assume that the parallel electric field is negligible.

As in our previous APL–OPM runs, we set the altitude of “detected” particle at $1.13 R_E$, which corresponds to the typical DMSP spacecraft altitude. The model DMSP trajectory is set to nearly noon-meridian orbit. We trace 19 electrons and ions with energies from 32 eV to 30 keV in 19 logarithmically equally spaced steps, the same energies as the 19 electron and ion channels in the DMSP SSJ4 instrument [Hardy *et al.*, 1984]. The magnetic coordinates used for displaying the DMSP and model calculations are the Altitude Adjusted Corrected Geomagnetic coordinates (AACGM) [Baker and Wing, 1989].

The present study investigates only the nightside polar rain electrons, which mainly consist of solar wind suprathermal electrons. We ran the model with the following input parameters: IMF (B_x, B_y, B_z) = (-3.4, -0.5, -12.3) nT, solar wind thermal $n = 11 \text{ cm}^{-3}$, $T_i = 1 \times 10^5 \text{ K}$ (8.6 eV), $T_e = 3 \times 10^4 \text{ K}$ (2.6 eV), $V = 400 \text{ km s}^{-1}$, suprathermal (halo) electron $n_s = 0.2 \text{ cm}^{-3}$, $T_s = 1 \times 10^6 \text{ K}$ (86 eV), $\kappa = 7$. The electric field is obtained from SuperDARN convection pattern for strongly southward IMF [Ruohoniemi and Greenwald, 1996]. This is essentially the same run for the strongly southward IMF case presented in Chapter 2, except that here we extend the run to the nightside whereas in Chapter 2, we only present the model calculation for the dayside. Figure 3.8 shows the model calculation of the polar rain electron spectra along the model DMSP path. The model calculation for the dayside showing particle precipitation in the open field line LLBL, cusp, and mantle is shown in Figure 6 in Wing *et al.* [2001] and is not shown here. In Figure 3.8, the spectra between 12:11:40 and 12:11:47 universal time (UT) represent

typical spatially uniform polar rain electrons. The small fluxes seen at 12:11:55 UT are just numerical artifacts. The energy-latitude dispersion can be seen between 12:11:50 and 12:12:01 UT, where the highest electron energy for each spectrum or latitude, which is marked by the white triangle, decreases with decreasing latitude. The last open field line is encountered slightly before 12:11:50 UT, which marks the time when the highest energy electron arrives in the ionosphere. After entering the magnetosphere, because of the dominant duskward electric field, the electrons undergo $\mathbf{E} \times \mathbf{B}$ equatorward convection as they move to the ionosphere. Hence, lower-energy electrons arrive at successively lower latitudes in the ionosphere. This energy-latitude dispersion is analogous to the dayside cusp ion dispersion resulting from the dayside reconnection, except that because of the $\mathbf{E} \times \mathbf{B}$ poleward convection in the cusp, the energy decreases with increasing latitude [e.g., *Wing et al.*, 1996; 2001]. This polar rain electron energy dispersion has been previously observed [*Shirai et al.*, 1997; *Zhang et al.*, 2011].

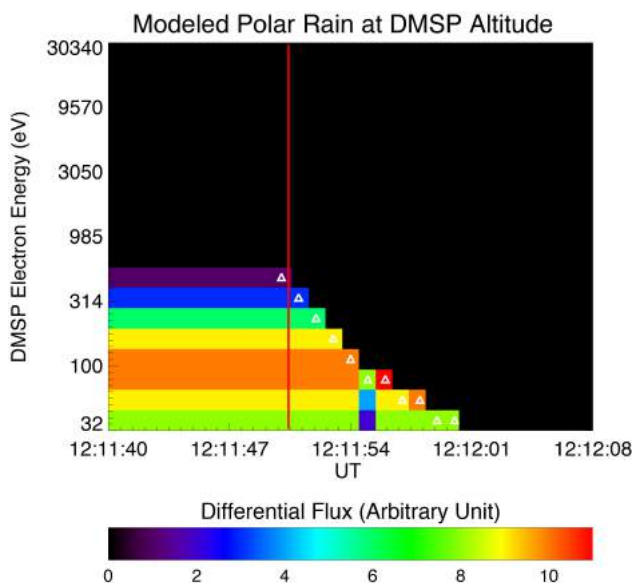


Figure 3.8. Polar rain electron dispersion from the APL–OPM model calculation. The electron spectra between 12:11:40 and 12:11:49 UT represent the typical polar rain. There is a clear electron energy-latitude dispersion after 12:11:49 UT. The white triangles, which indicate the highest energy detected at a given latitude, give a measure of the energy-latitude dispersion. They are used to determine the electron path lengths between DMSP altitude and magnetotail reconnections site. The vertical red line marks the location of the highest energy polar rain electrons in the dispersion region.

This simple model calculation successfully demonstrates quantitatively that the magnetotail reconnection and plasma $\mathbf{E} \times \mathbf{B}$ equatorward convection can lead to the polar rain energy-latitude dispersion near the open-closed boundary.

3.2.2 Estimation of electron path length

3.2.2.1 Estimation of electron path length in the model

In the model, the electron path length from the reconnection site to the polar ionosphere can be calculated. In general, the path length has a dependence on the energy. The lower-energy electrons would have more time to $\mathbf{E} \times \mathbf{B}$ drift to lower latitudes that have shorter magnetic field lines, resulting in shorter path lengths. For example, the 462 eV electrons (marked by the top or first white triangle in Figure 3.8) have a path length of $64 R_E$, whereas the 32 eV electrons (the bottom triangles in Figure 3.8) have a path length of $56 R_E$. The direct straight line distance ($50 R_E$) between the center of the Earth and the X-line is about 78% of the path length S ($64 R_E$) of the highest energy electron. This difference can be attributed to the curvature of the magnetic field lines and cross-field drift of the electrons.

A method for estimating the electron path length based on the polar rain electron energy dispersion has been developed [Shirai *et al.*, 1997; Alexeev *et al.*, 2006]. The method is briefly summarized here. An electron with a constant velocity V_1 would take time $(t_1 - t_0)$ to travel a distance S_1 [see equation (3.2)], where t_0 is the time of the reconnection (the last solar wind electron injection), t_1 is the time for the electron to be observed in the ionosphere (e.g., by DMSP satellite), and S_1 is electron path length from X-line to the ionosphere. Equation (3.3) applies to an electron with a different velocity (V_2). S_1 is not usually the same as S_2 .

$$t_1 - t_0 = \frac{S_1}{V_1} \quad (3.2)$$

$$t_2 - t_0 = \frac{S_2}{V_2} \quad (3.3)$$

While t_1 , t_2 , V_1 , and V_2 can be measured by low-altitude satellites, t_0 , S_1 , and S_2 are unknown. Equations (3.2) and (3.3) are not sufficient to solve the three unknown parameters. Hence, an assumption is needed. If we assume that $S_1 \approx S_2 = S$ and plasma is frozen in, we obtain equation (3.4),

$$\Delta t = t_1 - t_2 = S \left(\frac{1}{V_1} - \frac{1}{V_2} \right) \quad (3.4)$$

where Δt = the difference of the arrival time between the two electrons.

Because of nonzero $\mathbf{E} \times \mathbf{B}$ drift, within Δt the electrons also move a distance L in the direction of $\mathbf{E} \times \mathbf{B}$ drift at the ionosphere altitude. So, $\Delta t = L/V_p$, where V_p is the $\mathbf{E} \times \mathbf{B}$ drift speed. However, electron observations are usually made from satellites moving at speed V_s . Hence, Δt in the satellite reference frame (Δt^*) can be expressed as $\Delta t^* = L/V_s$, assuming that the X-line location and reconnection rate are steady or quasi-steady for at least several seconds. Therefore, $\Delta t = (V_s/V_p)\Delta t^*$ for the case where V_s is parallel to V_p . If V_s and V_p are not parallel, then a component of V_p that is parallel to V_s would be used instead. By replacing Δt in equation (3.4), we obtain the expression for the electron path length (S)

$$S = \frac{\left(\frac{V_s \Delta t^*}{V_p}\right)}{\left(\frac{1}{V_1} - \frac{1}{V_2}\right)} \quad (3.5)$$

This equation is similar to the one used by *Alexeev et al.* [2006]. In equation (3.5), the error in V_p is a major source of the uncertainty in S because V_s , Δt , V_1 , and V_2 can usually be accurately determined. Equations (3.4) and (3.5) are derived with the assumption $S_1 = S_2 = S$, which also introduces some inaccuracies.

Position	1 st	2 nd	3 rd	4 th	5 th	6 th
Time (UT)	12:11:50	12:11:51	12:11:52	12:11:53	12:11:54	12:11:55
Time relative to 1 st electron (s)	0	1	2	3	4	5
Energy (eV)	462	314	215	147	100	69
Path length (R_E)		43	39	36	32	29
Electron pair		(1 st , 2 nd)	(1 st , 3 rd)	(1 st , 4 th)	(1 st , 5 th)	(1 st , 6 th)

Table 3.1. Dispersion time, energy, and electron path lengths estimated by equation (3.5) in the model run shown in Figure 3.8 (see text). Row 5 lists the electron path lengths calculated from the given electron pairs.

The model is run with $V_s = 7.8 \text{ km s}^{-1}$, which is the DMSP satellite speed, and $V_p = \mathbf{E} \times \mathbf{B}$ drift = 1.7 km s^{-1} , where \mathbf{E} is the same as the model \mathbf{E} described in Section 3.2.1 and \mathbf{B} is obtained from the International Geomagnetic Reference Field (IGRF) at the DMSP satellite location. Using equation (3.5), we calculate S for five pairs of selected triangles in Figure 3.8: (1st, 2nd), (1st, 3rd), (1st, 4th), (1st, 5th), and (1st, 6th). Table 3.1 shows the time (UT) of these selected points, their

energies, and the resulting electron path lengths (S). There is a trade off in errors of using a pair of electrons that are close vs. far apart in energy. Using two electrons having a large energy difference, e.g., the pair (1st, 6th) in Table 3.1, would reduce the error in L and Δt^* , but, would decrease the validity of the assumption of $S_1 = S_2 = S$. The latter generally turns out to be a more dominant source of error. Table 3.1 shows that S ranges from 43 to 29 R_E and averages to 36 R_E , which are much shorter than the actual path lengths as determined from electron tracing in the model (64–56 with an average of 60 R_E). Hence, the calculation here shows that the method can underestimate the actual electron path length on average by about 40%. The best result comes from using the highest two energies, pair (1st, 2nd), which results in $S = 43 R_E$ and which underestimates the actual electron path length (64 R_E) by 33%.

The underestimation error would decrease with increasing electron energy and vice versa. As discussed in the beginning of this section, S decreases when lower energy electrons are used. Hence, using a pair of lower energy electrons even if they are from adjacent energy channels (minimizing $\Delta S = |S_1 - S_2|$) could lead to a larger error than using pair (1st, 2nd). For example, S for the pairs (2nd, 3rd), (3rd, 4th), and (4th, 5th) are 36, 30, and 24 R_E , respectively. For the same reason, we have not used the last five triangles in Figure 3.8, which would result in smaller electron path lengths and larger error than pair (1st, 2nd). The result suggests that the error has a dependency on the particle detector. A particle detector with finer energy scale would reduce $\Delta S = |S_1 - S_2|$ between two adjacent channels, leading to smaller error.

3.2.2.2 A couple examples from DMSP observations

To illustrate, we apply the above method to two real DMSP dispersion events: one for weakly northward and one for strongly southward IMF. We choose these two events because (1) we would like to show that even with unusually large polar rain electron energies, up to keV, the energy-latitude dispersion can still be observed and (2) higher energy would give more accurate estimates of the path length S and X-line distance. Figure 3.9a shows the polar rain dispersion event on 2002–04–17. The associated IMF is GSM $(x, y, z) = (-6, 13, 1)$ nT, indicating a weakly northward IMF B_z and a dominant IMF B_y . As discussed in Section 3.2.2.1, the method would give the most accurate estimate of S by using the two highest energy electrons (the top two triangles), which correspond to (19:48:23, 19:48:24) UT and electron energies (3040, 1393) eV

respectively. Using equation (3.5), $V_s = 7.8 \text{ km s}^{-1}$ (DMSP satellite speed), and ionospheric plasma drift speed along DMSP path $V_p = 1.73 \text{ km s}^{-1}$ (SuperDARN convection map [Ruohoniemi and Greenwald, 1996] and DMSP SSIES observations), we obtain path length $S = 49 R_E$. However, if the method underestimates S by 33% as obtained by the APL–OPM run in Section 3.2.2.1, the actual S is probably closer to $73 R_E$. Assuming the same ratio ($\sim 78\%$) between the reconnection X-line location ($50 R_E$) and the electron path length ($64 R_E$) obtained in the APL–OPM model run in Section 3.2.2.1, the X-line location is estimated at $x = 78\% \times (-73 R_E) = -57 R_E$. This estimate is somewhat crude. The model boundary is limited by the magnetic field model boundary, which is at $x = -50 R_E$. Hence, we cannot model any events that have X-line locations $< -50 R_E$. One may improve on our methodology by using particle in a cell (PIC) simulation or by using test particles in magnetohydrodynamic (MHD) simulation, both of which are computationally expensive and beyond the scope of the present study.

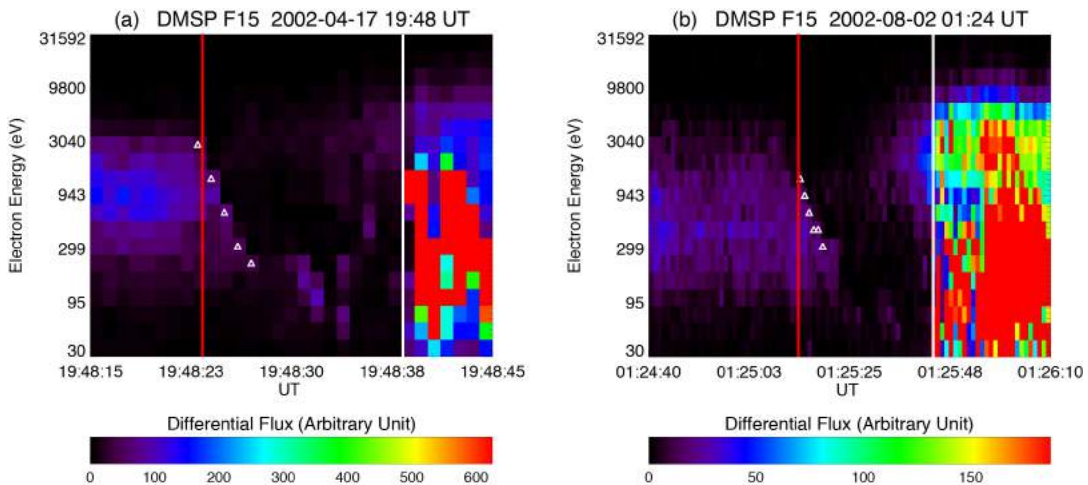


Figure 3.9. Polar rain electron dispersion observed by DMSP F15 at (a) 2002–04–17 19:48 UT and (b) 2002–08–02 01:24 UT. The white triangles, which indicate the highest energy detected at a given latitude, give a measure of the energy–latitude dispersion. The vertical red lines mark the location of the highest energy polar rain electrons in the dispersion region while the vertical white lines mark b6.

Figure 3.9b shows another example of polar rain electron dispersion on 2002–08–02. The two highest energy electrons (the top two triangles) correspond to (01:25:14, 01:25:15) and electron energies (1393, 640) eV respectively. The

IMF condition for this event is GSM $(x, y, z) = (1.5, -10, -11)$ nT, indicating a strongly southward IMF. Using the method, we obtained electron path length $S = 74 R_E$, but the actual S may be closer to $111 R_E$, assuming the same 33% underestimation error obtained in Section 3.2.2.1. The X-line location is estimated at $x = 78\% \times (-111 R_E) = -87 R_E$.

3.2.3 Where is the nightside magnetic field line open-closed boundary?

Many studies used the poleward edge of the subvisual drizzle (b6) or poleward edge of the auroral oval as the magnetic field open-closed boundary in the particle precipitation observations [e.g., *Boakes et al.*, 2008; *Longden et al.*, 2010]. *Hubert et al.* [2006] used the halfway point between b6 and b5 (b5e and b5i are assumed to be identical) as the demarcation for open-closed boundary. *Longden et al.* [2010] found that the open-closed boundary determined from IMAGE ultraviolet (UV) Wideband Imaging Camera (WIC) and Spectrographic Imager SI-13 images are systematically poleward of DMSP b6 on the nightside by about 1° – 2° in magnetic latitude, except perhaps near dawn for SI-13 open-closed boundary. Similarly, *Boakes et al.* [2008] found that IMAGE WIC open-closed boundary is systematically poleward of DMSP b6, except near dawn. The WIC (140 – 190 nm) and SI-13 (135 nm) emissions respond mostly to electron precipitation. Previous studies suggested correction algorithm for the magnetic field open-closed boundary obtained from auroral UV images based on the assumption that DMSP b6 gives the best estimate of this boundary [e.g., *Boakes et al.*, 2008].

Irrespective of the auroral imagery and DMSP particle boundary comparisons above, there may be a reason to expect that the open-closed boundary is located poleward of b6. The magnetic field line open-closed boundary should correspond to the last open field line. In the presence of the dawn-dusk electric field, the electrons on the last open field line in the magnetotail would $\mathbf{E} \times \mathbf{B}$ to lower latitude as they travel to ionosphere. As a result, the dispersion region is typically equatorward of the open-closed boundary. The amount of the equatorward displacement would depend on the electron velocity (energy), the poleward component of $\mathbf{E} \times \mathbf{B}$, and the electron path length from the magnetotail X-line to the ionosphere. In the model run discussed in Section 3.2.1, partly because of the moderate X-line distance ($50 R_E$), the last open field line is located

just slightly less than 0.1° poleward of the highest energy electrons in the energy-latitude dispersion region. Larger X-line distance would result in a larger displacement. Nevertheless, the highest energy electrons in the dispersion region can still serve as a better proxy for the open-closed boundary than b6, b5e, or b5i (the auroral oval poleward boundaries).

The highest energy electrons in the dispersion region are indicated with a vertical red line in Figures 3.6, 3.8, and 3.9, which can be taken as the latitudinal lower bound of the open-closed boundary. As can be seen in Figures 3.6, the vertical red line is poleward of b6, which is indicated by a vertical black line. For example, in Figure 3.6b, b6 is located at -71.5° MLat whereas the red line is located at -72.2° MLat. Hence, the open-closed boundary is located at least 0.7° or about 88 km more poleward than b6. In Figure 3.6d, the open-closed boundary is located at least 1.2° or 150 km poleward of b6 (b6 = 74.3° MLat and the red line = 75.5° MLat). The solar wind condition for the 1992–06–16 event shown in Figures 3.6a and 3.6b is fairly moderate, IMF GSM $(x,y,z) = (7, -2, -2)$ nT, $|V_{sw}|=360$ km s $^{-1}$, $n_{sw} = 7$ cm $^{-3}$. There is no solar wind data for the 1984–03–22 event shown in Figures 3.6c and 3.6d, but the magnetic activity indices indicate that the magnetic condition is moderately active, $K_p = 4+$, $D_{st} = -35$ nT, and $AL = -100$ nT. For the two events in Figures 3.9a and 3.9b, the open-closed boundary is located at least 0.7° (88 km) and 1.5° (165 km) poleward of b6, respectively. Our result is consistent with *Sergeev and Bosinger* [1993], which examines energetic (>30 keV) particle precipitation during moderately active times and concludes that the actual open-closed boundary may lay poleward of the auroral oval detected by auroral particles (0.3–20 keV).

However, the energy-latitude dispersion is not observed in every DMSP polar pass. It would be expected that the dispersion can only be observed when there is a significant $\mathbf{E} \times \mathbf{B}$ drift during the electron flight from the magnetotail X-line to the ionosphere. The conditions that would be favorable to observe the energy-latitude dispersion are strong dawn-dusk electric field, large X-line distance, and unusually low electron energy. The example shown in Figures 3.6a and 3.6b, the 1992–06–16 event, suggests that the polar rain electron energy-latitude dispersion can be observed even when the solar wind driver is mild and IMF B_y and B_z are relatively small. The examples shown in Figure 3.9 show that the dispersion can also be observed even when the polar rain electron energies are unusually high, in the order of a few keV, but the IMF B_y or B_z is unusually large for these two events. When the dispersion is not observable, the open-closed

boundary may be approximated by the location where polar rain ends near the nightside auroral oval or where the polar rain meets the auroral oval, in cases where they do meet.

3.2.4 The electron overhang

As can be seen in Figures 3.6 and 3.9, equatorward of the polar rain dispersion regions, there is sometimes a gap, a region of little electron precipitation [Meng and Kroehl, 1977], followed by hot electrons (up to several keV or even a few tens of keV) that are sometimes referred to as “electron overhang”, which can be seen as a poleward extension of the nightside auroral oval electrons. The electrons in the overhang region have energies that are similar to those in the plasma sheet and higher than those in the polar rain. The overhang region often overlaps with the polar rain dispersion region such that the same flux tube can contain electrons from both regions as shown in Figure 3.6. The overhang electrons are not well understood [Newell *et al.*, 1996], although in general, they are believed to originate from the plasma sheet [Shirai *et al.*, 1997]. The auroral UV open-closed boundary, which was sometimes found located poleward of b6 [e.g., Boakes *et al.*, 2008; Longden *et al.*, 2010], may correspond to the poleward boundary of the overhang electrons.

After reconnection, the supply of the solar wind electrons is shut off. So, after all the field-aligned polar rain electrons precipitate into the ionosphere, the loss cone would become empty, which may explain the gap region. Apparently, it takes some time for the plasma sheet electrons from the surrounding closed field lines to curvature and gradient drift into the newly closed field line and get pitch-angle scattered. Consistent with the curvature and gradient drifts, which are energy dependent, the higher energy electrons would first drift into the flux tube. Then, as the flux tube continues to convect earthward (or equatorward in the ionosphere), the lower energy plasma sheet electrons would arrive. This would be consistent with the energy-latitude dispersion often seen in the overhang region seen in Figures 3.6 and 3.9.

In order for the plasma sheet electrons to be observed by DMSP at low-altitude, there has to be a mechanism for pitch-angle scattering. A leading mechanism for pitch-angle scattering is electron interactions with waves such as VLF whistler-mode chorus wave [e.g., Thorne, 2010; Summers *et al.*, 1998; Gkioulidou *et al.*, 2012; Wing *et al.*, 2013]. However, the wave-electron

interaction may preferentially pitch-angle scatter electrons with certain energies. We plan to calculate the energy dependence of the wave-electron interaction in a future study.

3.3 Summary and conclusion

3.3.1 Dayside polar cap

The present study investigates the field-aligned electric fields in the adjacent polar cap region. APL–OPM predicts upward field-aligned electric field to retard electron entries into the magnetosphere in order to maintain charge quasi-neutrality. Such electric fields have been confirmed in a previous study that fitted DMSP spectra as well as in a study that compared ACE and DMSP electron distribution functions. However, field-aligned electric field with the opposite polarity can be occasionally found in the upward FAC region. Near the boundary layer on the duskside, there are discontinuities in convection electric field such that $\nabla \cdot \mathbf{E} < 0$, which can generate large-scale upward FACs, which may require upward field-aligned electric to draw more electrons downward when the electron density is too low. Generally, in the upward FAC region, upward electric fields that accelerate electrons downward are seen with the occurrence rates of 82%–96%, depending on the MLT, with no clear preference for IMF B_z . In contrast, the occurrence rates in the downward FAC regions are 3%–11%. It is not clear what causes upward electric field in the downward or no FAC regions. The APL–OPM does not take into account the effects of FAC and ionospheric outflows on field-aligned electric field.

The location of the upward and downward field-aligned electric fields may differ. Downward field-aligned electric fields should develop close to the magnetopause boundary to prevent the entry of excess electrons, while upward field-aligned electric fields are typically largest at lower altitude where they are required to overcome the mirror force.

The polar rain electrons located in the upward FAC region often show a ramping up of energy with increasing latitude. This may be attributed to evolution of the magnetosheath electrons that progressively have higher anti-sunward velocity and lower density with increasing distance from the subsolar point. At progressively higher latitude, the polar rain electrons originate from magnetosheath region that has higher anti-sunward velocity and lower density, both of which can increase upward accelerating potential drop. This would

continue until the magnetosheath velocity and density asymptotically reach those of solar wind, at which point the potential drop would plateau. As a result, the precipitating electron characteristic energy would also plateau. At latitudes poleward of the upward FAC region where the FAC is nearly zero or downward, polar rain electrons enter even further down the tail but they do not undergo such acceleration.

The DMSP automatic particle precipitation classification algorithm does not take into account the effect of upward field-aligned electric field in the upward FAC region. As a result, the algorithm can misclassify mantle or polar rain (with no significant ion precipitation) as BPS, leading to an unusual scenario where the magnetic field lines would be closed–open–closed–open from low to high latitude. Taking into account the electron acceleration in the upward FAC region, one would get the expected scenario of open–closed field lines from low to high latitude.

3.3.2 Nightside polar cap

APL–OPM successfully models the polar rain electron energy-latitude dispersion and demonstrates quantitatively that this dispersion results from the solar wind suprathermal electron entries in the last open field line and $\mathbf{E} \times \mathbf{B}$ equatorward convection. Using APL–OPM, we find that the existing method for obtaining electron path length from the X-line to the ionosphere underestimates path lengths by at least 33%. The best estimate is obtained by using the two highest energy electrons in the dispersion region.

The magnetic field line open-closed boundary is located slightly poleward of the highest energy electrons observed in the polar rain dispersion region, which, in turn is located poleward of b6, b5e, and b5i (DMSP auroral oval poleward boundaries). In our model run, partly because of the moderate X-line distance ($50 R_E$), the open-closed boundary is located just slightly less than 0.1° poleward of the highest energy electrons in the energy-latitude dispersion region. Larger X-line distance would result in a larger displacement. Regardless, the location of the highest energy electrons would be a more accurate proxy for the open-closed boundary than b6, b5i, or b5e. In the four DMSP cases examined, the open-closed boundary is located at least 0.7° – 1.5° poleward of b6. Previous studies presented formulas to correct the open-closed boundary location obtained from the auroral UV imagery based on the assumption that b6 being the best available proxy.

The present study suggests that these formulas need be modified. However, the polar rain energy-latitude dispersion is not always observable, which may depend on the magnetotail electric field, the X-line distance, and the polar rain electron energy. For a future study, we will investigate statistically how often the energy-latitude dispersion can be observed. Finally, the energy-latitude dispersion seen in the electron overhang may result from the plasma sheet electrons curvature and gradient drifts into the newly closed field line. The auroral UV open-closed boundary may correspond to the poleward boundary of this electron overhang.

3.4 References

- Alexeev, I. V., et al. (2006), Remote sensing of a magnetotail reconnection X-line using polar rain electrons, *Geophys. Res. Lett.*, 33, L19105, doi:10.1029/2006GL027243.
- Baker, K. B., and S. Wing (1989), A new magnetic coordinate system for conjugate studies at high latitudes, *J. Geophys. Res.*, 94(A7), 9139–9143, doi:10.1029/JA094iA07p09139.
- Block, L. P., and C.-G. Fälthammar (1991), Characteristics of magnetic-field aligned electric fields in the auroral acceleration region in *Auroral Physics*, eds. C.-I. Meng, M. J. Rycroft, and L. A. Frank, 109 – 118, Cambridge University Press, New York, USA.
- Boakes, P. D., Milan, S. E., Abel, G. A., Freeman, M. P., Chisham, G., Hubert, B., and Sotirelis, T. (2008): On the use of IMAGE FUV for estimating the latitude of the open/closed magnetic field line boundary in the ionosphere, *Ann. Geophys.*, 26, 2759–2769, doi:10.5194/angeo-26-2759-2008.
- Burke, W. J., M. S. Gussenhoven, M. C. Kelley, D. A. Hardy, and F. J. Rich (1982), Electric and magnetic field characteristics of discrete arcs in the polar cap, *J. Geophys. Res.*, 87 (A4), 2431–2443, doi:10.1029/JA087iA04p02431.
- Chaston, C. C., J. W. Bonnell, L. M. Peticolas, C. W. Carlson, J. P. McFadden, and R. E. Ergun (2002), Driven Alfvén waves and electron acceleration, *Geophys. Res. Lett.*, 29, 1535.
- Damiano, P. A., and J. R. Johnson (2012), Electron acceleration in a geomagnetic Field Line Resonance, *Geophys. Res. Lett.*, 39, L02102, doi:10.1029/2011GL050264.
- Dungey, J. W. (1961), Interplanetary magnetic fields and the auroral zones, *Phys. Rev. Lett.*, 6, 47–48.

- Eastwood, J. P. (2008), The science of space weather, *Phil. Trans. R. Soc. A*, 4489 – 4500, doi:10.1098/rsta.2008.0161.
- Echim, M. M., M. Roth, and J. De Keyser (2008), Ionospheric feedback effects on the quasi-static coupling between LLBL and postnoon/evening discrete auroral arcs, *Ann. Geophys.*, 26, 913–928.
- Fairfield, D. H., and J. D. Scudder (1985), Polar rain: Solar coronal electrons in the Earth's magnetosphere, *J. Geophys. Res.*, 90, 4055.
- Fairfield, D. H., S. Wing, P. T. Newell, J. M. Ruohoniemi, J. T. Gosling, and R. M. Skoug (2008), Polar rain gradients and field-aligned polar cap potentials, *J. Geophys. Res.*, 113, A10203, doi:10.1029/2008JA013437
- Fear, R.C., S.E. Milan, R. Maggiolo, A.N. Fazakerley, I. Dandouras, S.B. Mende, Direct observation of closed magnetic flux trapped in the high-latitude magnetosphere, *Science*, 19 December 2014: Vol. 346 no. 6216 pp. 1506-1510, DOI: 10.1126/science.1257377
- Gkioulidou, M., C.-P. Wang, S. Wing, L. R. Lyons, R. A. Wolf, and T.-S. Hsu (2012), Effect of an MLT dependent electron loss rate on the magnetosphere-ionosphere coupling, *J. Geophys. Res.*, 117, A11218, doi:10.1029/2012JA018032.
- Gou, X. C., Q. Q. Shi, A. M. Tian, W. J. Sun, M. W. Dunlop, S. Y. Fu, Q. G. Zong, G. Facskó, M. Nowada, Z. Y. Pu, B. Mailyan, T. Xiao, and X. C. Shen (2016), Solar Wind Plasma Entry Observed by Cluster in the High-Latitude Magnetospheric Lobes. *J. Geophys. Res.*, 120, doi: 10.1002/2015JA021578.
- Hardy, D. A., L. K. Schmitt, M. S. Gussenhoven, F. J. Marshall, H. C. Yeh, T. L. Shumaker, A. Hube, and J. Pantazis (1984), Precipitating Electron and Ion Detectors (SSJ/4) for the Block 5D/Flights 6-10 DMSP Satellites: Calibration and Data Presentation, Rep. AFGL-TR-84-0317, Air Force Geophys. Lab., Hanscom Air Force Base, Mass.
- Hoffman, R. A., R. A. Heelis, and J. S. Prasad (1985), A Sun-aligned arc observed by DMSP and AE-C, *J. Geophys. Res.*, 90(A10), 9697–9710, doi:10.1029/JA090iA10p09697.
- Hubert, B., S. E. Milan, A. Grocott, C. Blockx, S. W. H. Cowley, and J.-C. Gérard (2006), Dayside and nightside reconnection rates inferred from IMAGE FUV and Super Dual Auroral Radar Network data, *J. Geophys. Res.*, 111, A03217, doi:10.1029/2005JA011140.
- Iijima, T., and T. A. Potemra (1976), The Amplitude distribution of field-aligned currents at northern high latitudes observed by Triad, *J. Geophys. Res.*, 81, 2165-2174.

- Knight, L. (1973), Parallel electric fields, *Planet. Space Sci.*, 21, 741 – 750.
- Kitamura, N., K. Seki, Y. Nishimura, N. Terada, T. Ono, T. Hori, and R. J. Strangeway (2012), Photoelectron flows in the polar wind during geomagnetically quiet periods, *J. Geophys. Res.*, 117, A07214, doi:10.1029/2011JA017459.
- Longden, N., Chisham, G., Freeman, M. P., Abel, G. A., and Sotirelis, T. (2010): Estimating the location of the open-closed magnetic field line boundary from auroral images, *Ann. Geophys.*, 28, 1659-1678, doi:10.5194/angeo-28-1659-2010.
- Lyons, L. (1980), Generation of large-scale regions of auroral currents, electric potentials, and precipitation by the divergence of the convection electric field, *J. Geophys. Res.*, 85(A1), 17–24, doi:10.1029/JA085iA01p00017.
- Mailyan, B. et al. (2015), Transpolar arc observation after solar wind entry into the high-latitude magnetosphere, *J. Geophys. Res.*, 120, 3525–3534, doi:10.1002/2014JA020912.
- Meng, C.-I., and H. W. Kroehl (1977), Intense uniform precipitation of low-energy electrons over the polar cap, *J. Geophys. Res.*, 82, 2305.
- Milan, S. E., B. Hubert, and A. Grocott (2005), Formation and motion of a transpolar arc in response to dayside and nightside reconnection, *J. Geophys. Res.*, 110, A01212, doi:10.1029/2004JA010835.
- Newell, P. T., W. J. Burke, C.-I. Meng, E. R. Sanchez, and M. E. Greenspan (1991a), Identification and observations of the plasma mantle at low altitude, *J. Geophys. Res.*, 96, 34 – 45.
- Newell, P. T., S. Wing, C. I. Meng, and V. Sigillito (1991b), The Auroral Oval Position, Structure And Intensity of Precipitation From 1984 Onwards: An Automated On-Line Data Base, *J. Geophys. Res.*, 96, 5877-5882.
- Newell, P. T., W. J. Burke, E. R. Sanchez, C.-I. Meng, M. E. Greenspan, and C. R. Clauer (1991c), The low-latitude boundary layer and the boundary plasma sheet at low altitude: prenoon precipitation regions and convection reversal boundaries, *J. Geophys. Res.*, 96, 21,013 – 21,023.
- Newell, P. T., Y. I. Feldstein, Y. I. Galperin, and C.-I. Meng (1996), Morphology of nightside precipitation, *J. Geophys. Res.*, 101(A5), 10737–10748, doi:10.1029/95JA03516.
- Pedersen, A., C. A. Cattell, C.-G. Fälthammar, K. Knott, P.-A. Lindqvist, R. H. Manka, and F. S. Mozer (1985), Electric fields in the plasma sheet and plasma sheet boundary layer, *J. Geophys. Res.*, 90(A2), 1231–1242, doi:10.1029/JA090iA02p01231.

- Rich, F. J., D. A. Hardy, and M. S. Gussenhoven (1985), Enhanced ionosphere-magnetosphere data from the DMSP satellites, *Eos*, 66, 513.
- Ruohoniemi, J. M., and R. A. Greenwald (1996), Statistical patterns of high-latitude convection obtained from Goose Bay HF radar observations, *J. Geophys. Res.*, 101, 21,743.
- Sergeev, V. A., and T. Bösinger (1993), Particle dispersion at the nightside boundary of the polar cap, *J. Geophys. Res.*, 98(A1), 233–241, doi:10.1029/92JA01667.
- Shi, Q. Q. et al. (2013), Solar wind entry into the high-latitude terrestrial magnetosphere during geomagnetically quiet times., *Nat. Commun.*, 4, 1466, doi:10.1038/ncomms2476.
- Shirai, H., et al. (1997), Drop-off of the polar rain flux near the plasma sheet boundary, *J. Geophys. Res.*, 102, 2271–2278.
- Sitnov, M. I., N. A. Tsyganenko, A. Y. Ukhorskiy, and P. C. Brandt (2008), Dynamical data-based modeling of the storm-time geomagnetic field with enhanced spatial resolution, *J. Geophys. Res.*, 113, A07218, doi:10.1029/2007JA013003.
- Spreiter, J. R., and S. S. Stahara (1985), Magnetohydrodynamic and gasdynamic theories for planetary bow waves, in *Collisionless Shocks in the Heliosphere: Reviews of Current Research, Geophys. Monogr. Ser.*, vol. 35B, edited by T. Tsurutani and R. G. Stone, pp. 85–107, AGU, Washington, D. C.
- Summers, D., R. M. Thorne, and F. Xiao (1998), Relativistic theory of wave-particle resonant diffusion with application to electron acceleration in the magnetosphere, *J. Geophys. Res.*, 103(A9), 20,487–20,500, doi:10.1029/98JA01740.
- Thorne, R. M. (2010), Radiation belt dynamics: The importance of wave-particle interactions, *Geophys. Res. Lett.*, 37, L22107, doi:10.1029/2010GL044990.
- Su, Y.-J., J. L. Horwitz, G. R. Wilson, P. G. Richards, D. G. Brown, and C. W. Ho (1998), Self-consistent simulation of the photoelectron-driven polar wind from 120 km to 9 RE altitude, *J. Geophys. Res.*, 103(A2), 2279–2296, doi:10.1029/97JA03085.
- Watt, C. E. J., and R. Rankin (2009), Electron trapping in shear Alfvén waves that power the aurora, *Phys. Rev. Lett.*, 102, 045002.
- Wing, S., P. T. Newell, and T. G. Onsager (1996), Modeling the entry of magnetosheath electrons into the dayside ionosphere, *J. Geophys. Res.*, 101(A6), 13155–13167, doi:10.1029/96JA00395.
- Wing, S., and P. T. Newell (1998), Central plasma sheet ion properties as inferred

- from ionospheric observations, *J. Geophys. Res.*, 103(A4), 6785–6800, doi:10.1029/97JA02994.
- Wing, S., P. T. Newell, and J. M. Rouhoniemi (2001), Double cusp: Model prediction and observational verification, *J. Geophys. Res.*, 106, 25571.
- Wing, S., P. T. Newell, C.-I. Meng (2005), Cusp Modeling and Observations at Low Altitude, *Surveys in Geophysics*, 26: 341-367, doi:10.1007/s10712-005-1886-0.
- Wing, S., S. Ohtani, P. T. Newell, T. Higuchi, G. Ueno, and J. M. Weygand (2010), Dayside field-aligned current source regions, *J. Geophys. Res.*, 115, A12215, doi:10.1029/2010JA015837.
- Wing, S., S. Ohtani, J. R. Johnson, M. Echim, P. T. Newell, T. Higuchi, G. Ueno, and G. R. Wilson (2011), Solar wind driving of dayside field-aligned currents, *J. Geophys. Res.*, 116, A08208, doi:10.1029/2011JA016579.
- Wing, S., M. Gkioulidou, J. R. Johnson, P. T. Newell, and C.-P. Wang (2013), Auroral particle precipitation characterized by the substorm cycle, *J. Geophys. Res. Space Physics*, 118, 1022–1039, doi:10.1002/jgra.50160.
- Zhang, Y., L. J. Paxton, and H. Kil (2011), Nightside polar rain aurora boundary gap and its applications for magnetotail reconnection, *J. Geophys. Res.*, 116, A11214, doi:10.1029/2011JA016884.
- Zhu, L., R.W. Schunk, J.J. Sojka (1997), Polar cap arcs: a review, *Journal of Atmospheric and Solar-Terrestrial Physics*, 59, 1087-1126, 1364-6826, doi:10.1016/S1364-6826(96)00113-7.

Chapter 4

Solar wind energy transfer to the magnetosphere through low-latitude boundary layer

Chapter 3 presents the solar wind plasma and energy transfer to the magnetosphere in the aftermath of dayside reconnection. The solar wind plasma continues to enter the magnetosphere as the open field lines $\mathbf{E} \times \mathbf{B}$ convect to the nightside (region 1 in Figure 1.2). Another path for the solar wind to transfer energy and plasma to the magnetosphere is through low-latitude boundary layer (region 2 in Figure 1.2). This chapter discusses mainly the solar wind energy transfer, which drives the field-aligned current (FAC), while Chapter 5 reviews the solar wind plasma transfer through low-latitude boundary layer and its consequent transport within the magnetotail.

4.1 Introduction

The low-latitude boundary layer (LLBL) is a narrow region of persistent or intermittent flow located on the inner edge of the magnetopause [e.g., *Hones et al.*, 1972]. The boundary layer can play an important role in the transfer of mass, momentum, and energy from the solar wind to the magnetosphere [e.g., *Eastman et al.*, 1976]. One of the key features of the boundary layer is the transition in the plasma flow from magnetosheath flow velocity to the relatively stagnant flow in the magnetosphere. The velocity shear layer corresponds to a potential difference across the boundary, which can drive field-aligned currents [e.g., *Sonnerup*, 1980] into and out of the ionosphere as described by [e.g., *Iijima and Potemra*, 1976]. Moreover, plasma structures in the LLBL are well correlated with the occurrence of discrete auroral arcs at high-latitude in the early afternoon. *Echim et al.* [2007;

2008] recently developed a 1D kinetic model that describes magnetosphere-ionosphere coupling in a sheared boundary layer and provides profiles of field-aligned currents, potential drop, and precipitating electron energy flux.

Wing et al. [2011] examines the dependence of FAC density (J_{\parallel}), peak electron energy (as a proxy for the field-aligned potential drop ($\Delta\phi_{\parallel}$) [e.g., *Lyons*, 1980]), and electron energy flux (ϵ) on solar wind velocity (V_{sw}) and solar wind density (n_{sw}) in the afternoon upward FAC region located at the boundary layer or open field lines. The study finds that J_{\parallel} increases with increasing n_{sw} and V_{sw} , consistent with the model of *Echim et al.* [2008]. As V_{sw} increases, velocity shear at the boundary increases, which leads to higher potential drop across the boundary, which in turn drives larger J_{\parallel} . An increase in n_{sw} increases the number of electron current carriers, which tends to increase J_{\parallel} , assuming all other parameters remain the same. On the other hand, as n_{sw} , the number of current carriers, decreases and a parallel potential drop develops to draw more electrons downward to carry the current. Consequently, it is expected that $\Delta\phi_{\parallel}$ increases as n_{sw} decreases. This inverse relationship is seen in DMSP observations [*Wing et al.*, 2011] as well as in the model [*Echim et al.*, 2008]. In both the model and DMSP observations, $\Delta\phi_{\parallel}$ increases with increasing V_{sw} because larger V_{sw} drives more current, J_{\parallel} , which, in turn, requires larger $\Delta\phi_{\parallel}$, assuming other parameters remain the same.

This chapter has been published in the following papers:

Wing, S., and J. R. Johnson (2015), Theory and observations of upward field-aligned currents at the magnetopause boundary layer, *Geophys. Res. Lett.*, 42, 9149–9155, doi:10.1002/2015GL065464

Johnson, J. R., and S. Wing (2015), The dependence of the strength and thickness of field-aligned currents on solar wind and ionospheric parameters. *J. Geophys. Res. Space Physics*, 120, 3987–4008. doi: 10.1002/2014JA020312

Contribution statement:

S. Wing: contributed main ideas for the observations, wrote the code to analyze DMSP data, performed theory–data comparisons, provided useful discussions in Section 4.2, interpreted results, wrote the data and method, theory-data comparisons in Sections 4.3 and 4.4, wrote Sections 4.1 and 4.5.

J. R. Johnson: contributed ideas for the theory and derived the field-aligned current equations, wrote the theory component in Section 4.2, provided useful discussions in Sections 4.3 and 4.4, interpreted results. The field-aligned current equations are provided in this chapter for context so that the readers can better understand the theory–data comparisons.

The good comparisons of the observations presented in *Wing et al.* [2011] with the model of *Echim et al.* [2008] suggest that the model captures the general dependencies of these dayside magnetosphere–ionosphere (M–I) coupling parameters on V_{sw} and n_{sw} , and that much of the dynamics of these parameters could be understood from the model. Motivated by *Echim et al.* [2008] and *Wing et al.* [2011], we derive simple analytic expressions that capture the dependence of the upward field-aligned current and its spatial scale on solar wind and ionospheric parameters. As a starting point, we note that *Lyons* [1980] derives an expression for upward J_{\parallel} at the boundary layer and open field lines, but it does not include velocity shear layer thickness, Δ_m . We consider a similar approach as *Lyons* [1980], but we include Δ_m , which is an important parameter for estimating J_{\parallel} . For a given velocity shear and magnetic field (or electric field) at the boundary layer, the potential drop across the boundary and J_{\parallel} vary inversely with Δ_m . Moreover, FAC latitudinal thickness (Λ) scales with Δ_m . As shown in Sections 4.2 and 4.4, the dependence of J_{\parallel} on Δ_m also makes it possible to infer boundary layer structure from measurements of ionospheric and solar wind parameters, which is a significant advance not possible using the model of *Lyons* [1980].

The organization of this chapter is as follows. We develop a theory for upward FAC at the magnetopause boundary layer (Section 4.2). Then, we describe the observations and data analysis methodology (Section 4.3). Finally, we verify the analytical results through comparisons with the rigorous approach of *Echim* [2008], and with DMSP observations in the upward FAC region that is located at the boundary layer and open field lines (Section 4.4).

4.2 Analytical theory for upward FAC

4.2.1 Analytical model

The model of [*Echim et al.*, 2008] utilizes a kinetic approach for the magnetopause to compute a self-consistent boundary layer using prescribed density, temperature, and velocity moments in the magnetosheath and magnetosphere [*Echim et al.*, 2005]. The boundary layer model is coupled to the ionosphere through field-aligned currents, and solutions for the ionospheric potential are obtained by solving the current continuity equation in the ionosphere where the field-aligned currents are obtained from a nonlinear Knight relation [*Knight*, 1973].

In order to gain some simple understanding of the results presented in

[*Echim et al.*, 2008], we consider the current continuity equation of the ionosphere

$$\frac{d}{dx} \Sigma_p \frac{d\phi_i}{dx} = J_{\parallel} (\phi_m, \phi_i) \quad (4.1)$$

where Σ_p = Pedersen conductivity, ϕ_i = electric potential in the ionosphere, ϕ_m = electric potential in the magnetosphere. As in *Echim et al.* [2008], the profile of ϕ_m is determined primarily by the solar wind magnetosphere interaction at the magnetopause. In our model, the potential drop between the magnetosphere and ionosphere drives a parallel current out of the ionosphere determined by a linear Knight relation [*Knight*, 1973].

$$J_{\parallel} = \kappa (\phi_i - \phi_m) \quad (4.2)$$

where the Knight conductivity $\kappa = n_e e^2 / (2\pi m_e k_b T_e)^{0.5}$, n_e = electron number density, e = electron charge, m_e = electron mass, T_e = electron temperature, and k_b = Boltzman's constant. The linear Knight relation is obtained from an expansion of the nonlinear current-voltage relation when $1 \ll e(\phi_i - \phi_m)/T_e \ll B_i/B_m$, where B_m and B_i are the magnetic field strength at the magnetosphere/boundary layer and in the ionosphere at the bottom of the potential drop, respectively. For simplicity, we will assume that κ is constant throughout the shear layer, recognizing that the current profiles will be controlled by the value of density and temperature close to the current maximum. Observationally, the velocity shear layer tends to occur earthward of the magnetopause density gradient [*Paschmann et al.* 1993; *Phan et al.*, 1996], so the relevant density may be that of the low-latitude boundary layer. Although the model of *Echim et al.* [2008] employs a nonlinear Knight relation with densities specified by a Vlasov equilibrium model, we find that the general characteristics of the analytic solutions that we obtain are similar to the numerical results presented in *Echim et al.* [2008].

Assuming constant conductivity and combining equations (4.1) and (4.2), we find

$$L^2 \frac{d^2\phi_i}{dx^2} = (\phi_i - \phi_m) \quad (4.3)$$

where $L = \sqrt{\Sigma_p/\kappa}$ is the well known electrostatic auroral scale length [*Lyons*, 1980]. As in *Lyons* [1980] and *Echim et al.* [2008], we solve this equation in one dimension with ϕ_m specified as a function of the spatial coordinate. Equation (4.3) can be solved for the ionospheric potential, ϕ_i , using the method of Fourier transform where we take the Fourier transform of ϕ to be

$$\hat{\phi}(q) = \frac{1}{2\pi} \int_{-\infty}^{\infty} \phi(x) e^{-iqx} dx \quad (4.4)$$

with the inverse transform

$$\phi(x) = \int_{-\infty}^{\infty} \hat{\phi}(q) e^{iqx} dq \quad (4.5)$$

The Fourier transform of equation (4.3) is

$$\hat{\phi}_i(q) = \left(\frac{1}{1+q^2 L^2} \right) \hat{\phi}_m(q) \quad (4.6)$$

From equation (4.6), it is obvious that the magnetospheric potential maps to the ionospheric potential on scales larger than L (i.e., $qL \ll 1$) while a parallel potential drop can develop on smaller scales. The potential drop and field-aligned current are obtained in a similar manner by inverting their Fourier transforms,

$$\Delta\hat{\phi}(q) = \hat{\phi}_i(q) - \hat{\phi}_m(q) = -\left(\frac{q^2 L^2}{1+q^2 L^2} \right) \hat{\phi}_m(q) \quad (4.7)$$

$$\hat{J}_{\parallel}(q) = -\kappa \left(\frac{q^2 L^2}{1+q^2 L^2} \right) \hat{\phi}_m(q) \quad (4.8)$$

In the remainder of this section, we shall obtain and analyze the solution of equation (4.8) to determine how the field-aligned current depends on the magnetopause profile (controlled by solar wind-magnetosphere interactions) and ionospheric conditions (controlled by solar radiation and particle precipitation).

While the model of *Echim et al.* [2007] specifies the magnetospheric potential, ϕ_m , as the solution of a kinetic boundary layer model [*Echim et al.*, 2005], the general characteristics of the variation of the magnetospheric potential may also be specified by a more generic velocity (electric field) profile that retains the basic characteristics of the magnetopause boundary layer, which can be constrained by observations. The velocity profile in the boundary layer typically varies from an asymptotic flow, V_0 , to little or no flow on the inner edge of the boundary layer over the thickness of the boundary layer, Δ_m . We consider a simple velocity profile at the magnetopause boundary layer that captures these characteristics is

$$V_y(x_m) = \frac{V_0}{2} (1 + \tanh(x_m/\Delta_m)) \quad (4.9)$$

where x_m is the magnetospheric coordinate across the magnetopause boundary layer. This velocity profile is consistent with an electric field

$$E_x = -\frac{d\phi_m}{dx_m} = -V_y B_m \quad (4.10)$$

which is supported by a potential of the following form

$$\phi_m(x_m) = \frac{V_0 B_m}{2} [x_m + \Delta_m \log(2 \cosh(x_m/\Delta_m))] \quad (4.11)$$

where we have added an arbitrary constant so that the potential is zero at the inner (magnetospheric) edge of the LLBL.

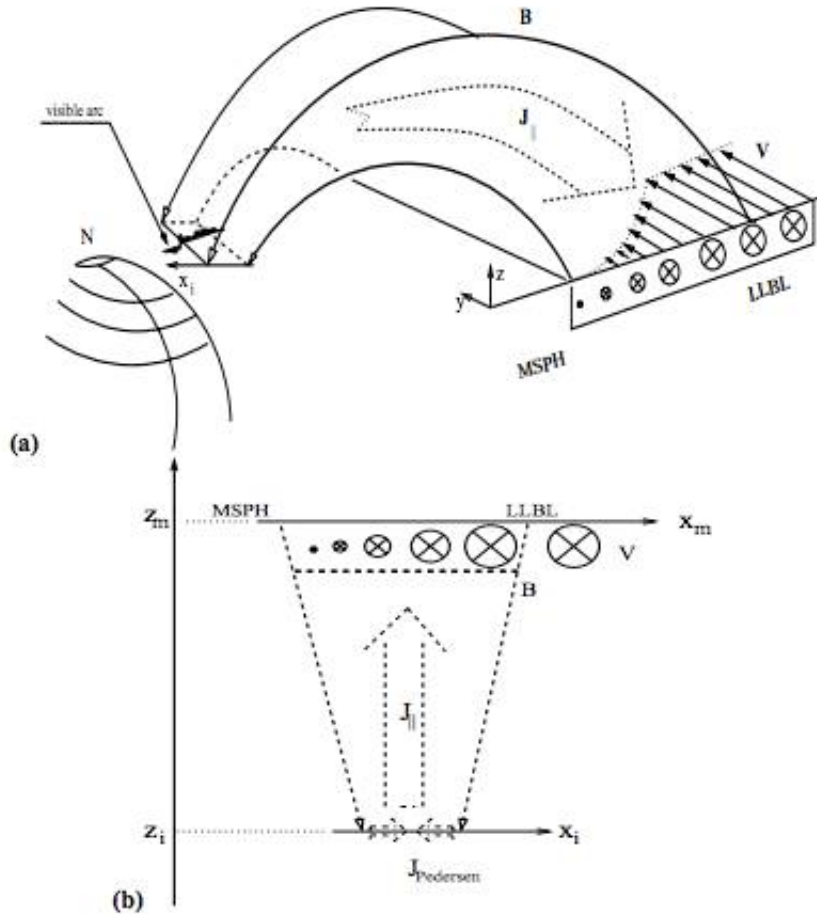


Figure 4.1. Diagram illustrating the geometry considered to study the coupling between a sheared flow LLBL and the ionosphere. (a) A schematic 3D view of the magnetosphere flank; (b) a simpler, conical geometry adopted to describe a flux tube extended from ionospheric altitudes (z_i) to the magnetosphere (z_m). The velocity profile is illustrated by circles with radius proportional to the local value of the shear velocity (adapted from *Echim et al.* [2007]).

To solve for the ionospheric potential in the ionosphere, it is necessary to express the magnetospheric potential as a function of the ionospheric coordinate at the ionospheric altitude, z_i . Using the simple conical mapping function used by *Echim et al.* [2007] and illustrated in Figure 4.1, we have $x_m = x_i \sqrt{B_i/B_m} = x_i \sqrt{b}$, $b = B_i/B_m$, and at 200km, $\sqrt{b} = 32$. In this case,

$$\phi_m(x_{im}) = \frac{V_0 B_m \sqrt{b}}{2} [x_i + \Delta_i \log(2 \cosh(x_i/\Delta_i))] \quad (4.12)$$

where $\Delta_i = \Delta_m/\sqrt{b}$ is the ionospheric scale length obtained by mapping the boundary layer thickness to ionospheric altitude.

Next, we obtain the Fourier transform of ϕ_m ,

$$\widehat{\phi}_m(q) = \frac{1}{2\pi} \int \phi_m(x_i) e^{-iqx_i} dx_i = \frac{V_0 B_m \sqrt{b}}{2} \left[i\delta'(q) - \frac{\Delta_i}{2q \sinh(\pi \Delta_i q/2)} \right] \quad (4.13)$$

The current is then obtained from the inverse transform of equation (4.8):

$$J_{\parallel}(x) = \kappa \frac{V_0 B_m \Delta_m}{2} \left(\frac{\pi e^{-|x|/L}}{2 \sin(\pi \alpha)} + \sum_{n=1}^{\infty} (-1)^n \frac{n e^{-2n|x|/\Delta_i}}{n^2 - \alpha^2} \right) \quad (4.14)$$

where $\alpha = \Delta_i/2L$.

In this model, currents are driven by the potential difference across the boundary layer. If the potential maps to the ionosphere, the potential difference across the ionosphere drives a Pedersen current in the negative x direction. Because the electric field in the boundary layer vanishes asymptotically as $x \rightarrow -\infty$, the ionospheric current must be diverted upward in the shear layer to maintain current continuity. The current peaks at the center of the shear layer, and the current envelope is mostly controlled by the larger of the parameters L or Δ_i . In the case that the ionosphere is an insulator, $L \rightarrow 0$, it does not carry a current and so there is no parallel current. When the ionosphere is a conductor, the current returns in a channel near the shear layer boundary. As the conductivity becomes larger ($L \rightarrow \infty$), the parallel current spreads over a larger and larger region. Similarly, if there is resistance ($\kappa \rightarrow 0$) along the field lines the parallel current must spread across field lines so that the total current can be returned. Detailed properties of the solution, such as the current maximum and width, will be further analyzed in the following sections. It should be noted that in order to save space, detailed derivations of some equations are left out, but they can be found in our published paper *Johnson and Wing* [2015]. However, this chapter provides sufficient derivations and equations for theory-data comparisons in Section 4.4.

4.2.2 Maximum current

The current has an extremum at $x_i = 0$ with a vanishing first derivative and

negative second derivative (except the singular case $\Delta_i \rightarrow 0$). The maximum value of the current is obtained by evaluating $J_{\parallel}(0)$,

$$J_{\parallel,max} = \kappa \frac{V_0 B_m \Delta_m}{2} \left(\frac{\pi}{2 \sin(\pi \alpha)} + \sum_{n=1}^{\infty} (-1)^n \frac{n}{n^2 - \alpha^2} \right) \quad (4.15)$$

Equation (4.15) can be expressed in terms of digamma function $\psi(z) = d \log \Gamma(z) / dz$ (not shown here, but readers are referred to our paper *Johnson and Wing* [2015]).

It is instructive to examine the behavior of the maximum current in the limit of small and large α . In the limit that $\alpha \rightarrow 0$, it can be shown that

$$\lim_{\alpha \rightarrow 0} J_{\parallel,max} \approx \kappa \frac{V_0 B_m \Delta_m}{4\alpha} = \kappa \frac{V_0 B_m L \sqrt{b}}{2} = \frac{1}{2} V_0 B_m \sqrt{b \kappa \Sigma_p} \quad (4.16)$$

This result shows that the maximum current does not depend on the width of the shear layer when the shear layer maps to scales smaller than the electrostatic auroral scale length, L . In the limit $\alpha \gg 1$, the maximum current can be expressed as

$$\lim_{\alpha \rightarrow \infty} J_{\parallel,max} \approx \kappa \frac{V_0 B_m \Delta_m}{8\alpha^2} \sim \frac{V_0 B_m b \Sigma_p}{2\Delta_m} \quad (4.17)$$

In the limit $\alpha \gg 1$, the magnetospheric potential maps to the ionosphere. Substituting $\phi_i = \phi_m$ in equation (4.1) and evaluating at $x_i=0$ gives the same maximum current as in equation (4.17).

Through the use of a Padé approximation, we may derive an expression for the current that is uniformly valid for both small and large α with a maximum relative error of 15% at $\alpha = 1$ and much less over most of the interval. Using this approach, we derive a simple expression for the maximum parallel field-aligned current,

$$J_{\parallel,max} \approx \kappa \frac{V_0 B_m \Delta_m}{4\alpha(1+2\alpha)} = \frac{\Sigma_p V_0 B_m b}{2(\Delta_m + \sqrt{b} L)} \quad (4.18)$$

With this simple relation, it is useful to consider how the current depends on solar wind and ionospheric parameters. The density profile in the sheath and boundary layer is roughly proportional to the solar wind density, so $L = \sqrt{\Sigma_p / \kappa} \sim n_{sw}^{-0.5}$. For conditions with $L \ll \Delta_i$ (high boundary layer density) the current is mostly controlled by the ionospheric conductance,

solar wind velocity and boundary layer thickness. On the other hand, for low boundary layer density, $L \gg \Delta_i$, $J_{\parallel,max} \sim \sqrt{n_{sw}}$, which is similar to the

dependence seen in Figure 8 of *Echim et al.* [2008].

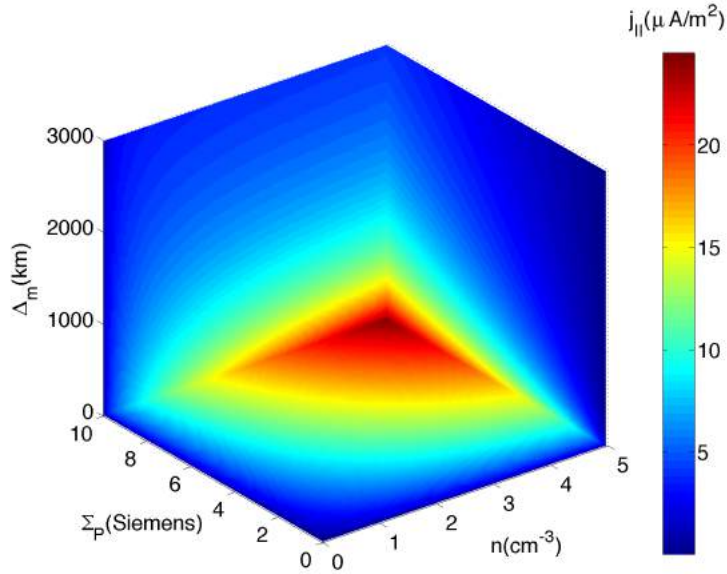


Figure 4.2. Maximum parallel current [equation (18)] as a function of boundary layer density, ionospheric conductivity, and velocity shear layer width with $V_0 = 200 \text{ km s}^{-1}$ and $B_m = 50 \text{ nT}$.

The maximum potential drop also corresponds to the maximum current at $x = 0$. In this case,

$$\Delta\phi_{\parallel, \max} = \frac{J_{\parallel}}{\kappa} \approx \frac{V_0 B_m \Delta_m}{4\alpha(1+2\alpha)} = \frac{V_0 B_m \sqrt{b} L}{2(1+\Delta_i/L)} \quad (4.19)$$

For $L \gg \Delta_i$, $\Delta\phi_{\max} \sim L \sim n_{sw}^{-0.5}$, while for $L \ll \Delta_i$, $\Delta\phi_{\max} \sim L^2 \sim n_{sw}^{-1}$. This behavior is consistent with the numerical solutions presented in *Echim et al.* [2008]. The dependence of the current and voltage on solar wind velocity is linear. This behavior is also similar to the solutions presented in Figure 6 of *Echim et al.* [2008].

The dependence of the current on the density, ionospheric conductivity, and shear layer width, Δ_m , is shown in Figure 4.2. From this figure, we see that J_{\parallel} increases with boundary layer density and height-integrated Pedersen ionospheric conductivity, while it decreases with increased shear layer width.

4.2.3 Width of the field-aligned current layer

The width of the field-aligned current layer (Λ) can be defined in a number of ways. For the present work, we use the full width at half maximum, which provides information about the global extent of the current profile. One approach is to determine the full width at half maximum directly from a numerical solution of equation (4.14). The full width at half maximum can also be established analytically from the appropriate limits $\alpha \rightarrow 0$ and $\alpha \rightarrow \infty$ of J_{\parallel} . In the limit of $\alpha \rightarrow 0$ ($\alpha \ll 1$), it can be shown that Λ where $J_{\parallel}(\Lambda) = 0.5 J_{\parallel, \max}$ [from equation (4.18)] is given by

$$\Lambda \sim (2 \ln 2) L(1 + 2\alpha) = (2 \ln 2) (L + \Delta_i) \quad (4.20)$$

For $\alpha \gg 1$, we find that

$$\Lambda = 2\Delta_i \operatorname{arcosh}(\sqrt{2}) = 2\Delta_i \ln(1 + \sqrt{2}) \quad (4.21)$$

A Padé approximation valid at small and large α may be constructed considering

$$\Lambda = \frac{(2 \ln 2) L}{1 + c\alpha} + 2 \ln(1 + \sqrt{2}) \Delta_i$$

The value of c can be chosen such that the power series for small α is satisfied. In this case,

$$\Lambda \approx (2 \ln 2) L + [2 \ln(1 + \sqrt{2}) - c \ln 2] \Delta_i \approx (2 \ln 2) (L + \Delta_i) \quad (4.22)$$

so that

$$c = 2 \left[\frac{\ln(1 + \sqrt{2})}{\ln 2} - 1 \right] \approx 0.5431 \quad (4.23)$$

and the result is accurate to within 5% for all values of α .

An even better approximation can be obtained by constraining the parameter, c , such that $\Lambda(\alpha=1) = 4.6$ as obtained numerically. In this case, $c = 0.29$, which provides accuracy of the approximate solution within 1% for any value of α so that

$$\Lambda = \frac{(2 \ln 2) L}{1 + 0.29\alpha} + 2 \ln(1 + \sqrt{2}) \Delta_i \quad (4.24)$$

In Figure 4.3, we provide the numerical value of the full width half maximum and for comparison the approximation shown in equation (4.24) as well as the percentage error between the curves. It should also be noted that the width of the velocity shear layer, Δ_i , can also be obtained from measurement of Λ and L by solving for the positive root of

$$1.0224 \alpha^2 + \left(3.5255 - 0.29 \frac{\Lambda}{L}\right) \alpha - \left(\frac{\Lambda}{L} - 1.3863\right) = 0 \quad (4.25)$$

for $\Lambda > 2 \ln 2 L$.

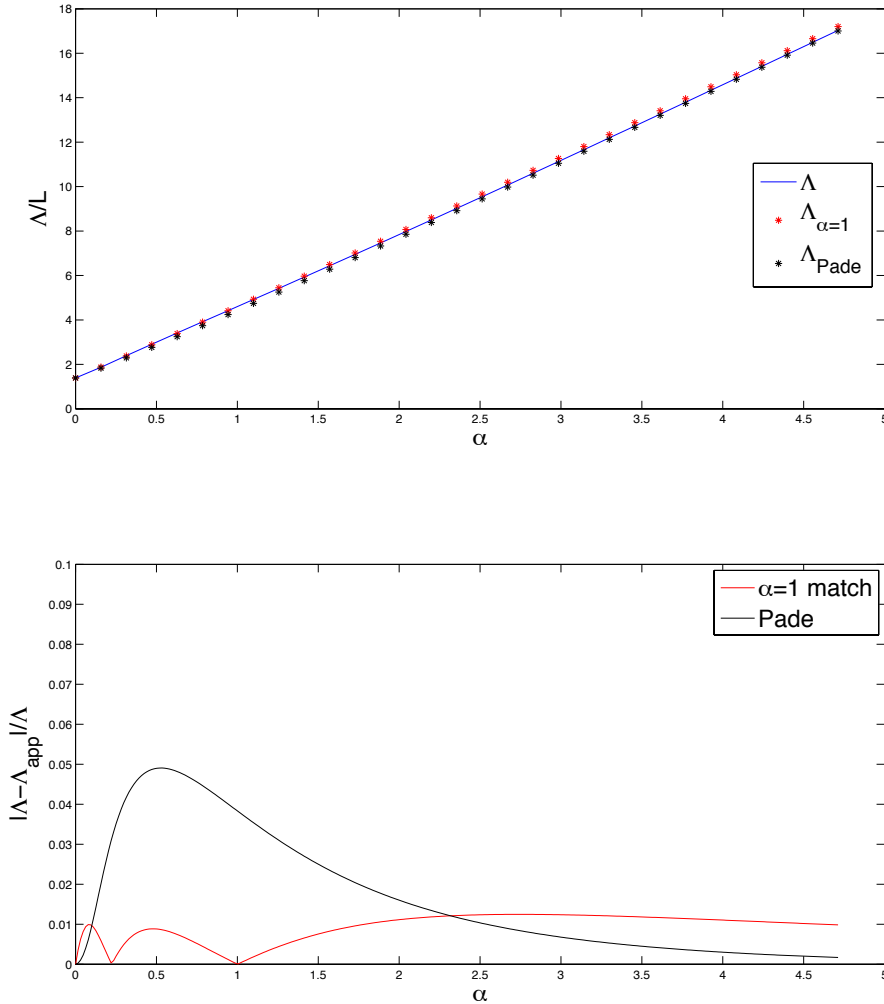


Figure 4.3. (top) The full width at half maximum, Λ , obtained from equation (4.14) as a function of α . The points displayed show the approximate values using the Padé approximation and the fit at $\alpha = 1$. (bottom) The relative error from using such a solution. The advantage of the uniform solution is that the error is distributed evenly and is roughly bounded by 1% compared to 5% for the Padé approximation.

It is apparent from our results that the current layer thickness has no dependence on solar wind velocity. This behavior is consistent with the numerical solutions shown in Figure 6 of *Echim et al.* [2008]. On the other hand, the current layer does depend on the density of the solar wind because $L \sim n_{sw}^{-0.5}$ so that for $\Delta_i \ll L$ the width $\Lambda \sim n_{sw}^{-0.5}$ decreases with increasing density as shown in Figure 8 of *Echim et al.* [2008]. This behavior is consistent with the fact that $\Delta_i \ll L$ for the parameters used in *Echim et al.* [2008].

4.3 Data and method

4.3.1 Data

The present study uses data from the particle (SSJ4/5) and magnetic field instruments on board of Defense Meteorological Satellite Program (DMSP) satellites. DMSP satellites are Sun-synchronous satellites in nearly circular polar orbit at an altitude of roughly 835 km and period of approximately 101 min per orbit.

The SSJ4 instrument package included on all recent DMSP flights uses curved plate electrostatic analyzers to measure ions and electrons from 32 eV to 30 keV in logarithmically spaced steps [*Hardy et al.*, 1984]. Because of its upward pointing and limited pitch-angle resolution, DMSP SSJ4 measures only highly field-aligned precipitating particles.

The DMSP magnetic field experiments consist of triaxial fluxgate magnetometers with a range of ± 65535 nT and one-bit resolution of 2 nT [*Rich et al.*, 1985]. The time resolution is 1 sec.

In the present study, we use over 20 years of simultaneous DMSP magnetic field and particle precipitation (SSJ4/5) observations, 1983–2006, to determine the source regions of R2, R1, and R0. However, not all DMSP satellites carried a magnetometer, although all carried the SSJ4/5 instrument during this period. Because we are interested only in the periods when there is simultaneous magnetic field and particle precipitation data, our data set is limited to the periods when both data sets are present. These periods are DMSP-F7 (1983 Dec–1988 Jan), F12 (1994 Sep–2002 Jul), F13 (1995 Mar–2006 Nov), F14 (1997 Apr–2006 Nov), F15 (1999 Dec–2006 Nov), and F16 (2003 Dec–2006 Nov).

Solar wind data are obtained from ACE, WIND, IMP8, ISEE1, and ISEE3

observations. The ACE SWEPAM and MAG, and the Wind MAG data were obtained from CDAWeb. The Wind 3DP data were obtained from the 3DP team directly. The ISEE1 and ISEE3 data were obtained from the University of California Los Angeles (UCLA). The IMP8 data came directly from the IMP teams. The solar wind was propagated with the minimum variance technique [Weimer *et al.*, 2003] to GSM $(x, y, z) = (17, 0, 0) R_E$ to produce 1-min files. For simplicity, a 10-min propagation time was estimated from $(17, 0, 0) R_E$ to the ionosphere (~ 2 min propagation time from $x = 17 R_E$ to the nominal magnetopause location at $x = 10 R_E$ with radial solar wind velocity $(V_{sw}) = 450 \text{ km s}^{-1}$; 5–6 min is added for the delay in magnetosheath assuming radial magnetosheath velocity $(V_{sh}) = V_{sw}/8$ and the bow shock location $\sim 13 R_E$ [e.g., Lockwood *et al.*, 1989; Spreiter and Stahara, 1985]; ~ 2 –3 min Alfvén wave propagation from the magnetopause to the ionosphere [e.g., Keller *et al.*, 2002; Lockwood *et al.*, 1989]). The exact propagation time is not crucial because 30-min averages were calculated and used. The 30-min averages are centered on the time of the DMSP encounter with the equatorward boundary of the FAC. These 30-min averages of solar wind and IMF parameters were assigned for the entire FAC encounter within an auroral oval crossing. Because DMSP crosses FACs or the auroral oval four times per orbit, typically four 30-min solar wind and IMF averages are calculated per orbit per spacecraft.

4.3.2 Method for obtaining field-aligned currents

For this study, we applied the automated algorithm that identifies the large-scale structure of FACs developed by Higuchi and Ohtani [2000]. The magnetic field obtained from the DMSP satellite is rotated such that two of its components lie on the horizontal plane (the plane parallel to the surface of the Earth). The minimum and maximum variances of the magnetic field are denoted by B_L and B_A , respectively. B_L is approximately in the latitudinal direction, typically the direction of the satellite trajectory, whereas B_A is in the azimuthal direction, approximately parallel to the FAC sheets. Thus, if FACs have large sheet structures, then the magnetic field variation should be confined primarily to B_A only. B_A increases or decreases as the satellite orbits the Earth. Then, the Higuchi and Ohtani [2000] algorithm uses the first-order B spline to fit line segments to B_A variations from the pole to approximately 40° magnetic latitude (MLat). If the distribution of large-scale ($> 1^\circ$) FACs can be approximated as infinite sheets, each line segment corresponds to a crossing of a FAC sheet. This

algorithm is essentially the automation of the way we visually examine a plot of satellite magnetic field data. Auroral crossings with data gaps are not processed. The variable R_{fit} gives a measure of the goodness of fit [Higuchi and Ohtani, 2000]. For the present study, we use the criterion $R_{fit} < 10$. This threshold for R_{fit} is not terribly sensitive. We could have used 8 or 12 as a threshold and the results would not have been significantly different. A more detailed description of the algorithm is given in *Higuchi and Ohtani* [2000].

4.3.3 Method for determining the source regions and particle precipitation morphology

Magnetospheric particles move along the magnetic field lines, and a fraction precipitate in the ionosphere. Thus, one may determine the source regions of FACs based on the signatures of the precipitating particles. The magnetospheric particles, however, may move across the field lines, for example, $\mathbf{E} \times \mathbf{B}$ motion. A well-known $\mathbf{E} \times \mathbf{B}$ effect is the dispersion in the cusp and mantle ions [e.g., *Reiff et al.*, 1977, *Onsager et al.*, 1993]. *Wing et al.* [1996; 2001] show that the evolution of the solar wind particle along the magnetopause entry points and parallel electric field may alter the characteristics of the solar wind origin particles so that they have different distributions in the ionosphere. Moreover, solar wind and IMF conditions may also alter the characteristics of the particle precipitation. For example, IMF B_y can introduce double cusp [*Wing et al.*, 2001] and positive IMF B_z introduces a significant cold dense component into the nominal magnetospheric particle population [*Wing et al.*, 2005b]. This is described in Chapter 2.

Many studies have tried to understand and characterize the complex signatures of the magnetospheric and solar wind origin of precipitating particles in the ionosphere, taking into account $\mathbf{E} \times \mathbf{B}$, parallel electric potential, and other effects [*Newell and Meng*, 1988; *Newell et al.*, 1991a; 1991b; 1991c; *Wing et al.*, 1996; 2001]. These studies have built a large body of knowledge that make it possible to develop an automated algorithm for identifying the approximate magnetospheric source regions of the particle precipitation. Some key ideas that are relevant to the analysis herein are presented below.

The particle precipitation identification algorithm classifies the dayside polar region into nine regions: radiation belt, central plasma sheet (CPS), boundary plasma sheet (BPS), open field line low-latitude boundary layer (open-LLBL),

LLBL, cusp, mantle, polar rain, and void.

As the name implies, the ionospheric radiation belt region contains particles that originate from the radiation belt in the magnetosphere. Morphologically, ionospheric CPS corresponds largely to diffuse aurorae while BPS corresponds to discrete aurorae where upward parallel electric field and electron accelerations are commonly found [e.g., *Winningham et al.*, 1975]. The dawn to noon CPS is mainly characterized by intense keV electrons, while the dusk to noon CPS by keV ions. Typically, BPS ions and electrons are less energetic and more structured than those of CPS. CPS particles correspond to the magnetospheric particles that originate from the nightside near-Earth central plasma sheet from 2100 to 0300 magnetic local time (MLT) and that have drifted to the dayside [e.g., *Winningham et al.*, 1975]. BPS is typically located poleward of CPS where particles have characteristics similar to magnetospheric particles that may originate from the distant plasma sheet and plasma sheet boundary layer (PSBL) and that have drifted to the dayside. BPS particles may also be associated with CPS particles that have gone through upward field-aligned electric field. The radiation belt, CPS, and BPS, are usually located in magnetically closed field lines (the foot-points for the field lines are rooted in both hemispheres.) It is harder to discern whether the LLBL is open or closed. Nonetheless, it is generally believed that the LLBL, which contains a mixture of low-energy magnetosheath-like particles and high-energy magnetospheric particles, is located near the magnetopause boundary. Perhaps, some LLBL is located on open field lines and some on closed field lines.

On the other hand, as discussed in Chapter 2, it has been far more certainly determined that open-LLBL, cusp, mantle, and polar rain are located on open field lines [e.g., *Wing et al.*, 1996; 2001; 2005a]. Open-LLBL is the region closest to the open-closed boundary. When the field line first becomes open, electrons having higher speeds than ions flow into the magnetosphere ahead of the ions. Thus, in this region, the ions and electrons have higher energies and lower fluxes than in the cusp because the bulk of the ions have not yet arrived. The electron entries are limited by the charge quasi-neutrality, which could be maintained by the presence of parallel electric field. Typically only ions with energies > 1 keV are present. In the cusp, the ions have reached the ionosphere and intense fluxes of ions and electrons are usually observed. In this region, the electrons and ions can enter the magnetosphere relatively freely because the numbers of magnetosheath ions and electrons are already balanced, resulting in little or no parallel electric field [*Wing et al.*, 1996; 2001; *Fairfield et al.*, 2008]. Typically, the ions have a

spectral peak of $> 10^8$ eV cm⁻² s eV sr. The typical average electron and ion energies, $\langle E_e \rangle$ and $\langle E_i \rangle$ are: $\langle E_e \rangle < 200$ eV and 300 eV $< \langle E_i \rangle < 3$ keV. The cusp ions often, but not always, exhibit energy-latitude dispersion, especially during periods of southward IMF. The northward IMF cusp typically has a dispersion that is reversed from that of southward IMF [e.g., *Woch and Lundin, 1992*]. IMF B_y introduces variations in the cusp dispersion, location, and even the formation of a double cusp [*Wing et al., 2001*].

In the mantle region, fewer ions can enter as the magnetosheath flow becomes increasingly tailward and larger, whereas the magnetospheric magnetic field (and hence precipitating particle velocity) becomes more sunward, a condition that is less favorable for particle entries. In this region, $\mathbf{j} \cdot \mathbf{E} < 0$, which means that the magnetic stress at the magnetopause is directed to decelerate the plasma [e.g., *Hill and Reiff, 1977; Cowley and Owen, 1989*]. Some of the solar wind thermal or core electron entries are limited by the ensuing parallel electric field that arises to maintain charge quasi-neutrality. In the mantle, the ions and electrons have lower energies and lower fluxes than those in the cusp, typically by a factor of 3–10. The typical mantle energies range from a few tens to 100 eV, but there are considerable variabilities. The mantle ions generally exhibit energy–latitude dispersions. Finally, in the polar rain region, no significant amount of ions enters the magnetosphere. This is discussed in Chapter 2.

A void is a region in which the particle precipitation falls below one count level of the detector, which has an energy range of 32 eV to 30 keV. As such, this definition of void is instrument dependent. It does not necessarily mean that the region is devoid of particle precipitation.

In addition to those nine regions, there are three more classifications: data gap, unclassified, and BPS*. Data gap refers to the rare occasions in which there are magnetometer data but no particle data, and hence the source region is unknown. Unclassified refers to rare occasions in which there are particle data, but the particle precipitation signature is ambiguous, having spectra that do not conform to any one of the nine regions. Finally, BPS* is the region that is classified as BPS by the particle precipitation region identification algorithm [*Newell and Meng, 1988; Newell et al., 1991a; 1991b; 1991c*], but some of the BPS particles really correspond to the mantle particles that have gone through the upward field-aligned electric field that sometimes exists within some upward R0 and R1 regions. Hence, unlike BPS, which is closed, BPS* may be open or closed.

4.3.4 Summary of data and method (putting it all together)

We now utilize the theoretical model to organize and interpret satellite data obtained from regions of upward field-aligned current and to validate the model. *Wing et al.* [2010] and *Wing et al.* [2011] have examined dayside field-aligned currents and precipitating populations. They found that at times much of the region 1 (R1) currents are located at the boundary layer or open field lines. In this study, we restrict ourselves to regions of upward R1 currents where a simple Knight-like current-voltage relation would be appropriate. The upward current is carried mostly by precipitating electrons. We use simultaneous particle precipitation to select FAC that is located at the boundary layer and open field lines. Basically, we select only passes where R1 is entirely located in LLBL, cusp, mantle, or/and polar rain. From satellite data, we are able to measure the currents and thickness (latitudinal width) of current layers from *Higuchi and Ohtani* [2000] algorithm. The solar wind parameters are inferred from satellite observations. Some ionospheric parameters are inferred from satellite observations and some from empirical models. We compare the dependence of currents on the solar wind parameters with predictions of the analytic model.

4.4 Theory-data comparisons

4.4.1 Field-aligned current density (J_{\parallel})

We calculate $J_{\parallel, \max}$ using equation (4.18) and parameters that are estimated observationally and through the use of empirical formulas, as described herein. We do not have measurements along the boundary layer. For simplicity, we use the approximation $V_0 = 0.15 V_{sw}$ and $B_m = 30$ nT. These values are similar to observations of the velocity shear and magnetic field at LLBL between noon and the dusk flank [e.g., *Fujimoto et al.*, 1998; *Vaisberg et al.*, 2001]. The magnetic field ratio at the DMSP altitude and magnetopause is taken to be $b = B_i/B_m \sim 1000$. $L = (\Sigma p/\kappa)^{0.5}$ is obtained using empirical formulas for Σp and solar wind parameters to infer κ . κ is computed using $n_e = n_{sw}$ [e.g., *Scudder et al.*, 1973; *Phan and Paschman*, 1996] and $T_e = 1 \times 10^6$ K [e.g., *Phan and Paschmann*, 1996].

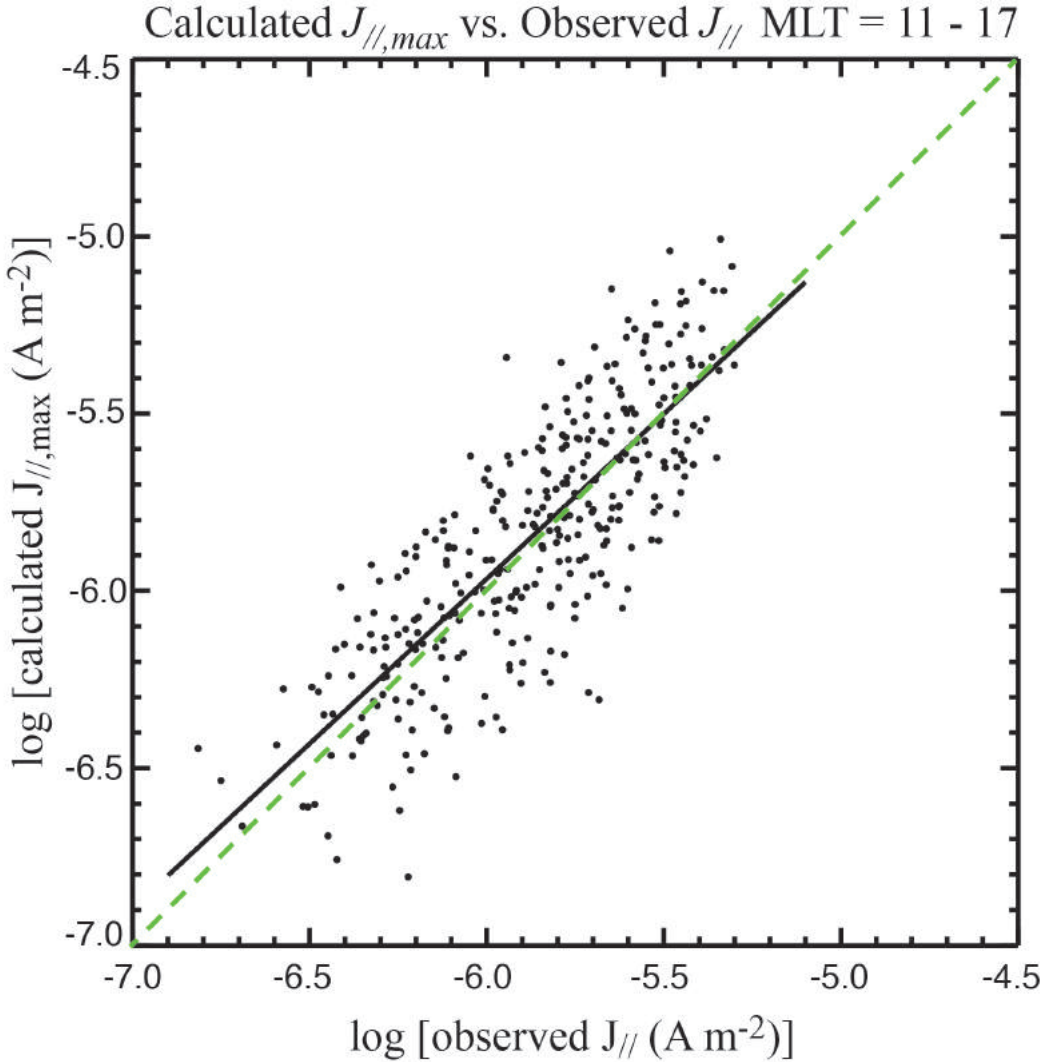


Figure 4.4. Calculated $J_{\parallel, \max}$ vs. observed J_{\parallel} for MLT = 1100–1700. The calculated $J_{\parallel, \max}$ is obtained from equation (4.18). If the calculated $J_{\parallel, \max}$ is linearly proportional to observed J_{\parallel} , then all the points would lie along the dashed line, which has a slope of one. The least square fit is plotted as solid line, which nearly matches the dashed line.

We assume $\Sigma_p = \Sigma_{p,s} + \Sigma_{p,e}$ where $\Sigma_{p,s} = 0.88(S_a \cos \chi)^{0.5}$ [Robinson and Vondrak, 1984] and $\Sigma_{p,e} = (40 \langle E_e \rangle \varepsilon^{0.5}) / (16 + \langle E_e \rangle^2)$, where S_a is the radio flux with 10.7 cm wavelength, χ is the solar zenith angle, $\langle E_e \rangle$ is the mean electron energy in keV, ε is the electron energy flux in ergs cm^{-2} [Robinson et al., 1987]. This formula for combining the effects of solar illumination and electron precipitation is deemed appropriate when the two ionization sources are well separated in altitude, providing two parallel channels for the currents to flow

[Wallis and Budzinski, 1981; Galand and Richmond, 2001]. The peak photoionization rate for solar extreme ultraviolet (EUV) light occurs around 100 km while the peak ionization rate for dayside boundary layer or open field line electrons with energies up to a few hundred eVs occurs above 200 km [Robinson and Vondrak, 1984, Rees, 1963].

However, when the two sources of ionization occur at identical altitude, then it may be more appropriate to use the formula $\Sigma_p = (\Sigma_{p,s}^2 + \Sigma_{p,e}^2)^{0.5}$ [Wallis and Budzinski, 1981]. This formula is more applicable for the closed field line regions where the precipitating electrons originating from the magnetosphere have energies of a few tens of keVs. Although we do not include such regions in our study, this alternative formula would not give significantly different results because $\Sigma_{p,s}$ dominates over $\Sigma_{p,e}$ in the region of interest (open field line/boundary layer, near noon/early afternoon).

Figure 4.4 shows the value of $J_{\parallel, \max}$ predicted by equation (4.18) using Δ_i obtained from the measured value of Λ and equation (4.25) vs. observed large scale J_{\parallel} that are located in the upward R1 at the boundary layer and on open field lines from 1100 to 1700 MLT. In the present statistical study, for simplicity, our method uses an automated procedure to obtain large scale FAC based on an infinite current sheet approximation. If the measured J_{\parallel} is approximately $J_{\parallel, \max}$ or is linearly proportional to $J_{\parallel, \max}$ ($J_{\parallel, \max} = cJ_{\parallel}$), then on the log-log plot, (1) the slope would be one and (2) any non-unity proportionality constant would shift the points in y direction by $\log(c)$ [the least square fit would yield a y -intercept of $\log(c)$]. As can be seen in Figure 4.4, the points tend to cluster along the dashed line, which has a slope of one, suggesting that this scenario has some basis. Figure 4.4 provides an empirical relationship between $J_{\parallel, \max}$ calculated from equation (4.18) and the observed J_{\parallel} . The figure shows that the calculated $J_{\parallel, \max}$ is highly correlated with the observed J_{\parallel} with correlation coefficient $r = 0.81$. The correlation is highly significant, the probability for two uncorrelated variables to give $|r| \geq 0.81$ is < 0.01 ($P < 0.01$, number of points $n = 361$). The least square fit returns $\log(J_{\parallel, \max_cal}) = (0.93 \pm 0.04) \log(J_{\parallel_obs}) + (0.03 \pm 0.01)$ where $J_{\parallel, \max_cal} =$ calculated maximum $J_{\parallel, \max}$ from equation (4.18) and $J_{\parallel_obs} =$ large scale J_{\parallel} derived from the DMSP magnetometer. The least square fit is plotted as a black solid line, which can be compared with a dashed line.

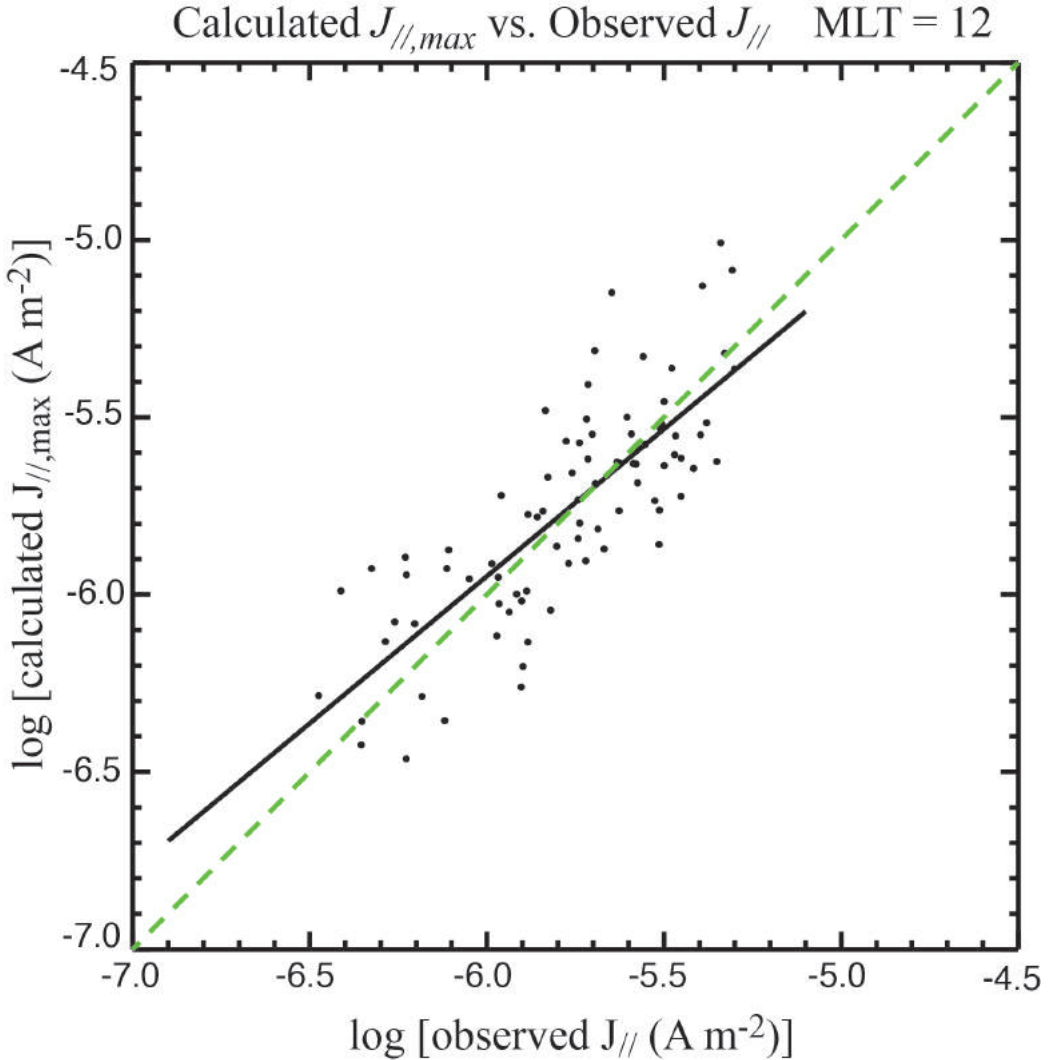


Figure 4.5. Calculated $J_{\parallel, \max}$ vs. observed J_{\parallel} for noon (MLT = 1200). The calculated $J_{\parallel, \max}$ is obtained from equation (4.18). The least square fit is plotted as solid line. If the calculated $J_{\parallel, \max}$ is linearly proportional to observed J_{\parallel} , then all the points would lie along the dashed line, which has a slope of one. The slope of least square fitted line (0.83 ± 0.07) is smaller than one, which may be attributed to the higher thermal current near noon and/or kinetic pressure gradient.

Figure 4.4 shows that the approximation $J_{\parallel, \max, \text{cal}} = cJ_{\parallel, \text{obs}}$ is fairly good, as can be seen by comparing the points, the black solid line, and the dashed line. However, the slope of the solid line, 0.93 ± 0.04 , is slightly lower than that of the dashed line (slope = 1). Figure 4.4 includes all points from 1100 to 1700 MLT. However, J_{\parallel} near noon may respond differently because the magnetic field lines map to the vicinity of the subsolar region where (1) the magnetosheath densities

and temperatures are high, which would lead to increased thermal currents and (2) the kinetic pressure gradient may contribute significantly to J_{\parallel} because the velocity shear is minimal [e.g., *Dekeyser and Echim, 2013*]. To check this effect, Figure 4.5 plots only the points from noon (1130–1230 MLT). The least square fit returns $\log(J_{\parallel,\text{max_cal}}) = (0.83 \pm 0.07) \log(J_{\parallel,\text{obs}}) + (0.05 \pm 0.03)$ and the correlation is highly significant $r = 0.79$ ($P < 0.01$, $n = 89$). The least square fit is plotted as the solid line, which deviates further from the dashed line (slope = 1) and the solid line in Figure 4.4.

Figure 4.6 plots the points for MLT = 1100–1700, excluding the points near noon. The least square fit returns $\log(J_{\parallel,\text{max_cal}}) = (0.96 \pm 0.04) \log(J_{\parallel,\text{obs}}) + (0.03 \pm 0.01)$ and the correlation is highly significant $r = 0.81$ ($P < 0.01$, $n = 272$). The least square fit (solid line) seems to match the dashed line the best among all three figures (Figures 4.4–4.6). Two things are worth noting about the fit. First, the slope is nearly unity suggesting $J_{\parallel,\text{max_cal}}$ is linearly proportional to $J_{\parallel,\text{obs}}$. Second, the small y -intercept of 0.03 suggests that the proportionality constant is nearly unity, $J_{\parallel,\text{max_cal}} \sim 1.07 J_{\parallel,\text{obs}}$.

The use of log-log plots is particularly useful to identify scaling relationships and to isolate the power law dependence of some parameters. Log-log plots have the useful property that unknown constants of proportionality are eliminated from the scaling relationships and just become an offset. Many of the model input parameters are only proportional to measured solar wind parameters, so it makes sense to use a log-log plot, and these parameters would provide an offset. Using the same data points in Figure 4.6, the correlation of predicted and observed J_{\parallel} in linear scale is $r = 0.75$, which is still highly significant, but lower than $r = 0.81$ for the correlation in the log-log scale, as expected.

Near the subsolar region, the magnetosheath densities and temperatures are higher, which may increase the thermal current, $J_t = n_e e V_t / \sqrt{2\pi}$, where J_t = thermal current, n_e = electron density at the boundary layer, V_t = electron thermal velocity at the boundary layer. The accelerating potential can be overestimated when J_{\parallel} is comparable to or smaller than J_t . To get a rough estimate of the thermal current, if we assume $n_e \sim 10 \text{ cm}^{-3}$ and $T_e \sim 2 \times 10^6 \text{ K}$ at the boundary layer near the subsolar region, then $J_t \sim 1 \times 10^{-6} \text{ A m}^{-2}$, which is comparable to points in the lower quartile in Figure 4.5. The kinetic pressure gradient could also modify J_{\parallel} and the accelerating potential [*Dekeyser and Echim, 2013*], particularly near the subsolar region where the velocity shear is minimal. Both thermal currents and kinetic pressure gradient are not taken into account in our model, e.g.,

equation (4.18). These factors may contribute to the less than unity slope obtained from the least square fit and larger y -intercept in Figure 4.5. However, Figures 4.4–4.6 show that despite not including thermal currents and kinetic pressure gradient, the model remarkably agrees with the data fairly well.

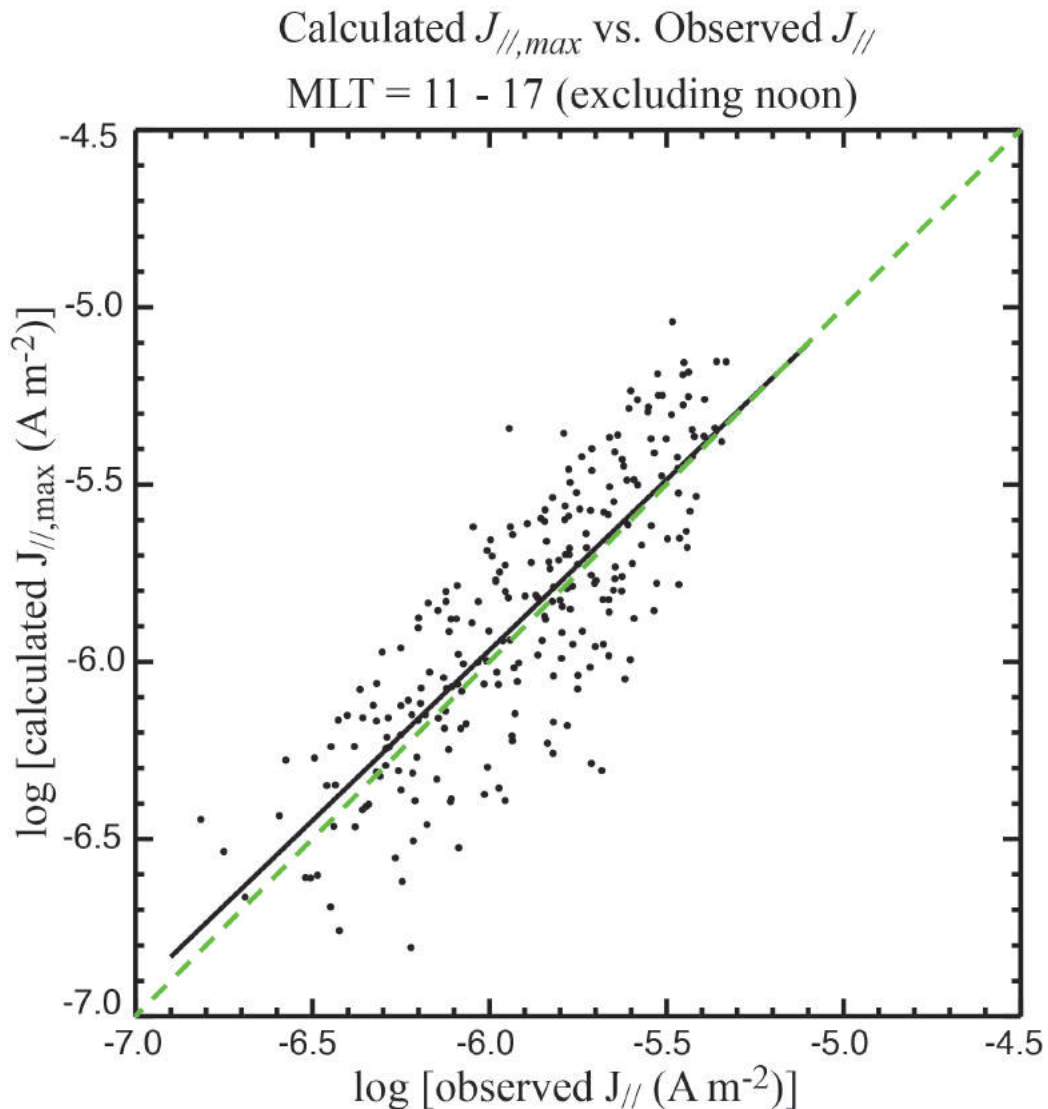


Figure 4.6. Calculated $J_{\parallel, \max}$ vs. observed J_{\parallel} for MLT = 1100–1700, excluding data near MLT = 1200. The calculated $J_{\parallel, \max}$ is obtained from equation (4.18). The least square fitted line (solid line) has a slope of 0.96 ± 0.04 , which agrees very well with that of the dashed line, which has a slope of one.

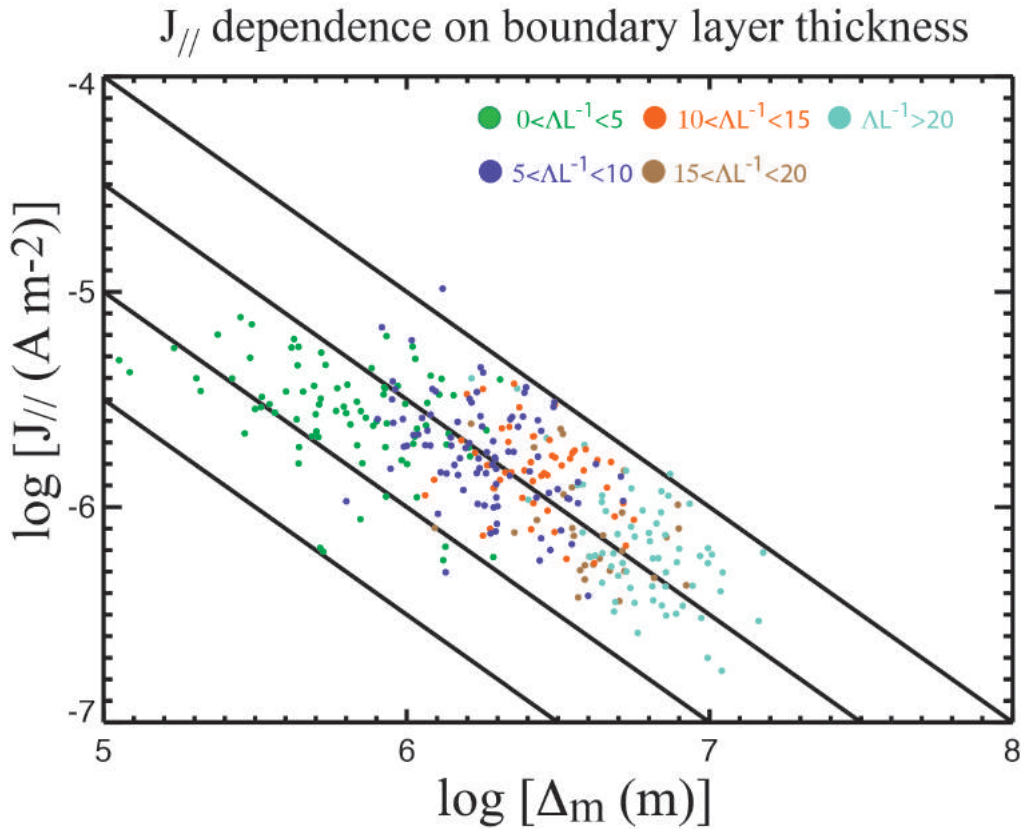


Figure 4.7. Field-aligned current density J_{\parallel} decreases with increasing Δ_m . The large scatter can be attributed partly to the large number of free parameters relating the two parameters as expressed in equation (4.18). The solid lines have slope = -1 , which is expected from equation (4.18). The lines do not fit green dots ($\Lambda/L < 5$) as well because for small α , J_{\parallel} should be independent of Δ_m , as indicated by equation (4.16). All data points come from 1100–1700 MLT.

Besides the thermal currents and kinetic pressure gradient, there may be other sources for the cross-field electric field in the boundary layer that are not related to velocity shear. All of these may introduce scatter in Figures 4.4–4.6. For example, the magnetopause processes such as reconnection, flux transfer events, and Kelvin-Helmholtz instability (KHI) may introduce small scale FACs [Miura and Pritchett, 1982], which would introduce noise or scatter in our figures. The present study only examines large scale FACs and we will leave smaller scale FACs for a future study.

Next, we investigate how J_{\parallel} varies with Δ_m and Σ_p . The dependence of J_{\parallel}

on the thickness of the boundary layer is shown in Figure 4.7, which plots $\log J_{\parallel}$ vs. $\log \Delta_m$. J_{\parallel} is obtained directly from DMSP magnetometer observations, while Δ_m is obtained from equation (4.24) and measured values of Λ and L . Figure 4.7 shows that the points tend to line along lines with a slope of -1 , which is expected from the large α limit of equation (4.18). The least square fit of the points for $\Lambda/L > 5$ has a slope of -0.8 ± 0.2 , which is within the theoretical prediction of equation (4.18). On the other hand, for $\Lambda/L < 5$, in the small α limit, the slope for the green dots is larger than -1 and closer to 0 because equation (4.16) shows that J_{\parallel} becomes independent of Δ_m in that limit. The selection of the range of Λ/L is based on Figure 4.3, which shows that $\alpha < 1$ corresponds to $\Lambda/L < 4.6$.

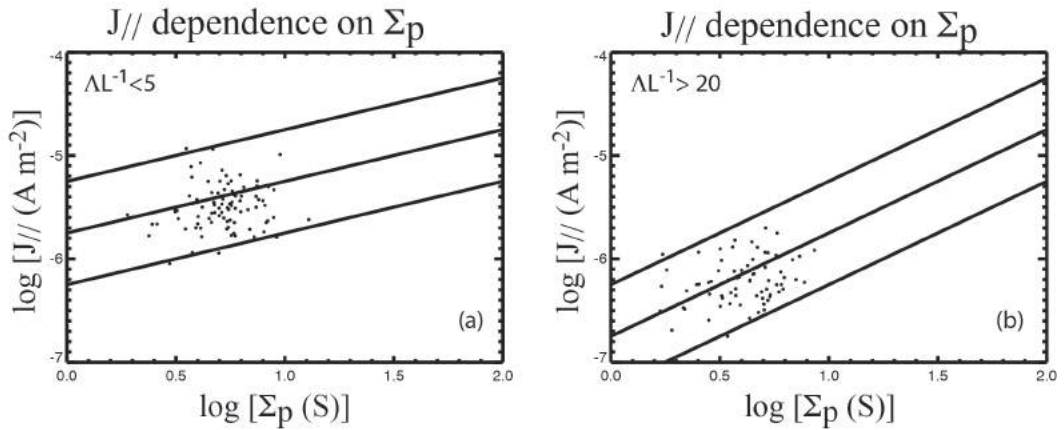


Figure 4.8. Field-aligned current density (J_{\parallel}) increases with Σ_p , but there is a dependence on α . (a) for $\Lambda/L < 5$ (small α), the points tend to align with lines of slope = 0.5, which is consistent with equations (4.16) and (4.18) while (b) for $\Lambda/L > 20$ (large α), the points tend to align with lines of slope = 1, which is consistent with equation (4.17). The large scatter can be attributed partly to the large number of free parameters relating the two parameters as expressed in equation (4.18). All data points come from 1100–1700 MLT.

The dependence of J_{\parallel} on Σ_p is shown in Figure 4.8, which plots $\log J_{\parallel}$ vs. $\log \Sigma_p$. Here, J_{\parallel} is obtained from DMSP magnetometer observations while Σ_p is obtained from DMSP SSJ4/5 observations, F10.7 record, and *Robinson and Vondrak* [1984] and *Robinson et al.* [1987] empirical formulas. Because the data come from the 1100 to 1700 MLT, Σ_p is mainly attributed to solar EUV as proxied by F10.7. To the first order, J_{\parallel} increases with Σ_p , as would be expected. Higher conductivity makes it easier for the currents to flow. However, the dependence of

J_{\parallel} on Σ_p has a dependence on Λ/L or α . For $\Lambda/L > 20$ ($\alpha \gg 1$), $J_{\parallel} \sim \Sigma_p$, as suggested by equation (4.17), but for values of $\alpha \ll 1$, $J_{\parallel} \sim \sqrt{\Sigma_p}$, as suggested by equation (4.16). Figure 4.8a plots $\log J_{\parallel}$ vs. $\log \Sigma_p$ for $\Lambda/L < 5$. From equation (4.16), the points are expected to align with lines of slope 0.5 (the slanted black lines). However, the least square fit of the points yields the slope of 0.2 ± 0.2 , $r = 0.13$, and $P = 0.2$. Figure 4.8b plots $\log J_{\parallel}$ vs. $\log \Sigma_p$ for $\Lambda/L > 20$. The least square fit yields the slope of 0.4 ± 0.2 , $r = 0.29$, and $P < 0.01$. From equation (4.17), the points are expected to lie along the lines of slope 1 (the slanted black lines). The scatter in Figures 4.7 and 4.8 are quite large because of the large number of parameters and the large uncertainties in each dependency as indicated in equations (4.16) and (4.17). In particular, in Figures 4.8a and 4.8b, the fits of the data points do not match the theoretical predictions well, which perhaps may be attributed the uncertainty in estimating Σ_p . Incidentally, *Wang et al.* [2005] also found large scatter in their J_{\parallel} vs. Σ_p plot, although they combined upward and downward currents for 1100–1300 MLT. Section 4.4.4 discusses the source of errors in our plot.

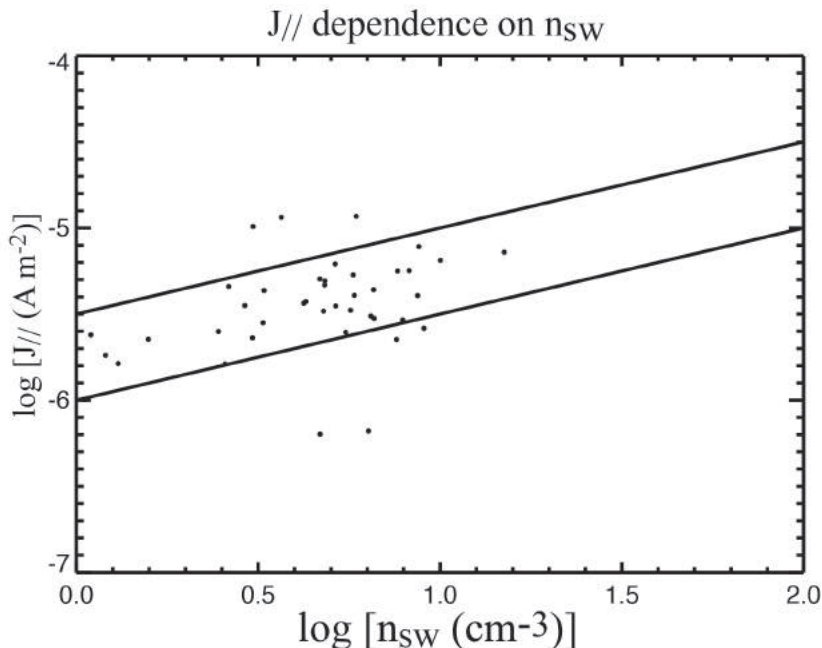


Figure 4.9. Field-aligned current density (J_{\parallel}) increases with n_{sw} for small α ($\Lambda/L < 3$) at 1100–1700 MLT. The solid black lines have slope = 0.5, which is expected from equations (4.16) or (4.18).

Figure 4.9 plots $\log J_{\parallel}$ vs. $\log n_{sw}$ for small α ($A/L < 3$). J_{\parallel} is obtained from DMSP magnetometer observations while n_{sw} is obtained from solar wind observations. Figure 4.9 also plots lines with slope = 0.5, which is the expected slope from equations (4.18) or (4.16). The figure shows that the points tend to line up along these lines, although the scatter is large. The least square fit results in $J_{\parallel} = n_{sw}^{(0.3 \pm 0.2)}$, $r = 0.31$, and $P < 0.03$.

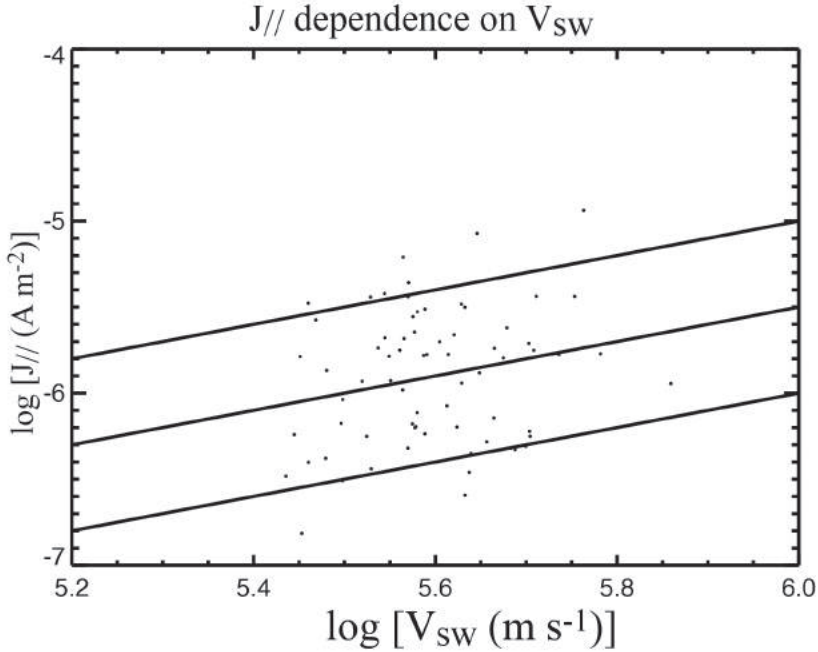


Figure 4.10. Field-aligned current density (J_{\parallel}) increases with V_{sw} at 1300–1700 MLT. The solid black lines have slope = 1, which is expected from equation (4.18).

Figure 4.10 plots $\log J_{\parallel}$ vs. $\log V_{sw}$ for 1300–1700 MLT. The reason for selecting these locations is that near noon, FAC would map to near the subsolar magnetopause where the boundary layer V would be small, which would not fit easily with points that come from the afternoon region, which map to magnetopause flank. J_{\parallel} is obtained from DMSP magnetometer observations while V_{sw} is obtained from solar wind observations. Figure 4.10 also plots lines with slope = 1, which is the expected slope from equation (4.18). This figure shows that the points tend to line up along these lines, but the fit is not very good (the scatter is large). The least square fit results in $J_{\parallel} = V_{sw}^{(0.8 \pm 0.5)}$, $r = 0.18$, and $P = 0.13$.

The large scatter in Figures 4.9 and 4.10 may result from the anti-correlation between V_{sw} and n_{sw} [e.g., *Richardson et al.*, 1996; *Hundhausen et al.*, 1970], e.g., the effect of large V_{sw} would tend to oppose the effect of small n_{sw} and vice versa. This and other sources of errors are discussed in Section 4.4.4.

4.4.2 FAC latitudinal width (Λ)

Although theoretical models have been developed to understand the boundary layer and field-aligned current profiles [e.g., *Lotko et al.*, 1987; *Phan et al.*, 1989; *Drakou et al.*, 1994; *Echim et al.*, 2007; 2008], the dependence of the thickness of the boundary layer (Δ_m) and the FAC latitudinal width (Λ) on M–I coupling and solar wind parameters have not been previously explored observationally in depth. The theoretical results presented in Section 4.2.3 provide a simple framework for exploring Λ . In particular, equations (4.20) and (4.21) provide expressions for the latitudinal width of the field-aligned current (Λ) for $\alpha \ll 1$ and $\alpha \gg 1$, respectively, and equation (4.24) gives a general expression relating Λ to the mapped boundary layer thickness, Δ_i , and electrostatic auroral scale length, L .

First, we investigate how Λ in the upward R1 boundary layer/open field regions varies with n_{sw} . Λ is obtained by applying the *Higuchi and Ohtani* [2000] algorithm to DMSP magnetometer data as described in Section 4.3. For comparison with the theoretical model, we note that the density dependence in the model comes through κ , which corresponds to the density of the electron source population that carries the field-aligned currents, which can range between the sheath and magnetospheric density, but most likely corresponds to LLBL densities. Because the density in the boundary layer scales with the solar wind density in the kinetic boundary layer models [*Echim et al.*, 2008], the solar wind density (which is monitored continuously) can provide a reasonable proxy for the boundary layer density. For conditions satisfying $\alpha \ll 1$, equation (4.20) suggests that $\Lambda \sim L \sim n_{sw}^{-0.5}$.

Figure 4.11 shows $\log \Lambda$ vs. $\log n_{sw}$, for $\Lambda/L < 5$ (small α) at 1100–1700 MLT, although most of the points come from 1100–1300 MLT because the frequency of the upward R1 located on the boundary layer or open field lines decreases in the late afternoon and near dusk *Wing et al.* [2010]. The *Higuchi and Ohtani* [2000] algorithm only detects large scale FACs and has a minimum threshold of Λ of about 30 km. There are 97 points that satisfy the $\Lambda/L < 5$

criterion. Figure 4.11 shows that all the points tend to lie along the lines of slope = -0.5 , suggesting that $\Lambda \sim n_{sw}^{-0.5}$, which is consistent with equation (4.20). The least square fit yields $\log(\Lambda) = -(0.47 \pm 0.06) \log(n_{sw}) + (5.1 \pm 0.05)$ or $\Lambda \sim n_{sw}^{-(0.47 \pm 0.06)}$. The correlation is highly significant, with $r = -0.60$ and $P < 0.01$. We note that the anti-correlation of Λ with n_{sw} is also consistent with the model calculation of *Echim et al.* [2008].

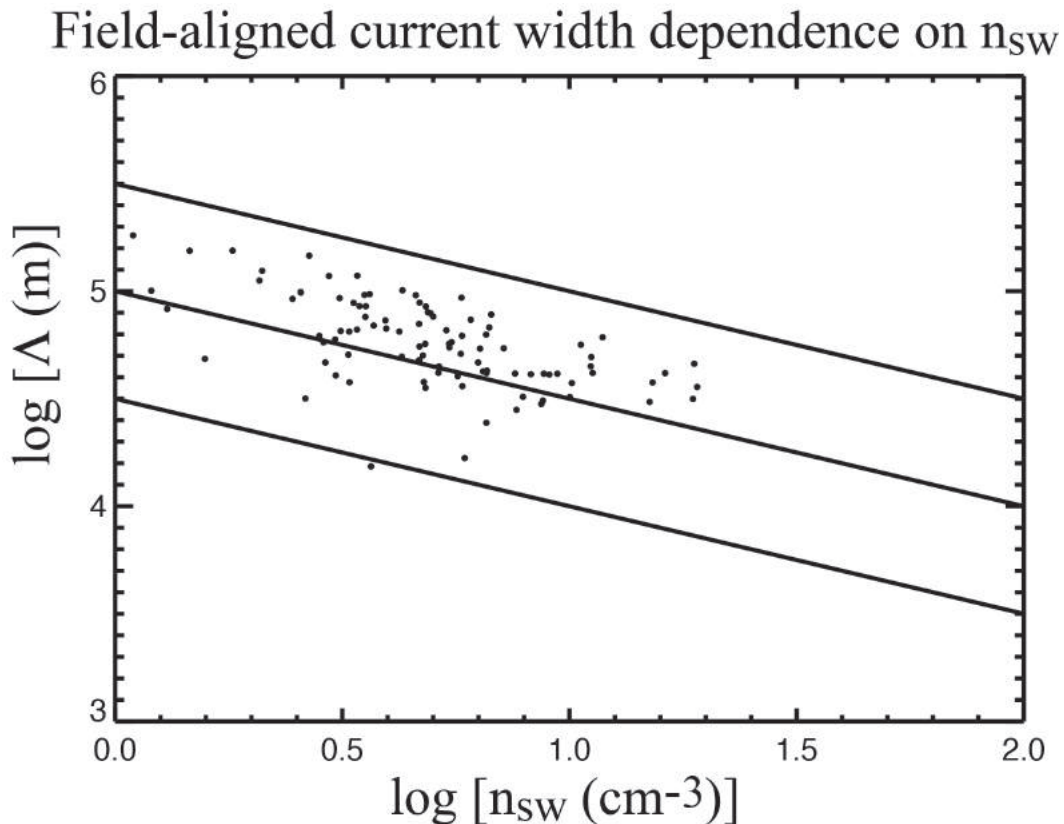


Figure 4.11. Field-aligned current width (Λ) decreases with increasing n_{sw} for small α ($\Lambda/L < 5$) at 1100–1700 MLT. The solid black lines have slope = -0.5 , which is the expected slope from equation (4.20) for small α .

Next, we examine how Λ varies with L . $L = \sqrt{\Sigma_p/k}$ is calculated using empirical formulas for Σ_p and solar wind parameters to infer κ . The Knight conductivity, $\kappa = n_e e^2 / (2\pi m_e k_b T_e)^{0.5}$, is computed using $n_e = n_{sw}$ [e.g., *Scudder et al.*, 1973; *Phan and Paschmann*, 1966] and $T_e = 10^6$ K [*Phan and Paschmann*, 1996]. We assume $\Sigma_p = \Sigma_{p,s} + \Sigma_{p,e}$, as discussed in Section 4.4.1.

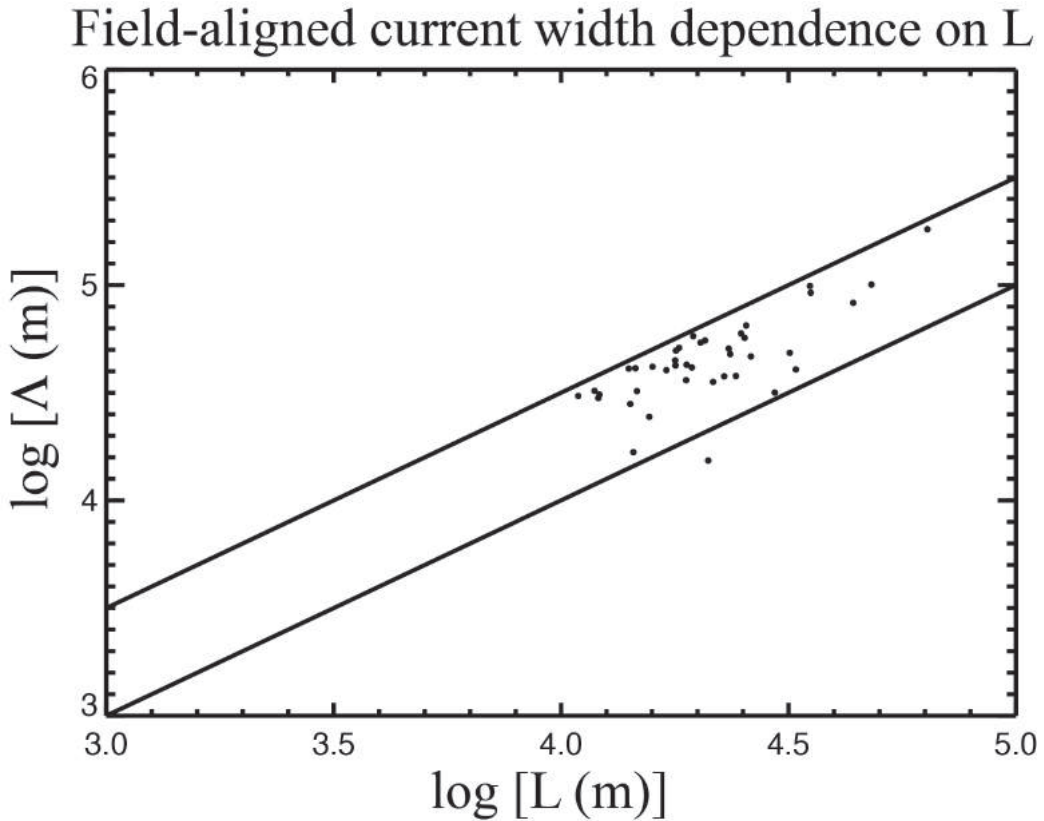


Figure 4.12. Field-aligned current width (Λ) as a function of L for small α ($\Lambda/L < 5$) at 1100–1700 MLT. The solid black lines have a slope = 1, which is the expected slope from equation (4.20).

Figure 4.12 shows $\log \Lambda$ vs. $\log L$ for $\Lambda/L < 5$ for 1100–1700 MLT, as in Figure 4.11. Lines with a slope of 1 [note that $\Lambda \sim L$ for $\alpha \ll 1$ from equation (4.20)] are also shown in Figure 4.12. As can be seen in the figure, the lines fit the points fairly well. The figure and equation (4.20) suggest that J_{\parallel} becomes more localized as L decreases. The least square fit yields $\log(\Lambda) = (0.9 \pm 0.1) \log(L) + (0.9 \pm 0.5)$ or $\Lambda \sim L^{(0.9 \pm 0.1)}$. The correlation is highly significant, $r = 0.74$ and $P < 0.01$. The large scatter likely results from uncertainties in the estimates of Σ_p and κ . The estimation of Σ_p relies on the accuracies of the *Robinson et al.* [1987] and *Robinson and Vondrak* [1984] empirical formulas and the accuracies of $\langle E_e \rangle$, ε , and solar EUV flux. The estimation of κ relies on the accuracies of estimations of our proxies for n_e and T_e . Section 4.4.4 discusses further the sources of uncertainty.

4.4.3 Thickness of the boundary layer (Δ_m)

From equations (4.24) and (4.25), one can obtain Δ_i from L and Λ , both of which can be observed, as discussed in Section 4.4.2. By definition, $\Delta_m/\Delta_i \sim (B_i/B_m)^{0.5}$ and assuming $B_i/B_m \sim 1000$, we can obtain Δ_m . Moreover, Δ_m can also be obtained from equation (4.18), which relates Δ_m to $J_{||}$, Σ_p , L , V_0 , and B_m , which can be estimated using observations and empirical formulas. For simplicity, we use the approximation V_0 at the magnetopause $V_0 = 0.20 V_{sw}$ and $B_m = 20$ nT. This value is similar to observations of the velocity shear and magnetic field at the low-latitude boundary layer between noon and the dusk flank [e.g., *Fujimoto et al.*, 1998; *Vaisberg et al.*, 2001]. These parameters can then be used to obtain Δ_m using equation (4.18).

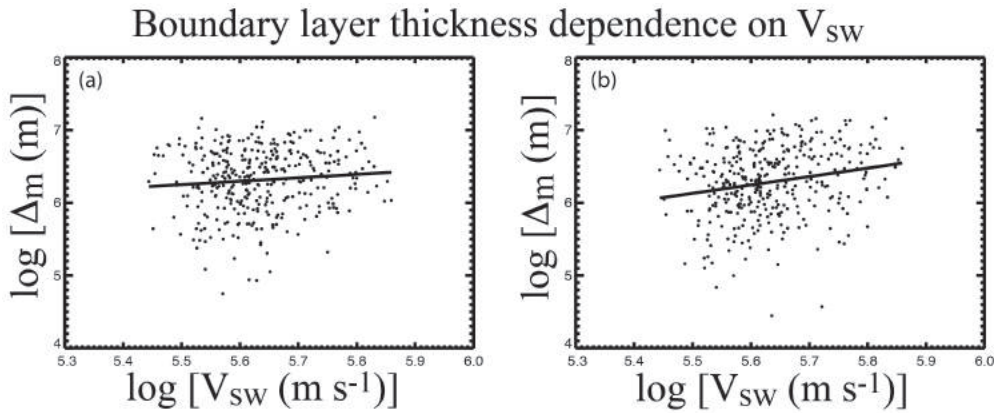


Figure 4.13. The magnetospheric boundary layer (Δ_m) has some dependence on V_{sw} . Δ_m is calculated using two methods: (a) from equation (4.24) and $\Delta_m/\Delta_i \sim (B_i/B_m)^{0.5}$ and (b) from equation (4.18). Both methods return a mean $\Delta_m \sim 3 \times 10^6$ m ($\sim 0.5 R_E$). The least square fit is plotted as a black line. The x axis ranges from $V_{sw} \sim 200$ km s^{-1} to 1000 km s^{-1} . All data points come from 1100–1700 MLT.

Figures 4.13a and 4.13b plot $\log \Delta_m$ as a function of $\log V_{sw}$ where Δ_m is obtained independently from equations (4.24) and (4.18), respectively. The data points come from 1100–1700 MLT, as in previous plots. Figure 4.13 shows that Δ_m obtained from either method has roughly the same value. The mean value of $\Delta_m \sim 3 \times 10^6$ m ($\sim 0.5 R_E$) using either equations (4.24) or (4.18). So, the boundary layer thickness obtained from the two methods are consistent with each other and with previously reported values of the boundary layer thickness, [e.g., *Eastman and Hones*, 1979; *Phan and Paschmann*, 1996; *Safrankova et al.*, 2007].

The maximum and minimum of Δ_m in Figure 4.13a are 1.5×10^7 and 5.6×10^4 m, respectively, whereas the maximum and minimum of Δ_m in Figure 4.13b are 1.6×10^7 and 2.8×10^4 m, respectively. The first and third quartile values in Figure 4.13a are 1.1×10^6 and 4.4×10^6 m, respectively, whereas the corresponding values in Figure 4.13b are 9.4×10^5 and 4.3×10^6 m, respectively. Figure 4.13 shows that the scatter can be quite large. However, in situ observations at the boundary layer also reveal similar variability in boundary layer thickness [e.g., *Eastman and Hones, 1979; Phan and Paschmann, 1996; Safrankova et al., 2007*]. Section 4.4.4 discusses some of the sources of these uncertainties.

The data shown in Figure 4.13a yields a correlation coefficient $r = 0.09$ and $P = 0.09$ whereas the data in Figure 4.13b has $r = 0.2$ and $P < 0.01$. The low r reflects the large scatter or variability in the data, but the low P indicates a statistically significant trend, particularly in Figure 4.13b. A least squares analysis supports the existence of a weak trend such that Δ_m increases with V_{sw} . In Figure 4.13a (from equation (4.24)), the least square fit yields $\log(\Delta_m) = (0.5 \pm 0.3) \log(V_{sw}) + (0.4 \pm 0.1)$ or $\Delta_m \sim V_{sw}^{(0.5 \pm 0.3)}$. In Figure 4.13b (from equation (4.18)), the least square fit yields $\log(\Delta_m) = (1.1 \pm 0.3) \log(V_{sw}) + (-0.2 \pm 0.2)$ or $\Delta_m \sim V_{sw}^{(1.1 \pm 0.3)}$. That the trend seen in Figure 4.13b is meaningful is reflected in the relatively small uncertainty in the slope. The general trend of increased boundary layer with increased V_{sw} is expected if the KH mode contributes to the formation of the LLBL because the KH mode becomes more unstable as V_{sw} increases. Moreover, a survey based on in situ Cluster observations provides evidence that the electron LLBL is widened by the KH mechanism [*Foullon et al., 2008*]. In our study, most of the observed FACs come from 1100 to 1300 MLT, which map to the dayside magnetopause where the magnetosheath velocity is relatively small and the KH modes may not have adequate time to fully develop. Because KH vortices are expected to develop along the flanks, where the field-lines map to late afternoon-dusk or early morning-dawn sectors, it would be interesting to examine Δ_m vs. V_{sw} along the flanks for comparison. It should also be noted that the large scatter in our data suggests that V_{sw} is only one of many parameters that can affect Δ_m , and prediction of the boundary layer thickness as a function of velocity alone would not be reliable without consideration of other controlling variables.

4.4.4 Sources of uncertainties

Figures 4.4–4.13 show that the data scales relatively well with expected power law dependence from the analytical relationships. However, the data exhibits significant scatter. In this section we discuss possible sources of uncertainty that may contribute to this scatter. We select the FAC data covering 1100–1700 MLT, which maps to the magnetopause region ranging from the pre-noon all the way to the dusk flank or even the nightside flank. In our analysis we assume simple scaling relations between the solar wind parameters and those in the boundary layer, assuming $V_0 = 0.15 V_{sw}$ and magnetosheath $n_e = n_{sw}$, respectively. While a simple scaling relation may be adequate to capture power law dependence, parameters such as velocity and density obviously vary along the flanks and in the boundary layer leading to large scatter in the data. The realistic value of V_0 may vary by a factor of 2 or 3 [e.g., *Fujimoto et al.*, 1998; *Phan et al.*, 1997; *Vaisberg et al.*, 2001; *Dimmock and Nykyri*, 2013], but because the plots are in log-log format, this difference would amount to a shift in the y -intercept by 0.3–0.5, which would translate to scatter by that amount for those parameters that depend on V_0 . Similar considerations also apply to the magnetosheath density. Additionally, V_{sw} anti-correlates with n_{sw} [e.g., *Richardson et al.*, 1996; *Hundhausen et al.*, 1970], which complicates the efforts to isolate the effects of V_{sw} or n_{sw} . How to untangle V_{sw} from n_{sw} and vice versa is a topic covered in Chapter 6.

Moreover, for simplicity, the present study uses an automated procedure to obtain large scale J_{\parallel} from magnetometer data. If $J_{\parallel,obs}$ is linearly proportional to J_{\parallel,max_cal} ($J_{\parallel,max_cal} = c J_{\parallel,obs}$), then any non-unity proportionality constant would introduce a shift in the y direction, as discussed in Section 4.4.1. However, if $J_{\parallel,obs}$ is not linearly proportional to J_{\parallel,max_cal} , then it would affect the slope as well, but the result seems to suggest that the slope is nearly one, except for the points near noon.

Σ_p is estimated from the *Robinson and Vondrak* [1984] and *Robinson et al.* [1987] empirical formulas, but the actual value of Σ_p is difficult to estimate and these empirical formulas can, at times, have large uncertainty. The Knight κ parameter was calculated from n_e , which was obtained from solar wind observation, but T_e is assumed to be 1×10^6 K [*Phan et al.*, 1997]. We have also used $B_m = 30$ nT [*Phan et al.*, 1997; *Vaisberg et al.*, 2001]. A variation by a factor of 2 would introduce a shift in the y -direction by 0.3, as the case for V_0 . Interestingly, at the boundary layer, from the subsolar region to the dusk flank, V_0 would increase while B_m would decrease. Hence, the product the product $V_0 B_m \sim E_0$ would not

vary much, as can be seen in MHD simulations (S. Merkin, private communication, 2014). Thus, although the parameters that depend on V_{sw} or (velocity shear V_0) have large scatter, as shown in Figure 4.10, the parameters that depend on the product $V_{sw}B_m$ (or V_0B_m) may have less scatter. The value of $b = B_i/B_m$ is assumed to be 1000, but in reality, it can vary along the flank.

Another source of uncertainty is the algorithm [Newell and Meng, 1988; Newell *et al.*, 1991a, 1991b, 1991c] that is used to determine whether the FAC is located on open or closed field lines or at the boundary layer. This algorithm has been widely used in many studies for over two decades, but it is difficult to quantitatively determine its accuracy and in fact, it has never been quantitatively validated.

In addition to uncertainties in parameters, the model itself has limitations. The currents in the model are driven by a potential difference across the magnetopause. Although we have attributed this electric potential to the velocity shear associated with convection, there may be other sources for the cross-field electric field in the boundary layer. In some regions, such as the subsolar region, the kinetic pressure gradient could be as significant as the convection/shear if the magnetosheath and the magnetospheric densities/temperatures are significantly different [e.g., Dekeyser and Echim, 2013]. The model also assumes a constant Pedersen conductivity in the ionosphere, although the Pedersen conductance is more generally a nonlinear function of the ionospheric and magnetospheric potential because it depends on the precipitating electron flux [Lundin and Sandahl, 1978; Echim *et al.*, 2008]. However, it should be noted that our empirical specification of the Pedersen conductivity used in the data analysis does take into account a contribution from precipitating electrons, so this effect is taken into account to some extent.

The model also assumes a linear current-voltage relationship based on the Knight relation, which ignores thermal current and nonlinear saturation as well as restricting the magnetospheric electron distribution function to be Maxwellian. Observations of intense localized peaks in current associated with energetic electron flux generally suggests that the current exceeds the thermal current, J_t (see discussion in Section 4.4.1). While most of the currents observed in this study exceed typical thermal currents in the boundary layer, the weaker currents may be comparable ($J_t \sim 0.1\text{--}1 \mu\text{A m}^{-2}$ for $n_e \sim 0.5\text{--}10 \text{ cm}^{-3}$ and $T_e \sim 100 \text{ eV}$); however, scaling relations may still apply even when the currents are comparable. Moreover, most of the scaling relations shown in this chapter are tested with a

subset of data with $\alpha < 1$ ($A/L < 5$), which have currents that are generally much larger than the thermal current. Finally, because the dayside currents are relatively weak ($J_{\parallel} \ll J_t$), nonlinear corrections to the Knight relation are unnecessary.

Although the linear approximation may lead to an overestimate of field-aligned potential when thermal currents are significant, the remarkable similarity of the analytical scaling relations with observations and their similarity to the maximum current and width to the numerical solutions of *Echim et al.* [2008] (which include a self-consistent treatment of the nonuniform magnetopause boundary layer including pressure gradients, nonlinear Pedersen conductivity, and nonlinear Knight relation) suggest that the simple relations probably capture the most important physical dependencies on the solar wind and ionospheric parameters.

It may be possible that in a super low density plasma, current densities induced in the plasma may reach high or even relativistic speeds, leading to a significant inertia. However, the LLBL electrons typically have temperatures in the order of 100s eV and densities in the order of 10s cm^{-3} . Observationally, the electrons that carry the currents are not relativistic. Moreover, the electron inertia generated in this manner is probably generally negligible as quasi-neutrality is established much more rapidly than Alfvénic timescales (it is the Alfvén waves that redistribute the currents when there is a perturbation to the magnetic field). Observations show that, most of the time, magnetospheric plasma operates in the regime where linear Knight relation [*Knight*, 1973] is valid.

Finally, magnetopause processes such as reconnection, flux transfer events, and KHI may introduce small scale FACs, which would introduce noise or scatter in our figures. The present study only examines large scale FACs. We plan to examine smaller scale FACs in a follow-up study.

4.5 Summary and conclusion

Our study provides a theoretical framework to analyze the coupling between the magnetosphere and ionosphere near the magnetopause boundary. We develop simplified analytical expressions for the dependence of the upward field-aligned currents and their structure on solar wind and ionospheric parameters that provide similar dependence as nonlinear kinetic models of the boundary layer. Using simultaneous measurements of solar wind and DMSP particle and

magnetometer data, we examine in the upward R1 at 1100–1700 MLT, the scaling relations of the M–I coupling parameters J_{\parallel} , Δ , Λ , Σ_p , and κ with each other and with solar wind parameters. We find that the observations are well organized by our simple analytical expressions.

We derive an analytical theory for $J_{\parallel, \max}$ generation from the velocity shear at the magnetopause boundary layer. The theory gives a simple formula for calculating $J_{\parallel, \max}$ using parameters that can be observed in ionosphere and solar wind, empirical formulas for conductivities, and simple scaling of magnetosheath velocity and density from solar wind observations. Our results suggest that the analytical theory can predict observed J_{\parallel} fairly well (our method, which uses an automated procedure, does not allow us to observe $J_{\parallel, \max}$). The least square fit of calculated $J_{\parallel, \max}$ vs. observed J_{\parallel} returns $\log(J_{\parallel, \max, \text{cal}}) = (0.96 \pm 0.04) \log(J_{\parallel, \text{obs}}) + (0.03 \pm 0.01)$ for data points from 1100–1700 MLT, excluding data from noon. Near noon (MLT = 1200), the slope of the least square fitted line is lower, $\log(J_{\parallel, \max, \text{cal}}) = (0.83 \pm 0.07) \log(J_{\parallel, \text{obs}}) + (0.05 \pm 0.03)$.

The remarkable agreement between theory and observations suggests that the theory captures the essential physics governing the solar wind interaction with the magnetosphere and energy transfer to the magnetosphere-ionosphere system via field-aligned currents.

We also examine how the mapping of boundary layer structure, Δ_m , maps to ionospheric scales, Λ , and how the mapping depends on the auroral electrostatic scale length, L . In particular, we show observationally that $\Lambda \sim n_{sw}^{-0.5}$ and $\Lambda \sim L$ when $\Lambda/L < 5$, in agreement with the theoretical predictions. Using low altitude and solar wind observations, we infer reasonably well the sheared boundary layer thickness (Δ_m), which was found to be around 3000 km (consistent with in situ observations) and which appears to have some dependence on V_{sw} . Our results indicate that these methods could serve as the basis for development of general tools for inferring boundary layer structures [Simon Wedlund *et al.*, 2013]. While there can be significant advantages to using this simplified analytic model for data analysis and modeling, it is also important to recognize the model limitations discussed in Section 4.4.4 that may in some circumstances require a more comprehensive numerical treatment [e.g., Echim *et al.*, 2008].

4.6 References

- Cowley, S. W. H., and C. J. Owen (1989), A simple illustrative model of open flux tube motion over the dayside magnetopause, *Planet. Space Sci.*, *37*, 1461–1475.
- De Keyser, J., and M. Echim (2013), Electric potential differences across auroral generator interfaces, *Ann. Geophys.*, *31*, 251–261, doi:10.5194/angeo-31-251-2013.
- Dimmock, A. P., and K. Nykyri (2013), The statistical mapping of magnetosheath plasma properties based on THEMIS measurements in the magnetosheath interplanetary medium reference frame, *J. Geophys. Res. Space Physics*, *118*, 4963–4976, doi:10.1002/jgra.50465.
- Drakou, E., B. U. Ö. Sonnerup, and W. Lotko (1994), Self-consistent steady state model of the low-latitude boundary layer, *J. Geophys. Res.*, *99*, 2351–2364, doi:10.1029/93JA02094.
- Eastman, T. E., E. W. Hones Jr., S. J. Bame, and J. R. Asbridge (1976), The magnetospheric boundary layer: Site of plasma, momentum and energy transfer from the magnetosheath into the magnetosphere, *Geophys. Res. Lett.*, *3*, 685–688, doi:10.1029/GL003i011p00685.
- Eastman, T. E., and E. W. Hones Jr. (1979), Characteristics of the magnetospheric boundary layer and magnetopause layer as observed by Imp 6, *J. Geophys. Res.*, *84*, 2019–2028, doi:10.1029/JA084iA05p02019.
- Echim, M. M., J. F. Lemaire, and M. Roth (2005), Self-consistent solution for a collisionless plasma slab in motion across a magnetic field, *Phys. Plasmas*, *7*, 072904, doi:10.1063/1.1943848.
- Echim, M. M., M. Roth, and J. de Keyser (2007), Sheared magnetospheric plasma flows and discrete auroral arcs: A quasi-static coupling model, *Ann. Geophys.*, *25*, 317–330, doi:10.5194/angeo-25-317-2007.
- Echim, M. M., M. Roth, and J. de Keyser (2008), Ionospheric feedback effects on the quasi-stationary coupling between LLBL and postnoon/ evening discrete auroral arcs, *Ann. Geophys.*, *26*, 913–928, doi:10.5194/angeo-26-913-2008.
- Fairfield, D. H., and J. D. Scudder (1985), Polar rain: Solar coronal electrons in the Earth's magnetosphere, *J. Geophys. Res.*, *90*, 4055 - 4068.
- Fairfield, D. H., S. Wing, P. T. Newell, J. M. Ruohoniemi, J. T. Gosling, and R. M. Skoug (2008), Polar rain gradients and field-aligned polar cap potentials, *J. Geophys. Res.*, *113*, A10203, doi:10.1029/2008JA013437.
- Foullon, C., C. J. Farrugia, A. N. Fazakerley, C. J. Owen, F. T. Gratton, and R. B.

- Torbert (2008), Evolution of Kelvin-Helmholtz activity on the dusk flank magnetopause, *J. Geophys. Res.*, *113*, A11203, doi:10.1029/2008JA013175.
- Fujimoto, M., T. Mukai, H. Kawano, M. Nakamura, A. Nishida, Y. Saito, T. Yamamoto, and S. Kokubun (1998), Structure of the low-latitude boundary layer: A case study with Geotail data, *J. Geophys. Res.*, *103*, 2297–2308, doi:10.1029/97JA02946.
- Galand, M., and A. D. Richmond (2001), Ionospheric electrical conductances produced by auroral proton precipitation, *J. Geophys. Res.*, *106*, A1117, doi:10.1029/1999JA002001.
- Hardy, D. A., L. K. Schmitt, M. S. Gussenhoven, F. J. Marshall, H. C. Yeh, T. L. Shumaker, A. Hube, and J. Pantazis (1984), Precipitating Electron and Ion Detectors (SSJ/4) for the Block 5D/Flights 6-10 DMSP Satellites: Calibration and Data Presentation, Rep. AFGL-TR-84-0317, Air Force Geophys. Lab., Hanscom Air Force Base, Mass.
- Hill, T. W., and P. H. Reiff (1977), Evidence of magnetospheric cusp proton acceleration by magnetic merging at the dayside magnetopause, *J. Geophys. Res.*, *82*, 3623-3628.
- Higuchi, T., and S.-I. Ohtani (2000), Automatic identification of large-scale field-aligned current structures, *J. Geophys. Res.*, *105*, 25,305–25,316, doi:10.1029/2000JA900073.
- Hones, E. W., J. R. Asbridge, S. J. Bame, M. D. Montgomery, S. Singer, and S.-I. Akasofu (1972), Measurements of magnetotail plasma flow made with vela 4b, *J. Geophys. Res.*, *77*(28), 5503–5522, doi:10.1029/JA077i028p05503.
- Hundhausen, A. J., S. J. Bame, J. R. Asbridge, and S. J. Sydoriak (1970), Solar wind proton properties: Vela 3 observations from July 1965 to June 1967, *J. Geophys. Res.*, *75*(25), 4643–4657, doi:10.1029/JA075i025p04643
- Iijima, T., and T. A. Potemra (1976), The amplitude distribution of field-aligned currents at northern high latitudes observed by Triad, *J. Geophys. Res.*, *81*, 2165–2174, doi:10.1029/JA081i013p02165.
- Johnson, J. R., and S. Wing (2015), The dependence of the strength and thickness of field-aligned currents on solar wind and ionospheric parameters. *J. Geophys. Res. Space Physics*, *120*, 3987–4008. doi: 10.1002/2014JA020312
- Keller, K. A., M. Hesse, M. Kuznetsova, L. Rastätter, T. Moretto, T. I. Gombosi, and D. L. DeZeeuw (2002), Global MHD modeling of the impact of a solar wind pressure change, *J. Geophys. Res.*, *107*(A7), 1126, doi:10.1029/2001JA000060.
- Knight, S. (1973), Parallel electric fields, *Planet. Space Sci.*, *21*, 741–750.

- Lockwood, M., P. E. Sandholt, S. W. H. Cowley, and T. Oguti (1989), Interplanetary magnetic field control of dayside auroral activity and the transfer of momentum across the dayside magnetopause, *Planet. Space Sci.*, *37*, 1347–1365, doi:10.1016/0032-0633(89)90106-2.
- Lotko, W., B. U. O. Sonnerup, and R. L. Lysak (1987), Nonsteady boundary layer flow including ionospheric drag and parallel electric fields, *J. Geophys. Res.*, *92*, 8635–8648, doi:10.1029/JA092iA08p08635.
- Lundin, R., and I. Sandahl (1978), Some characteristics of the parallel electric field acceleration of electrons over discrete auroral arcs as observed from two rocket flights, in *European Sounding Rocket, Balloon and Related Research, With Emphasis on Experiments at High Latitudes, ESA Spec. Publ.*, vol. 135, edited by T. Halvorsen and B. Battrock, pp. 125–136, European Space Agency, Noordwijk, Netherlands.
- Lyons, L. R. (1980), Generation of large-scale regions of auroral currents, electric potentials, and precipitation by the divergence of the convection electric field, *J. Geophys. Res.*, *85*, 17–24, doi:10.1029/JA085iA01p00017.
- Miura, A., and P. L. Pritchett (1982), Nonlocal stability analysis of the MHD Kelvin-Helmholtz instability in a compressible plasma, *J. Geophys. Res.*, *87*(A9), 7431–7444, doi:10.1029/JA087iA09p07431.
- Newell, P. T., and C.-I. Meng (1988), The cusp and the cleft/boundary layer: Low-altitude identification and statistical local time variation, *J. Geophys. Res.*, *93*, 14,549–14,556, doi:10.1029/JA093iA12p14549.
- Newell, P. T., C.-I. Meng, E. R. Sanchez, W. J. Burke, and M. E. Greenspan (1991a), Identification and observations of the plasma mantle at low altitude, *J. Geophys. Res.*, *96*, 35–45, doi:10.1029/90JA01760.
- Newell, P. T., S. Wing, C.-I. Meng, and V. Sigillito (1991b), The auroral oval position, structure, and intensity of precipitation from 1984 onward: An automated on-line data base, *J. Geophys. Res.*, *96*, 5877–5882, doi:10.1029/90JA02450.
- Newell, P. T., E. R. Sanchez, C.-I. Meng, W. J. Burke, M. E. Greenspan, and C. R. Clauer (1991c), The low-latitude boundary layer and the boundary plasma sheet at low altitude: Prenoon precipitation regions and convection reversal boundaries, *J. Geophys. Res.*, *96*, 21,013–21,023, doi:10.1029/91JA01818.
- Onsager, T. G., C. A. Kletzing, J. B. Austin, and H. MacKiernan (1993), Model of magnetosheath plasma in the magnetosphere: Cusp and mantle particles at low-altitudes, *Geophys. Res., Lett.*, *20*, 479–482.
- Paschmann, G., W. Baumjohann, N. Sckopke, T.-D. Phan, and H. Luehr (1993),

- Structure of the dayside magnetopause for low magnetic shear, *J. Geophys. Res.*, *98L*, 13,409–13,422, doi:10.1029/93JA00646.
- Phan, T. D., and G. Paschmann (1996), Low-latitude dayside magnetopause and boundary layer for high magnetic shear 1. Structure and motion, *J. Geophys. Res.*, *101*, 7801–7816, doi:10.1029/95JA03752.
- Phan, T. D., B. U. O. Sonnerup, and W. Lotko (1989), Self-consistent model of the low-latitude boundary layer, *J. Geophys. Res.*, *94*, 1281–1293, doi:10.1029/JA094iA02p01281.
- Phan, T. D., D. Larson, J. McFadden, R. P. Lin, C. Carlson, M. Moyer, K. I. Paularena, M. McCarthy, G. K. Parks, H. Rème, T. R. Sanderson, and R. P. Lepping (1997), Low-latitude dusk flank magnetosheath, magnetopause, and boundary layer for low magnetic shear: Wind observations, *J. Geophys. Res.*, *102*, 19,883–19,896, doi:10.1029/97JA01596.
- Rees, M. H. (1963), Auroral ionization and excitation by incident energetic electrons, *Planet. Space Sci.*, *11*(10), 1209–1218, doi:10.1016/0032-0633(63)90252-6.
- Reiff, P. H., T. W. Hill, and J. L. Burch (1977), Solar wind plasma injection at the dayside magnetospheric cusp, *J. Geophys. Res.*, *82*, 479–491.
- Rich, F. J., D. A. Hardy, and M. S. Gussenhoven (1985), Enhanced ionosphere-magnetosphere data from the DMSP satellites, *Eos*, *66*, 513.
- Richardson, J. D., J. W. Belcher, A. J. Lazarus, K. I. Paularena, and P. R. Gazis (1996), Statistical properties of the solar wind, in *Solar Wind Eight, AIP Conf. Proc.*, *382*, edited by D. Winterhalter et al., pp. 483–486, Am. Inst. of Phys., Melville, New York, doi:10.1063/1.51433.
- Robinson, R. M., and R. R. Vondrak (1984), Measurements of E region ionization and conductivity produced by solar illumination at high latitudes, *J. Geophys. Res.*, *89*, 3951–3956, doi:10.1029/JA089iA06p03951.
- Robinson, R. M., R. R. Vondrak, K. Miller, T. Dabbs, and D. Hardy (1987), On calculating ionospheric conductances from the flux and energy of precipitating electrons, *J. Geophys. Res.*, *92*, 2565–2569, doi:10.1029/JA092iA03p02565.
- Safránková, J., Z. Nemecek, L. Prech, J. Simunek, D. Sibeck, and J.-A. Sauvaud (2007), Variations of the flank LLBL thickness as response to the solar wind dynamic pressure and IMF orientation, *J. Geophys. Res.*, *112*, A07201, doi:10.1029/2006JA011889.
- Scudder, J. D., D. L. Lind, and K. W. Ogilvie (1973), Electron observations in the solar wind and magnetosheath, *J. Geophys. Res.*, *78*, 6535–6548,

doi:10.1029/JA078i028p06535.

- Simon Wedlund, C., H. Lamy, B. Gustavsson, T. Sergienko, and U. Brändström (2013), Estimating energy spectra of electron precipitation above auroral arcs from ground-based observations with radar and optics, *J. Geophys. Res. Space Physics*, *118*, 3672–3691, doi:10.1002/jgra.50347.
- Sonnerup, B. U. Ö. (1980), Theory of the low-latitude boundary layer, *J. Geophys. Res.*, *85*, 2017–2026, doi:10.1029/JA085iA05p02017.
- Spreiter, J. R., and S. S. Stahara (1985), Magnetohydrodynamic and gasdynamic theories for planetary bow waves, in *Collisionless Shocks in the Heliosphere: Reviews of Current Research, Geophys. Monogr. Ser.*, vol. 35, edited by B. T. Tsurutani and R. G. Stone, pp. 85–107, AGU, Washington D. C.
- Vaisberg, O. L., V. N. Smirnov, L. A. Avanov, J. H. Waite, J. L. Burch, D. L. Gallagher, and N. L. Borodkova (2001), Different types of low-latitude boundary layer as observed by interball tail probe, *J. Geophys. Res.*, *106*(A7), 13,067–13,090, doi:10.1029/2000JA000154.
- Wallis, D. D., and E. E. Budzinski (1981), Empirical models of height integrated conductivities, *J. Geophys. Res.*, *86*(A1), 125–137, doi:10.1029/JA086iA01p00125.
- Wang, H., H. Lühr, and S. Y. Ma (2005), Solar zenith angle and merging electric field control of field-aligned currents: A statistical study of the Southern Hemisphere, *J. Geophys. Res.*, *110*, A03306, doi:10.1029/2004JA010530.
- Weimer, D. R., D. M. Ober, N. C. Maynard, M. R. Collier, D. J. McComas, N. F. Ness, C. W. Smith, and J. Watermann (2003), Predicting Interplanetary Magnetic Field (IMF) propagation delay times using the minimum variance technique, *J. Geophys. Res.*, *108*(A1), 1026, doi:10.1029/2002JA009405.
- Wing, S. P. T. Newell, and T. G. Onsager (1996), Modeling the entry of magnetosheath electrons into the dayside ionosphere, *J. Geophys. Res.*, *101*, 13,155–13,167.
- Wing, S., Patrick T. Newell, and J. Michael Ruohoniemi (2001), Double cusp: Model prediction and Observational Verification, *J. Geophys. Res.*, *106*, 25,571–25,593.
- Wing, S., P. T. Newell, C.-I. Meng (2005a), Cusp Modeling and Observations at Low Altitude, *Survey Geophys.*, *26*: 341–367, doi:10.1007/s10712-005-1886-0.
- Wing, S., J. R. Johnson, P. T. Newell, and C.-I. Meng (2005b), Dawn-dusk asymmetry in the northward IMF plasma sheet, *J. Geophys. Res.*, *110*, A08205, doi:10.1029/2005JA011086.

- Wing, S., S.-I. Ohtani, P. T. Newell, T. Higuchi, G. Ueno, and J. M. Weygand (2010), Dayside field-aligned current source regions, *J. Geophys. Res.*, *115*, A12215, doi:10.1029/2010JA015837.
- Wing, S., S.-I. Ohtani, J. R. Johnson, M. Echim, P. T. Newell, T. Higuchi, G. Ueno, and G. R. Wilson (2011), Solar wind driving of dayside field-aligned currents, *J. Geophys. Res.*, *116*, A08208, doi:10.1029/2011JA016579.
- Wing, S., and J. R. Johnson (2015), Theory and observations of upward field-aligned currents at the magnetopause boundary layer, *Geophys. Res. Lett.*, *42*, 9149–9155, doi:10.1002/2015GL065464
- Winningham, J. D., F. Yasuhara, S.-I. Akasofu, and W. J. Heikkila (1975), The latitudinal morphology of 10-eV to 10-keV electron fluxes during magnetically quiet and disturbed times at the 2100-0300 MLT sector, *J. Geophys. Res.*, *80*, 3148.
- Woch, J., M. Yamauchi, R. Lundin, T. A. Potemra, and L. J. Zanetti (1993), The low-latitude boundary layer at mid-altitudes: Relation to large-scale Birkeland currents, *Geophys. Res. Lett.*, *20*, 2251-2254.

Chapter 5

Auroral particle precipitation characterized by the substorm cycle

5.1 Introduction

In Chapter 2, we develop a model for the solar wind entry into the Earth's magnetosphere through reconnection, which is the region labeled 1 in Figure 1.2. Chapter 3 discusses solar wind entries in the open field line regions in the polar cap. The dayside reconnection opens the previously closed magnetic field line, allowing the solar wind to enter the magnetosphere all the way from the dayside to the nightside until the field line reconnects with another open field line to form a closed field line. Chapter 4 discusses the energy transfer from the solar wind to the magnetosphere along the low-latitude boundary layer (LLBL), which generates field-aligned currents. The field-aligned current is generated because velocity shear at LLBL generates electric potential drop across the magnetopause boundary. It turns out that the same velocity shear at LLBL can also allow solar wind to enter the magnetosphere. Much of the solar wind that enters the magnetosphere ends up in the magnetotail region called the plasma sheet (region 3 in Figure 1.2). However, it should be noted that not all the plasma sheet particles originate from the solar wind. A fraction originates from the ionosphere. Then, periodically some of this plasma is injected (arrow 4 in Figure 1.2) into the inner magnetosphere (region 5 in Figure 1.2) through processes such as geomagnetic storm and substorm. Substorms occur roughly every few hours on the average whereas storms occur less frequently, in the order of once or a few times a month, depending on the solar cycle. This chapter focuses only on substorms. The field-aligned magnetospheric particles precipitate in the ionosphere in the region called the auroral oval where they can be detected by ionospheric satellites. In the magnetosphere, the field-aligned particles are replenished through pitch-angle

scattering. The electrons can be pitch-angle scattered by waves while the ions can be pitch-angle scattered by the neutral current sheet at the equatorial plane of the magnetosphere. In general, the nightside auroral precipitating particles originate from the plasma sheet and outer inner magnetosphere whereas the dayside auroral precipitation particles originate from the plasma sheet particles that have drifted around to the dayside. Hence, the auroral oval particle precipitation provides a “window” that allows us to look into the particles and processes in the magnetosphere.

In this chapter, we start by reviewing the various paths for the solar wind to enter the plasma sheet. Then we discuss the characteristics of the auroral oval ion and electron precipitation throughout the substorm cycle.

5.2 Review of the solar wind entries into the plasma sheet

The Earth’s magnetosphere on the nightside is stretched out in an elongated fashion that resembles a tail like configuration, which is often referred to as magnetotail. The magnetotail is fundamentally important for understanding

This chapter has been published in the following papers:

- Wing, S., J. R. Johnson, and E. Camporeale, Dawn-dusk asymmetries in the auroral particle precipitation and their modulations by substorm in Dawn-Dusk Asymmetry in Planetary Plasma Environments (eds C. Forsyth, S. Haaland, and A. Runov), John Wiley & Sons, Inc, Hoboken, NJ, manuscript accepted, 2016.
- Wing, S. and Johnson, J. R. (2015), Solar Wind Entry Into and Transport Within Planetary Magnetotails, in Magnetotails in the Solar System (eds A. Keiling, C. M. Jackman and P. A. Delamere), John Wiley & Sons, Inc, Hoboken, NJ. doi: 10.1002/9781118842324.ch14.
- Wing, S., M. Gkioulidou, J. R. Johnson, P. T. Newell, and C.-P. Wang (2013), Auroral particle precipitation characterized by the substorm cycle, *J. Geophys. Res. Space Physics.*, 118, doi:10.1002/jgra.50160.

Contribution statement:

- S. Wing: contributed main ideas, wrote the code to analyze DMSP data, interpreted results, performed most of the work, wrote the three papers listed above.
- J. R. Johnson: contributed useful comments and discussions.
- E. Camporeale: provided useful comments and discussions.
- M. Gkioulidou: contributed RCM–Dungey simulation and model–data comparisons.
- P. T. Newell: contributed code for DMSP data processings and displays.
- C.-P. Wang: suggested initial idea for some of the work.

dynamical processes in the magnetosphere such as geomagnetic storms and substorms. A region in the magnetotail that is usually characterized by high plasma density ($n \geq \sim 0.5 \text{ cm}^{-3}$) and ratio of plasma pressure over magnetic pressure (plasma β) $\geq \sim 1$ is called the plasma sheet, which is an important source population for inner magnetosphere, ring current, radiation belt, and auroral precipitation.

It is believed that there are two plasma sources for the plasma sheet, namely, the solar wind and the ionosphere. Their relative importance depends on solar wind and geomagnetic conditions. It is well established that plasma sheet properties such as density, pressure, and temperature are correlated with solar wind conditions [e.g., Borovsky *et al.*, 1998a; Terasawa *et al.*, 1997; Wing and Newell, 2002; Nagata *et al.*, 2007]. However, the path the solar wind takes to reach the plasma sheet and the subsequent plasma transport within the plasma sheet are not always clear.

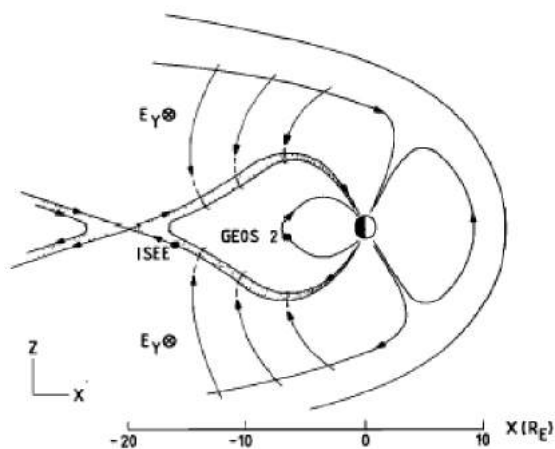


Figure 5.1. An illustration showing the electric and magnetic field lines on the nightside for southward IMF. After reconnection on the dayside, the open field line convects over the pole to the nightside where due to the duskward electric field, the field line would $\mathbf{E} \times \mathbf{B}$ toward the equatorial plane where it would reconnect once more to form closed field line that is part of the plasma sheet (from Figure 11 of Pedersen *et al.* [1985]).

During southward Interplanetary Magnetic Field (IMF), reconnection can occur at the low-latitude magnetopause on the dayside where the IMF and the Earth's magnetic field line are nearly anti-parallel [Crooker, 1979]. After reconnection, the open field lines would convect to the nightside toward the lobe region. Because of the solar wind duskward electric field, these open field lines would $\mathbf{E} \times \mathbf{B}$ drift to the equatorial region where they would once again reconnect

[e.g. *Pedersen et al.*, 1985; *Keiling et al.*, 2004]. This process is depicted in Figure 5.1 (see also Figure 2.2). Once reconnected, the field line, which is filled with magnetosheath plasma, becomes part of the plasma sheet. In essence, the magnetosheath plasma is now captured in the plasma sheet. Subsequently, this newly closed field line would $\mathbf{E} \times \mathbf{B}$ convect sunward to the dayside, returning the magnetic flux back to the dayside. This process is known as the Dungey cycle [*Dungey*, 1961], although the solar wind entry into the plasma sheet during southward IMF can be more complicated than the Dungey cycle and can involve other processes.

In the anti-parallel merging model [*Crooker*, 1979], the reconnection would occur at high-latitude poleward of the cusp in the lobe during northward IMF. After the reconnection, the footpoint of the newly reconnected field line would initially move sunward before being swept away to the nightside, but the solar wind electric field is dawnward, instead of duskward for southward IMF case. So, the entry mechanism for northward IMF may not be as simple and straightforward as the scenario portrayed in the Dungey cycle. The intrigue and the difficulty only deepened when it was discovered that compared to southward IMF conditions, more solar wind particles enter the magnetotail during northward IMF conditions, which can lead to the formation of cold, dense plasma sheet (temperature < 1 KeV and density $> 1 \text{ cm}^{-3}$) [e.g., *Terasawa et al.*, 1997; *Fujimoto et al.*, 1998; *Wing and Newell*, 2002; *Stenuit et al.*, 2002; *Øieroset et al.*, 2008].

It turns out, reconnection can still play important roles in transporting solar wind plasma into the magnetotail during periods of northward IMF. A special case of high-latitude reconnection, where the Earth's field lines are reconnected at both hemispheres forming a newly closed field line filled with magnetosheath plasma ("double cusp reconnection") [*Song and Russell*, 1992; *Le et al.*, 1996; *Sandholt et al.*, 1999; *Fuselier et al.*, 2002]. Magnetohydrodynamic (MHD) simulations have been performed to show that this process can effectively bring magnetosheath plasma into plasma sheet [*Raeder et al.*, 1995; 1997]. This process is depicted in Figure 5.2, which can be contrasted with Figure 5.1. Figure 5.2, from an MHD simulation [*Li et al.*, 2005], shows the time sequence of a field line as it convects with the solar wind, crosses the bow shock, and then reconnects sequentially in short order with lobe field lines in each hemisphere. After that, the field line, along with the captured magnetosheath plasma, slowly (on a time scale of 1–3 hr) convects into the tail. Initially, the newly closed dayside field line would move sunward and then it would move tailward to the flanks.

Øieroset et al. [2005] reported a fairly good agreement in the plasma sheet temperature and density between an MHD simulation in which double cusp reconnection fills the plasma sheet and Cluster satellite observations in a case study. MHD simulations for northward IMF conditions replicate the development of a low-latitude boundary layer detected by the five THEMIS spacecraft as they encountered the magnetopause boundary [*Li et al.*, 2009].

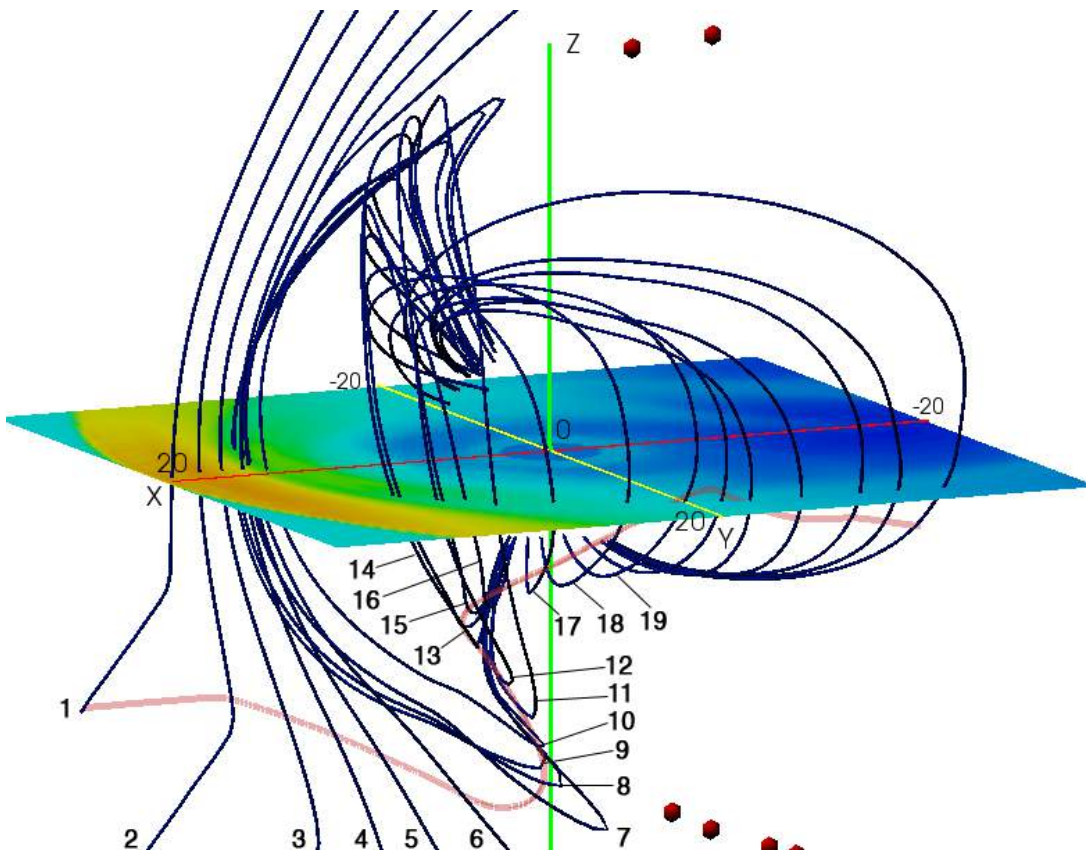


Figure 5.2. Three dimensional visualization of the solar wind plasma entry due to double cusp reconnection during northward IMF (from *Li et al.* [2005]). The color of the equatorial plane indicates the plasma density. The dark blue line shows the frozen-in magnetic field lines. The red dots are the magnetic nulls. The red, yellow, and green axes are GSE x , y , and z axes, respectively. The numbers 1–19 indicate the progression of the field line in time.

Another possible solar wind entry mechanism is Kelvin-Helmholtz Instability (KHI). Kelvin-Helmholtz waves grow along an inhomogeneous velocity shear layer (as found on the flank magnetopause) and eventually develop a rolled up vortex pattern in density and magnetic field, as illustrated in Figure 5.3.

KHI has been successfully simulated with MHD code [e.g., *Otto and Fairfield, 2000; Nakamura and Fujimoto, 2005; Nykyri and Otto, 2001; Nykyri et al., 2006; Claudepierre et al., 2008; Guo et al., 2010; Merkin et al., 2013*]. Signatures of these vortices have been found on the dusk and dawn flanks of the magnetosphere [e.g., *Fairfield et al., 2000; Fujimoto et al., 2003; Hasegawa et al., 2006*]. Moreover, reconnection in the nonlinear stage of the KHI could lead to the detachment of plasma from the vortex structures, leading to significant magnetopause transport [e.g., *Otto and Fairfield, 2000; Nykyri et al., 2006*]. Hybrid simulations have indicated that ion blobs could become detached from the vortex structure of the KHI and could provide filaments, producing a mixing of plasma in the shear layer [*Thomas and Winske, 1991; 1993; Fujimoto and Terasawa, 1994; 1995*]. *Hasegawa et al. [2006]* noted that there is an inverse relationship between the magnetospheric plasma density and tailward flow speed in KH vortices, leading to the development of an algorithm for detecting rolled up KH vortices with a single spacecraft. A comprehensive review of KHI is provided by *Johnson et al. [2014]*.

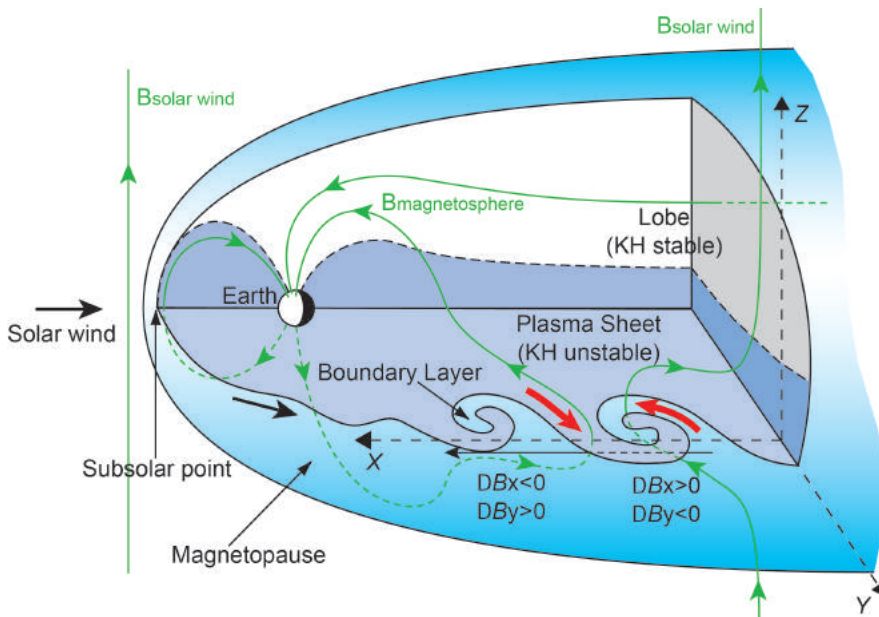


Figure 5.3. Three dimensional view of the magnetosphere showing the KH vortices at the duskside magnetopause (from *Hasegawa et al. [2004]*).

Large-amplitude Alfvén waves have also been observed on the magnetospheric boundary [e.g., *Tsurutani et al., 1982; LaBelle and Treumann, 1988; Anderson and Fuselier, 1994*]. There is evidence that the waves could be

the result of mode conversion of magnetosheath compressions in the sharp magnetopause gradients at the magnetopause [Lee *et al.*, 1994; Johnson and Cheng, 1997; Johnson *et al.*, 2001]. Because the wavelength of the mode converted waves are on the order of the ion gyroradius, they can lead to efficient convective and diffusive transport of ions across the magnetopause, as illustrated in Figure 5.4 [Johnson and Cheng, 1997; Chen, 1999; Chaston *et al.*, 2008]. The mode conversion process has been simulated with 2D hybrid simulations [Lin *et al.*, 2010] showing linear mode conversion, and 3D simulations [Lin *et al.*, 2012] showing nonlinear decay of the mode converted waves such that transport is greatly enhanced because of the development of modes with large azimuthal wave number. Kinetic Alfvén waves (KAWs) also lead to nonlinear plasma heating because of the large amplitudes observed at the magnetopause [Johnson and Cheng, 2001; Chaston *et al.*, 2008].

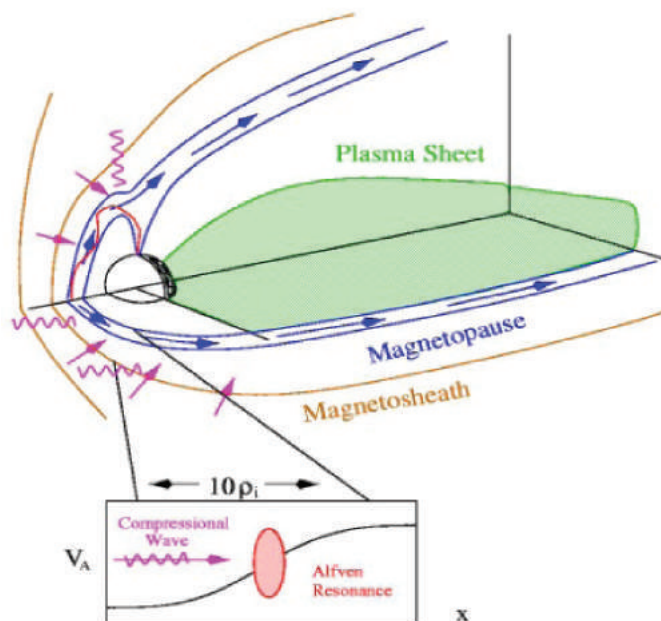


Figure 5.4. Three dimensional view of the magnetosphere showing kinetic Alfvén waves in the magnetosheath leading to solar wind/magnetosheath plasma entry into the magnetosphere.

These three processes are not necessarily mutually exclusive and have all been demonstrated to be capable to transport plasma across magnetic boundaries. For example, KH waves can excite KAW [Sibeck *et al.*, 1999]. KAWs have been observed in conjunction with reconnection and Kelvin-Helmholtz structures

[Chaston *et al.*, 2005, 2007, 2009]. Nishino *et al.* [2007] also observed bidirectional electrons and cold protons inside a KH vortical structure, which they interpreted as a signature reconnection. Additionally, they observed electron and ion heating, which they attributed to wave-particle interactions such as KAW heating [Johnson and Cheng, 1997; 2001]. Taylor and Lavraud [2008] found that there could be three distinct ion populations, which can be interpreted as evidence for KAW, KHI, and reconnection processes. KHI and KAW can also play significant roles in the plasma entry during southward IMF.

It has been a challenge to distinguish which of these three mechanisms can play a more significant role and under what conditions. Recent observations have attempted to identify several potential discriminators based on both *in situ* and remote sensing methods. One of the potential discriminators is the filling rate. Each entry mechanism may lead to a different entry or filling rate. Another potential discriminator is the dawn-dusk asymmetries. Dawn-dusk asymmetries are particularly interesting because they may be related to how upstream boundary conditions (e.g. Parker spiral magnetic field orientation) affect the various entry mechanisms, which can be tested by observation and theory. Another potential discriminator is the specific entropy or entropy per unit volume ($s = P/\rho^\gamma$ where P = plasma pressure, ρ = mass density, and γ is polytropic index = 5/3). Changes in the entropy profiles may be indicators that nonadiabatic processes are operating in conjunction with plasma transport, and how the entropy change is likely related to the entry mechanism [e.g., Wing and Johnson, 2009; Johnson and Wing, 2009; Wing and Johnson, 2010].

Once the solar wind plasma enters the magnetotail, it will be distributed throughout the plasma sheet by the transport processes within the magnetotail or plasma sheet. The plasma can get heated and energized during these processes. Some of the transport processes such as curvature and gradient drifts introduce dawn-dusk asymmetries in the particles, especially for the hot component. Transport within the plasma sheet has been described with MHD models, which conserve total entropy ($S = PV^\gamma$ where V = flux tube volume). Total entropy conservation provides important constraints on the accessibility of plasma to the plasma sheet and governs the redistribution of plasma when flux tubes are depleted of total entropy due to nonadiabatic processes such as reconnection, plasma diffusion, and wave-particle interactions [e.g., Wing and Johnson, 2009; Johnson and Wing, 2009; Wing and Johnson, 2010].

Wing and Johnson [2015] and *Wing et al. [2014]* provide more in depth reviews of solar wind entry into and transport within the plasma sheet.

5.3 Substorm and auroral particle precipitation

A substorm is an important and common process that cycles through storing and releasing energy in the Earth's magnetosphere. Substorms occur in other planetary magnetospheres in our solar system and perhaps even in exoplanetary magnetospheres [e.g., *Mauk et al., 1997; Berthomier et al., 2012*]. There are generally three phases of a substorm: growth, expansion, and recovery. The growth phase typically begins in the quiescent period at the time of the southward turning of the interplanetary magnetic field (IMF) [e.g., *Tanskanen et al., 2002*] and ends at the onset of the expansion phase (commonly referred to as the substorm onset). During the growth phase, the auroral oval expands equatorward, the aurora and the electrojet gradually intensify, the plasma sheet thins, and the magnetospheric magnetic field lines stretch (become tail-like), as the solar wind energy is stored in the magnetotail. The expansion phase begins at the end of the growth phase. During the expansion phase the auroral oval brightens and expands poleward, eastward, and westward, the westward electrojet significantly increases, and the magnetic field configuration in the inner plasma sheet changes rapidly from the stretched tail-like configuration to a more dipolar configuration. The expansion phase is followed by the recovery phase, during which the magnetosphere returns back to its original undisturbed state. The start of the recovery phase is usually signaled by the waning of the substorm aurora and weakening of the westward electrojet. The recovery phase ends when the magnetosphere reaches its normal undisturbed state. A more detailed description of substorm phases can be found in *Lui [1991]*.

Many space phenomena or parameters cycle with the substorm cycle of growth–expansion–recovery phases. The waxing-waning of the auroral oval, the stretching-unstretching of the magnetotail, and loading–unloading of the magnetotail energy mentioned above are just a few examples of such parameters. Auroral particle precipitation is an important parameter because it provides a measure of magnetospheric energy input into the ionosphere. It can be used to indicate a state of the magnetosphere, and as such it should be affected by the substorm cycle.

Using ground magnetic field observations and indices derived from these

observations such as aurora electrojet indices, AL or AE, various studies estimated that the growth phase takes approximately 30–60 min, the expansion phase approximately 10–60 min, and the recovery phase approximately 30–120 min [e.g., *Bargatze et al.*, 1999; *Horwitz*, 1985; *Pulkkinen et al.*, 1994; *McPherron et al.*, 1986; *Huang et al.*, 2003; *Baker et al.*, 1981]. Based on these estimates for the growth, expansion, and recovery phases, *Huang et al.* [2003] estimated that the complete substorm cycle takes approximately 2–3 hr. In comparison, *Tanskanen et al.* [2002] reported that the average duration of the substorm, from the beginning of the growth phase to the end of the recovery phase, is approximately 4 hr. They determined the substorm from a proxy for westward electrojet index (AL), which is named IL index and which is derived from IMAGE data [*Kallio et al.*, 2000]. However, the substorm cycle of the auroral particle precipitation is not as well known. The substorm phase durations obtained from magnetospheric particle or magnetic field observations have been found to differ from those determined from the ground magnetic field observations, AE, AL, or IL indices [e.g., *Pulkkinen et al.*, 1994; *Baker et al.*, 1994].

Wing et al. [2007] presented plasma sheet pressure, temperature, and density 2D profiles for the substorm growth, expansion, early recovery, and late recovery phases. Subsequently, *Wing and Johnson* [2009] presented 2D profiles of specific entropy ($s = P/n^\gamma$), total entropy ($S = P^{1/\gamma} V$), and the total content ($N = nV$) of the plasma sheet for the same substorm phases. Both studies used Defense Meteorological Satellite Program (DMSP) observations to infer the plasma sheet properties. Moreover, both studies used a substorm database in which not only the onset time but also the start of the recovery phase had been carefully identified. However, the database had only 180 substorm events and as a result, some regions, particularly postmidnight, had poor data coverage.

Recently, using an order of magnitude more substorm events, 4861 events, *Newell et al.* [2010] performed a superposed epoch analysis of the substorm onset to obtain statistical electron precipitation maps of wave, mono-energetic, and diffuse aurora from 4 to 6 min after substorm onset in 2 min time resolutions. These maps were obtained from DMSP SSJ/4/5 particle observations in the interval 1996–2007. These maps are quite useful in providing the global pictures of the electron precipitations minutes around the substorm onset, but they do not show the dynamics for the entire substorm cycle. *Newell et al.* [2010] also calculated the aurora power obtained by integrating the nightside auroral electron and ion precipitation from 1800 to 0600 magnetic local time (MLT) and from 50°

to 90° magnetic latitude (MLat). These integrated auroral powers were calculated from 2 hr before to 2 hr after substorm onset at 2-min resolution. Unfortunately, at 2-min resolution, the statistics limit interpretation of the results and it is difficult to ascertain any trend within the substorm cycle because of large fluctuations, except at the substorm onset, when the values significantly increase. Moreover, the 2 hr after onset may not be enough time to cover the entire expansion and recovery phases [e.g., *Horwitz*, 1985].

The present study is an extension of the *Wing et al.* [2007], *Wing and Johnson* [2009] and *Newell et al.* [2010] studies. As in the *Newell et al.* [2010] study, the present study examines the substorm cycles in the auroral electron and ion precipitation, but on a larger time scale, covering nearly the entire substorm cycle of the electron and ion aurora. Also as in the *Newell et al.* [2010] study, the present study distinguishes three types of electrons: diffuse, wave or broadband, and monoenergetic.

The diffuse aurora electrons are most likely field-aligned plasma sheet electrons that precipitate in the ionosphere. The electrons in the loss cone (the field-aligned electrons) are replenished by the pitch-angle scattering resulting from electron interactions with the very low frequency (VLF) whistler-mode chorus waves [e.g., *Thorne*, 2010; *Reeves et al.*, 2009; *Summers et al.*, 1998]. When precipitating electrons exhibit a broad energy spectrum, they are classified as wave or broadband aurora electrons. These electrons may result from the electron interaction with the dispersive Alfvén waves [*Chaston et al.*, 2002; 2003; 2008], which are often observed around the time of substorm dipolarization [*Lessard et al.*, 2006]. The monoenergetic electrons, on the other hand, may indicate the presence of the parallel electric field that accelerates the electrons downward and may be associated with the evolution of the global upward current system in the plasma sheet. The monoenergetic electrons may also result from the electron interaction with low frequency Alfvén waves/ballooning modes that accelerate electrons [e.g., *Pritchett and Coroniti*, 2010; *Damiano and Johnson*, 2012]. The present study examines the characteristics and dynamics of these three types of electrons and ions throughout the substorm cycle. This can help illuminate the processes that form these electrons, the regions where they operate, and the time scales at which these processes operate within the substorm cycle. Substorm-led magnetic field dipolarization releases a large amount of energy, some of which is used to energize particle precipitation. The present study quantifies the energy gained by each type of electron during substorms. The growth phase signatures in

these electron, if there are any, should be of interest to space weather studies that aim to predict substorm onsets.

Finally, the Rice Convection Model (RCM) has been used to simulate plasma transport in the magnetotail [Toffoletto *et al.*, 2003]. The present study simulates the ion precipitation by using the RCM combined with a Dungey force-balanced magnetic field solver and strong diffusion. The simulation results are subsequently compared with the DMSP observations.

5.4 DMSP particle data set

Data from the SSJ/4 electrostatic analyzers on the DMSP series satellites (F12 through F15), and the SSJ/5 detector on F16 were used. The time period covered is from 1996 to 2007, although there are no onsets identified in the years 2003–2006. No DMSP F17 data were used because of uncertainties about the data quality (and F15 was used only for 2001).

The DMSP satellites are in sun-synchronous, nearly circular polar orbits at approximately 845 km altitude, with orbital inclinations of 98.7° . The orbits of the DMSP satellites are such that the least-covered regions are postnoon and especially postmidnight, except at high magnetic latitudes. The SSJ/4 and SSJ/5 instruments included on all these flights use curved plate electrostatic analyzers to measure electrons and ions with one complete spectrum each obtained per second. The satellites are three-axis stabilized; and the detector apertures always point toward local zenith. At the latitudes of interest in this paper, this means that only highly field-aligned particles well within the atmospheric loss cone are observed.

5.5 The substorm database

Most substorm studies determine the substorm onsets from either ground magnetic field observations (or indices derived from these observations) or from optical observations of aurora. The substorm onsets in the present study were determined from the latter. As in *Newell et al.* [2010], the present study combines two separate substorm databases: (1) the Polar UVI substorm database [Liou *et al.*, 1997; 2001] and (2) the IMAGE substorm database [Frey *et al.*, 2004]. There are 4861 substorm events in this combined substorm dataset. One difference between the present study and the *Newell et al.* [2010] study is that the present study explicitly selects only isolated substorms that are separated by at least 5 hr from

other substorms in this database. Of the 4861 substorm events in the original combined dataset, 1677 events, or about 34%, are isolated substorms. Ideally, we would like to have more than 5 hr of separation between substorms, but this would further reduce the size of the dataset, which would negatively impact the statistics of the analysis. It should be noted that our selection of isolated substorms is based on observations from Polar and IMAGE, but these satellites do not cover the auroral oval continuously. Nonetheless, most of the selected substorms should still be isolated. This is because in both the Polar UVI and IMAGE substorm databases, only substorms having clear substorm onset signatures were carefully selected manually. This criterion favors isolated substorms, although not necessarily those separated by more than 5 hr.

The Polar UVI database was constructed from the observations of Lyman–Birge–Hopfield (LBH) bands of N_2 , which are stimulated by atmospheric secondaries, and thus responsive to primary precipitating electrons above a few hundred eV in energy (and ions as well, although the energy flux of the latter is typically far smaller). Although storms were not explicitly excluded, one typically cannot identify a single substorm during a storm from auroral imagery. The LBHL and LBHS filters were both used to improve time resolution. More information on the Polar UVI imager and substorm database can be found in *Liou et al.* [1997; 2001].

The IMAGE substorm database was constructed from the IMAGE FUV Wideband Imaging Camera (140–180 nm) observations [*Frey et al.*, 2004]. The IMAGE FUV observations are similar to the Polar UVI observations, which primarily respond to the N_2 LBH lines. The selection criteria were quite similar as well. *Frey et al.* [2004] excluded substorms that occurred within 30 min of a previous onset, but in the present study, we broadened this criterion to exclude onsets that occurred within 5 hr of other substorms.

5.6 Methodology

The algorithms and method of model construction were recently described by *Newell et al.* [2009; 2010]. Here only a brief version of the approach is outlined.

5.6.1 Electron aurorae

The precipitating electrons are classified into three categories: diffuse, monoenergetic, and wave/broadband. Our algorithm for classifying monoenergetic electrons is as follows: (1) Identifies the differential energy flux peak, and subsequently looks at the drops one and two energy channels above and below the peak. If the differential energy flux drops to 30% or less of the peak within these two steps (at energies above and below the peak), then the event is considered monoenergetic. (2) The differential energy flux must be above 1.0×10^8 ($\text{eV cm}^2 \text{ s sr eV}^{-1}$) at the peak channel. (3) If either the average energy is below 80 eV or the differential energy flux peak is below 100 eV, the spectrum is not considered “accelerated.” Such events may be spacecraft charging (some low-acceleration potentials are excluded by this rule).

The algorithm for classifying wave or broadband precipitation is that if three or more energy channels have $dJ_E/dE > 2.0 \times 10^8$ ($\text{eV cm}^2 \text{ s sr eV}^{-1}$), an event is considered broadband. There are some caveats, which are listed in *Newell et al.* [2010] and are not repeated here.

The electrons that are not classified as either broadband or monoenergetic are counted as diffuse. Hence, all electrons are classified. Figure 5.5 presents an example of monoenergetic, broadband, and diffuse electron spectrum.

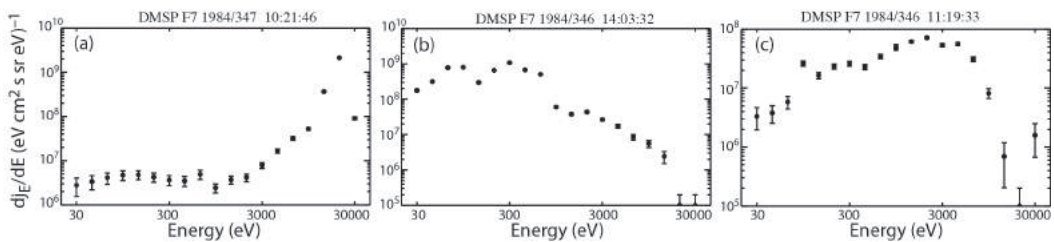


Figure 5.5. An example of monoenergetic (a), broadband (b), and diffuse (c) electron spectrum. The y-axis is the electron differential energy flux and the x-axis is the electron energy. The monoenergetic electron shows an “inverted V” signature. The broadband acceleration shows energization across a few or several energy channels. The diffuse electron typically (not always) shows a Maxwellian or Kappa distribution. ((a) and (b) are adapted from *Newell et al.* [2009].)

It has been established that both ions and electrons have a Kappa distribution in the magnetotail [*Christon et al.*, 1991; *Wing and Newell*, 1998; *Kletzing et al.*, 2003], and in diffuse precipitation. Although broadband and

monoenergetic spectra generally drop sharply above the accelerating range, diffuse aurora may at times have a significant fraction of its energy flux outside the DMSP detector upper limit (30 keV). This is particularly true for ions, especially plasmashet ions within 10–20 R_E , where temperatures can be 5–10 keV (recall the energy flux peaks at twice the temperature) [Wing and Newell, 1998; 2002]. In order to take into account the electrons having $30 \text{ keV} < \text{energy} < 50 \text{ keV}$, for simplicity, the diffuse spectra were thus extrapolated to 50 keV, with a Maxwellian fit. This upper limit is slightly more than one additional energy channel beyond the measurements. Fitting a Maxwellian distribution requires fewer free parameters than a Kappa distribution and hence can be more robust in the cases when there are a few data points within a spectrum [e.g., Wing and Newell, 1998].

5.6.2 Ion aurora

Observationally, the signatures of the parallel electric fields and waves are less clear on ions than on electrons. It is harder to develop an automated algorithm to classify ions. Hence, we make no attempt to classify ions for the present study. The ion aurora is constructed using every spectrum, regardless of how the electron component is classified. Like the diffuse electron, ion spectra are extrapolated from the measured limit of 30 keV up to 50 keV, under the assumption that the spectra is Maxwellian, with a temperature equal to half the differential energy flux peak.

5.6.3 Model construction

The model resolution here is 48 MLT bins by 40 MLat bins in 15-min time steps. The analysis begins 2 hr before onset and extends to 3 hr after. The MLat range is 50° – 90° , with data from the two hemispheres combined. Thus, although the identification of a substorm onset is nearly all from the northern hemisphere global images, the particle precipitation maps contain roughly equal amounts of northern and southern hemispheric data.

The procedure consists of analyzing every DMSP spectrum in the interval 1996–2007 and classifying the precipitation as either monoenergetic, broadband, or diffuse aurora as described in Newell *et al.* [2009; 2010], and the resulting comprehensive list of classified spectra is examined. Then the time of each spectral observation at 1-sec resolution is compared with the list of substorm onsets. If the particle observation time is within 2 hr before onset and 3 hr after

onset, it is added to the appropriate bin (determined from MLat, MLT, and time from onset). Energy and number fluxes as well as pressure are obtained from each electron and ion spectra.

There are altogether approximately 3.4×10^7 spectra or points. The number of points in each bin ranges from 0 to approximately 2800. Finally, the median energy and number fluxes as well as ion pressure are computed for each bin. Auroral precipitation power in each bin is also computed by multiplying the physical surface area of each grid by the median energy flux in each bin. The auroral precipitation power is later used to compute the nightside precipitation powers as described in Section 5.7.2. Note that our method is similar to the method used in *Newell et al.* [2010], except that they calculated the mean rather than the median in each bin. It turns out that the energy fluxes have non-Gaussian distributions. Figure 5.6 shows an example of an electron and an ion energy flux distribution from a randomly selected (MLat, MLT) bin. The distributions have an extended tail of high-energy fluxes that are consistent with the SME distribution, which is well correlated with Polar UVI power (see Figure 4 in *Newell and Gjerloev* [2011]). Therefore, the median would characterize a typical substorm event better than the mean, which may characterize stronger substorms.

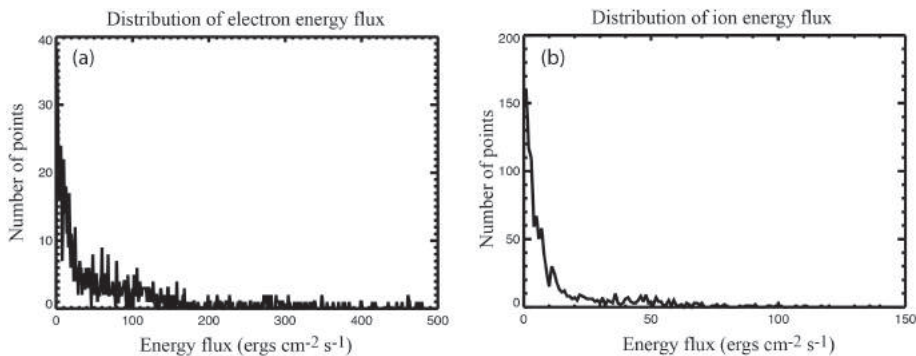


Figure 5.6. An example of a randomly selected electron (a) and ion (b) energy flux distribution in an (MLat,MLT) bin. Both distributions have high-energy flux tails suggesting non-Gaussian distributions.

5.7 Auroral particle precipitation characterized by substorm phases

5.7.1 Particle precipitation maps throughout the substorm cycle

Diffuse aurora electron energy flux

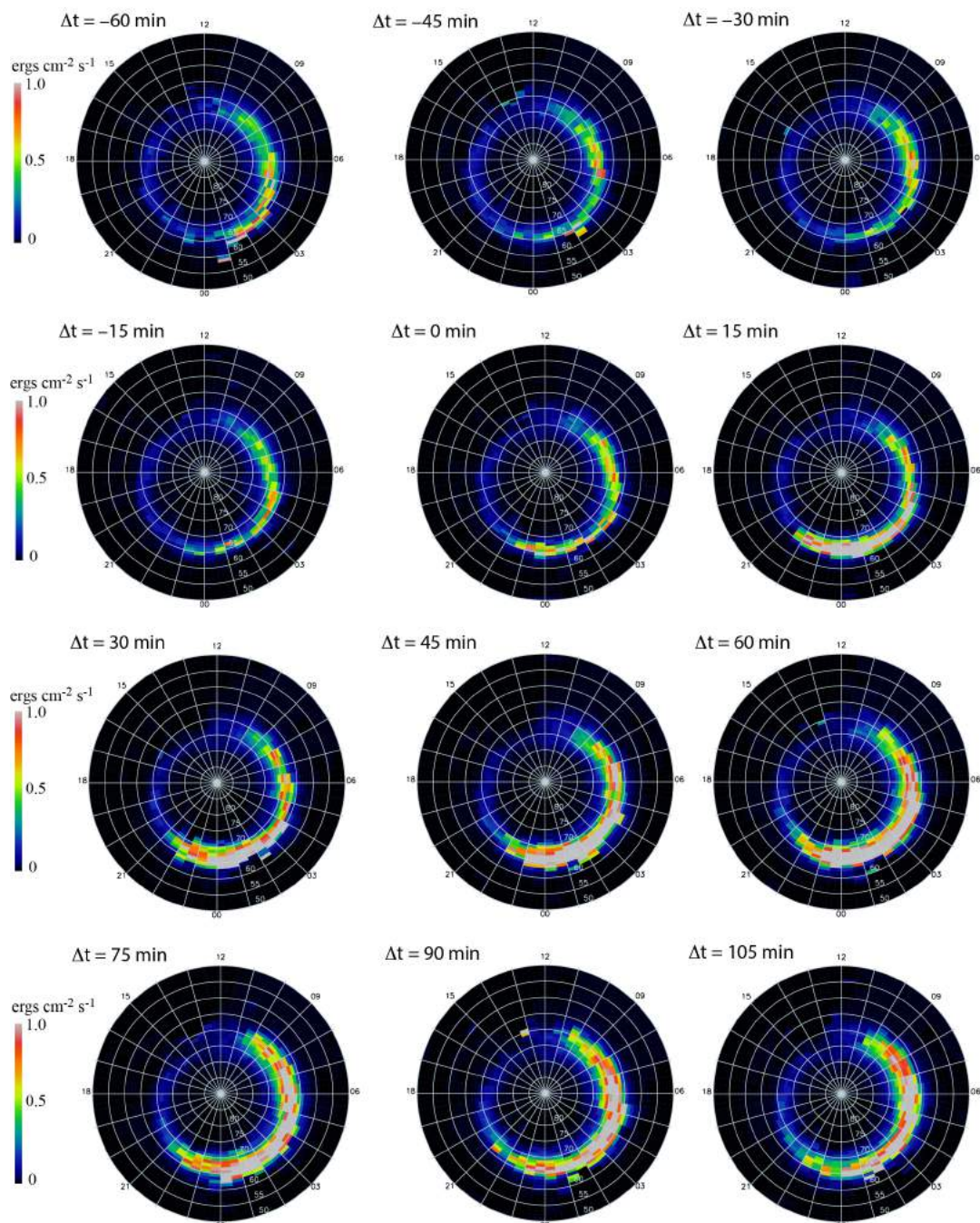


Figure 5.7. Diffuse aurora electron energy flux from 1 hr before to 1 hr and 45 min after the substorm onset. Each map shows the median energy flux over a 15 min interval centered at the time labeled. The substorm onset occurs at $\Delta t = 0$ min.

Monoenergetic aurora electron energy flux

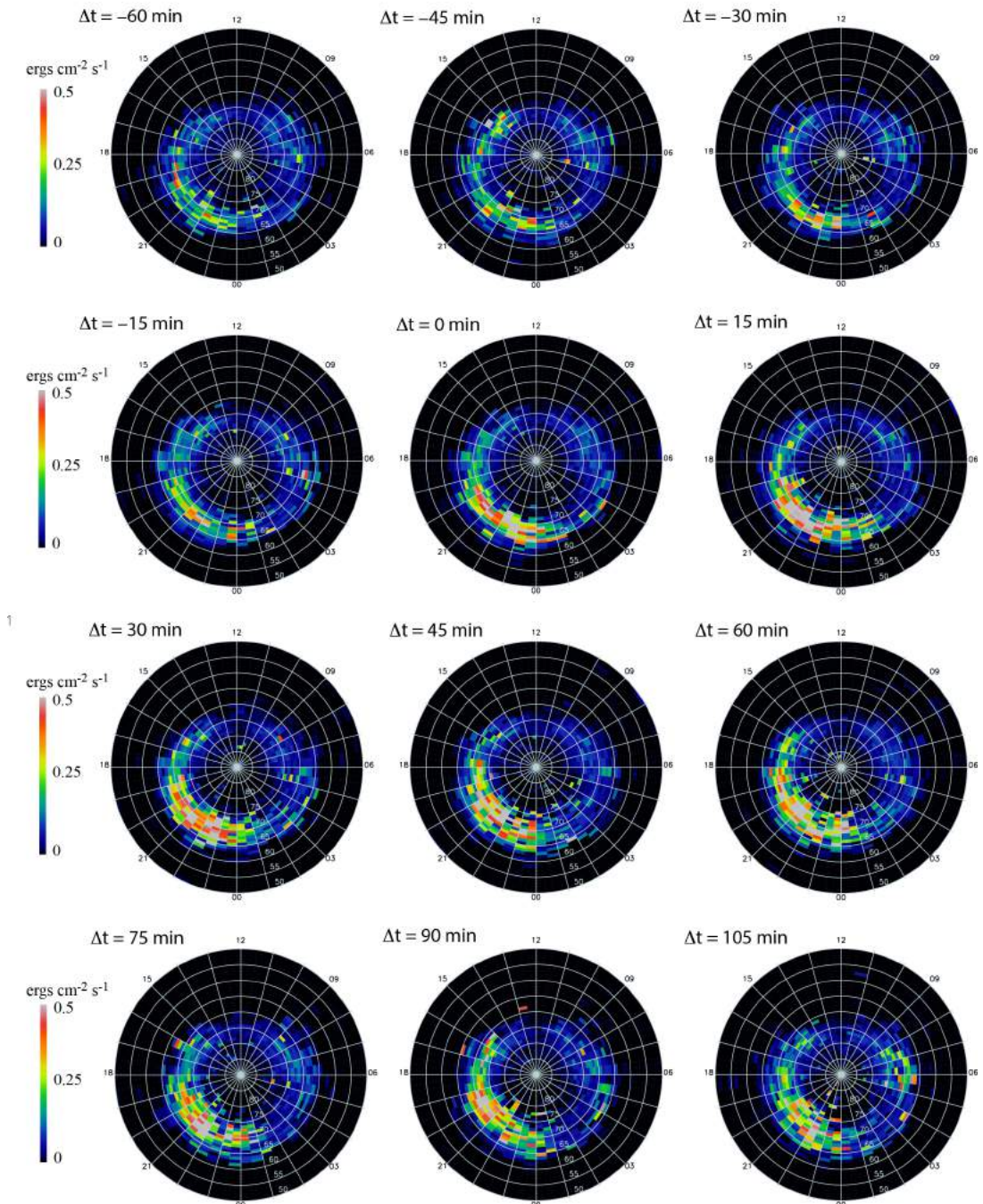


Figure 5.8. Monoenergetic aurora electron energy flux from 1 hr before to 1 hr and 45 min after the substorm onset in the same format as in Figure 5.7. The substorm onset occurs at $\Delta t = 0 \text{ min}$.

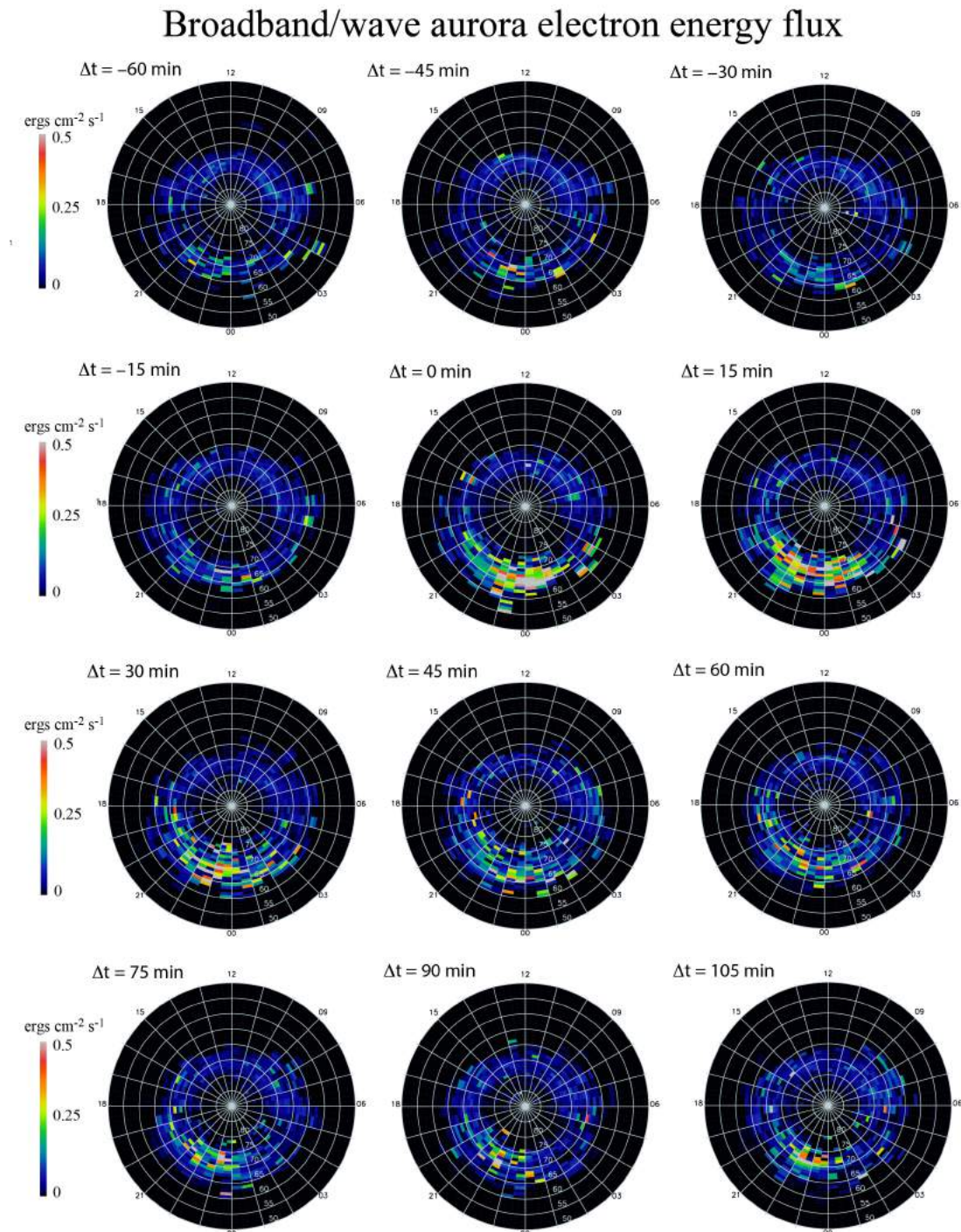


Figure 5.9. Broadband/wave aurora electron energy flux from 1 hr before to 1 hr and 45 min after the substorm onset in the same format as in Figure 5.7. The substorm onset occurs at $\Delta t = 0$ min.

Aurora ion energy flux

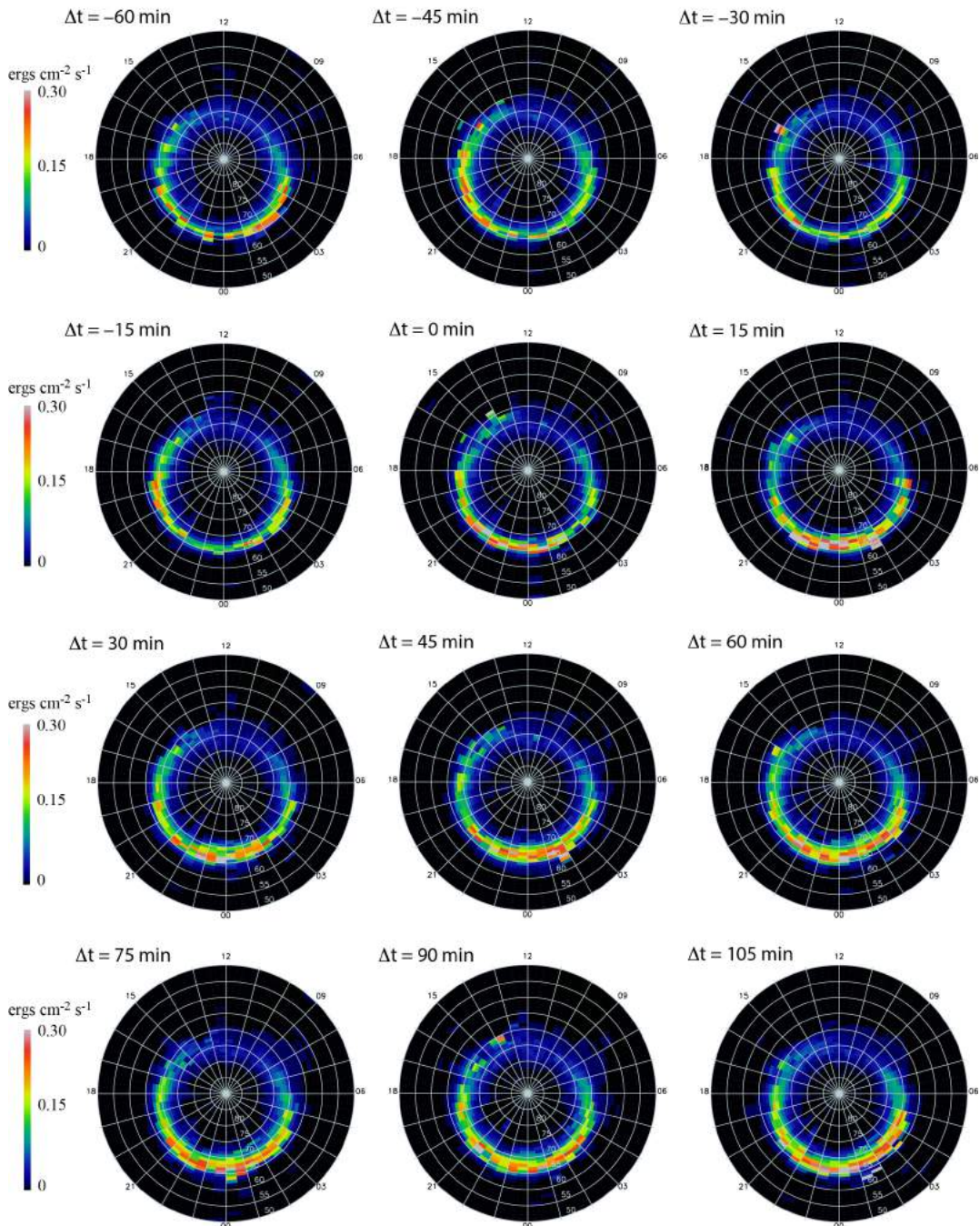


Figure 5.10. Aurora ion energy flux from 1 hr before to 1 hr and 45 min after the substorm onset in the same format as in Figure 5.7. The substorm onset occurs at $\Delta t = 0$ min.

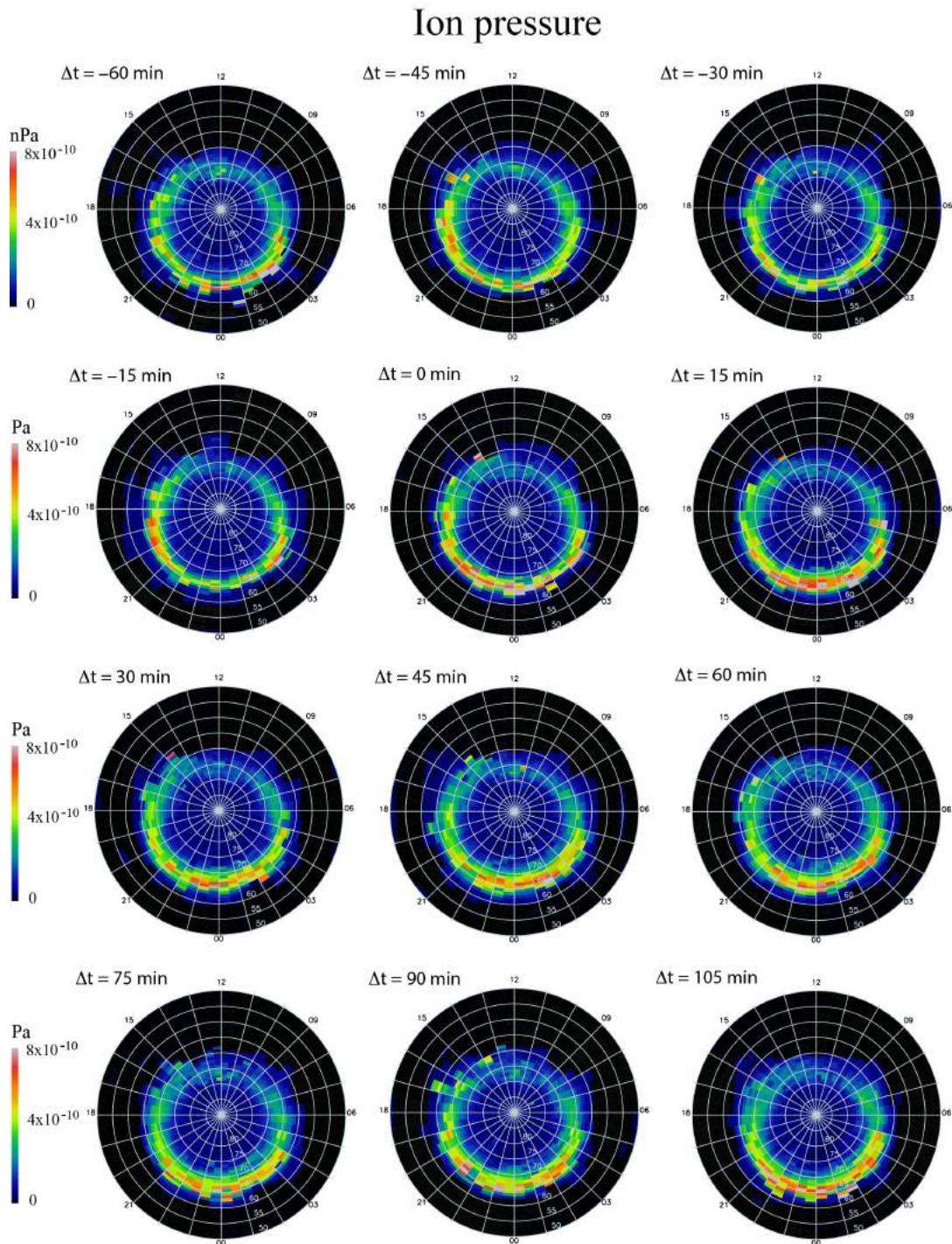


Figure 5.11. Ion pressure from 1 hr before to 1 hr and 45 min after the substorm onset. The substorm onset occurs at $\Delta t = 0$ min.

The technique used here consists of compiling electron and ion precipitation maps at 15-min cadence for 2 hr before onset and 3 hr after onset for each type of aurora. Figures 5.7–5.9 present diffuse, monoenergetic, and wave auroral electron energy flux maps and Figure 5.10 presents auroral ion energy flux map. Because of space limitation, only maps for 1 hr before onset and 1 hr and 45 min after onset are displayed. Figures 5.7–5.9 can be compared to Figures 1–3 in *Newell et al.* [2010], which show the three kinds of precipitating electron energy fluxes, but only for several min before and after substorm onset. Figure 5.7 shows that the diffuse aurora electron energy flux increases around substorm onset, consistent with the finding in *Newell et al.* [2010]. However, Figure 5.7 also shows that after onset, the energy flux continues to increase and remains at an elevated level for at least 2 hr after onset, reaching a maximum at about 1 hr after onset (the time when the maximum is reached can be determined more easily from Figure 5.12, which is discussed in Section 5.7.2). Moreover, it appears that at and after onset, the increase of the diffuse electron energy flux is confined approximately in the sector spanning 2200–0900 MLT.

Figure 5.8 shows the monoenergetic auroral electron energy flux for the same interval as in Figure 5.7. However, its characteristics are quite different from those for the diffuse aurora. The monoenergetic aurora is concentrated mainly in the dusk-midnight sector. It appears to reach a maximum at 15 min after substorm onset. The monoenergetic aurora electron energy starts increasing approximately 1 hr and 15 min before onset and increases more significantly at substorm onset. This can be more clearly seen in Figure 5.13 and discussed in Section 5.7.2.

Figure 5.9 shows the wave or broadband aurora electron energy flux from 1 hr before onset to 1 hr and 45 min after onset. The wave aurora rises after onset in the 2100–0200 MLT interval. Like the monoenergetic aurora, the wave aurora appears to wane or to start waning approximately 15 min after onset.

Figure 5.10 shows aurora ion energy flux in the same format as Figures 5.7–5.9. Apparently, ion aurora too is enhanced after onset, but most of the enhancement occurs in the sector spanning 2100–0500 MLT. The enhancement appears to continue for at least 1 hr and 45 min after onset as shown in Figure 5.10, but actually the enhancement lasts for at least 3 hr after onset (not shown). *Wing et al.* [2007] and *Wing and Johnson* [2009] show that ion pressure and density increase at postmidnight in the recovery phase. Here, the pressure profile is investigated further with a database containing an order of magnitude more

substorm events. Figure 5.11 shows the median pressure profile in the same interval as in Figures 5.7–5.10. Figure 5.11 shows that before the substorm onset, the pressure peaks in the interval 1800–2100 MLT. There is a second peak at 0200–0500 MLT. However, after the substorm onset, the pressure increases mostly in the sector 2100–0500 MLT, the same local time sector where ion aurora is energized, and persists for a long time, for at least 1 hr and 45 min in Figure 5.11 (and actually longer as shown in Figure 5.15).

5.7.2 The nightside particle precipitation powers throughout the substorm cycle

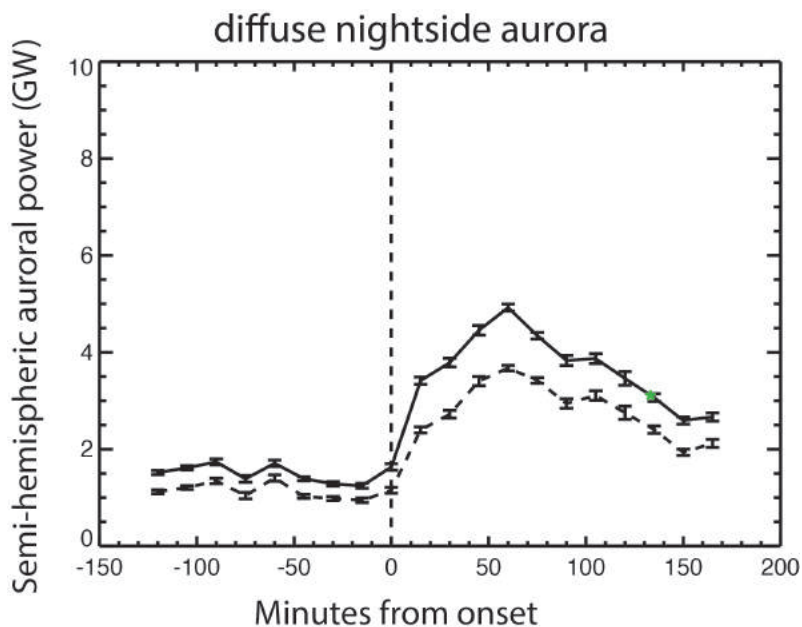


Figure 5.12. The nightside semihemispheric diffuse auroral electron power spanning the interval 2 hr before to 3 hr after substorm onset. The solid line shows the entire nightside power obtained from integrating the diffuse electron powers in all bins in 1800–0600 MLT and 50° – 90° MLat. The dashed line shows the midnight–dawn powers obtained from integrating the diffuse electron power in all bins in 0000–0600 MLT and 50° – 90° MLat. Each point in the plot is obtained from a map such as the one shown in Figure 5.7 (because of space limitation, Figure 5.7 only shows the maps for 1 hr before to 1 hr and 45 min after the substorm onset). The power increases sharply at substorm onset, reaching a maximum at approximately 1 hr after onset. The nightside diffuse electron power comes mainly from the midnight–dawn sector.

Figures 5.7–5.11 present the particle precipitation energy flux and ion pressure maps during the substorm cycle. In this Section, we examine the evolution of the nightside particle precipitation power quantitatively from 2 hr before onset to 3 hr after. Note that given our isolated substorm criterion (substorms are separated by more than 5 hr), by restricting our analysis to 2 hr before onset and 3 hr after, we avoid the situation in which the same data point is counted by two bins simultaneously, by one bin before onset and one after. For example, hypothetically, a data point that fell in the bin for 4 hr after onset could also fall in the bin for 1 hr before onset. The dayside particle precipitation powers do not change much with substorm cycle and hence are not presented.

The solid line in Figure 5.12 shows the diffuse electron auroral power for the entire nightside (hemispheric power). The procedure for calculating precipitation power is described in Section 5.6.3. Each single data point on the solid line represents the integral of diffuse electron auroral powers in all bins from 1800 to 0600 MLT, and from 50° to 90° MLat at 15-min time resolution. So, each image in Figure 5.7 contributes one point on the solid line in Figure 5.12 and the x -coordinate of the point corresponds to the center of the 15-min bin. The dashed line in Figure 5.12 plots the same thing, except it is plotted for the midnight-dawn sector, 0000–0600 MLT. This procedure is similar the one used in *Newell et al.* [2010].

In Figure 5.12, the entire nightside diffuse aurora power reaches a minimum at 15 min before onset. Then, it increases at onset and continues to increase after onset, reaching a maximum at 1 hr after onset. The nightside diffuse aurora power has a huge range during the substorm solar cycle, approximately 1.2 GW at 15 min before onset to 4.9 GW at about 1 hr after onset. Therefore, substorm-led magnetospheric reconfiguration typically increases the diffuse aurora electron power by 310%. The error bars in Figures 5.11–5.13 are derived from the standard deviation of the median, σ_{median} , where $\sigma_{\text{median}} = 1.25 \sigma_{\text{dist}}/\sqrt{n}$; σ_{dist} is the centroid 68% of the distribution, e.g., 16th–84th percentile of the distribution; and n is the number of points in the sample [e.g., *Kenney and Keeping*, 1951; *Hodges and Lehmann*, 1967]. For example, in Figure 5.12, the error bar = $(\sum \sigma_{\text{median}}^2)^{0.5}$ of all bins in 50°–90° MLat and 1800–0600 MLT.

The nightside diffuse electron aurora power is dominated by the power in the midnight-dawn sector. As can be seen from Figure 5.12, the diffuse auroral power for midnight-dawn sector (dashed line) constitutes approximately 70–80% of the power for the entire nightside (solid line).

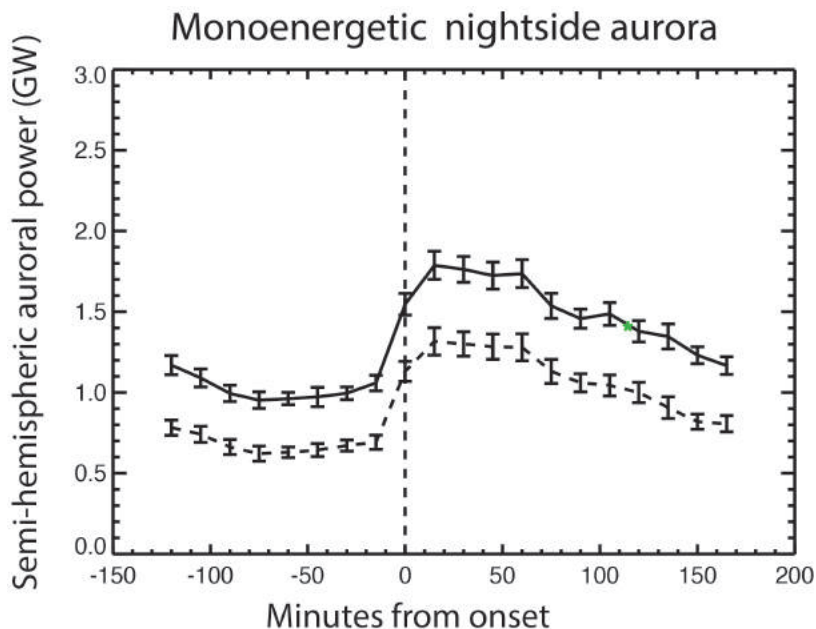


Figure 5.13. The nightside semihemispheric monoenergetic auroral electron power spanning the interval 2 hr before to 3 hr after substorm onset in the same format as in Figure 5.12. The solid line shows the power for the entire nightside obtained from integrating the monoenergetic electron powers in all bins in 1800–0600 MLT and 50°–90° MLat while the dashed line shows the dusk-midnight sector power obtained from integrating the powers in all bins 1800–2400 MLT and 50°–90° MLat. The nightside monoenergetic electron power comes mostly from the dusk-midnight sector. The power increases sharply at onset and takes approximately 3 hr to return to the level at 2 hr before onset. The power appears to start increasing approximately 1 hr and 15 min before substorm onset.

In Figure 5.13, the solid line plots the evolution of the nightside electron monoenergetic aurora power obtained by integrating from 1800 to 0600 MLT and from 50° to 90° MLat. In contrast to the diffuse aurora power, there is some indication that the monoenergetic aurora power actually starts increasing slowly at about 1 hr and 15 min before onset. The monoenergetic power increases drastically at onset. After onset, the power continues to increase, but only for a short time, reaching the maximum at 15 min after onset. The nightside monoenergetic aurora power is dominated by the power in the dusk-midnight sector, 1800–2400 MLT, which is plotted as the dashed line in Figure 5.13. From the comparison of the solid and dashed lines, it can be seen that approximately 60–75% of the monoenergetic nightside aurora power come from the dusk-midnight

sector. In other words, the power of the dusk-midnight sector is larger than that of midnight-dawn sector by approximately a factor of 1.5–3. The substorm increases the monoenergetic aurora electron power by 71% from 1.05 GW at 15 min before onset to 1.8 GW at 15 min after onset.

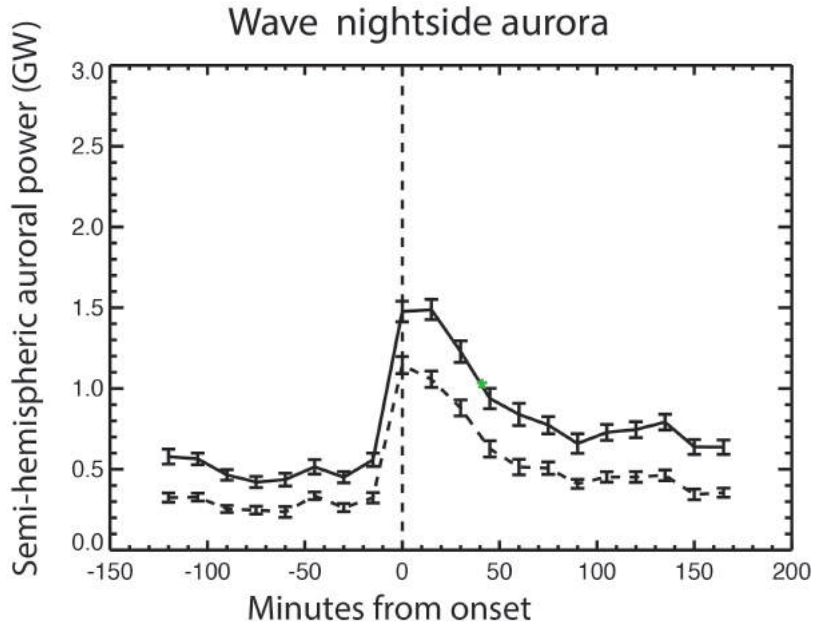


Figure 5.14. The nightside semihemispheric wave/broadband auroral electron power spanning the interval 2 hr before to 3 hr after substorm onset in the same format as in Figure 5.12. As in Figures 5.12 and 5.13, the solid line shows the power for the entire nightside obtained by integrating the wave electron powers in all bins in 1800–0600 MLT and 50°–90° MLat while the dashed line shows the power obtained by integrating all powers in all bins in 2100–0200 MLT and 50°–90° MLat. The wave electron power rises sharply at substorm onset, and reaches a maximum at 15 min after onset, but the power decreases quickly thereafter.

Figure 5.14 plots the hemispheric nightside auroral powers for broadband or wave aurora. The solid line plots the wave aurora power integrated for the entire nightside, 1800–0600 MLT, whereas the dashed line plots the power integrated from 2100 to 0200 MLT (both are also integrated from 50° to 90° MLat). Figure 5.9 shows that substorms increase the wave aurora electron energy flux mainly at 2100–0200 MLT. Comparing the two curves in Figure 5.14, we can see that the power at 2100–0200 MLT constitutes approximately 50–75% of the total nightside power. Apparently, substorms increase the integrated power from 0.56

GW at 15 min before onset to 1.5 GW at 15 min after onset, which represents a 170% increase. Similar to monoenergetic aurora, the wave aurora peaks at 15 min after onset.

Figure 5.15 plots the median ion pressure for the entire nightside from 2 hr before onset to 3 hr after. At each 15-min time step, the median of all the bins in 50° – 90° MLat and 1800–0600 MLT is calculated. The error bar is σ_{median} . The median is much lower than the average ion pressure in the aurora oval because the median covers the region outside of the auroral oval where the pressures are lower than those within auroral oval (see Figure 5.11.) Figure 5.15 shows that the pressure increases after the substorm onset and remains elevated for at least 3 hr after onset relative to the value at 15 min before onset. The substorms increase the ion pressure by 30%, from 1×10^{-10} nPa at 15 min before onset to 1.3×10^{-10} nPa at 15 min after onset. The ion aurora power variation is not shown, but its variation follows roughly the same pattern as the ion pressure variation.

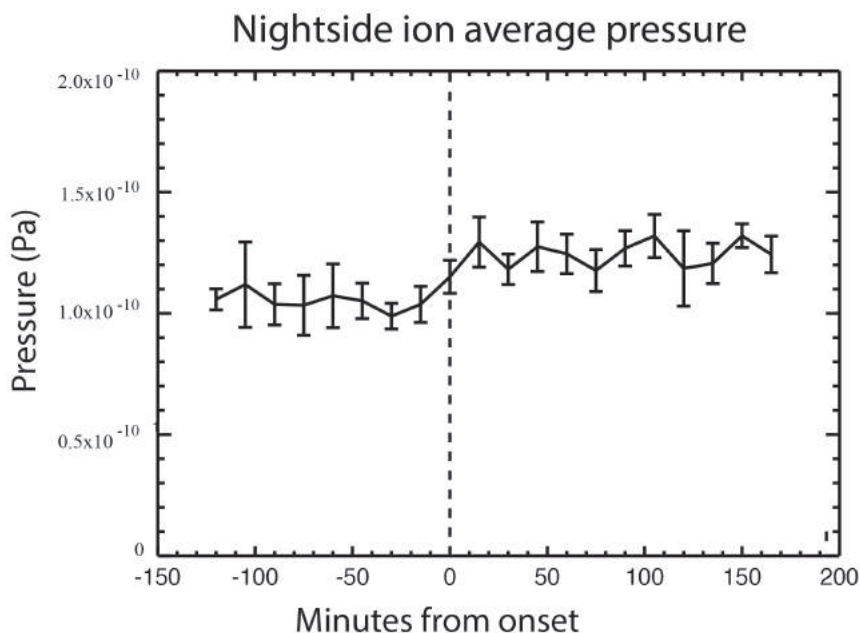


Figure 5.15. The nightside median ion pressure in the sector 1800–0600 MLT and 50° – 90° MLat. The pressure increases after substorm onset and remains elevated (relative to the value at 15 min before onset) for at least 3 hr. Note the pressure is low because the median is obtained from a wide latitudinal region, including the region outside the auroral oval where pressure is lower than that within the auroral oval.

	total substorm cycle	growth phase	expansion phase	recovery phase	Δt at half max
diffuse electrons	> 5hr	?	1 hr	>4 hr?	~1.2 hr
broadband electrons	~ 5 hr	1.25 hr	0.25 hr	~3.50 hr	~0.42 hr
monoenergetic electrons	~ 5 hr	1.25 hr	0.25 hr	~3.50 hr	~1.6 hr

Table 5.1. Summary of the time scales of the substorm cycles and phases from electron precipitation perspective. The growth and recovery phases for the diffuse electrons are hard to determine (see text). Δt at half max denotes the time it takes to reach half maximum from the maximum auroral power at end of the expansion phase, which gives a measure of how quickly the auroral power decays after reaching the maximum value.

The monoenergetic and wave electron powers complete or nearly complete the entire substorm cycle within the 5-hr interval examined, 2 hr before onset to 3 hr after onset. That is, 3 hr after onset, the powers finally reach roughly the values as those at 2 hr before onset. On the other hand, the diffuse electron aurora and ion aurora powers appear to require more than 5 hr to complete the cycle. Table 5.1 summarizes the time scales for the substorm cycles and phases for the three types of electrons.

The approach of quantifying the substorm effect on aurora powers is different in the present study from that of *Newell et al.* [2010] in three significant ways. First, they calculated the mean energy fluxes, instead of the median. Second, they calculated aurora powers at 2-min resolution, which shows high fluctuations perhaps due to small sampling sizes. Then, they compared the averaged powers 0–2 hr before onset to those at 0–2 hr after onset. As shown in Figures 5.12–5.14, the aurora powers do not vary as a step function, before and after onset, but rather they vary continuously throughout the substorm cycle, although they significantly increase around the substorm onset. Finally, not all substorms in the *Newell et al.* [2010] study are isolated substorms. In fact, 66% of their substorms are separated by less than 5 hr. As a result, in the *Newell et al.* [2010] study, the same data point could be counted by a bin before onset and another bin after onset. The present study avoids this ambiguity by restricting the analysis to the interval 2 hr before onset to 3 hr after.

5.7.3 The electron auroral dawn-dusk asymmetry

Previous sections present and discuss the electron energy fluxes for all three types of electron aurorae. The dawn-dusk asymmetries in diffuse and monoenergetic electron aurorae can be seen prominently in the electron energy fluxes in Figures 5.7, 5.8, and 5.9. In this section, we examine more quantitatively the dawn-dusk asymmetries and how these asymmetries are modulated by substorms.

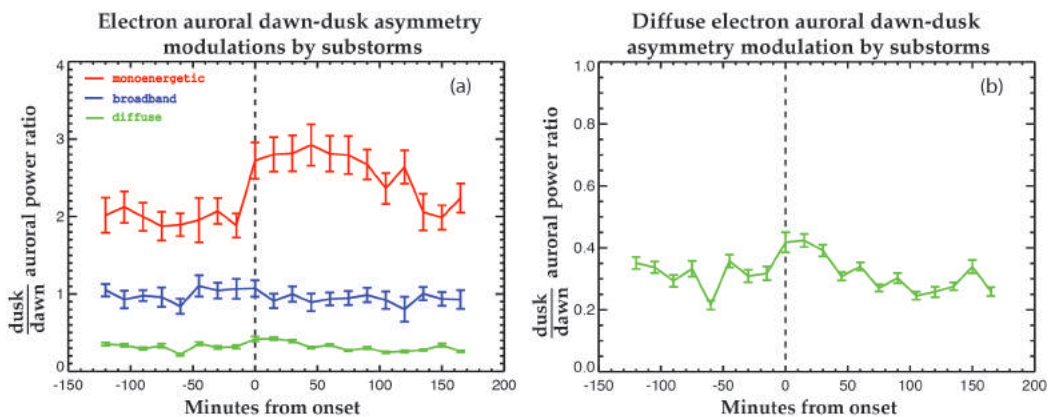


Figure 5.16. Electron auroral power dawn-dusk asymmetries modulations by substorms. (a) the ratio of dusk (2400–0600 MLT) to dawn (1800–2400 MLT) auroral power for monoenergetic (red), broadband (blue), and diffuse (green) electrons. The monoenergetic electron auroral power is larger at dusk than at dawn and this asymmetry increases after substorm onset. The asymmetry does not get back to its growth phase value until ~ 135 min after onset. In contrast, broadband electron auroral power does not show much dawn-dusk asymmetry. The diffuse electron auroral power has the opposite asymmetry from that of monoenergetic electron auroral power (the ratio < 1). At 0–30 min after substorm onset, the diffuse electron auroral power dawn-dusk asymmetry decreases a bit. This can be seen more clearly in (b), which plots the same dusk/dawn auroral power ratio as in (a), except that the scale of the y -axis is smaller.

Figure 5.16a plots the ratio of dusk (2400–0600 MLT) to dawn (1800–2400 MLT) auroral power for monoenergetic (red), broadband (blue), and diffuse (green) electrons. The monoenergetic electron auroral power is larger at dusk than at dawn and this asymmetry, as measured by the dusk/dawn power ratio, increases after substorm onset. The asymmetry does not return to its growth phase value until ~ 135 min after onset. The increase of the asymmetry after the substorm onset may be related to the increase of Alfvén wave activities at premidnight after

onset as discussed in Section 5.9.4.

The broadband electron auroral power does not show significant dawn-dusk asymmetry. This can be seen by the dusk/dawn power ratio (blue line) that hovers around one in Figure 5.16a.

The diffuse electron auroral power has the opposite asymmetry from that of monoenergetic electron auroral power with the power at dawn larger than that at dusk (the dusk/dawn power ratio < 1). At 0–30 min after substorm onset, the dusk/dawn power ratio increases a bit, suggesting a smaller dawn-dusk asymmetry. This asymmetry can be seen more clearly in Figure 5.16b. The smaller dawn-dusk asymmetry after onset may be attributed to the plasma sheet electron injection and energization that occurs over a wide local time after onset, including at premidnight. The dusk/dawn power ratio minimum at –45 min before onset may be due to the interference from the long recovery phase of the preceding substorm (> 4 hr).

5.8 Comparisons of DMSP observations and RCM simulation

As shown in Figures 5.7 and 5.10, there are clear MLT variations in both electron and ion diffuse aurora precipitation. To investigate what processes can contribute to these MLT variations, *Gkioulidou et al.* [2012] evaluated the role of MLT-dependent electron precipitation rate by comparing the DMSP electron diffuse aurora precipitation with that from simulations of the Rice Convection Model (RCM) [*Toffoletto et al.*, 2003] combined with a Dungey force-balanced magnetic field solver (hereafter referred to as RCM–Dungey) [*Gkioulidou et al.*, 2011]. Here, we compare the DMSP ion aurora precipitation with the one obtained from the RCM–Dungey simulations with a fixed ion precipitation rate to evaluate whether the observed MLT variation can be accounted for by ion magnetic drift alone.

5.8.1 The RCM–Dungey simulation

The RCM–Dungey calculates the bounce-averaged electric and magnetic drift of ions and electrons assuming isotropic distributions along the magnetic field lines and slow flow approximation, within self-consistently computed electric and magnetic fields. The combined model maintains force-balance in the equatorial

plane. The auroral height-integrated Pedersen and Hall conductivities are estimated by the electron precipitation from the simulated plasma distributions, using the *Robinson et al.* [1987] empirical formula.

Gkioulidou et al. [2012] conducted substorm growth phase simulations using RCM-Dungey with different electron precipitation rates and evaluated these precipitation rates by comparing the simulated precipitating electron energy fluxes with DMSP diffuse aurora electron precipitation. More specifically, they conducted simulations using six different scattering rates, which can be divided into two groups. The first group assumes the strong diffusion loss rate everywhere and 2/3 and 1/3 of that rate, whereas the second group assumes the MLT-dependent loss rate, based on wave activity, established by *Chen and Schulz* [2001] (hereafter referred as the Chen rate) and 2/3, and 1/3 of that rate. The magnitude and spatial distribution of waves vary with geomagnetic activity, but the Chen rate does not include this variability. The decisions to use the particular fractions chosen for both rates were motivated by the study of *Schumaker et al.*, [1989], where data from near-geosynchronous SCATHA satellite in conjunction with polar-orbiting P78-1 revealed that the average lifetimes of plasma sheet electrons exceed those for the case of isotropy by a factor between 2 and 3 for $Kp \leq 2$ (between 1/2 and 1/3 of strong diffusion loss rate), and 1.5 for $Kp > 2$ (2/3 of strong diffusion loss rate).

The location of the RCM-Dungey outer boundary is specified as a $15-R_E$ circle centered at $x = -5 R_E$ and $y = 0$ in the equatorial plane, and reaches $x = -20 R_E$ at midnight and $|y| = 15 R_E$ (on the dawn and dusk sides). The latitudes in the ionosphere that map to the outer boundary vary as the magnetic field changes. The inner boundary is at $r \sim 2 R_E$. Along the outer boundary, the proton and electron distributions at different MLT are established from a fitting of two-component Kappa distributions to statistical results of substorm growth phase periods observed by Geotail and THEMIS from 1996 to 2010. Substorm onsets were obtained from the list of *Hsu and McPherron* [2012] that is based on an appropriate change of AL. The data have been sorted into three time-ranges 120–60, 60–30, and 30–0 min before the substorm onset. Only isolated substorms, i.e., those that occurred at least 3 hr after the previous substorm, were used. For initial plasma conditions, we use plasma distributions obtained from our previous RCM run [*Wang et al.*, 2011], where we started with an empty magnetosphere and plasma from the tail boundary moved into the inner magnetosphere under many hours of enhanced convection. The boundary conditions and temporal variations of

the polar cap potential drop of that previous run are shown in Figure 5 of *Wang et al.* [2011]. In this simulation, we first ran simulations with constant cross polar-cap potential drop ($\Delta\Phi_{PC}$) of 40 kV for 5 simulation hours and then gradually increased $\Delta\Phi_{PC}$ to 60 kV over 2 hr ($t = 5-7$ hr). The magnetic field was updated every 10 min to maintain force balance with the RCM pressures. For more details on the simulation setup and the electron precipitation rates see *Gkioulidou et al.* [2012].

The investigation above showed that the simulation using a more realistic, MLT-dependent Chen rate produces electron precipitating energy flux profiles that agree better with the DMSP electron energy fluxes in their MLT distributions, compared with simulations using maximum precipitation rate against strong diffusion everywhere. In fact, using 1/3 of the Chen rate resulted in the closest agreement between observed and simulated precipitating electron energy fluxes. Similarly, in this paper, by comparing the simulated precipitating ion energy fluxes with the observed ones from DMSP, we could determine whether the drift physics alone can account for the azimuthal distribution of the ion aurora, and also, whether assuming that ions undergo strong diffusion everywhere is a realistic approximation.

Electron precipitation into the ionosphere affects the ionospheric conductance, which, in turn, affects the convection electric field and, as a result, the penetration of the ion plasma sheet into the inner magnetosphere. Therefore, because *Gkioulidou et al.* [2012] have established that using 1/3 of the Chen electron scattering rate resulted in precipitating electron energy fluxes that were the closest to the observed ones from DMSP, in this paper we compare the DMSP ion precipitation with the simulated ion precipitation using 1/3 of the Chen electron scattering rate.

One of the main mechanisms to cause ion pitch-angle scattering in the plasma sheet is the current sheet scattering [e.g., *Speiser*, 1965; *Lyons and Speiser*, 1982; *Sergeev et al.*, 1983; 1993]. Ions with gyroradius comparable to or larger than the magnetic field curvature radius undergo pitch-angle scattering due to violation of the first adiabatic invariant $\mu = E_{\perp}/B$. More specifically, this nonadiabatic scattering of the energetic ions happens whenever they encounter the equatorial current sheet along their orbit, and provides rapid filling of the loss cone. Higher-energy ions are more likely to be scattered to the loss cone than the lower energy ones. The scattering is also expected to weaken with decreasing radial distance and from the nightside to dayside as the magnetic field lines become less stretched. Another important scattering mechanism is through interaction with

electromagnetic ion cyclotron (EMIC) waves [e.g., *Jordanova et al.*, 2001]. Therefore, the ion precipitation rate can vary with ion energy and location. However, unlike the location- and energy-dependent Chen rate we used for electron precipitation in the simulation, no such ion precipitation rate has yet been established to be incorporated into our simulation. Thus, as mentioned above, we simply assumed that ions of all energies are under strong pitch-angle diffusion everywhere, that is, the maximum precipitation rate for ions. This assumption is valid for the tail plasma sheet, where the ion distribution is approximately isotropic [e.g., *Stiles et al.*, 1978; *Wing and Newell*, 1998; *Wing et al.*, 2005], but becomes less appropriate in the inner magnetosphere (inside $\sim 10 R_E$), where the distributions can become highly anisotropic. Nevertheless, using a fixed ion precipitation rate allows us to evaluate whether magnetic drift alone can account for the MLT variations in the DMSP precipitation.

5.8.2 RCM precipitating ion energy flux

RCM-Dungey and DMSP ion energy flux near the end of the growth phase

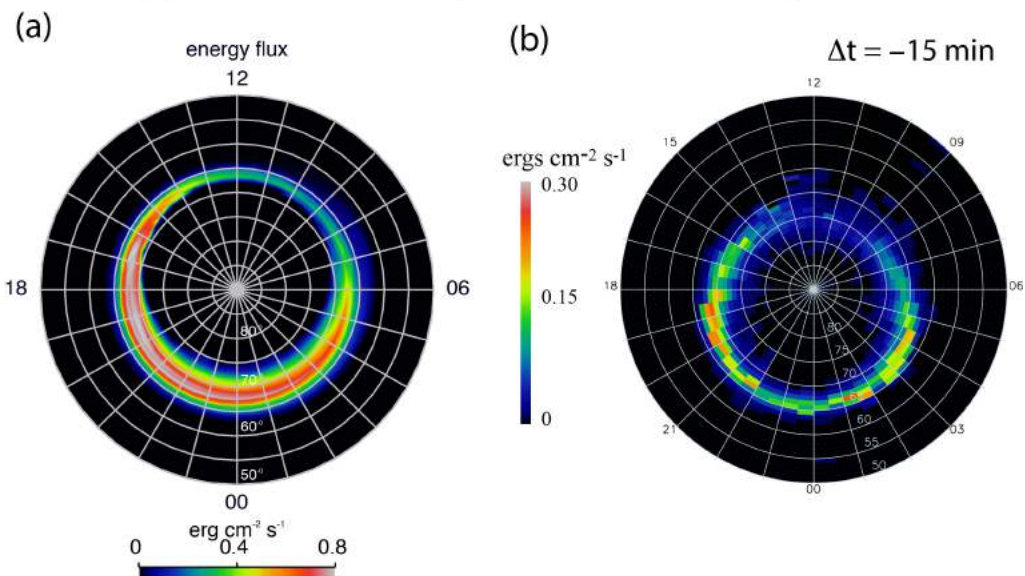


Figure 5.17. The precipitating ion energy flux near the end of the growth phase for (a) RCM-Dungey model and (b) DMSP observations. The RCM-Dungey ion energy flux is taken after running the simulation for 6 hr and 45 min, whereas the DMSP observation is for 15 min before substorm onset (taken from Figure 5.12). Note that the two color bars have different scales.

Figure 5.17 shows the simulated ion precipitating energy fluxes at 6 hr and 45 min of our run and the observed DMSP ion aurora precipitation 15 min before the onset (also shown in Figure 5.10). The RCM simulation shows that the precipitating energy flux maximizes in the dusk–midnight sector. This can be attributed to more energetic ions magnetic drifting toward dusk. DMSP observations also show a peak around 1800–2000 MLT. However, the simulated magnitudes are a factor of ~ 2 larger compared with the observed ones (please note the different color bars). This indicates that the assumed maximum ion precipitation rate overestimates the real precipitation rate.

On the other hand, DMSP observations show a second peak around 0200–0500 MLT, which is not seen in the RCM–Dungey simulation. The pressure map also shows a second peak at the same location as can be seen in Figure 5.11. These ion pressure and energy flux maxima can be attributed to a peak in the ion number flux (not shown). The pressure peak around 0200–0500 MLT in the plasma sheet has been previously observed and attributed to a density peak during active times [e.g., Korth *et al.*, 1999; Wing and Newell, 1998] and during growth phase [Wing *et al.*, 2007; Wing and Johnson, 2009]. The present study obtains the same result with a larger database than the Wing *et al.* [2007] and Wing and Johnson [2009] studies. The dawn density enhancement during high magnetic activity may result from the cold solar wind ion entry on the dawn flank and flow stagnation when enhanced $\mathbf{E} \times \mathbf{B}$ and corotation are nearly cancelled by the curvature and gradient drifts [e.g., Friedel *et al.*, 2001]. Another possible mechanism also presumes solar wind ion entry along the dawn flank, but additionally, an enhanced $\mathbf{E} \times \mathbf{B}$ pushing the solar wind origin ions closer to Earth where the flux tube volume is smaller and hence ions have higher density [Wang *et al.*, 2003]. Because the maximum ion precipitation rate is used in this simulation, it is also not clear whether the relative weaker precipitation near midnight seen in observation can be a result of MLT variation in the ion precipitation rate. Figure 5.10 shows that the dawn peak persists after onset. This may be associated with substorm injection and flow stagnation. However, RCM does not include substorm injection physics and hence even if RCM had stagnation point, it might not show energy flux peak near dawn.

In conclusion, our comparison of the MLT distributions in DMSP ion precipitating energy fluxes with a simulation taking into account drift physics reveal that the duskward magnetic drift of the more energetic ions can account for one of the two precipitation peaks, the one toward dusk. However, the simulation

cannot account for the second peak, the one toward dawn, probably because of a lack of substorm injection physics or other physical processes. In addition, a more realistic ion precipitation rate should be included in a future simulation to evaluate the combined effect of magnetic drift and precipitation rate.

5.9 Discussion and summary

5.9.1 Summary of key observations

Substorms change the magnetospheric configuration, e.g., when the magnetic field lines change from stretched tail-like to more dipolar configurations. During this process, a huge amount of energy is released, some of which energizes precipitating particles. On the nightside, ion and all three types of electron (diffuse, monoenergetic, and wave) energy fluxes and powers increase at or shortly after substorm onset. However, the energy increases differ for each type of aurora. The increases are 71%, 170%, and 310% for the monoenergetic, wave, and diffuse electron aurora powers, respectively. In contrast, the ion pressure increases only by 30%. Among the electron aurorae, the wave aurora has the smallest power, followed by the monoenergetic aurora, whereas the diffuse aurora has the largest power. The ion aurora power and energy flux are comparable to those of the wave electron aurora during the growth phase, but after the onset the wave electron aurora power and energy fluxes increase much more than those of the ion aurora. Substorms appear to energize ion aurora less than electron aurora of any kind.

The MLT distribution of each type of aurora also differs. The diffuse electron aurora can be observed mainly in 2200–0900 MLT. However, the monoenergetic electron aurora power comes mainly from the dusk-midnight sector, whereas the wave aurora power comes mainly from the region centered at premidnight, spanning roughly 2100 to 0200 MLT. Near the end of the growth phase, i.e., $\Delta t = -30$ to -15 min, the ion energy flux and pressure peak at 1800–2100 MLT sector, which can be attributed to the ion curvature and gradient westward drifts toward dusk. There is also a second peak at 0200–0500 MLT in both ion energy flux and pressure maps, which can be attributed to cold solar wind ion entry along the dawn flank, flow stagnation, and enhanced $\mathbf{E} \times \mathbf{B}$ as discussed in Section 5.8.2. After substorm onset, the ion pressure and energy flux in the 2100–0500 MLT sector increase and persist at an elevated level for a long time. These increases can be associated with the increase in the ion number flux (not

shown). This is consistent with *Wing et al.* [2007] and *Wing and Johnson* [2009], which show that the postmidnight pressure and density increase in the recovery phase.

The rest of this section examines the substorm cycle, diffuse, wave and monoenergetic electron aurorae.

5.9.2 Electron and ion aurora substorm cycles

It is hard to determine when the growth phase begins in the particle precipitation. In the present study, the growth phase onset can be defined as the time when the power is at minimum before the substorm onset. Using this definition, the monoenergetic and wave electron aurora growth phases start at approximately 1 hr and 15 min before onset. The growth phase signature for the diffuse electron aurora is not so clear. The minimum at 15 min before onset in the diffuse aurora power in Figure 5.12 is not likely the start of the growth phase. All types of electron and ion aurorae increase substantially at the substorm onset. So, the growth phase ends roughly at the same time for all electron and ion aurorae. In other words, the substorm onsets obtained from optical observations seem to agree with those obtained from the particle precipitation. The 1 hr and 15 min duration of the growth phase for the monoenergetic and wave electron aurorae is at the upper end of the range of the growth phase obtained from ground magnetic field observations [e.g., *Bargatze et al.*, 1999; *Huang et al.*, 2003].

The end of the expansion phase can be defined as the time when the maximum power is reached. The diffuse aurora expansion phase duration is longer than that of the other two electron aurorae. The duration of the expansion phase of the diffuse aurora is 1 hr, whereas that of the monoenergetic and wave aurorae is only about 15 min. It is interesting to note that the recovery phase onset for the electron diffuse aurora, ~1 hr after substorm onset, is comparable to the start of the plasma sheet recovery reported in *Baker et al.* [1994]. They reported that plasma sheet recoveries, e.g., expansion of plasma sheet, reduction of cross-tail current, etc., can occur at 10–120 min after substorm onset with a median delay of 45 min. Their substorm onsets were determined from the ground magnetic field observations. The short expansion phase duration in the electron wave aurora may result from the quick damping of the waves as discussed in Section 5.9.4.

It is a challenge to determine the end of the recovery phase, primarily

because it is hard to determine when the quiet time state is reached and what the quiet time power ought to be. The quiet time power may be defined as the minimum power reached at the start of the growth phase. In Figures 5.12–5.14, it can be seen that the diffuse aurora power decreases at 1–3 hr after onset, whereas the monoenergetic and wave aurora powers decrease in the interval 15 min–3 hr after onset. This would suggest that the recovery phase durations are at least 2 hr for the diffuse aurora and 2 hr and 45 min for the monoenergetic, and wave electron aurorae.

For the wave and monoenergetic electron aurorae, the powers at 3 hr after onset are approximately the same as those at 2 hr before onset. The declining power in the interval 2–1 hr before the substorm onset in the wave and monoenergetic electron aurorae may suggest that some of the points in this interval come from the recovery phase of the preceding substorm. Assuming that (1) the minimum power before the substorm onset is the baseline for the quiet time power and (2) many points in the interval 2–1 hr before onset could also be in the interval 3–4 hr after onset, given our criterion for isolated substorms and so the durations of the monoenergetic and wave electron aurora recovery phases can be estimated to be 3 hr and 45 min or ~ 4 hr. It is harder to determine the recovery time for the diffuse electron aurora. In the period 2–0 hr before onset, the diffuse electron aurora power generally declines. Perhaps, some or many of the points in this interval may actually come from the recovery phase of the preceding substorm. This result may suggest that the recovery phase duration for the diffuse electron aurora could be more than 4 hr, but in order to get a better estimate, one would have to use substorms that are separated by more than 7 or 8 hr. It would not be possible to use such separations in the present dataset without severely degrading the statistics.

The recovery durations of all three types of the electron precipitation are larger than the 0.5–2 hr recovery duration obtained from the ground magnetic field observations [e.g., *Bargatze et al.*, 1999; *McPherron et al.*, 1986; *Baker et al.*, 1981; *Huang et al.*, 2003; *Horwitz*, 1985]. *Pulkkinen et al.* [1994] reported that the recovery period of the geosynchronous magnetic field and energetic particle observations is on the order of 1–3 hr. They attributed the long recovery of the near-Earth magnetic field to the effect of the developing ring current. However, it is not clear whether this can explain the long recovery period of the precipitating electrons, some of which map farther out than geosynchronous orbit.

The duration of the substorm cycle has been reported to be approximately

2–3 hr [e.g., *Huang et al.*, 2003] or 4 hr [e.g., *Tanskanen et al.*, 2002] based on substorm onsets determined by the ground magnetic field observations or indices derived from these observations such as AE, AL or IL. However, monoenergetic and wave electron aurora powers complete the entire substorm cycle within the 5-hr interval examined. That is, 3 hr after onset, the aurora powers finally reach roughly the values at 2 hr before onset. The diffuse electron aurora cycle is more than 5 hr. So, the durations of the substorm cycle in all electron aurorae appear larger than or at the upper end of the range of those obtained from ground magnetic field observations. These long durations can be attributed mostly to the longer durations of the recovery phases in the three types of electron aurorae.

It is interesting to note that wave and monoenergetic electron aurora powers have similar substorm cycle dynamics, i.e., phases' durations, which differ from those of the electron diffuse aurora power. This is discussed further in Section 5.9.4.

The substorm energizes the precipitating ions less than the precipitating electrons. Perhaps, partly because of this, it is harder to ascertain the ion pressure cycle. The ion pressure increases only by a relatively small amount after onset, but it seems to persist at the elevated level (relative to the value 15 min before onset) for a long time. There is no clear indication that the power declines within 3 hr after the substorm onset.

5.9.3 Diffuse electron aurora

As shown in Figure 5.7, the diffuse electron aurora can be observed mainly in 2200–0900 MLT. The diffuse electrons are the magnetospheric field-aligned electrons that precipitate into the ionosphere. As the plasma sheet electrons $\mathbf{E} \times \mathbf{B}$ convect earthward, they also curvature and gradient drift eastward toward dawn. The field-aligned component of these electrons are quickly lost through the loss cone, but they are replenished by pitch-angle scattering. A leading mechanism for pitch-angle scattering is VLF whistler-mode chorus wave–electron interactions [e.g., *Thorne*, 2010; *Reeves et al.*, 2009; *Summers et al.*, 1998]. Studies have shown that whistler-mode chorus waves are excited in the region spanning premidnight to noon, which includes the region where the diffuse electrons are observed, at 2200–0900 MLT. Apparently, around 0900 MLT the diffuse electron flux decreases, which may suggest that the whistler-mode chorus waves start weakening. In the magnetosphere, the electrons continue to drift eastward,

circling the earth, but they are only observed in the ionosphere when and where there are whistler-mode chorus waves to pitch-angle scatter them. The diffuse electron aurora is discussed further in the companion paper [Gkioulidou *et al.*, 2012].

5.9.4 Broadband (wave) electron aurora

As mentioned above, substorms appear to energize wave electron aurora the most, relative to its value prior to onset. Wave aurora is characterized by precipitating electrons having a broad energy spectrum. Such precipitation is thought to result from electron interaction with dispersive Alfvén waves [Chaston *et al.*, 2002, 2003, 2008]. Typical Poynting fluxes in Alfvén waves at high-latitude have been shown sufficient to account for 30-35% of auroral luminosity [Wygant *et al.*, 2002; Keiling *et al.*, 2002]. The survey of Chaston *et al.* [2007] found that up to 40% of the total electron energy deposited in the ionosphere is associated with dispersive Alfvén waves, and that an even larger fraction of energy deposition peaks in the premidnight region where substorms are most common.

Lessard *et al.* [2006] noted a connection between dipolarization events observed in the magnetotail and dispersive Alfvén waves observed above the ionosphere, which are associated with the broadband electron precipitation. Observations of Pi1B (irregular bursty pulsations with periods from 1 to 40 sec) were detected by GOES 9, FAST, and at the ground in conjunction with a substorm. While GOES detected compressional magnetic field fluctuations along with dipolarization at geosynchronous orbit, FAST (which was conjugate to GOES) detected shear Alfvén waves as a broad band ELF wave spectrum. The ratio of $\delta E/\delta B$ for the waves was consistent with Doppler-shifted dispersive Alfvén waves that have been reported [Stasiewicz *et al.*, 2000; Chaston *et al.*, 2008], suggesting that compressional waves mode convert to dispersive shear Alfvén waves in this region. These same waves were also observed by ground-based magnetometers on conjugate field lines.

Because transfer of energy by Alfvén waves is most efficient when the perpendicular wavelength is small [Hasegawa, 1976; Lysak and Song, 2003; Damiano *et al.*, 2007], it is additionally necessary that there be cascade of energy from large scales to small scales [Chaston *et al.*, 2008]. Cross-scale coupling may result from linear phase mixing in inhomogeneity [Lysak and Song, 2011], nonlinear wave-wave cascade [Schekochihin *et al.*, 2009 and references therein] or

by nonlinear wave-particle interactions [*Damiano and Johnson, 2012*].

Electrons with broadband energy distribution are consistent with acceleration in a time-varying parallel electric field [*Chaston et al., 2002*] that is associated with small-scale dispersive Alfvén waves. Electrons can be resonantly trapped in the wave potential of an Alfvén wave pulse [*Kletzing, 1994*] typically leading to the development of a velocity-dispersed beam in front of the pulse [*Watt et al., 2005*]. At lower altitude, the electrons escape the potential well and precipitate into the ionosphere as an energy-dispersed population [*Watt and Rankin, 2009*].

In the transient response models [e.g., *Nishida, 1979; Kan et al., 1982; Hull et al., 2010*], the magnetospheric reconfiguration and diversion of the cross-tail currents by the current wedge are communicated to the ionosphere by Alfvén waves. The wave aurora that results from the initial substorm pulse may be expected to last a few Alfvén bounce periods because Alfvén waves damp kinetically on electrons absorbing most of the wave energy after a few reflections via wave-particle interactions [*Lysak and Song, 2003; Damiano and Johnson, 2012*] and/or Joule dissipation in the ionosphere [*Hull et al., 2010*]. Wave aurora power peaks following onset and remains elevated for about 15 minutes, consistent with the decay time of Alfvén waves. Figure 5.14 shows that after the rapid decay of the main Alfvén waves in the interval 15–45 min after onset, there seems to be residual Alfvén waves that slowly decay starting at approximately 45 min after onset.

Figures 5.12–5.14 suggest that wave and monoenergetic electron aurora powers have similar substorm cycle dynamics, i.e., phases' durations, which differ from those of the electron diffuse aurora power. There may be a link between wave and monoenergetic electrons. For example, recently, *Hull et al. [2010]* suggested that Alfvén waves can lead to the formation of density cavities and quasi-static parallel electric fields. However, Figures 5.8 and 5.9 show that monoenergetic and wave electrons are not always observed in the same region. They seem to overlap roughly in the region spanning 2100–0100 MLT. Westward of the overlapping region, e.g., $MLT < 2100$, monoenergetic electrons can be observed without significant wave electrons. Conversely, eastward of the overlapping region, e.g., $MLT > 0100$, wave electrons can be observed without significant monoenergetic electrons.

5.9.5 Monoenergetic electron aurora

The ion and diffuse electron aurora powers and energy fluxes do not significantly increase until 0–15 min before substorm onset. However, the monoenergetic and wave electron aurora powers and energy fluxes start increasing approximately 1 hr and 15 min before onset as shown in Figures 5.13 and 5.14. This suggests that any substorm prediction algorithm may do better examining the monoenergetic and wave electron aurorae than diffuse aurora.

The increase of monoenergetic electron aurora about 1 hr and 15 min prior to onset is suggestive of a correlation between monoenergetic electron precipitation and the growth phase magnetic field configuration. As the tail stretches during the growth phase, field-aligned currents intensify [McPherron, 1972; Watanabe and Iijima, 1993; Wing and Sibeck, 1997; Tsyganenko and Sibeck, 1994; Tsyganenko *et al.*, 1993; Zanetti and Potemra, 1986]. In the upward field-aligned current region, the current-voltage relationship implies that the parallel potential drop would increase in order to maintain higher currents by drawing more electrons downward. Hence, an increase in the monoenergetic electron aurora may simply be an indicator of elongation of the tail that occurs during the growth phase. Figure 5.8 shows that the monoenergetic electrons can be observed mainly in the dusk-midnight sector. This would be consistent with the increase in the upward region-1 field-aligned current (R1) in the dusk-midnight sector during the growth phase. In the midnight-dawn sector, R1 may also increase, but here R1 is downward and so fewer monoenergetic electrons would be expected. Region-2 field-aligned current (R2) at the midnight-dawn sector also flows upward, but few monoenergetic electrons are observed at this location. This may result from the higher electron density on the dawnside than on the duskside magnetosphere due to the eastward curvature and gradient drifts of the electrons.

Another possibility for the increase in monoenergetic precipitation is the development of low-frequency waves that accelerate electrons, but do not lead to global instability. One such possibility is the kinetic-ballooning/interchange mode discussed by Pritchett and Coroniti [2010], which operates in a stretched-tail configuration with a minimum in B_z . These modes are thought to be associated with interchange heads, which generate auroral streamers and contribute to the monoenergetic electron precipitation. Many studies have shown that an auroral streamer is a fast flow signature in the ionosphere [e.g., Nakamura *et al.*, 2001; Sergeev *et al.*, 2004]. Fast flows have been attributed to reconnection leading to flux tubes having depleted total entropy (S), which initiate unstable growth of

ballooning and interchange instabilities resulting in earthward propagation of flux tubes [e.g., *Birn et al.*, 2009; 2011; *McPherron et al.*, 2011; *Wing and Johnson*, 2009; 2010; *Wolf et al.*, 2009]. Fast flows have also been attributed to current disruption leading to field-line collapse [*Lui*, 1994; *Wolf et al.*, 2009]. *Baumjohann et al.* [1999] showed that earthward fast flow occurrence rate increases sharply about 15 min before substorm onset, consistent with the sharp increase of the nightside monoenergetic aurora power at 15 min before onset in Figure 5.13.

Fast flows are also observed following substorm onset, in the expansion and even recovery phases. For example, *Baumjohann et al.*, [1999] showed that the earthward fast flow occurrence rate peaks between 0 and 60 min after onset depending on the GSM x location of the fast flow. The superposition of these peaks may give the broad peak in the monoenergetic aurora power seen in the interval 15–60 min after onset in Figure 5.13. These fast flows can launch low frequency global Alfvén waves that are associated with monoenergetic precipitation [*Damiano and Johnson*, 2012]. Regardless of how they are formed, fast flows have been observed more frequently in the dusk-midnight than the midnight-dawn sector in the tail [e.g., *McPherron et al.*, 2011]. This dawn-dusk asymmetry has also been seen in RCM-Equilibrium (RCM-E) simulation and has been attributed to the ion westward curvature and gradient drifts [e.g., *Zhang et al.*, 2008]. We will investigate the possible links of monoenergetic electrons to fast flows and magnetic field stretching in our future studies.

5.9.6 Is there any link between broadband and monoenergetic electrons?

As shown in Table 5.1 and Figures 5.13 and 5.14, the substorm dynamics of broadband and monoenergetic electrons are more similar to each other than to those of diffuse electrons. For example, both broadband and monoenergetic electron powers peak 15 min after onset whereas diffuse electron power peaks 1 hr after onset. There may be a link between the mechanisms for broadband and monoenergetic electrons. Although bits and pieces of the link have been presented in the previous sections, here we put it all together in one section in order to make a stronger case for the possible link between broadband and monoenergetic electrons.

Substorms increase the Alfvén wave activities in the magnetotail [e.g.,

Lessard et al., 2006]. The high frequency Alfvén wave interaction with electrons lead to time-varying parallel electric fields that accelerate electrons, resulting in the broadband signature in the electrons [*Chaston et al.*, 2002; 2003; 2008]. This is consistent with the broadband electron energy flux increase after substorm onset around 2100–0200 MLT, as shown in Figure 5.14. However, Alfvén waves can also be responsible for the monoenergetic electrons. For example, *Hull et al.* [2010] suggests that the Alfvén waves can lead to the formation of density cavities and quasi-static parallel electric fields. The low frequency Alfvén waves can accelerate electrons that lead to the monoenergetic signature [*Damiano and Johnson*, 2012; *Pritchett and Coroniti*, 2010]. After a few Alfvén bounce periods, the Alfvén waves damp due to electron energy absorption and/or Joule dissipation [*Hull et al.*, 2010; *Lysak and Song*, 2003; *Damiano and Johnson*, 2012]. As a result, the broadband auroral electron power decays after a few Alfvén bounce periods (~ 15 min), as seen in Figure 5.14. On the other hand, the low frequency Alfvén waves damp more slowly, which is consistent with the slower decay of the monoenergetic electron power seen in Figure 5.13. The decay time scales can be illustrated with the time it takes the power to reach its half maximum value from the maximum value at the end of the expansion phase. As can be seen in Figures 5.12–5.14 and summarized in Table 5.1, the time it takes to reach half maximum is ~ 1.6 hr for the monoenergetic electrons, but only ~ 0.42 hr for broadband electrons.

Figure 5.14 shows that after reaching its maximum value, the broadband electron power initially decays rapidly and then slowly. This two stage decay of the broadband electron power suggests that after the rapid decay of the main Alfvén waves in the interval 15–45 min after onset, there seems to be residual Alfvén waves that slowly decay that can be seen at approximately 45 min after onset. These residual Alfvén waves seem to linger on for the rest of the recovery period, which has the same time scale as the recovery period for the monoenergetic electrons.

However, a significant amount of monoenergetic electrons are likely produced by quasi-static electric fields that can be attributed to mechanisms other than low frequency Alfvén waves. For example, in upward field-aligned current regions, quasi-static electric fields can arise when the magnetospheric electron density is too low to carry the currents [*Knight*, 1973]. Figures 5.8 and 5.10 show that monoenergetic and broadband electrons are not always observed in the same region. They seem to overlap roughly in the region spanning 2100–0100 MLT. Westward of the overlapping region, e.g., $\text{MLT} < 2100$, monoenergetic electrons

can be observed without significant broadband electrons.

5.10 References

- Anderson, B. J., and S. A. Fuselier (1994), Response of thermal ions to electromagnetic ion cyclotron waves, *J. Geophys. Res.*, 99, 19413-19425.
- Baker, D. N., E. W. Hones, Jr., P. R. Higbie, and R. D. Belian (1981), Global properties of the magnetosphere during a substorm growth phase: A case study, *J. Geophys. Res.*, 86, 8941–8956.
- Baker, D. N., T. I. Pulkkinen, E. W. Hones Jr., R. D. Belian, R. L. McPherron, and V. Angelopoulos (1994), Signatures of the substorm recovery phase at high-altitude spacecraft, *J. Geophys. Res.*, 99, 10,967-10,979.
- Bargatze, L. F., T. Ogino, R. L. McPherron, and R. J. Walker (1999), Solar wind magnetic field control of magnetospheric response delay and expansion phase onset timing, *J. Geophys. Res.*, 104, 14,583-14,599.
- Baumjohann, W., M. Hesse, S. Kokubun, T. Mukai, T. Nagai, and A. A. Petrukovich (1999), Substorm dipolarization and recovery, *J. Geophys. Res.*, 104(A11), 24,995–25,000, doi:10.1029/1999JA900282.
- Berthomier et al. [2012], Alfvén: magnetosphere–ionosphere connection explorers, *Exp. Astron.*, 33, 445–489, doi:10.1007/s10686-011-9273-y.
- Birn, J., M. Hesse, K. Schindler, and S. Zaharia (2009), Role of entropy in magnetotail dynamics, *J. Geophys. Res.*, 114, A00D03, doi:10.1029/2008JA014015.
- Birn, J., R. Nakamura, E. V. Panov, and M. Hesse (2011), Bursty bulk flows and dipolarization in MHD simulations of magnetotail reconnection, *J. Geophys. Res.*, 116, A01210, doi:10.1029/2010JA016083.
- Borovsky, J. E., M. F. Thomsen, and R. C. Elphic (1998a), The driving of the plasma sheet by the solar wind, *J. Geophys. Res.*, 103, 17,617–17,639.
- Borovsky, J. E., M. F. Thomsen, R. C. Elphic, T. E. Cayton, and D. J. McComas (1998b), The transport of plasma sheet material from the distant tail to geosynchronous orbit, *J. Geophys. Res.*, 103, A9, 20,297–20,331.
- Chaston, C. C., J. W. Bonnell, L. M. Peticolas, C. W. Carlson, J. P. McFadden, and R. E. Ergun (2002), Driven Alfvén waves and electron acceleration, *Geophys. Res. Lett.*, 29, 1535.
- Chaston, C. C., J. W. Bonnell, C. W. Carlson, J. P. McFadden, R. E. Ergun, and R. J. Strangeway (2003), Properties of small-scale Alfvén waves and accelerated electrons from FAST, *J. Geophys. Res.*, 108, 8003,

- doi:10.1029/2002JA009420.
- Chaston, C. C., T. D. Phan, J. W. Bonnell, F. S. Mozer, M. Acun, M. L. Goldstein, A. Balogh, M. Andre, H. Reme, and A. Fazakerley (2005), Drift-Kinetic Alfvén Waves Observed near a Reconnection X Line in the Earth's Magnetopause, *Phys. Rev. Lett.*, 95(6), 065002.
- Chaston, C. C., C. W. Carlson, J. P. McFadden, R. E. Ergun, and R. J. Strangeway (2007), How important are dispersive Alfvén waves for auroral particle acceleration?, *Geophys. Res. Lett.*, 34, L07101, doi:10.1029/2006JG029144.
- Chaston, C., et al. (2008), Turbulent heating and cross-field transport near the magnetopause from THEMIS, *Geophys. Res. Lett.*, 35, L17S08, doi:10.1029/2008GL033601.
- Chen, L. (1999), Theory of plasma transport induced by low-frequency hydromagnetic waves, *J. Geophys. Res.*, 104(A2), 2421–2427, doi:10.1029/1998JA900051.
- Chaston, C.C., J.R. Johnson, M. Wilber, M. Acuna, M.L. Goldstein, and H. Reme (2009), Kinetic Alfvén Wave Turbulence and Transport through a Reconnection Diffusion Region, *Phys. Rev. Lett.*, 102, 015001.
- Chen, M. W., and M. Schulz (2001), Simulations of diffuse aurora with plasma sheet electrons in pitch angle diffusion less than everywhere strong, *J. Geophys. Res.*, 106(A12), 28,949–28,966, doi:10.1029/2001JA000138.
- Christon, S. P., D. J. Williams, D. G. Mitchell, C. Y. Huang, and L. A. Frank (1991), Spectral Characteristics of Plasma Sheet Ion and Electron Populations during Disturbed Geomagnetic Conditions, *J. Geophys. Res.*, 96(A1), 1–22, doi:10.1029/90JA01633.
- Claudepierre, S. G., S. R. Elkington, and M. Wiltberger (2008), Solar wind driving of magnetospheric ULF waves: Pulsations driven by velocity shear at the magnetopause, *J. Geophys. Res.*, 113, A05218, doi:10.1029/2007JA012890.
- Crooker, N. U. (1979), Dayside merging and cusp geometry, *J. Geophys. Res.*, 84(A3), 951–959, doi:10.1029/JA084iA03p00951.
- Damiano, P. A., A. N. Wright, R. D. Sydora, and J. C. Samson (2007), Energy dissipation via electron energization in standing shear Alfvén waves, *Phys. Plasmas*, 14, 062,904.
- Damiano, P. A., and J. R. Johnson (2012), Electron acceleration in a geomagnetic Field Line Resonance, *Geophys. Res. Lett.*, 39, L02102, doi:10.1029/2011GL050264.
- Dungey, J. W. (1961), Interplanetary magnetic field and the auroral zone, *Phys. Res. Lett.*, 6, 47.

- Fairfield, D. H., A. Otto, T. Mukai, S. Kokubun, R. P. Lepping, J. T. Steinberg, A. J. Lazarus, and T. Yamamoto (2000), Geotail observations of the Kelvin-Helmholtz instability at the equatorial magnetotail boundary for parallel northward fields, *J. Geophys. Res.*, *105*, 21,159-21,173.
- Frey, H. U., S. B. Mende, V. Angelopoulos, and E. F. Donovan (2004), Substorm onset observations by IMAGE-FUV, *J. Geophys. Res.*, *109*, A10304, doi:10.1029/2004JA010607.
- Fujimoto, M., and T. Terasawa (1994), Anomalous ion mixing within an MHD scale Kelvin-Helmholtz vortex, *J. Geophys. Res.*, *99*, 8601-8614.
- Fujimoto, M., and T. Terasawa (1995), Anomalous ion mixing within an MHD scale Kelvin-Helmholtz vortex, 2, Effects of inhomogeneity, *J. Geophys. Res.*, *100*, 12,025-12,034.
- Fujimoto, M., T. Terasawa, T. Mukai, Y. Saito, T. Yamamoto, and S. Kokubun (1998), Plasma entry from the flanks of the near-Earth magnetotail: Geotail observations, *J. Geophys. Res.*, *103*(A3), 4391-4408, doi:10.1029/97JA03340.
- Fujimoto, M., T. Tonooka, and T. Mukai (2003), Vortex-like fluctuations in the magnetotail flanks and their possible roles in plasma transport, in *Earth's Low-Latitude Boundary Layer*, edited by P. Newell, and T. Onsager, *Geophysical Monograph*, pp. 241-251, AGU.
- Fuselier, S. A., J. Berchem, K. J. Trattner, and R. Friedel (2002), Tracing ions in the cusp and low-latitude boundary layer using multispacecraft observations and a global MHD simulation, *J. Geophys. Res.*, *107*, A9, 1226, doi:10.1029/2001JA000130.
- Friedel, R. H. W., H. Korth, M. G. Henderson, and M. F. Thomsen (2001), Plasma sheet access to the inner magnetosphere, *J. Geophys. Res.*, *106*, 5845-5858.
- Gkioulidou, M., C.-P. Wang, and L. R. Lyons (2011), Effect of self-consistent magnetic field on plasma sheet penetration to the inner magnetosphere: Rice convection model simulations combined with modified Dungey force-balanced magnetic field solver, *J. Geophys. Res.*, *116*, A12213, doi:10.1029/2011JA016810.
- Gkioulidou, M., C.-P. Wang, S. Wing, L. R. Lyons, R. A. Wolf, and T.-S. Hsu (2012), Effect of an MLT dependent electron loss rate on the magnetosphere-ionosphere coupling, *J. Geophys. Res.*, *117*, A11218, doi:10.1029/2012JA018032.
- Guo, X. C., C. Wang, and Y. Q. Hu (2010), Global MHD simulation of the Kelvin-Helmholtz instability at the magnetopause for northward interplanetary

- magnetic field, *J. Geophys. Res.*, 115, A10218, doi:10.1029/2009JA015193.
- Hasegawa, A. (1976), Particle acceleration by MHD surface wave and formation of the aurora, *J. Geophys. Res.*, 81, 5083.
- Hasegawa, H., M. Fujimoto, T.-D. Phan, H. Rème, A. Balogh, M. W. Dunlop, C. Hashimoto, and R. TanDokoro (2004), Transport of solar wind into Earth's magnetosphere through rolled-up Kelvin-Helmholtz vortices, *Nature*, 430, 755-758.
- Hasegawa, H., M. Fujimoto, K. Takagi, Y. Saito, T. Mukai, and H. Rème (2006), Single-spacecraft detection of rolled-up Kelvin-Helmholtz vortices at the flank magnetopause, *J. Geophys. Res.*, 111, A09203, doi:10.1029/2006JA011728.
- Hodges, J. L., Jr., and E. L. Lehmann (1967), *J. Am. Stat. Ass.*, 62, 319, 926–931.
- Horwitz, J. L. (1985), The substorm as an internal magnetospheric instability: Substorms and their characteristic time scales during intervals of steady interplanetary magnetic field, *J. Geophys. Res.*, 90, 4164–4170.
- Hsu, T.-S., and R. L. McPherron (2012), A Statistical Analysis of Substorm Associated Tail Activity, *Adv. in Space Research*, 50(10), 1317–1343, doi:10.1016/j.asr.2012.06.034.
- Huang, C.-S., G. D. Reeves, J. E. Borovsky, R. M. Skoug, Z. Y. Pu, and G. Le (2003), Periodic magnetospheric substorms and their relationship with solar wind variation, *J. Geophys. Res.*, 108(A6), 1255, doi:10.1029/2002JA009704.
- Hull, A. J., M. Wilber, C. C. Chaston, J. W. Bonnell, J. P. McFadden, F. S. Mozer, M. Fillingim, and M. L. Goldstein (2010), Time development of field-aligned currents, potential drops, and plasma associated with an auroral poleward boundary intensification, *J. Geophys. Res.*, 115, A06211, doi:10.1029/2009JA014651.
- Johnson, J. R., and C. Z. Cheng (1997), Kinetic Alfvén waves and plasma transport at the magnetopause, *Geophys. Res. Lett.*, 24, 1423-1426.
- Johnson, J. R., and C. Z. Cheng (2001), Stochastic ion heating at the magnetopause due to kinetic Alfvén waves, *Geophys. Res. Lett.*, 28, 4421 – 4424.
- Johnson, J. R., C. Z. Cheng, and P. Song (2001), Signatures of mode conversion and kinetic Alfvén waves at the magnetopause, *Geophys. Res. Lett.*, 28(2), 227-230.
- Johnson, J. R., and S. Wing (2009), Northward interplanetary magnetic field plasma sheet entropies, *J. Geophys. Res.*, 114, A00D08, doi:10.1029/2008JA014017.

- Johnson, J. R., S. Wing, and P. A. Delamere (2014), Kelvin Helmholtz Instability in Planetary Magnetospheres, *Space Sci. Rev.*, 184, 1 – 31, doi:10.1007/s11214-014-0085-z.
- Jordanova, V. K., C. J. Farrugia, R. M. Thorne, G. V. Khazanov, G. D. Reeves, and M. F. Thomsen (2001), Modeling ring current proton precipitation by electromagnetic ion cyclotron waves during the May 14–16, 1997, storm, *J. Geophys. Res.*, 106(A1), 7–22, doi:10.1029/2000JA002008.
- Kallio, E. I., T. I. Pulkkinen, H. E. J. Koskinen, A. Viljanen, J. A. Slavin, and K. Ogilvie (2000), Loading-unloading processes in the nightside ionosphere, *Geophys. Res. Lett.*, 27(11), 1627–1630, doi:10.1029/1999GL003694.
- Kan, J. R., D. U. Longenecker, and J. V. Olson (1982), A transient response model of Pi 2 pulsations, *J. Geophys. Res.*, 87(A9), 7483–7488, doi:10.1029/JA087iA09p07483.
- Keiling, A., J. R. Wygant, C. Cattell, W. Peria, G. Parks, M. Temerin, F. S. Mozer, C. T. Russell, and C. A. Kletzing (2002), Correlation of Alfvén wave Poynting flux in the plasma sheet at 4–7 *RE* with ionospheric electron energy flux, *J. Geophys. Res.*, 107, 1132, doi:10.1029/2001JA900140.
- Keiling, A., *et al.* (2004), New properties of energy-dispersed ions in the plasma sheet boundary layer observed by Cluster, *J. Geophys. Res.*, 109, A05215, doi:10.1029/2003JA010277.
- Kenney, J. F., and E. S. Keeping (1951), *Mathematics of Statistics part two*, 2nd edition, pp. 370–371, D. V. Nostrand Co. Inc., Princeton, NJ, USA.
- Kletzing, C. A. (1994), Electron Acceleration by Kinetic Alfvén Waves, *J. Geophys. Res.*, 99(A6), 11,095–11,103, doi:10.1029/94JA00345.
- Kletzing, C. A., J. D. Scudder, E. E. Dors, and C. Curto (2003), The auroral source region: plasma properties of the high altitude plasma sheet, *J. Geophys. Res.*, 108, 1360, doi:10.1029/2002JA009678.
- Knight, S. (1973), Parallel electric fields, *Planet. Space Sci.*, 21, 741–750.
- Korth, H., M. F. Thomsen, J. E. Borovsky, and D. J. McComas (1999), Plasma sheet access to geosynchronous orbit, *J. Geophys. Res.*, 104, 25,047–25,061.
- LaBelle, J. , and R. A. Treumann (1988), Plasma waves at the dayside magnetopause, *Space Sci. Rev.*, 47, 175.
- Le, G., C. T. Russell, J. T. Gosling, and M. F. Thomsen (1996), ISEE observations of low-latitude boundary layer for northward interplanetary magnetic field: Implications for cusp reconnection, *J. Geophys. Res.*, 101, 27,239.
- Lee, L. C., J. R. Johnson, and Z. W. Ma (1994), Kinetic Alfvén waves as a source of plasma transport at the dayside magnetopause, *J. Geophys. Res.*, 99,

- 17,405-17,411.
- Lessard, M. R., E. J. Lund, S. L. Jones, R. L. Arnoldy, J. L. Posch, M. J. Engebretson, and K. Hayashi (2006), Nature of Pi1B pulsations as inferred from ground and satellite observations, *Geophys. Res. Lett.*, *33*, L14108, doi:10.1029/2006GL026411.
- Li, W., J. Raeder, J. Dorelli, M. Øieroset, and T. D. Phan (2005), Plasma sheet formation during long period of northward IMF, *Geophys. Res. Lett.*, *32*, L12S08, doi:10.1029/2004GL021524.
- Li, W., J. Raeder, M. Øieroset, and T. D. Phan (2009), Cold dense magnetopause boundary layer under northward IMF: Results from THEMIS and MHD simulations, *J. Geophys. Res.*, *114*, A00C15, doi:10.1029/2008JA013497.
- Lin, Y., J. R. Johnson, and X. Y. Wang (2010), Hybrid simulation of mode conversion at the magnetopause, *J. Geophys. Res.*, *115*, A04208, doi:10.1029/2009JA014524.
- Lin Y., Jay R. Johnson, and X. Wang (2012), Three-Dimensional Mode Conversion Associated with Kinetic Alfvén Waves, *Phys. Rev. Lett.*, *109*, 125003, 10.1103/PhysRevLett.109.125003.
- Liou, K., P. T. Newell, C.-I. Meng (1997), A. T. Y. Lui, M. Brittnacher, and G. Parks, Dayside auroral activity as a possible precursor of substorm onsets: a survey using POLAR UVI imagery, *J. Geophys. Res.*, *102*, 19835-19844.
- Liou, K., P. T. Newell, D. G. Sibeck, C.-I. Meng, M. Brittnacher, and G. Parks (2001), Observation of IMF and seasonal effects in the location of auroral substorm onset, *J. Geophys. Res.*, *106*, 5799.
- Lui, A. (1994), Mechanisms for the substorm current wedge, in *Substorms 2: Proceedings of the Second International Conference on Substorms*, Fairbanks, Alaska, March 7–11, 1994, edited by J. R. Kan, J. D. Crave, and S.-I. Akasofu, pp. 195–203, Univ. of Alaska, Fairbanks, Alaska.
- Lui, A. T. Y. (1991), Extended consideration of a synthesis model for magnetospheric substorms, in *Magnetospheric Substorms*, pp. 43-60, *Geophys. Monog.*, *64*, edited by J. R. Kan, T. A. Potemra, S. Kokubun, and T. Ijima, AGU, Washington D.C.,
- Lyons, L. R. and T. W. Speiser (1982), Evidence for current sheet acceleration in the geomagnetic tail, *J. Geophys. Res.*, *87*(A4), 2276–2286, doi:10.1029/JA087iA04p02276.
- Lysak, R. L., and Y. Song (2003), Kinetic theory of the Alfvén wave acceleration of auroral electrons, *J. Geophys. Res.*, *108*, 8005, doi:10.1029/2002JA009406.

- Lysak, R. L., and Y. Song (2011), Development of parallel electric fields at the plasma sheet boundary layer, *J. Geophys. Res.*, *116*, A00K14, doi:10.1029/2010JA016424, [printed 117(A1), 2012].
- Mauk, B. H., D. J. Williams, and R. W. McEntire (1997), Energy-time dispersed charged particle signatures of dynamic injections in Jupiter's inner magnetosphere, *Geophys. Res. Lett.*, *24*(23), 2949–2952, doi:10.1029/97GL03026.
- McPherron, R. L. (1972), Substorm related changes in the geomagnetic tail: The growth phase, *Planet. Spa. Sci.*, *29*, 1521–1539.
- McPherron, R. L., T. Terasawa, and A. Nishida (1986), Solar wind triggering of substorm expansion onset, *J. Geomag. Geoelectr.*, *38*, 1089–1108.
- McPherron, R. L., T.-S. Hsu, J. Kissinger, X. Chu, and V. Angelopoulos (2011), Characteristics of plasma flows at the inner edge of the plasma sheet, *J. Geophys. Res.*, *116*, A00133, doi:10.1029/2010JA015923.
- Merkin, V. G., J. G. Lyon, and S. G. Claudepierre (2013), Kelvin-Helmholtz instability of the magnetospheric boundary in a three-dimensional global MHD simulation during northward IMF conditions, *J. Geophys. Res. Space Physics*, *118*, 5478–5496, doi:10.1002/jgra.50520.
- Nagata, D., S. Machida, S. Ohtani, Y. Saito, and T. Mukai (2007), Solar wind control of plasma number density in the near-Earth plasma sheet, *J. Geophys. Res.*, *112*, A09204, doi:10.1029/2007JA012284.
- Nakamura, R., W. Baumjohann, M. Brittmacher, V. A. Sergeev, M. Kubyshkina, T. Mukai, and K. Liou (2001), Flow bursts and auroral activations, *J. Geophys. Res.*, *106*(A6), 10,777–10,789.
- Nakamura, T. K. M., and M. Fujimoto (2005), Magnetic reconnection within rolled-up MHD-scale Kelvin-Helmholtz vortices: Two-fluid simulations including finite electron inertial effects, *Geophys. Res. Lett.*, *32*, L21102, doi:10.1029/2005GL023362.
- Newell, P. T., T. Sotirelis, and S. Wing (2009), Diffuse, monoenergetic, and broadband aurora: the global precipitation budget, *J. Geophys. Res.*, *114*, A09207, doi:10.1029/2009JA014326.
- Newell, P. T., A. R. Lee, K. Liou, S.-I. Ohtani, T. Sotirelis, and S. Wing (2010), Substorm cycle dependence of various types of aurora, *J. Geophys. Res.*, *115*, A09226, doi:10.1029/2010JA015331.
- Newell, P. T., and J. W. Gjerloev (2011), Substorm and magnetosphere characteristic scales inferred from the SuperMAG auroral electrojet indices, *J. Geophys. Res.*, *116*, A12232, doi:10.1029/2011JA016936.

- Nishida, A. (1979), Possible origin of transient dusk-to-dawn electric field in the nightside magnetosphere, *J. Geophys. Res.*, 84(A7), 3409–3412, doi:10.1029/JA084iA07p03409.
- Nishino, M. N., M. Fujimoto, T. Terasawa, G. Ueno, K. Maezawa, T. Mukai, and Y. Saito (2007), Geotail observations of temperature anisotropy of the two-component protons in the dusk plasma sheet, *Ann. Geophys.*, 25, 769 – 777.
- Nykyri, K. and A. Otto (2001), Plasma transport at the magnetospheric boundary due to reconnection in Kelvin-Helmholtz vortices, *Geophys. Res. Lett.*, 28, 3565-3568.
- Nykyri, K., A. Otto, B. Lavraud, C. Mouikis, L. M. Kistler, A. Balogh, and H. Reme (2006), Cluster observations of reconnection due to the Kelvin-Helmholtz instability at the dawnside magnetospheric flank, *Ann. Geophys.*, 24, 2619 – 2643.
- Øieroset, M., J. Raeder, T. D. Phan, S. Wing, J. P. McFadden, W. Li, M. Fujimoto, H. Rème, and A. Balogh (2005), Global cooling and densification of the plasma sheet during an extended period of purely northward IMF on October 22-24, 2003, *Geophys. Res. Lett.*, 32, L12S07, doi:10.1029/2004GL021523.
- Øieroset, M., T. D. Phan, V. Angelopoulos, J. P. Eastwood, J. McFadden, D. Larson, C. W. Carlson, K.-H. Glassmeier, M. Fujimoto, and J. Raeder (2008), THEMIS multi-spacecraft observations of magnetosheath plasma penetration deep into the dayside low-latitude magnetosphere for northward and strong B_y IMF, *Geophys. Res. Lett.*, 35, L17S11, doi:10.1029/2008GL033661.
- Otto, A., and D. H. Fairfield (2000), Kelvin-Helmholtz instability at the magnetotail boundary: MHD simulation and comparison with Geotail observations, *J. Geophys. Res.*, 105, 21,175-21,190.
- Pedersen, A., C. A. Cattell, C.-G. Fälthammar, K. Knott, P.-A. Lindqvist, R. H. Manka, and F. S. Mozer (1985), Electric fields in the plasma sheet and plasma sheet boundary layer, *J. Geophys. Res.*, 90(A2), 1231–1242, doi:10.1029/JA090iA02p01231.
- Pritchett, P. L., and F. V. Coroniti (2010), A kinetic ballooning/interchange instability in the magnetotail, *J. Geophys. Res.*, 115, A06301, doi:10.1029/2009JA014752.
- Pulkkinen, T. I., D. N. Baker, P. K. Toivanen, R. J. Pellinen, R. H. W. Friedel, and A. Korth (1994), Magnetospheric field and current distributions during the substorm recovery phase, *J. Geophys. Res.*, 99, 10,955-10,966.
- Raeder, J., R. J. Walker, and M. Ashour-Abdalla (1995), The structure of the

- distant geomagnetic tail during long periods of northward IMF, *Geophys. Res. Lett.*, *22*, 349.
- Raeder et al. (1997), Boundary layer formation in the magnetotail: Geotail observations and comparisons with a global MHD simulation, *Geophys. Res. Lett.*, *24*, 951.
- Reeves, G. D., A. Chan, and C. Rodger (2009), New Directions for Radiation Belt Research, *Space Weather*, *7*, S07004, doi:10.1029/2008SW000436.
- Robinson, R. M., R. R. Vondrak, K. Miller, T. Dabbs, and D. Hardy (1987), On calculating ionospheric conductances from the flux and energy of precipitating electrons, *J. Geophys. Res.*, *92*, 2565-2569.
- Sandholt, P. E., C. J. Farrugia, S. W. H. Cowley, W. F. Denig, M. Lester, J. Moen, and B. Lybekk (1999), Capture of magnetosheath plasma by the magnetosphere during northward IMF, *Geophys. Res. Lett.*, *26*, 2833-2836.
- Schumaker, T. L., M. S. Gussenhoven, D. A. Hardy, and R. L. Carovillano (1989), The relationship between diffuse auroral and plasma sheet electron distributions near local midnight, *J. Geophys. Res.*, *94*(A8), 10,061–10,078, doi:10.1029/JA094iA08p10061.
- Schekochihin, A. A., S. C. Cowley, W. Dorland, G. W. Hammett, G. G. Howes, E. Quataert, and T. Tatsuno (2009), Astrophysical Gyrokinetics: Kinetic and Fluid Turbulent Cascades in Magnetized Weakly Collisional Plasmas, *Astrophysical Journal Supplemental Series*, *182*, 310-377, doi:10.1088/0067-0049/182/1/310.
- Sergeev, V. A., E. M. Sazhina, N. A. Tsyganenko, J. A. Lundblad and F. Soraas (1983), Pitch-angle scattering of energetic protons in the magnetotail current sheet as the dominant source of their isotropic precipitation into the nightside ionosphere, *Planet. Space Sci.*, *31*, 1147–1155.
- Sergeev, V. A., M. Malkov, and K. Mursula (1993), Testing the isotropic boundary algorithm method to evaluate the magnetic field configuration in the tail, *J. Geophys. Res.*, *98*, 7609-7620.
- Sergeev, V.A., K. Liou, P. T. Newell, S.-I. Ohtani, M. R. Hairston, and F. Rich (2004), Auroral streamers: Characteristics of associated precipitation, convection and field-aligned currents, *Ann. Geophys.*, *22*, 537–548.
- Sibeck, D. G., et al. (1999), Comprehensive study of the magnetospheric response to a hot flow anomaly, *J. Geophys. Res.*, *104*(A3), 4577–4593, doi:10.1029/1998JA900021.
- Song, P., and C. T. Russell (1992), Model of the formation of the low-latitude boundary layer for strongly northward interplanetary magnetic field, *J.*

- Geophys. Res.*, 97, 1411.
- Speiser, T. W. (1965), Particle trajectories in model current sheets: 1. Analytical solutions, *J. Geophys. Res.*, 70(17), 4219–4226, doi:10.1029/JZ070i017p04219.
- Stasiewicz, K., P. Bellan, C. Chaston, C. Kletzing, R. Lysak, J. Maggs, O. Pokhotelov, C. Seyler, P. Shukla, L. Stenflo, A. Streltsov, and J. E. Wahlund (2000), Small scale Alfvénic structure in the aurora, *Space Science Rev.*, 92, 423.
- Stiles, G. S., E. W. Hones Jr., S. J. Bame, and J. R. Asbridge (1978), Plasma Sheet Pressure Anisotropies, *J. Geophys. Res.*, 83(A7), 3166–3172, doi:10.1029/JA083iA07p03166.
- Stenuit, H., M. Fujimoto, S. A. Fuselier, J.-A. Sauvaud, S. Wing, A. Fedorov, E. Budnik, S. P. Savin, K. J. Trattner, V. Angelopoulos, J. Bonnel, T. D. Phan, T. Mukai, and A. Pedersen (2002), Multi-spacecraft study oin the dynamics of the dusk-flank magnetosphere under northward IMF: January 10-11, 1997, *J. Geophys. Res.*, 107(A10), 1333, doi:10.1029/2002JA9009246.
- Summers, D., R. M. Thorne, and F. Xiao (1998), Relativistic theory of wave-particle resonant diffusion with application to electron acceleration in the magnetosphere, *J. Geophys. Res.*, 103(A9), 20,487–20,500, doi:10.1029/98JA01740.
- Tanskanen, E., T. I. Pulkkinen, and H. E. J. Koskinen (2002), Substorm energy budget during low and high solar activity: 1997 and 1999 compared, *J. Geophys. Res.*, 107(A6), 1086, 10.1029/2001JA900153.
- Taylor, M. G. G. T., and B. Lavraud (2008), Observation of three distinct ion populations at the Kelvin-Helmholtz-unstable magnetopause, *Ann. Geophys.*, 26, 1559 – 1566.
- Terasawa, T. et al. (1997), Solar wind control of density and temperature in the near-Earth plasma sheet: WIND/GEOTAIL collaboration, *Geophys. Res. Lett.*, 24, 935-938.
- Thomas, V. A., and D. Winske (1991), Kinetic simulation of the Kelvin-Helmholtz instability at the Venus ionopause, *Geophys. Res. Lett.*, 18, 1943-1946.
- Thomas, V. A., and D. Winske (1993), Kinetic simulations of the Kelvin-Helmholtz instability at the magnetopause, *J. Geophys. Res.*, 98, 11,425-11,438.
- Thorne, R. M. (2010), Radiation belt dynamics: The importance of wave-particle interactions, *Geophys. Res. Lett.*, 37, L22107, doi:10.1029/2010GL044990.
- Toffoletto, F., S. Sazykin, R. Spiro, and R. Wolf (2003), Inner magnetospheric

- modeling with the Rice Convection Model, *Space Science Reviews*, 107, 175-196.
- Tsurutani, B. T., E. J. Smith, R. R. Anderson, K. W. Ogilvie, J. D. Scudder, D. N. Baker, and S. J. Bame (1982), Lion roars and nonoscillatory drift mirror waves in the magnetosheath, *J. Geophys. Res.*, 87, 6060-6072.
- Tsyganenko, N. A., and D. G. Sibeck (1994), Concerning Flux Erosion from the Dayside Magnetosphere, *J. Geophys. Res.*, 99(A7), 13,425–13,436, doi:10.1029/94JA00719.
- Tsyganenko, N. A., D. P. Stern, and Z. Kaymaz (1993), Birkeland Currents in the Plasma Sheet, *J. Geophys. Res.*, 98(A11), 19,455–19,464, doi:10.1029/93JA01922.
- Wang, C-P, L. R. Lyons, M. W. Chen, R. A. Wolf, and F. R. Toffoletto (2003), Modeling the inner plasma sheet protons and magnetic field under enhanced convection, *J. Geophys. Res.*, 108 (A2), 1074, doi:10.1029/2002JA0009620.
- Wang, C.-P., M. Gkioulidou, L. R. Lyons, R. A. Wolf, V. Angelopoulos, T. Nagai, J. M. Weygand, and A. T. Y. Lui (2011), Spatial distributions of ions and electrons from the plasma sheet to the inner magnetosphere: Comparisons between THEMIS-Geotail statistical results and the Rice convection model, *J. Geophys. Res.*, 116, A11216, doi:10.1029/2011JA016809.
- Watanabe, M., and T. Iijima (1993), Substorm Growth Phase on the Magnetotail, *J. Geophys. Res.*, 98(A10), 17,299–17,316, doi:10.1029/93JA01474.
- Watt, C. E. J., and R. Rankin (2009), Electron trapping in shear Alfvén waves that power the aurora, *Phys. Rev. Lett.*, 102, 045002.
- Watt, C. E. J., R. Rankin, I. J. Rae, and D. M. Wright (2005), Self-consistent electron acceleration due to inertial Alfvén wave pulses, *J. Geophys. Res.*, 110, A10S07, doi:10.1029/2004JA010877.
- Wing, S., and D. G. Sibeck (1997), The effects of interplanetary magnetic field Z-component and the solar wind dynamic pressure on the magnetospheric magnetic field line, *J. Geophys. Res.*, 102, 7207–7216.
- Wing, S., and P. T. Newell (1998), Central plasma sheet ion properties as inferred from ionospheric observations, *J. Geophys. Res.*, 103, 6785–6800.
- Wing, S., and P. T. Newell (2002), 2D plasma sheet density profile for northward and southward IMF, *Geophys. Res. Lett.*, 29(9), 10.1029/2001GL013950.
- Wing, S., J. R. Johnson, P. T. Newell, and C.-I. Meng (2005), Dawn-dusk asymmetry in the northward IMF plasma sheet, *J. Geophys. Res.*, 110, A08205, doi:10.1029/2005JA011086.
- Wing, S., J. W. Gjerloev, J. R. Johnson, and R. A. Hoffman (2007), Substorm

- plasma sheet ion pressure profiles, *Geophys. Res. Lett.*, 34, L16110, doi:10.1029/2007GL030453.
- Wing, S., and J. R. Johnson (2009), Substorm entropies, *J. Geophys. Res.*, 114, A00D07, doi:10.1029/2008JA013989.
- Wing, S., and J. R. Johnson (2010), Introduction to special section on Entropy Properties and Constraints Related to Space Plasma Transport, *J. Geophys. Res.*, 115, A00D00, doi:10.1029/2009JA014911.
- Wing, S., J. R. Johnson, C. C. Chaston, M. Echim, C. P. Escoubet, B. Lavraud, C. Lemon, K. Nykyri, A. Otto, J. Raeder, and C.-P. Wang (2014), Review of solar wind entry into and transport within the plasma sheet, *Space Science Reviews*, 184, 33 – 86, doi:10.1007/s11214-014-0108-9.
- Wing, S. and Johnson, J. R. (2015), Solar Wind Entry Into and Transport Within Planetary Magnetotails, in *Magnetotails in the Solar System* (eds A. Keiling, C. M. Jackman and P. A. Delamere), John Wiley & Sons, Inc, Hoboken, NJ. doi: 10.1002/9781118842324.ch14.
- Wolf, R. A., Wan, X. Xing, J. Zhang, and S. Sazykin (2009), Entropy and plasma sheet transport, *J. Geophys. Res.*, 114, A00D05, doi:10.1029/2009JA014044.
- Wygant, J. R., et al. (2002), Evidence for kinetic Alfvén waves and parallel electron energization at 4–6 *RE* altitudes in the plasma sheet boundary layer, *J. Geophys. Res.*, 107, 1201, doi:10.1029/2001JA900113.
- Zanetti, L. J., and T. Potemra (1986), The relationship of Birkeland and ionospheric current systems to the interplanetary magnetic field, in *Solar Wind-Magnetosphere Coupling*, edited by Y. Kamide and J. A. Slavin, pp. 547–562, Terra Sci., Tokyo.
- Zhang, J.-C., R. A. Wolf, S. Sazykin, and F. R. Toffoletto (2008), Injection of a bubble into the inner magnetosphere, *Geophys. Res. Lett.*, 35, L02110, doi:10.1029/2007GL032048.

Chapter 6

Information theoretical approach to discovering solar wind drivers of the outer radiation belt

Chapters 2 and 3 discuss how solar wind can enter the magnetosphere through the dayside reconnection and in the open field lines (region 1 in Figure 1.2). Chapter 5 discusses how the solar wind can enter the magnetosphere through low-latitude boundary layer (region 2 in Figure 1.2). Much of the solar wind plasma ends up in the plasma sheet (region 3 in Figure 1.2). As discussed in Chapter 5, periodically, the plasma sheet plasma is injected (arrow 4 in Figure 1.2) into the inner magnetosphere by substorms (region 5 in Figure 1.2), which release enormous amount of energy into the magnetosphere. One manifestation of the energy release can be seen in the energization of the auroral particle precipitation. Additionally, through particle injections into the inner magnetosphere, substorms provide seed (energy \sim hundreds of keV) and source (energy \sim tens of keV) particles and energy for the radiation belt [Jaynes *et al.*, 2015]. The solar wind driving of the radiation belt (region 5 in Figure 1.2) is the topic of this chapter.

6.1 Introduction

The Earth's radiation belt is inhabited by electrons having energies of a few hundreds of keVs or higher, which are often referred to as “killer electrons” because of the potential damages when they encounter satellites. For example, the radiation belt electrons with energies of a few MeVs or higher can penetrate deep into spacecraft components while those with energies lower than one MeV can lodge on the surface of the spacecraft bodies, leading to devastating electrical discharges.

To explain the origin of the MeV electrons in the radiation belt, studies suggested that the storm and substorm injection process from plasma sheet into the inner magnetosphere accelerates low energy (e.g., a few keV) electrons to a few hundred keVs. Once in the inner magnetosphere, electrons interact with ultra low frequency (ULF) waves [e.g., *Elkington et al.*, 1999; *Rostoker et al.*, 1998; *Ukhorskiy et al.*, 2005; *Mathie and Mann*, 2000; 2001], very low frequency (VLF) waves [e.g., *Summers et al.*, 1998; *Omura et al.*, 2007; *Thorne et al.*, 2011; *Simms et al.*, 2015; *Camporeale*, 2015; *Camporeale and Zimbardo*, 2015], or magnetosonic waves [e.g., *Horne et al.*, 2007; *Shprits et al.*, 2008], which can energize electrons to MeV energy range.

Enhancements of ULF waves can be associated with increased occurrences of Kelvin-Helmholtz instability (KHI) along the magnetopause flanks due to large solar wind velocity (V_{sw}) [e.g., *Johnson et al.*, 2014; *Engebretson et al.*, 1998; *Vennerstrom*, 1999]. Indeed, studies have shown that V_{sw} is a dominant, if not the most dominant, driver of geosynchronous relativistic electron fluxes (herein J_e refers to geosynchronous MeV electron energy flux) [e.g., *Paulikas and Blake*, 1979; *Baker et al.*, 1990; *Li et al.*, 2001; 2005; *Vassiliadis et al.*, 2005; *Ukhorskiy et al.*, 2004; *Rigler et al.*, 2007; *Kellerman and Shprits*, 2012; *Reeves et al.*, 2011]. However, the geosynchronous electron response to V_{sw} has a lag time that is energy dependent. For example, *Li et al.* [2005] finds that the average lag times of 50 keV to 1.1 MeV electrons approximately range from -4 to 25 hours, respectively. For MeV electrons, a lag time of about 2 days has been consistently observed in many studies [e.g., *Baker et al.*, 1990; *Vassiliadis et al.*, 2005; *Reeves et al.*, 2011;

This chapter comes from a manuscript that has been submitted to Journal of Geophysical Research:

Wing, S., J. R. Johnson, E. Camporeale, and G. D. Reeves, Information theoretical approach to discovering solar wind drivers of the outer radiation belt, submitted to *J. Geophys. Res.*, 2016.

Contribution statement:

S. Wing: contributed main ideas, wrote the code to analyze LANL data, interpreted results, performed most of the work, wrote the journal paper.

J. R. Johnson: introduced information theory to S. Wing, contributed some code, contributed useful discussions.

E. Camporeale: suggested radiation belt as a topic and LANL data for the work, contributed Figure 6.12, contributed useful discussions.

G. D. Reeves: contributed LANL data.

Balikhin et al., 2011; *Lyatsky and Khazanov*, 2008a], suggesting the time scale needed to accelerate electrons to MeV energy range.

In contrast to V_{sw} , which correlates with J_e , solar wind density (n_{sw}) anticorrelates with J_e for reasons that are not entirely clear [e.g., *Lyatsky and Kazanov*, 2008a; *Kellerman and Shprits*, 2012]. *Li et al.* [2005] suggests that an increase in n_{sw} increases solar wind dynamic pressure (P_{dyn}), which, in turn, pushes the magnetopause inward, leading to electron losses. However, *Lyatsky and Khazanov* [2008a] argues that the poor correlation between P_{dyn} and J_e suggests that compression of the magnetosphere is probably not the main factor. Moreover, the effectiveness of n_{sw} at influencing J_e is also not clear. Some studies found that n_{sw} has weaker effects than V_{sw} on J_e [e.g., *Vassiliadis et al.*, 2005; *Rigler et al.*, 2007; *Kellerman and Shprits*, 2012]. However, *Balikhin et al.* [2011] finds that J_e has the strongest dependence on n_{sw} with a lag of 1 day.

The interpretation of the relationship between n_{sw} and J_e is complicated by the anticorrelation between V_{sw} and n_{sw} [e.g., *Hundhausen et al.*, 1970]. Because J_e and V_{sw} are correlated, the anticorrelation between J_e and n_{sw} could simply be coincidence. A few studies attempted to separate the effects of n_{sw} from V_{sw} by using methods that bin the data into small intervals of V_{sw} and n_{sw} [e.g., *Lyatsky and Khazanov*, 2008a]. This type of analysis has offered insights into solar wind driving of J_e , but it does not address the question of how much additional information n_{sw} provides to J_e , given V_{sw} and vice versa. Other studies showed that interplanetary magnetic field (IMF) and other solar wind parameters can also contribute to J_e variations [e.g., *Balikhin et al.*, 2011; *Rigler et al.*, 2007; *Vassiliadis et al.*, 2005; *Li et al.*, 2005; *Onsager et al.*, 2007; *Simms et al.*, 2014], but presently, it is not entirely clear quantitatively given the main driver, e.g., V_{sw} (or n_{sw}), how much additional information these parameters provide to J_e . This knowledge can help radiation belt modelers decide what input parameters to consider for their models.

The solar wind–magnetosphere and solar wind–radiation belt systems have been shown to be nonlinear [e.g., *Wing et al.*, 2005a; *Johnson and Wing*, 2005; *Reeves et al.*, 2011; *Kellerman and Shprits*, 2012]. An example is presented in Figure 6.1, which plots $\log J_e(t + \tau)$ vs. $V_{sw}(t)$ for $\tau = 0, 1, 2,$ and 7 days. The figure, which is similar to Figure 9 in *Reeves et al.* [2011], shows that the relationship between J_e and V_{sw} is nonlinear. For nonlinear system, qualitative linear correlational analysis can be misleading [e.g., *Balikhin et al.*, 2010; 2011]. Moreover, correlational analysis cannot establish causalities. On the other hand,

as described below, information theory can help identify nonlinearities in the system and information transfer from input to output parameters.

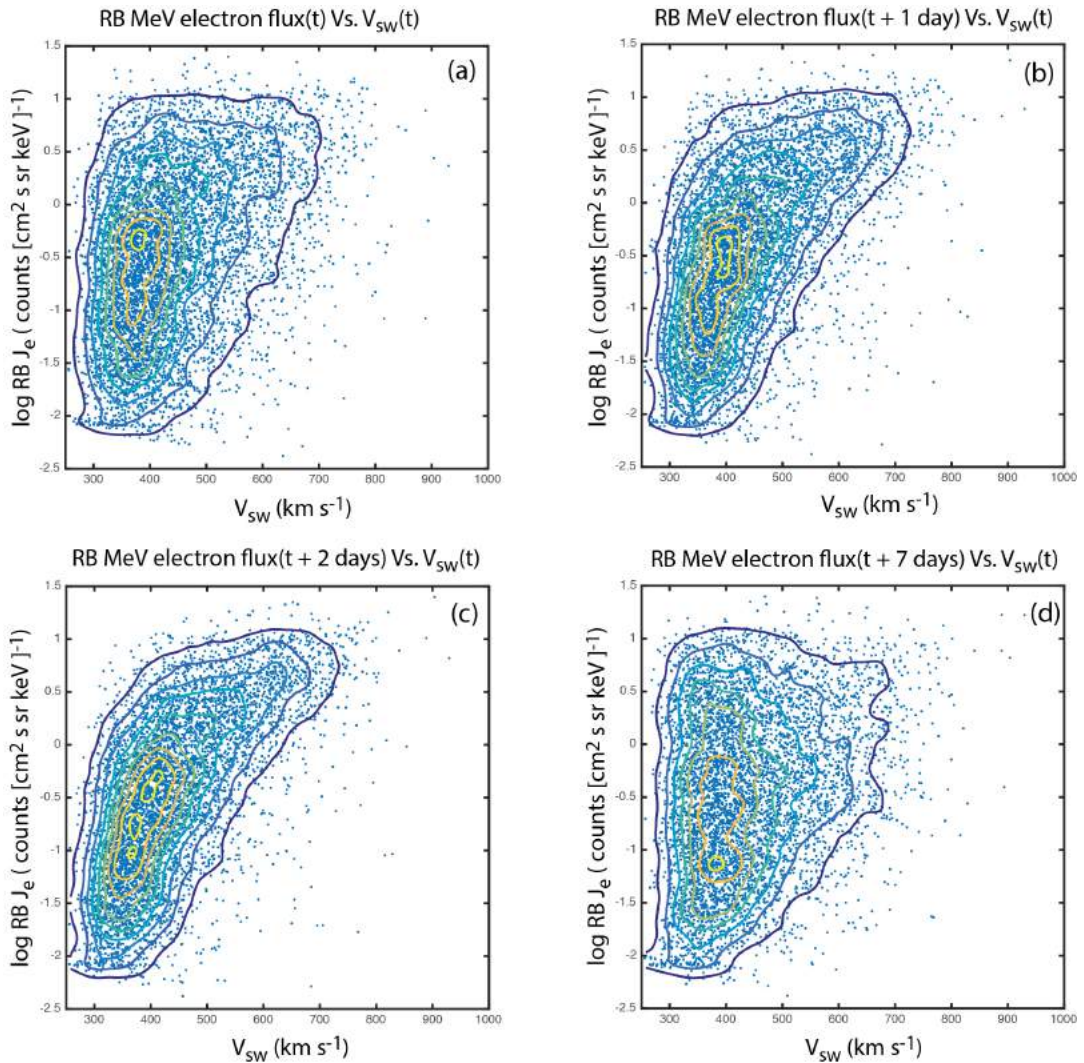


Figure 6.1. Scatter plots of $\log J_e(t + \tau)$ vs. $V_{sw}(t)$ for $\tau = 0, 1, 2,$ and 7 days in panels (a), (b), (c), and (d), respectively. The data points are overlain with density contours showing the nonlinear trends. The panels show that J_e has dependence on V_{sw} for $\tau = 0, 1,$ and 2 days and the dependence is strongest for $\tau = 2$ days. (d) At large τ , e.g., $\tau = 7$ day, J_e dependence on V_{sw} is very weak. The triangle distribution [Reeves *et al.*, 2011] can be seen in panels (a), (b), and (c). This is essentially the same as Figure 9 in Reeves *et al.* [2011], except that no density contours are drawn and Figure 6.1d plots $\tau = 7$ days instead of $\tau = 3$ days.

Although information theoretical tools are still considered novel in space physics and space weather, a few studies have successfully applied these tools to solve problems in these fields. For example, *Johnson and Wing* [2005] applied mutual information and cumulant based analysis to discover the nonlinear dependencies inherent in the Kp time series. *Materassi et al.* [2011] applied mutual information to characterize the influence and timing of solar wind forcing of the ionospheric scintillations. *De Michelis et al.* [2011] applied transfer entropy to establish transfer of information from AL to SYM-H indices on a time scale shorter than 10 hr. More recently, *Johnson and Wing* [2014] applied conditional redundancy to examine the roles of internal vs. external triggering in substorms.

In the present study, we investigate further the linear and nonlinear relationships between solar wind parameters and geosynchronous relativistic electrons using tools that are based on information theory. In particular, we apply mutual information [e.g., *Li*, 1990; *Tsonis*, 2001], conditional mutual information [e.g., *Wyner*, 1978], and transfer entropy [e.g., *Schreiber*, 2000] to determine the solar wind drivers of J_e and to quantify how much information is transferred from solar wind parameters to J_e .

The scatter plots of J_e vs. V_{sw} in Figure 6.1 panels a–c look like a triangle, which *Reeves et al.* [2011] refers to as the triangle distribution. The mystifying part of the triangle distribution is that high values of J_e are observed for all V_{sw} conditions. The present study probes deeper at this triangle distribution using information theory.

6.2 Data set

Most studies of geosynchronous MeV electrons have been performed with data having 1-day resolution [e.g., *Reeves et al.*, 2011; *Balikhin et al.*, 2011; *Kellerman and Shprits*, 2012]. As pointed by *Reeves et al.* [2011], because of the asymmetry of the geomagnetic field along the geosynchronous orbit, geosynchronous electron fluxes exhibit a diurnal or magnetic local time (MLT) variation as well as latitude-longitude dependence. However, these effects are reduced in daily resolution data.

The present study uses the same dataset in *Reeves et al.* [2011]. The data and format description can be found at <ftp://ftop.agu.org/apend/ja/2010ja015735>. This dataset contains daily averages of electron fluxes obtained from Energetic

Sensor for Particles (ESP) [Meier *et al.*, 1996] and Synchronous Orbit Particle Analyzer (SOPA) [Belian *et al.*, 1992] on board of all seven Los Alamos National Laboratory (LANL) geosynchronous satellites from 22 Sep 1989 to 31 Dec 2009. The present study only examines the fluxes of electrons with energy range of 1.8–3.5 MeVs (which is referred herein as J_e). A detailed description of the dataset and its processing are given in Reeves *et al.* [2011]. The daily and hourly averaged solar wind data 1989–2009 come from OMNI dataset provided by NASA (<http://omniweb.gsfc.nasa.gov/>). The LANL and solar wind data are merged. The LANL dataset has 7187 data points (days of data), out of which, 6438 data points have simultaneous solar wind observations.

6.3 Mutual Information, conditional mutual information, and transfer entropy

Dependency is a key discriminating statistic that is commonly used to understand how systems operate. The standard tool used to identify dependency is cross-correlation. Considering two variables, x and y , the correlation analysis essentially tries to fit the data to a 2D Gaussian cloud, where the nature of the correlation is determined by the slope and the strength of correlation is determined by the width of the cloud perpendicular to the slope.

By nature, the response of the radiation belts to solar wind variables is nonlinear [Reeves *et al.*, 2011; Kellerman and Shprits, 2012] as evidenced by the triangle distribution in J_e vs. V_{sw} seen in Figure 6.1 panels a–c. Such a distribution is not well described by a Gaussian cloud of points and is not well characterized by a slope. For such distributions, it is better to use a statistical based measure such as mutual information (MI) [Tsonis, 2001; Li, 1990; Darbellay and Vajda, 1999]. Mutual information between two variables, x and y , compares the uncertainty of measuring variables jointly with the uncertainty of measuring the two variables independently. The uncertainty is measured by the entropy. In order to construct the entropies, it is necessary to obtain the probability distribution functions, which in this study are obtained from histograms of the data based on discretization of the variables (i.e. bins).

Suppose that two variables, x and y , are binned so that they take on discrete values, \hat{x} and \hat{y} , where

$$\hat{x} \in \{x_1, x_2, \dots, x_n\} \equiv \mathfrak{X}_1; \quad \hat{y} \in \{y_1, y_2, \dots, y_m\} \equiv \mathfrak{X}_2. \quad (6.1)$$

The variables may be thought of as letters in alphabets \aleph_1 and \aleph_2 , which have n and m letters, respectively. The extracted data can be considered as sequences of letters. The entropy associated with each of the variables is defined as

$$H(x) = - \sum_{\aleph_1} p(\hat{x}) \log p(\hat{x}) ; \quad H(y) = - \sum_{\aleph_2} p(\hat{y}) \log p(\hat{y}) \quad (6.2)$$

where $p(\hat{x})$ is the probability of finding the word \hat{x} in the set of x -data and $p(\hat{y})$ is the probability of finding word \hat{y} in the set of y -data. To examine the relationship between the variables, we extract the word combinations (\hat{x}, \hat{y}) from the dataset. The joint entropy is defined by

$$H(x, y) = - \sum_{\aleph_1 \aleph_2} p(\hat{x}, \hat{y}) \log p(\hat{x}, \hat{y}) \quad (6.3)$$

where $p(\hat{x}, \hat{y})$ is the probability of finding the word combination (\hat{x}, \hat{y}) in the set of (x, y) data. The mutual information is then defined as

$$\text{MI}(x, y) = H(x) + H(y) - H(x, y) \quad (6.4)$$

In the case of Gaussian distributed data, the mutual information can be related to the correlation function; however, it also includes higher order correlations that are not detected by the correlation function. Hence, MI is a better measure of dependency for variables having a nonlinear relationship [Johnson and Wing, 2005].

While MI is useful to identify nonlinear dependence between two variables, it does not provide information about whether the dependence is causal or coincidental. Herein, we use the working definition that if there is a transfer of information from x to y , then x causes y . In this case, it is useful to consider conditional dependency with respect to a conditioner variable z that takes on discrete values, $\hat{z} \in \{z_1, z_2, \dots, z_n\} \equiv \aleph_3$. The conditional mutual information [Wyner, 1978]

$$\text{CMI}(x, y | z) = \sum_{\aleph_1 \aleph_2 \aleph_3} p(\hat{x}, \hat{y}, \hat{z}) \log \frac{p(\hat{x}, \hat{y} | \hat{z})}{p(\hat{x} | \hat{z}) p(\hat{y} | \hat{z})} = H(x, z) + H(y, z) - H(x, y, z) - H(z) \quad (6.5)$$

determines the mutual information between x and y given that z is known. In the case where z is unrelated, $\text{CMI}(x, y | z) = \text{MI}(x, y)$, but in the case that x or y is known based on z , then $\text{CMI}(x, y | z) = 0$. CMI therefore provides a way to determine how much additional information is known given another variable. CMI can be seen as a special case of the more general conditional redundancy that allows the variable z to be a vector [e.g., Prichard and Theiler, 1995; Johnson and Wing, 2014].

A common method to establish causal-relationships between two time series, e.g., $[x_t]$ and $[y_t]$, is to use a time-shifted correlation function [e.g., *Borovsky et al.*, 1998]

$$r(\tau) = \frac{\langle x_t y_{t+\tau} \rangle - \langle x \rangle \langle y \rangle}{\sqrt{\langle x^2 \rangle - \langle x \rangle^2} \sqrt{\langle y^2 \rangle - \langle y \rangle^2}} \quad (6.6)$$

where r = correlation coefficient and τ = lag time. The results of this type of analysis may not be particularly clear when the correlation function has multiple peaks or there is not an obvious asymmetry. Additionally, correlational analysis only detects linear correlations. If the feedback involves nonlinear processes, its usefulness may be seriously limited.

Alternatively, time shifted mutual information, $MI(x(t), y(t+\tau))$, can be used to detect causality in nonlinear systems, but this too suffers from the same problems as time-shifted correlation when it has multiple peaks and long range correlations.

A better choice for studying causality is the one-sided transfer entropy [*Schreiber*, 2000]

$$TE_{x \rightarrow y}(\tau) = \sum_t p(y_{t+\tau}, yp_t, x_t) \log \left(\frac{p(y_{t+\tau} | yp_t, x_t)}{p(y_{t+\tau} | yp_t)} \right) \quad (6.7)$$

where $yp_t = [y_t, y_{t-\Delta}, \dots, y_{t-k\Delta}]$, $k+1$ = dimensionality of the system, and Δ = first minimum in MI. Transfer entropy (TE) can be considered as a specialized case of conditional mutual information:

$$TE_{x \rightarrow y}(\tau) = CMI(y(t+\tau), x(t) | yp(t)) \quad (6.8)$$

where $yp(t) = [y(t), y(t-\Delta), \dots, y(t-k\Delta)]$. The transfer entropy can be considered as a conditional mutual information that detects how much average information is contained in an input, x , about the next state of a system, y , that is not contained in the past history, yp , of the system [*Prokopenko et al.*, 2013]. In the absence of information flow from x to y , $TE(x \rightarrow y)$ vanishes. Also, unlike correlational analysis and mutual information, transfer entropy is directional, $TE(x \rightarrow y) \neq TE(y \rightarrow x)$. The transfer entropy accounts for static internal correlations, which can be used to determine whether x and y are driven by a common driver or whether x drives y or y drives x .

6.4 Applying information theory to radiation belt MeV electron data

6.4.1 Radiation belt MeV electron flux vs. V_{sw}

A good starting point for our analysis is Figure 9 in *Reeves et al.* [2011], which is replotted in Figure 6.1 with some modifications. As in *Reeves et al.* [2011], the present paper uses the convention that V_{sw} is positive in the antisunward direction. Consistent with *Reeves et al.* [2011], Figure 6.1 shows that (1) the correlation is best at $\tau = 2$ days (Figure 6.1c); (2) the relationship between $\log J_e$ and V_{sw} is nonlinear, which can be seen more clearly in the data density contours; and (3) the data point distribution looks like a triangle. This so called triangle distribution is discussed further in Section 6.5.4.

The blue curve in Figure 6.2a shows the correlation coefficient of $[\log J_e(t + \tau), V_{sw}(t)]$. Note that herein, unless otherwise stated, all linear and nonlinear analyses performed with J_e uses $\log J_e$ values. Figure 6.2a shows that the linear correlation coefficient peaks at $\tau_{max} = 2$ days with $r = 0.63$. There is a smaller peak at $\tau = 29$ days ($r = 0.42$), which can be attributed to the 27 day synodic solar rotation. The red curve shows the correlation coefficient of $[J_e(t), V_{sw}(t + \tau)]$. The red curve has a small peak at $\tau = 25$ days ($r = 0.39$) because of the 27 day solar rotation. That is, $J_e(t)$ correlates best with $V_{sw}(t - 2$ days), but $V_{sw}(t - 2$ days) correlates with $V_{sw}([t - 2$ days] + 27 days). Because the large number of data points ($n > 5772$), the three peak correlation coefficients are highly significant with $P < 0.01$ (the probability of two random variables giving a correlation coefficient as large as r is < 0.01).

However, the relationship between J_e and V_{sw} is nonlinear and hence, linear cross correlation may not capture the full extent of the relationship, as described in Section 6.3. Although the correlation coefficient may give some indication about the sign and strength of the relationship, it is not quantitatively precise [*Reeves et al.*, 2011]. In order to take into account the nonlinearities in the relationship, we apply mutual information and transfer entropy.

Figure 6.2b plots the mutual information (MI) of $[J_e(t + \tau), V_{sw}(t)]$ (blue curve) and $[J_e(t), V_{sw}(t + \tau)]$ (red curve) as well as transfer entropy (TE) of $[J_e(t + \tau), V_{sw}(t)]$ (yellow curve) and $[J_e(t), V_{sw}(t + \tau)]$ (purple curve). For simplicity, we assume $k = 0$ in equations (6.7) and (6.8) (the solar wind–magnetosphere system has a low dimension [e.g., *Roberts*, 1991; *Roberts et al.*, 1991; *Sharma et al.*,

1993]). As described in Section 6.3, mutual information provides a measure of nonlinear correlation between the two parameters while the transfer entropy provides a measure of transfer of information from one variable to another. Herein, we adopt the convention that forward direction is the direction for information transfer from a solar wind parameter to J_e and backward direction is the opposite. So, blue and yellow curves plot the forward MI and TE while red and purple curves plot the backward MI and TE, respectively.

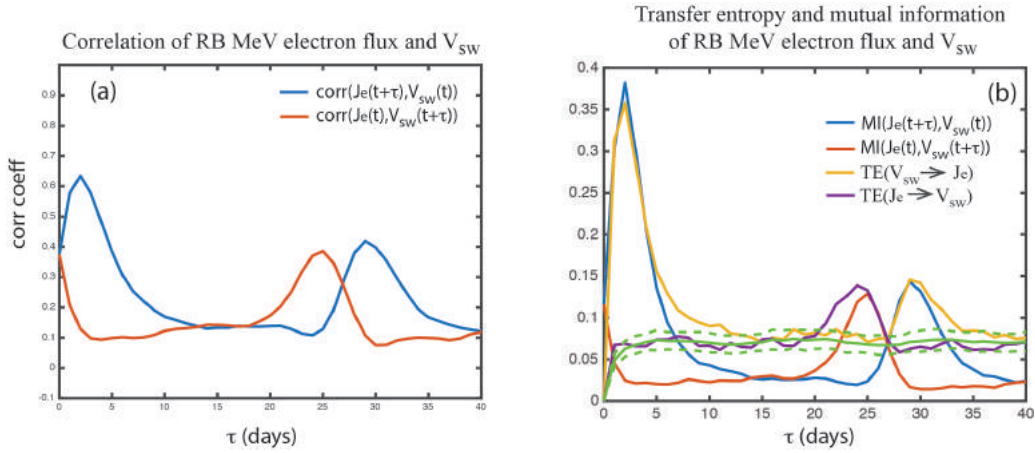


Figure 6.2. (a) Correlation coefficient of $[J_e(t + \tau), V_{sw}(t)]$ (blue) and $[J_e(t), V_{sw}(t + \tau)]$ (red). (b) $\text{MI}[J_e(t + \tau), V_{sw}(t)]$ (blue), $\text{MI}[J_e(t), V_{sw}(t + \tau)]$ (red), $\text{TE}[J_e(t + \tau), V_{sw}(t)]$ (yellow) and $\text{TE}[J_e(t), V_{sw}(t + \tau)]$ (purple). The solid and dashed green curves are the mean and the 3σ from the mean of the noise. The transfer of information from V_{sw} to J_e ($V_{sw} \rightarrow J_e$) peaks at $\tau_{max} = 2$ days.

The forward and backward mutual information peak at $\tau_{max} = 2$ and 25 days, respectively. Also, the forward mutual information has a secondary peak at $\tau = 29$ days. The results suggest that the response may be dominated by the linear dynamics in this case, although in general this is not necessarily the case. The forward transfer entropy from V_{sw} to J_e , $\text{TE}(V_{sw} \rightarrow J_e)$, peaks at $\tau_{max} = 2$ days (yellow curve), suggesting that the transfer of information from V_{sw} to geosynchronous MeV electrons has a 2 days delay. Similar to MI and correlational analysis, $\text{TE}(V_{sw} \rightarrow J_e)$ has a small peak at $t = 29$ days. The backward TE, $\text{TE}(J_e \rightarrow V_{sw})$, has a peak at $\tau_{max} = 24$ days (purple). The backward peak in the transfer entropy raises some questions about how well TE is able to eliminate the self correlation of the solar wind. The self correlations are probably

better eliminated by using a two element vector of V_{sw} that includes $V_{sw}(t)$ and $V_{sw}(t - \Delta)$ to capture more of the dynamics of V_{sw} .

In order to get a measure of the significance of $\text{TE}(V_{sw} \rightarrow J_e)$, we calculate noise = $\text{TE}[V_{sw} \rightarrow \text{sur}(J_e)]$ where $\text{sur}(J_e)$ is the surrogate data of J_e , which is obtained by randomly permuting the order of the time series array J_e . The mean and standard deviation of the noise are calculated from an ensemble of 100 random permutations $\text{TE}[V_{sw} \rightarrow \text{sur}(J_e)]$. The mean noise and 3σ (standard deviation) from the mean noise are plotted with solid and dashed green curves, respectively, in Figure 6.2b. The maximum TE, $\text{TE}[J_e(t + 2 \text{ days}), V_{sw}(t)]$ has peak information transfer (it_{max}) = 0.30, signal to noise ratio (snr) = 5.7 and significance = 94σ where it_{max} = peak – mean noise, snr = peak/mean noise and significance = $it_{max}/\sigma(\text{noise})$. From the snr , it_{max} , and significance, we conclude that there is a significant transfer of information from V_{sw} to J_e with a 2 days delay. Note that the linear correlation, MI, and TE analyses are consistent with the previous studies [e.g., Baker *et al.*, 1990; Vassiliadis *et al.*, 2005; Reeves *et al.*, 2011; Balikhin *et al.*, 2011; Lyatsky and Khazanov, 2008a].

The $\text{TE}(V_{sw} \rightarrow J_e)$ (yellow) curve shows that V_{sw} has little influence on the geosynchronous MeV electrons after a delay of 7–10 days, which is essentially the prediction or information horizon. This result is consistent with Figure 6.1d, which shows poor correlation in $\log J_e(t + 7 \text{ days})$ vs. V_{sw} distribution.

6.4.2 Radiation belt MeV electron flux vs. n_{sw}

We repeat the above analyses for J_e vs. n_{sw} . Figure 6.3 plots $J_e(t + \tau)$ vs. n_{sw} for $\tau = 0, 1, 2,$ and 7 days. It shows that (1) J_e anticorrelates with n_{sw} and (2) $J_e(t + 1 \text{ day})$ vs. n_{sw} (panel b) has the most negative slope, suggesting the best anticorrelation. The anticorrelation is shown more clearly in Figure 6.4a, which plots $\text{corr}[J_e(t + \tau), n_{sw}(t)]$ (blue curve, forward direction) and $\text{corr}[J_e(t), n_{sw}(t + \tau)]$ (red curve, backward direction). The blue curve shows $\tau_{min} = 1 \text{ day}$ ($r = -0.40$) and a secondary minimum at $\tau = 28 \text{ days}$ ($r = -0.23$). The latter can be attributed to solar rotation. The red curve shows $\tau_{min} = 26 \text{ days}$ ($r = -0.22$), which again can be attributed to solar rotation. Although the correlation coefficients are smaller, all three of them are still highly significant ($P < 0.01$) due to the large number of data points.

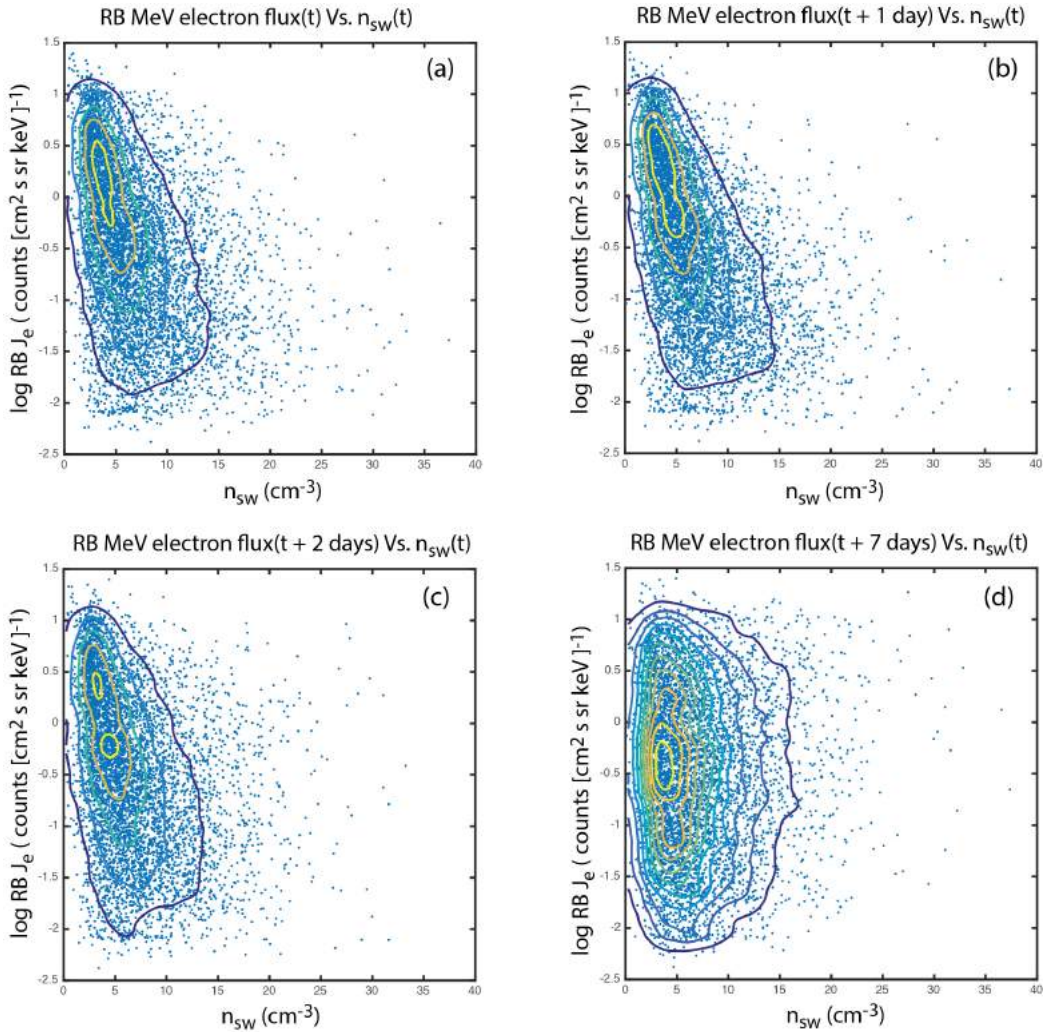


Figure 6.3. J_e anticorrelates with n_{sw} . Scatter plots of $\log J_e(t + \tau)$ vs. $n_{sw}(t)$ for $\tau = 0, 1, 2,$ and 7 days in panels (a), (b), (c), and (d), respectively. The data points are overlain with density contours, which show the trends. The panels show that J_e has dependence on n_{sw} for $\tau = 0, 1,$ and 2 days. The slope of the contours is most negative for $\tau = 1$ day, suggesting strongest dependence on n_{sw} at $\tau = 1$ day. (d) At large τ , e.g., $\tau = 7$ day, J_e dependence on n_{sw} vanishes.

Figure 6.4b is similar to Figure 6.2b, except that it shows MI and TE for (J_e, n_{sw}) . Forward MI and TE, both have $\tau_{max} = 1$ day, which is consistent with Figure 6.2a. Note that unlike correlational analysis, MI and TE only give positive values for both correlations and anticorrelations. The forward TE, $\text{TE}(n_{sw} \rightarrow J_e)$ is not as large as $\text{TE}(V_{sw} \rightarrow J_e)$ shown in Figure 6.2b, but TE at $\tau = 1$ day is still significant. $\text{TE}[n_{sw}(t) \rightarrow J_e(t + 1 \text{ day})]$ has $it_{max} = 0.13$, $snr = 4.4$ and significance = 42σ . This

result suggests that there is a transfer of information from n_{sw} to geosynchronous MeV electrons with 1 day delay.

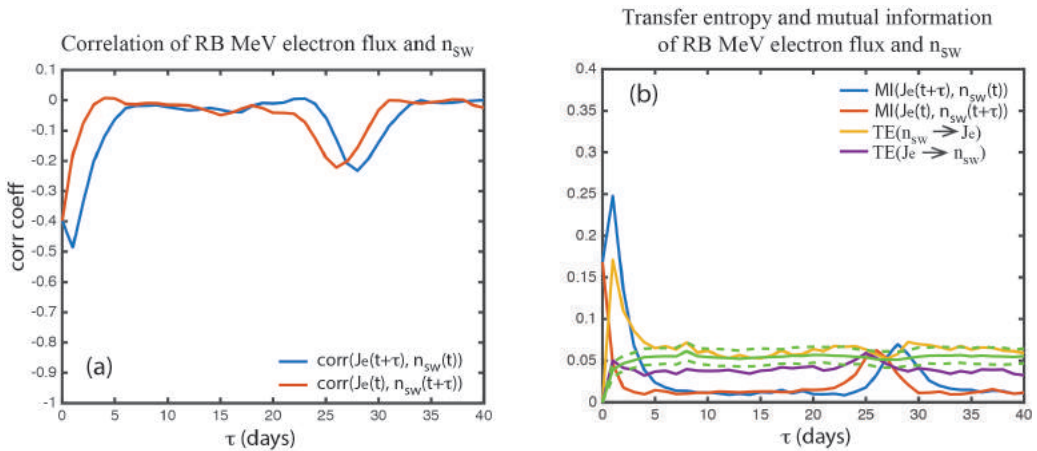


Figure 6.4. (a) Correlation coefficient of $[J_e(t + \tau), n_{sw}(t)]$ (blue) and $[J_e(t), n_{sw}(t + \tau)]$ (red). (b) $\text{MI}[J_e(t + \tau), n_{sw}(t)]$ (blue), $\text{MI}[J_e(t), n_{sw}(t + \tau)]$ (red), $\text{TE}[J_e(t + \tau), n_{sw}(t)]$ (yellow) and $\text{TE}[J_e(t), n_{sw}(t + \tau)]$ (purple). The solid and dashed green curves are the mean and 3σ from the mean of the noise. The transfer of information from n_{sw} to J_e ($n_{sw} \rightarrow J_e$) peaks at $\tau_{max} = 1$ day.

Besides lag time and peak size, there are other differences between Figures 6.2b and 6.4b that are noteworthy. First, in the forward direction, there is little information transfer from n_{sw} to J_e after 4 days. That is, $\text{TE}[J_e(t + \tau), n_{sw}(t)]$ for $\tau > 4$ days is in the noise level, which is consistent with Figure 6.3d for $\tau = 7$ days. Second, the TE peaks due to solar rotation in the forward and backward directions are a lot smaller and in fact, are at the noise level. This suggests that unlike V_{sw} , there is little information transfer from the n_{sw} to J_e one solar rotation later. Practically, there is no information flow in the backward direction, from J_e to n_{sw} at any lag because $\text{TE}[J_e(t), n_{sw}(t + \tau)]$ (purple curve) is small and within noise level for all τ . In contrast, $\text{corr}[J_e(t), n_{sw}(t + \tau)]$ and $\text{MI}[J_e(t), n_{sw}(t + \tau)]$ are still significant for small τ and $\text{corr}[J_e(t), n_{sw}(t + \tau)]$ has a significant value that is due to solar rotation. This illustrates that TE does not always give the same results as correlation and MI.

6.4.3 Anticorrelation of V_{sw} and n_{sw} and its effect on radiation belt

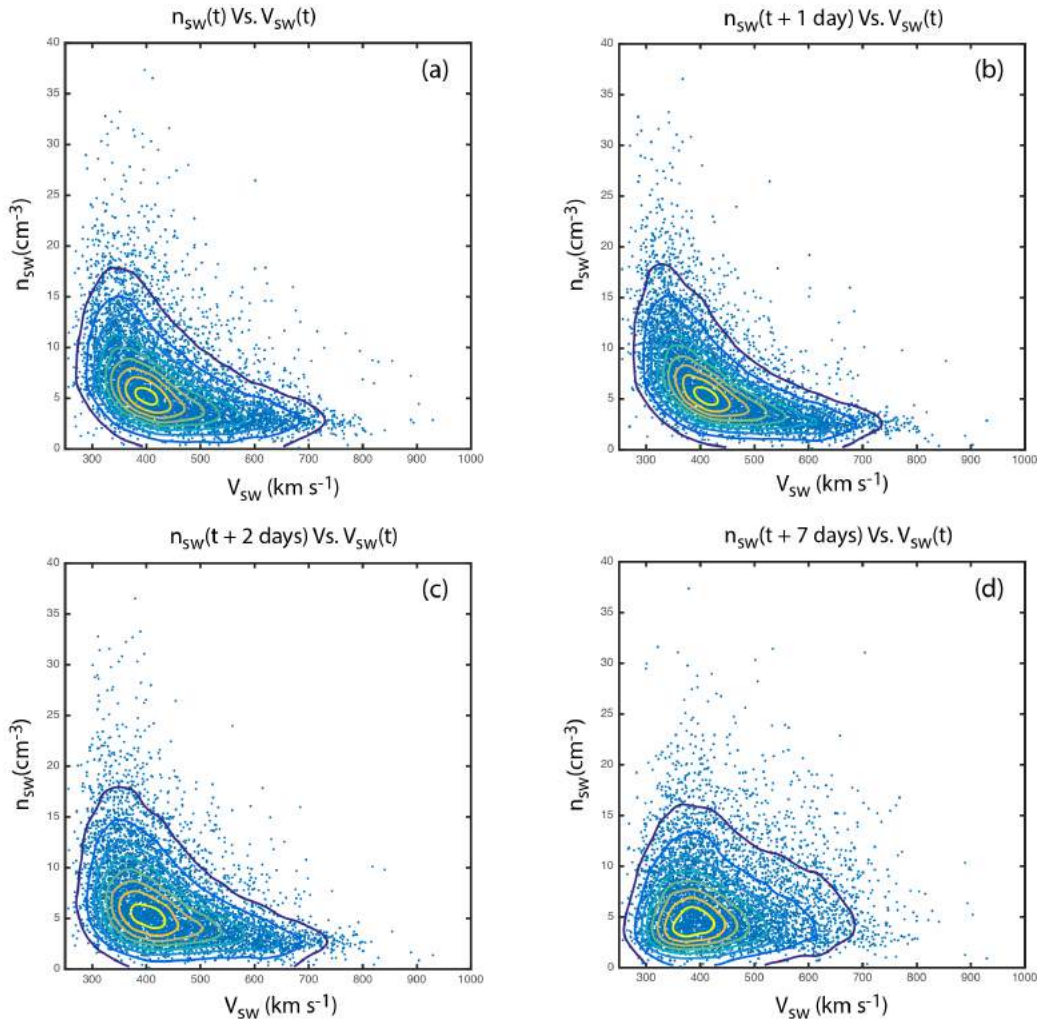


Figure 6.5. n_{sw} anticorrelates with V_{sw} . Scatter plots of $n_{sw}(t + \tau)$ vs. $V_{sw}(t)$ for $\tau = 0, 1, 2,$ and 7 days in panels (a), (b), (c), and (d), respectively. The data points are overlain with density contours showing strongly nonlinear trends. The panels show that n_{sw} has dependence on V_{sw} for $\tau = 0, 1,$ and 2 days and the dependence is strongest for $\tau = 1$ day. (d) At large τ , e.g., $\tau = 7$ day, n_{sw} dependence on V_{sw} is very weak.

In Section 6.4.1, we show that $J_e(t + 2 \text{ days})$ linearly and nonlinearly correlate with $V_{sw}(t)$. It is well known that n_{sw} anticorrelates with V_{sw} [e.g., *Hundhausen et al.*, 1970]. However, if the anticorrelation was instantaneous, that is, $n_{sw}(t + 0 \text{ day})$ anticorrelates with $V_{sw}(t)$, then we would expect that $J_e(t + 2 \text{ days})$

to anticorrelate with $n_{sw}(t)$. However, in Section 6.4.2, we show that $J_e(t + 1 \text{ day})$ linearly and nonlinearly anticorrelate with $n_{sw}(t)$, suggesting that other factors may be involved.

To investigate this, we plot in Figure 6.5 $n_{sw}(t + \tau)$ vs. $V_{sw}(t)$ in the same format as in Figures 6.1 and 6.3. Figure 6.5 suggests that n_{sw} anticorrelates with V_{sw} and the relationship is not linear.

Figure 6.6a plots $\text{corr}[n_{sw}(t + \tau), V_{sw}(t)]$ (blue curve) and $\text{corr}[n_{sw}(t), V_{sw}(t + \tau)]$ (red curve). The blue curve has a minimum at $\tau_{min} = 1 \text{ day}$ ($r = -0.56$) and a secondary minimum at $\tau = 28 \text{ days}$ ($r = -0.32$). The red curve has a minimum at $\tau_{min} = 26 \text{ days}$ ($r = -0.30$).

Figure 6.6b plots TE and MI for (n_{sw}, V_{sw}) in a similar manner as in Figures 6.2b and 6.4b. Both, MI and TE for $[n_{sw}(t + \tau), V_{sw}(t)]$, blue and yellow curves, respectively, show a peak at $\tau_{max} = 1 \text{ day}$, which is consistent with the linear correlational analysis. $\text{TE}[n_{sw}(t + 1 \text{ day}), V_{sw}(t)]$ has $it_{max} = 0.20$, $snr = 7.4$ and $\text{significance} = 95\sigma$.

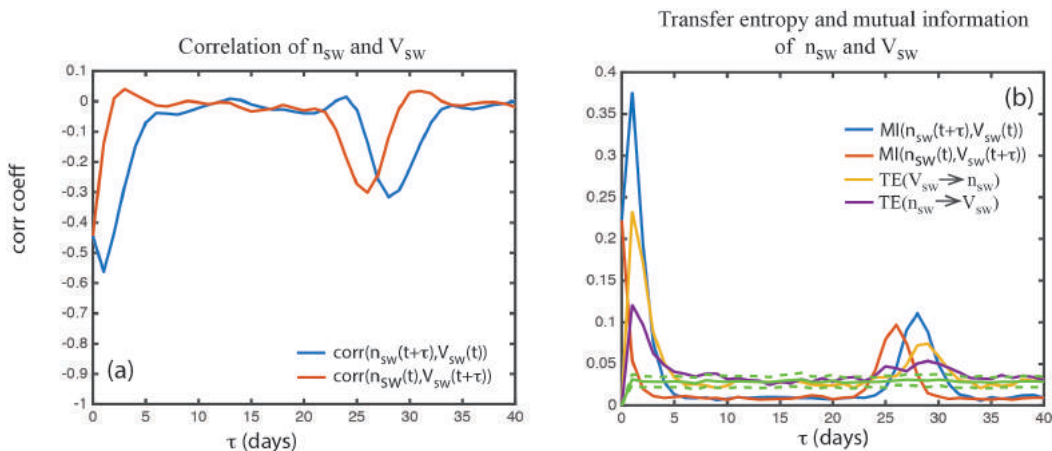


Figure 6.6. (a) Correlation coefficient of $[n_{sw}(t + \tau), V_{sw}(t)]$ (blue) and $[n_{sw}(t), V_{sw}(t + \tau)]$ (red). (b) $\text{MI}[n_{sw}(t + \tau), V_{sw}(t)]$ (blue), $\text{MI}[n_{sw}(t), V_{sw}(t + \tau)]$ (red), $\text{TE}[n_{sw}(t + \tau), V_{sw}(t)]$ (yellow) and $\text{TE}[n_{sw}(t), V_{sw}(t + \tau)]$ (purple). The solid and dashed green curves are the mean and 3σ from the mean of the noise. The transfer of information from n_{sw} to J_e ($n_{sw} \rightarrow V_{sw}$) peaks at $\tau_{max} = 1 \text{ day}$.

From the considerations of the lag times, it is entirely possible that anticorrelation of $[J_e(t + 1 \text{ day}), n_{sw}(t)]$ is caused by $[J_e(t + 2 \text{ days}), V_{sw}(t)]$ correlation and the anticorrelation of $[n_{sw}(t + 1 \text{ day}), V_{sw}(t)]$. Note by correlation here we mean both linear and nonlinear correlations. However, we cannot rule

out that n_{sw} may also influence J_e independently of V_{sw} . To investigate this, we perform CMI calculation as described in Section 6.4.4.

So far, we have determined the lag times at daily resolution because we use daily solar wind and LANL data. The LANL higher time resolution data are not yet available, but the OMNI solar wind data are available at hourly resolution. Hence, we can investigate the $\text{corr}(n_{sw}, V_{sw})$ at hourly resolution.

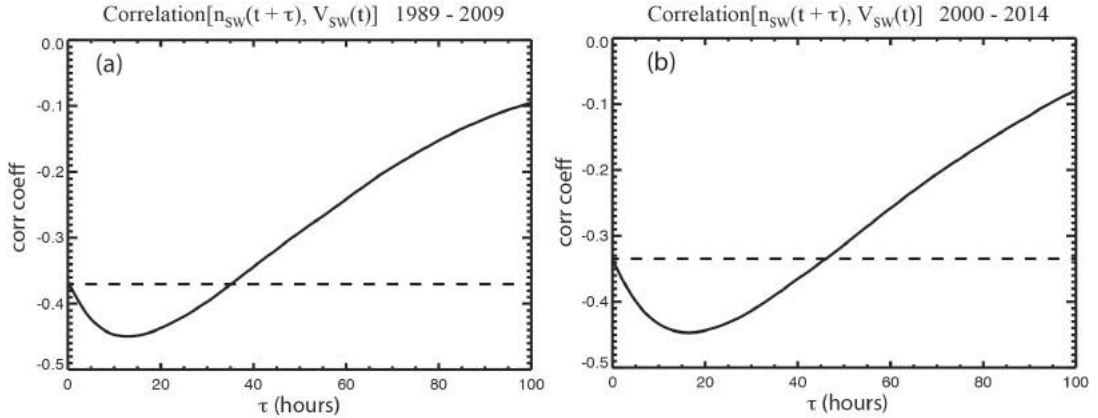


Figure 6.7. Correlation coefficient of $[n_{sw}(t + \tau), V_{sw}(t)]$ for (a) 1989–2009 and (b) 2000–20014 at hourly resolution. The anticorrelation improves with increasing τ , reaching minimum at $\tau_{min} = 14$ and 16 hr in (a) and (b), respectively. The correlation coefficient finally reaches the same value as that at $\tau = 0$ hr (the dashed line) at $\tau = 36$ and 46 hr in (a) and (b).

Figure 6.7a plots the $\text{corr}[n_{sw}(t + \tau), V_{sw}(t)]$ for $\tau = 0$ –100 hr (solid curve). It shows that the correlation reaches a minimum at $\tau_{min} = 14$ hr for the data interval used in the present study 1989–2009. It also shows that n_{sw} anticorrelation with V_{sw} has a broad minimum. To quantify the width of the minimum, we draw a dashed horizontal line that intersects the solid curve at $\tau = 0$ hr and show that the anticorrelation does not worsen than that at $\tau = 0$ hr until $\tau = 36$ hr. However, τ_{min} , the correlation coefficient at τ_{min} , and the width of the minimum are time dependent, which may be related to solar cycle. As an example, Figure 6.7b shows that for the period 2000–2014, $\tau_{min} = 17$ hr and the width of the minimum using the above criterion is about 46 hr. Moreover, Figure 6.6b shows that $\text{TE}[n_{sw}(t + \tau), V_{sw}(t)]$ does not reach the noise level until $\tau > 3$ days, suggesting a rather long period when V_{sw} affects the trailing density, n_{sw} .

6.4.4 Ranking of solar wind parameters based on information transfer to radiation belt electrons

From our analysis above, V_{sw} is a stronger driver of J_e than n_{sw} , i.e., V_{sw} transfers more information to J_e than n_{sw} . For example, $\text{TE}[V_{sw}(t) \rightarrow J_e(t + 2 \text{ days})]$ has $it_{max} = 0.30$ and $snr = 5.7$ while $\text{TE}[n_{sw}(t) \rightarrow J_e(t + 1 \text{ days})]$ has $it_{max} = 0.13$ and $snr = 4.4$. Because V_{sw} anticorrelates with n_{sw} , there is some embedded dependence, so it is necessary to use conditional mutual information (CMI) to determine how much information passes from n_{sw} to J_e , given V_{sw} and vice versa.

To calculate how much information flows from n_{sw} to J_e , given V_{sw} , we calculate $\text{CMI}[J_e(t + \tau), n_{sw}(t) | V_{sw}(t)]$, which is plotted as blue curve in Figure 6.8a. Using a similar approach as for TE, we determine a noise level on surrogates $\text{CMI}[\text{sur}[J_e(t + \tau)], n_{sw}(t) | V_{sw}(t)]$. The mean and σ of the noise are calculated in the same manner as TE (described in Section 6.4.1) and used to determine the significance of the results. The mean noise and 3σ are plotted as solid and dashed green curves respectively. Figure 6.8a shows that $\text{CMI}[J_e(t + \tau), n_{sw}(t) | V_{sw}(t)]$ peaks at $\tau_{max} = 0$ day with $it_{max} = 0.091$ and $snr = 3.2$. The $\tau_{max} = 0$ day suggests that J_e response lag time to n_{sw} is less than 24 hr.

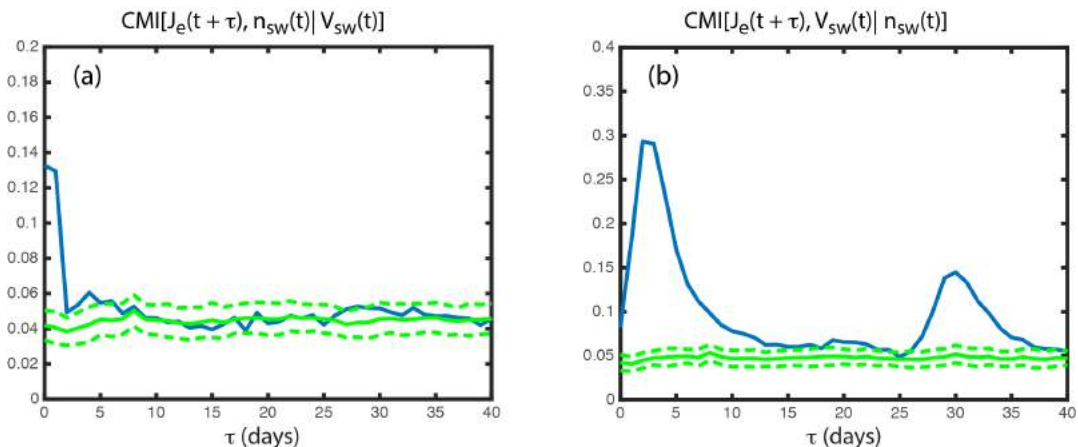


Figure 6.8. Blue curve showing (a) $\text{CMI}[J_e(t + \tau), n_{sw}(t) | V_{sw}(t)]$, and (b) $\text{CMI}[J_e(t + \tau), V_{sw}(t) | n_{sw}(t)]$. The solid and dashed green curves are the mean and 3σ from the mean of the noise. (a) Unlike $\text{TE}[J_e(t + \tau), n_{sw}(t)]$, which peaks at $\tau_{max} = 1$ day, $\text{CMI}[J_e(t + \tau), n_{sw}(t) | V_{sw}(t)]$ peaks at $\tau_{max} = 0$ day ($it_{max} = 0.091$). The smaller τ_{max} comes about because CMI removes the effect of V_{sw} on J_e (see text). (b) The peak in $\text{CMI}[J_e(t + \tau), V_{sw}(t) | n_{sw}(t)]$ ($it_{max} = 0.25$) is broader and has slightly higher snr than that of $\text{TE}[J_e(t + \tau), V_{sw}(t)]$ in Figure 6.2b because CMI removes the effect of n_{sw} , which anticorrelates with J_e . V_{sw} transfers about 2.7 times more information to J_e than n_{sw} .

We can now revisit the J_e response lag times to V_{sw} and n_{sw} . Earlier we establish that $J_e(t + 2 \text{ days})$ correlates with $V_{sw}(t)$ (Figure 6.2), $J_e(t + 1 \text{ day})$ anticorrelates with $n_{sw}(t)$ (Figure 6.4), but $n_{sw}(t + 1 \text{ day})$ anticorrelates with $V_{sw}(t)$ (Figure 6.6). However, our CMI analysis (Figure 6.8) shows that **given** V_{sw} , J_e response lag time to n_{sw} is 0 day ($< 24 \text{ hr}$). This suggests that the $J_e(t + 1 \text{ day})$ anticorrelation with $n_{sw}(t)$ seen in Figure 6.4 mainly comes from $J_e(t + 2 \text{ days})$ correlation with $V_{sw}(t)$ and $V_{sw}(t)$ anticorrelation with $n_{sw}(t + 1 \text{ day})$.

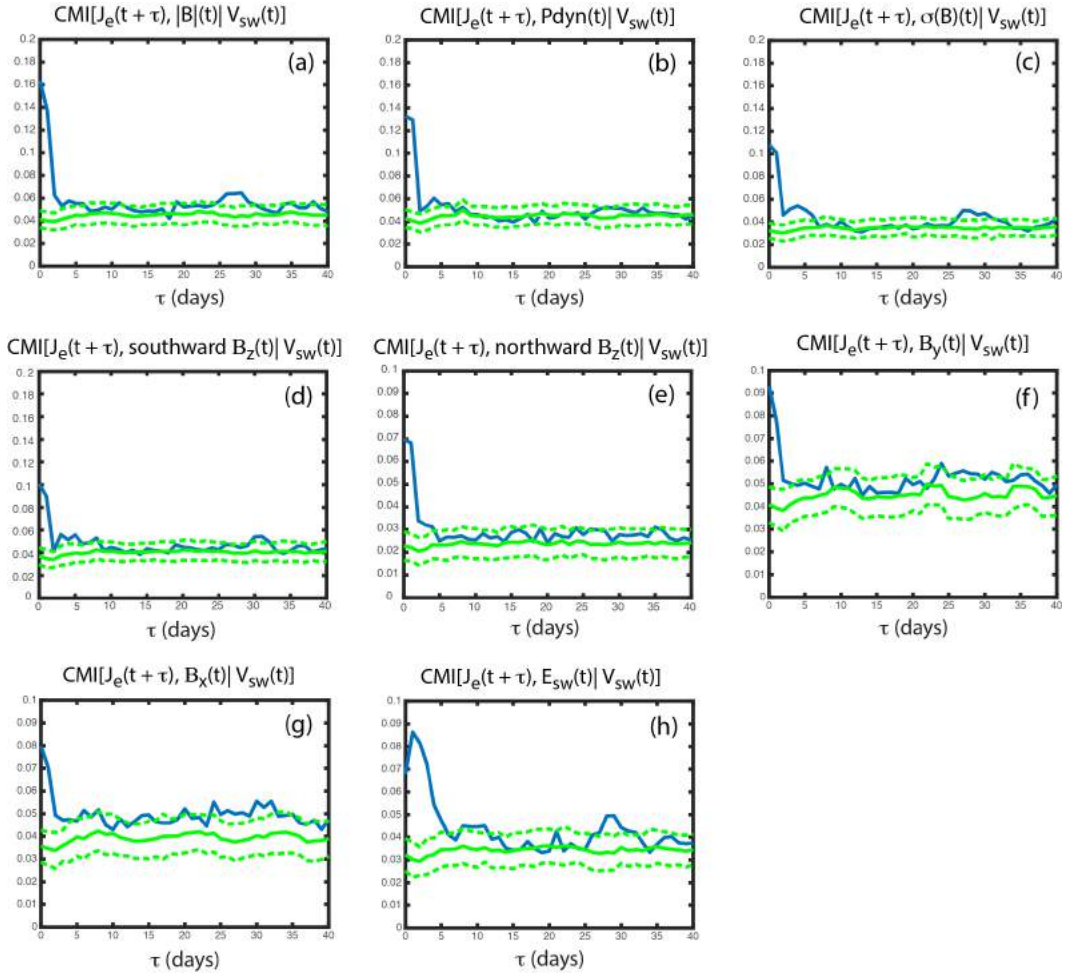


Figure 6.9. Panels a–h plot CMI solar wind parameter with J_e , given V_{sw} for $|\mathbf{B}|$, P_{dyn} , $\sigma(\mathbf{B})$, southward IMF B_z , northward IMF B_z , IMF B_y , IMF B_x , and E_{sw} respectively, as solid blue curves. The solid and dashed green curves are the mean and 3σ from the mean of the noise. The relationships are summarized in Table 6.1. Note that the scale of the y-axis is 0–0.2 for panels a–d and 0–0.1 for panels e–h.

We also calculate $\text{CMI}[J_e(t + \tau), V_{sw}(t) | n_{sw}(t)]$, which is plotted in Figure 6.8b as solid blue curve. The blue curve peaks at $\tau = 2$ days with $it_{max} = 0.25$ which is about 2.7 times larger than the it_{max} of 0.091 for $\text{CMI}[J_e(t + \tau), n_{sw}(t) | V_{sw}(t)]$. Thus, V_{sw} transfers more information to J_e than n_{sw} does.

Interestingly, the peak in $\text{CMI}[J_e(t + \tau), V_{sw}(t) | n_{sw}(t)]$ (Figure 6.8b) is broader than the peak in $\text{TE}[J_e(t + \tau), V_{sw}(t)]$ (Figure 6.2b). The former also has slightly higher snr (6.6) than the latter (5.7). Removing the effect of n_{sw} , which anticorrelates with J_e , has the effect of lowering the noise and increasing the snr .

The above analysis suggests that V_{sw} is the major driver of J_e . Next, we investigate whether other solar wind parameters also contribute to J_e . We calculate the information transfer from $|\text{IMF } \mathbf{B}|$, P_{dyn} , $\sigma(\text{IMF } B)$, southward IMF B_z , northward IMF B_z , IMF B_y , IMF B_x , and solar wind electric field (E_{sw}) to J_e , given V_{sw} . The northward (southward) IMF B_z is calculated from the daily average of the hourly IMF B_z when IMF $B_z > 0$ (IMF $B_z < 0$). The results are plotted in Figure 6.9. Table 6.1 gives the ranking based on the it_{max} of various solar wind parameters. Thus, the ranking gives the importance of each solar wind parameter based on the information transfer to J_e . Table 6.1 also lists τ_{max} for the curves in Figures 6.8 and 6.9, which signifies the lag time when information transfer to J_e maximizes.

Note that the ranking in Table 6.1 is obtained with daily resolution data. It is possible that the ranking of some parameters may change if the data are analyzed at higher time resolution. For example, some studies showed that southward IMF B_z can influence J_e [e.g., *Li et al.*, 2005; *Onsager et al.*, 2007; *Miyoshi and Kataoka*, 2008], but southward IMF B_z is only ranked number 5 in Table 6.1. IMF fluctuates with periods of northward and southward IMF at minutes or tens of minutes timescale. Thus, the low ranking of the southward IMF B_z most likely result from the fluctuations of IMF B_z within one day period [e.g., *Li et al.*, 2001; *Balikhin et al.*, 2011; *Reeves et al.*, 2011]. Consistent with our result, *Li et al.* [2001] found IMF B_z is poorly correlated with J_e at daily resolution. Interestingly, although southward IMF B_z has higher it_{max} than northward IMF B_z , northward IMF B_z has lower noise level and hence higher snr than southward IMF B_z . The τ_{max} for E_{sw} is 1 day, which may be the average of $\tau_{max} = 2$ days for V_{sw} and $\tau_{max} = 0$ day for IMF B_z or IMF $|\mathbf{B}|$.

rank	solar wind parameters	peak information transfer (it_{max})	signal to noise ratio at τ_{max}	significance at τ_{max} (σ)	τ_{max} (days)	prediction horizon (days)
1	V_{sw}	0.25	6.6	94	2	10*
2	$ \mathbf{B} $	0.12	3.9	48	0	2
3	n_{sw}	0.091	3.2	34	0	2
3	P_{dyn}	0.091	3.2	33	0	2
4	$\sigma(B)$	0.075	3.9	48	0	2
5	IMF $B_z <$	0.064	2.7	26	0	2
6	E_{sw}	0.056	2.9	22	1	5
7	IMF B_y	0.052	2.3	20	0	2
8	IMF $B_z >$	0.048	3.1	22	0	2
9	IMF B_x	0.044	2.2	19	0	2

Table 6.1. Ranking of the importance of the solar wind parameters based on information transfer to geosynchronous Mev electron flux (J_e) at τ_{max} , where τ_{max} is the lag time when the information transfer peaks. The peak information transfer (it_{max}) = peak – mean noise, the signal to noise ratio = peak/noise, and significance = $it_{max}/\sigma(\text{noise})$. Noise is calculated from surrogate data (see Section 6.4.1). The prediction horizon gives the lag time when there is no information transfer from the solar wind parameter to J_e . Note that n_{sw} and P_{dyn} are both ranked at number 3 because they have similar it_{max} . Northward IMF has slightly higher snr than southward IMF because northward IMF has lower noise level than southward IMF. * excluding the effect of solar rotation.

6.4.5 Detecting changes in the system dynamic

As described in Section 6.3, transfer entropy from x to y , $TE(x \rightarrow y)$, gives a measure of information transfer from variable x to y . In the solar wind–magnetosphere system, the solar wind driving of the magnetosphere is not constant, depending on the strength of the driver and internal dynamics [e.g., *Wing et al.*, 2005a; *Johnson and Wing*, 2005]. So, the system dynamics may not be stationary. The dynamics of the system can be detected by applying TE to a sliding window of data. Figure 6.10 shows the behavior of windowed $TE[V_{sw}(t) \rightarrow J_e(t + 2 \text{ days})]$ over the course of 0–2500 days since 1989 Jan 1 (a sliding 50 day window is used). One of the key features of the figure is the variation in TE over the course of seven years, indicative of nonstationary dynamics. There are periods when TE has higher values, suggesting stronger solar wind–radiation belt coupling and vice versa. Sections 6.5.4 and 6.5.5 discuss applications of this to the observed triangle distribution [*Reeves et al.*, 2011] and to modeling, respectively.

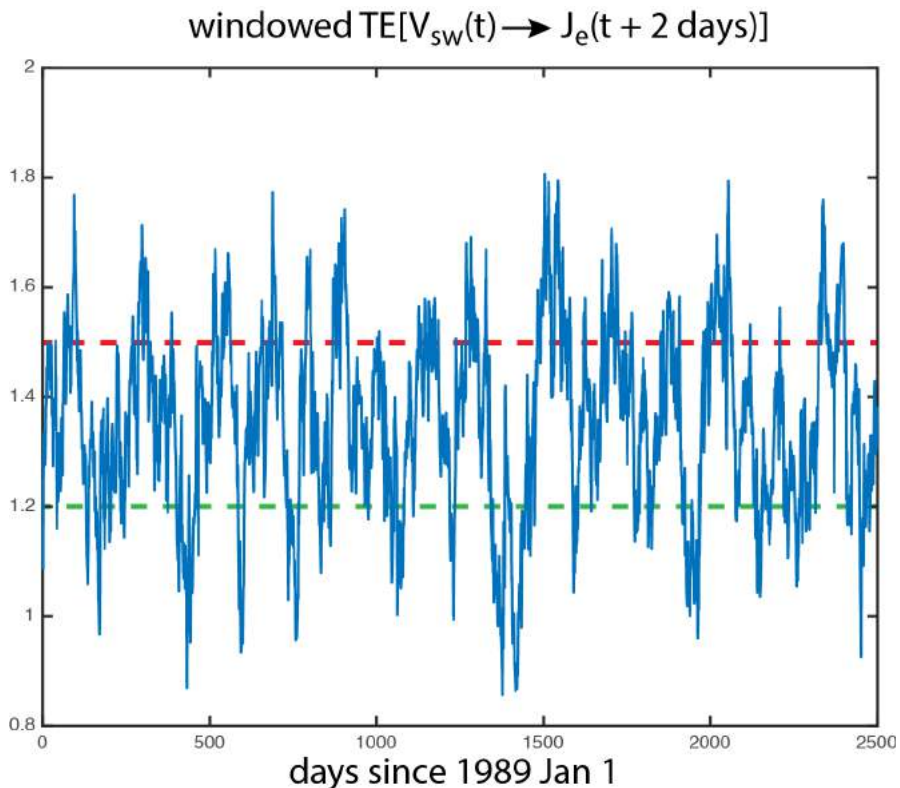


Figure 6.10. Blue curve showing windowed $TE[J_e(t + 2 \text{ days}), V_{sw}(t)]$ over the course of 0–2500 days after 1989 Jan 1. The dynamics in the solar wind–outer radiation belt system changes with time, showing periods of high and low TEs.

6.5 Discussion

6.5.1 Solar wind velocity driving geosynchronous MeV electron flux

Studies suggested that substorm or storm injection processes from the plasma sheet into the inner magnetosphere accelerate low energy electrons from a few keV to ~ 100 keV and once in the inner magnetosphere, wave-electron interactions accelerate the electrons further to several MeV [e.g., *Lyatsky and Khazanov, 2008a; Baker and Kanekal, 2008*]. The mechanisms for accelerating the electrons to MeV energy range generally fall into two categories. In the first mechanism, electron interactions with ULF waves can increase radial diffusion or nonadiabatic transport of electrons resulting in acceleration [e.g., *Baker et al., 1998; Li and Temerin, 2001; Li et al., 2005; Elkington et al., 1999; Rostoker et al., 1998; Ukhorskiy et al., 2005; Mathie and Mann, 2000; 2001; Reeves, 2007; Shprits et al., 2009; Green and Kivelson, 2004; Kellerman and Shprits, 2012*]. The second mechanism is often referred to as local acceleration where acceleration can occur when low energy electrons interact with locally grown waves such as VLF whistler mode waves [*Summers et al., 1998; 2007; Omura et al., 2007; Horne et al., 2005*], or fast magnetosonic waves [e.g., *Horne et al., 2007; Shprits et al., 2008*]. These two mechanisms are not necessarily mutually exclusive.

Figure 6.1 shows that the relationship between J_e and V_{sw} is nonlinear and hence it is necessary to use information theoretical tools to discover the full extent of the relationships between these two parameters. Previous correlational analyses show that $J_e(t + 2 \text{ days})$ correlates best with $V_{sw}(t)$ [e.g., *Reeves et al., 2011; Lyatsky and Khazanov, 2008a*], but correlational analysis only establishes linear correlation and does not establish causality. The present study establishes that $J_e(t + 2 \text{ days})$ and $V_{sw}(t)$ are nonlinearly correlated. Moreover, using TE, we establish that there is an information transfer or causality from V_{sw} to J_e with the same 2 day delay. This result is consistent at least with the first electron acceleration mechanism mentioned above. Large V_{sw} can increase the occurrences of KHI along the magnetopause flanks [e.g., *Fairfield et al., 2000; Johnson et al., 2014; Wing et al., 2005b*], leading to enhancements of ULF waves within the magnetosphere [e.g., *Engebretson et al., 1998; Vennerstrom, 1999*] and electron acceleration. Thus, the process to accelerate the electrons to MeV energy range takes two days, as previously suggested [e.g., *Kellerman and Shprits,*

2012, Reeves *et al.*, 2011]. V_{sw} may also be tied to the local acceleration mechanism through substorm particle injections [e.g., Baker and Kanekal, 2008; Kissinger *et al.*, 2011; Tanskanen, 2009; Kellerman and Shprits, 2012].

6.5.2 n_{sw} and V_{sw} anticorrelation

The anticorrelation of n_{sw} and V_{sw} is well known [e.g., Hundhausen *et al.*, 1970], but the long lag time for this anticorrelation is relatively unknown. The anticorrelation may result from the solar wind high speed streams that originate from the coronal holes, which have higher velocities and lower densities than the background solar wind. Surprisingly, the anticorrelation peaks at $\tau = 14\text{--}16$ hr, depending on the year. It is not clear what causes the lag time to peak at 14–16 hr. This lag time may result from the compression of the leading edge of the high speed stream structure when it encounters the denser background solar wind. Such compression may create slower and denser structure at the leading edge of the high speed stream. As a result, the anticorrelation at the leading edge of the high speed stream is not as good as that at the trailing edge, which may preserve better the high speed–low density structure. Figure 6.6b suggests that there is information transfer from V_{sw} to n_{sw} up to 3–5 days, suggesting perhaps the longevity of the high speed stream structure is about 3–5 days. This property needs to be further investigated.

The correlational analyses of $[n_{sw}(t + 1 \text{ day}), V_{sw}(t)]$ and $[J_e(t + 2 \text{ day}), V_{sw}(t)]$ return correlation coefficients of -0.56 and 0.63 , respectively. So, the former has a slightly lower correlation than the latter (the two set of data have similar size). However, the scatter plots in Figures 6.5b and 6.1c show that both sets of data exhibit nonlinear behaviors. Hence, the linear correlational analysis may not capture the full extent of their relationships. Indeed, analyses with transfer entropy reveal that $\text{TE}[n_{sw}(t + 1 \text{ day}), V_{sw}(t)]$ has comparable significance (95σ) to that of $\text{TE}[J_e(t + 2 \text{ day}), V_{sw}(t)]$ (94σ).

The significant transfer of information from V_{sw} to n_{sw} has implications to the studies of solar wind driving of the magnetosphere that involve n_{sw} and V_{sw} . These studies should take into account the strong anticorrelation between n_{sw} and V_{sw} that can persist even at large lag times. For example, any attempt to isolate the effects of $n_{sw}(V_{sw})$ on the magnetosphere would need to effectively remove the effects of $V_{sw}(n_{sw})$ using CMI or similar methods.

6.5.3 Solar wind density driving geosynchronous MeV electron flux

Balikhin et al. [2011] investigated the control of solar wind parameters on J_e and found that the most dominant solar wind parameter is n_{sw} , which controls about 78% of the variance of J_e with one day lag while V_{sw} only controls 11% of the variance. On the other hand, *Vassiliadis et al.* [2005] examined the geoeffectiveness of 17 solar wind and magnetospheric parameters and found that n_{sw} is weakly linked to J_e in the outer radiation belts. Other studies found that V_{sw} is the most dominant driver of J_e [e.g., *Li et al.*, 2001; *Vassiliadis et al.*, 2005; *Kellerman and Shprits*, 2012; *Ukhorskiy et al.*, 2004].

The present study finds that $J_e(t + 1 \text{ day})$ anticorrelates with $n_{sw}(t)$. The lag time of 1 day is consistent with that found in *Balikhin et al.* [2011]. However, $n_{sw}(t + 1 \text{ day})$ anticorrelates with $V_{sw}(t)$. Moreover, $\text{CMI}[J_e(t + \tau), n_{sw}(t) | V_{sw}(t)]$ peaks at $\tau = 0$ day, suggesting that given V_{sw} , J_e responds to n_{sw} in < 24 hr. Hence, J_e response lag time of 1 day to n_{sw} in Figure 6.4 and in *Balikhin et al.* [2011] can be attributed mainly to $J_e(t + 2 \text{ days})$ correlation with $V_{sw}(t)$, and $V_{sw}(t)$ anticorrelation with $n_{sw}(t + 1 \text{ day})$. Figure 6.8 and Table 6.1 show that V_{sw} by far is the dominant driver of J_e , transferring 2.7 times more information to J_e than n_{sw} does.

Lyatsky and Khazanov [2008b] assumed that the anticorrelation of V_{sw} and n_{sw} is weak in their analysis of the effect of Kp and n_{sw} on J_e . They concluded that n_{sw} has a strong effect on J_e within 2 days before geomagnetic disturbances. However, some of the effects attributed to n_{sw} may be due to V_{sw} in their study. Figures 6.6 and 6.7 show that the anticorrelation of V_{sw} and n_{sw} is not trivial and any attempt to interpret the effects of n_{sw} and V_{sw} on J_e should take into account the anticorrelation of V_{sw} and n_{sw} . To illustrate, $\text{TE}[n_{sw}(t) \rightarrow J_e(t + 1 \text{ days})]$ has $it_{max} = 0.13$, but removing the effects of V_{sw} , the it_{max} drops $\sim 30\%$ to 0.091 ($\text{CMI}[J_e(t + 0 \text{ day}), n_{sw}(t) | V_{sw}(t)] = 0.091$).

An increase in n_{sw} would increase solar wind dynamic pressure (P_{dyn}), which, in turn, would push the magnetopause inward, leading to electron losses at the high L shell [e.g., *Li et al.*, 2001]. Furthermore, the magnetopause compression would drive ULF waves [e.g., *Korotova and Sibeck*, 1995; *Kepko and Spence*, 2003; *Claudepierre et al.*, 2010] leading to fast radial diffusion, which redistributes the losses to the magnetopause to lower L shells, including at geosynchronous orbit [*Shprits et al.*, 2006; *Kellerman and Shprits*, 2012; *Turner et al.*, 2012]. *Ukhorskiy et al.* [2006] uses a test particle simulation to demonstrate

this scenario, which is known as magnetopause shadowing. However, *Lyatsky and Khazanov* [2008a] reports that the correlation between P_{dyn} and J_e is poor and suggests that compression of the magnetosphere is probably not the main factor for the electron losses. *Kellerman and Shprits* [2012] examines various mechanisms for the losses and suggest that further investigation is needed. Our result suggests that based on information transfer from n_{sw} to J_e , any mechanism for n_{sw} anticorrelation with J_e has to operate within < 24 hr (Figure 6.8a). We note that the magnetospheric compression due to an increase in n_{sw} or P_{dyn} would be nearly instantaneous, although it is not clear how long it would take for the electron losses to redistribute radially. We also note that as shown in Table 6.1, based on transfer of information to J_e , P_{dyn} is ranked number 3 (tie with n_{sw}) because $CMI[J_e(t + \tau), P_{dyn}(t) | V_{sw}(t)]$ has properly taken out the effect of V_{sw} and hence the responses to n_{sw} and P_{dyn} are similar. In any case, the importance of P_{dyn} to J_e is not as insignificant as previously suggested.

6.5.4 Revisiting the triangle distribution

Reeves et al. [2011] is the first to note the right triangle distribution exhibited in Figure 6.1a. Figure 6.1a plots $J_e(t + \tau)$ vs. $V_{sw}(t)$ with no delay, $\tau = 0$. However, we note that as shown in Figures 6.1b and 6.1c, even with $\tau = 1$ or 2 days, respectively, the triangle distribution is still evident albeit not as prominent as for $\tau = 0$. For example, the triangle distribution can still be seen in Figure 6.1c, which is replotted in Figure 6.11a without the contour overlays. *Reeves et al.* [2011] notes that the left hand side of the triangle forms because V_{sw} rarely goes below 300 km s^{-1} . The hypotenuse of the triangle suggests that the lower limit of J_e more or less increases with V_{sw} . The top side of the triangle suggests that J_e saturates, which can be attributed to local instabilities [*Kennel and Petschek*, 1966]. *Reeves et al.* [2011] considers this and other possible explanations for the J_e saturation. As noted by *Reeves et al.* [2011], the most interesting and perhaps mystifying aspect of the triangle distribution is that high J_e is observed for all V_{sw} conditions and the variability of J_e at lower V_{sw} is much larger than that at higher V_{sw} .

Reeves et al. [2011] notes that the triangle distribution appears in the declining phase of the solar maximum, but it vanishes during solar maximum (although high J_e and low V_{sw} points still appear during solar maximum). This dependence of solar cycle suggests that perhaps the mode in which the solar wind

couples to magnetosphere/radiation belt can be a factor. We probe the possible effects of solar wind–radiation belt coupling further with information theoretical tools. Particularly, we separate the points in Figure 6.11a based on the information transfer from V_{sw} to J_e .

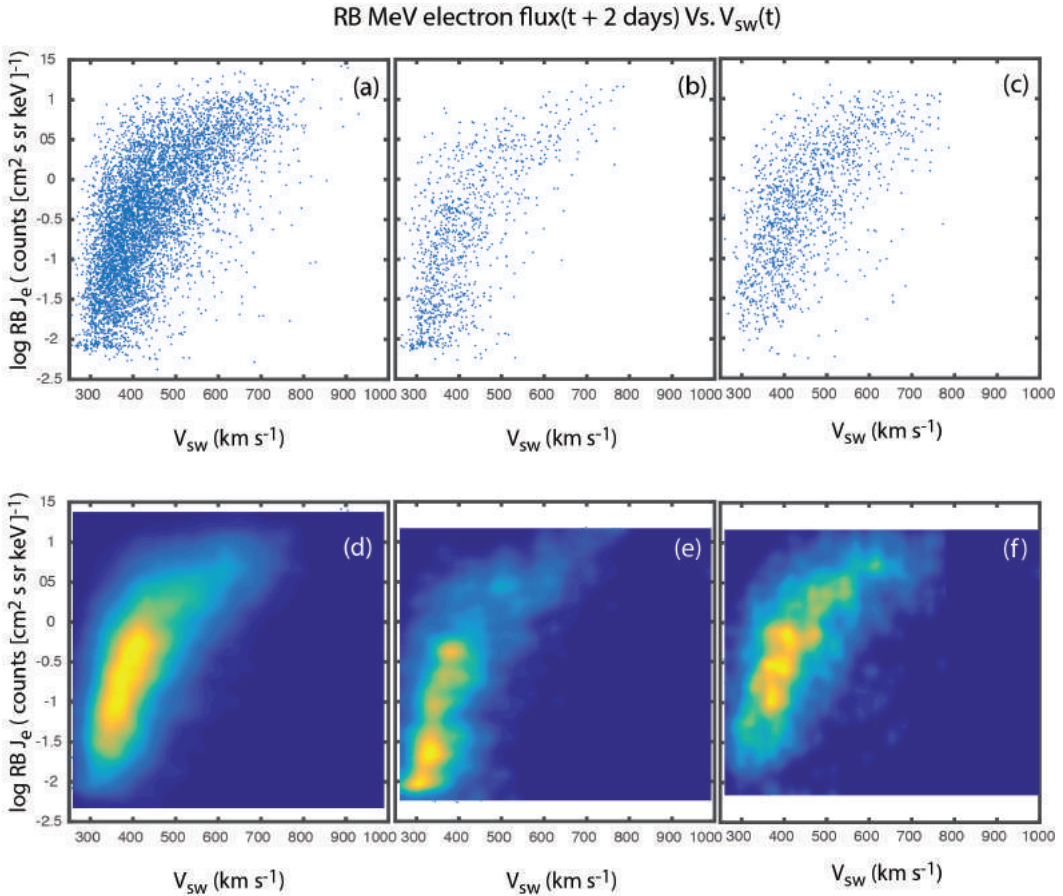


Figure 6.11. (a) Scatter plot of $\log J_e(t + 2 \text{ days})$ vs. $V_{sw}(t)$ showing the triangle distribution. This is similar to Figure 6.1c, but without the density contours. (b) The points in (a) are plotted when $\text{TE}[J_e(t + 2 \text{ days}), V_{sw}(t)] < 1.2$ (below the green dashed line in Figure 6.10). (c) The points in (a) are plotted when $\text{TE}[J_e(t + 2 \text{ days}), V_{sw}(t)] > 1.5$ (above the red dashed line in Figure 6.10). The distributions in (b) and (c) differ and both do not have the same triangle distribution as in (a). Panels (d), (e), and (f) show the data density maps of the data in panels (a), (b), and (c), respectively. Panels (e) and (f) reinforce the differences in the data distributions in panels (b) and (c).

Figure 6.11b shows $J_e(t + 2 \text{ days})$ vs. $V_{sw}(t)$ when $\text{TE}[V_{sw}(t) \rightarrow J_e(t + 2 \text{ days})]$ is below 1.2, below the dashed green line in Figure 6.10. Figure 6.11c plots the points when TE is above 1.5, above the dashed red line in Figure 6.10. It is clear that the data distribution in Figure 6.11b looks different than that in Figure 6.11c. Also, the triangle distribution in Figure 6.11a is not reproduced in Figure 6.11b nor in Figure 6.11c. Although Figure 6.11c still shows a triangle, the triangle, which is not a right triangle, shows a different characteristic that that in Figure 6.11a.

Figures 6.11b and 6.11c contrast the differences between low and high TE cases. Figure 6.11b shows that (1) most of the points tend to have $V_{sw} < 500 \text{ km s}^{-1}$ and (2) excluding points with $V_{sw} > 500 \text{ km s}^{-1}$, J_e tends to have only weak dependency on V_{sw} and the distribution looks more like a rectangle than a triangle. On the other hand, Figure 6.11c shows that (1) the points tend to have more uniform distribution in velocity; (2) the hypotenuse of the triangle in Figure 6.11a that shows the lower limit of J_e increases with V_{sw} can still be seen, (3) unlike in Figure 6.11a where the left side of the triangle is nearly parallel to the y -axis, the left side of the triangle now has a positive slope, suggesting that J_e increases with V_{sw} ; and (4) for $V_{sw} \geq 600 \text{ km s}^{-1}$, the higher limit of J_e saturates as in Figure 6.11a. In general, Figure 6.11c shows stronger dependence of J_e on V_{sw} than Figures 6.11a or 6.11b. The large spread of J_e at lower V_{sw} in the parent triangle distribution in Figure 6.11a appears smaller in Figure 6.11c. Thus, during the periods when TE is large, there is a large information transfer from V_{sw} to J_e , and we can see that indeed there is a stronger dependence of J_e on V_{sw} .

Figures 6.11d, 6.11e, and 6.11f show the data density maps of Figures 6.11a, 6.11b, and 6.11c, respectively. Figures 6.11e and 6.11f help draw sharper contrasts between the distributions in Figures 6.11b and 6.11c. There are proportionally more points with higher J_e and stronger dependency of J_e on V_{sw} in Figure 6.11f than in in Figure 6.11e.

We investigate further the large spread of J_e at lower V_{sw} that can be seen in Figure 6.11a. The $\log J_e$ vs. V_{sw} data in Figure 6.11a are binned in $0.3 \text{ counts (cm}^2 \text{ s sr keV)}^{-1} \times 30 \text{ km s}^{-1}$ bins. From Figure 6.10, we have calculated windowed TE for each point in the dataset. We then assign the windowed TE for each point in the $\log J_e$ vs. V_{sw} bins. Figure 6.12 shows the mean TE in each bin. Bins with fewer than 15 points are not displayed. The figure shows that for $V_{sw} < 500 \text{ km s}^{-1}$, there is a large spread of J_e . However, these J_e s are well ordered by TE. Large TE corresponds to large J_e and conversely small TE corresponds to

small J_e . This suggests for $< 500 \text{ km s}^{-1}$, when there is small information transfer from V_{sw} to J_e , J_e is small and vice versa. We have also binned the data in Figure 6.11b in similar manner and obtained similar result, albeit with higher noise due to lower statistics in the bins.

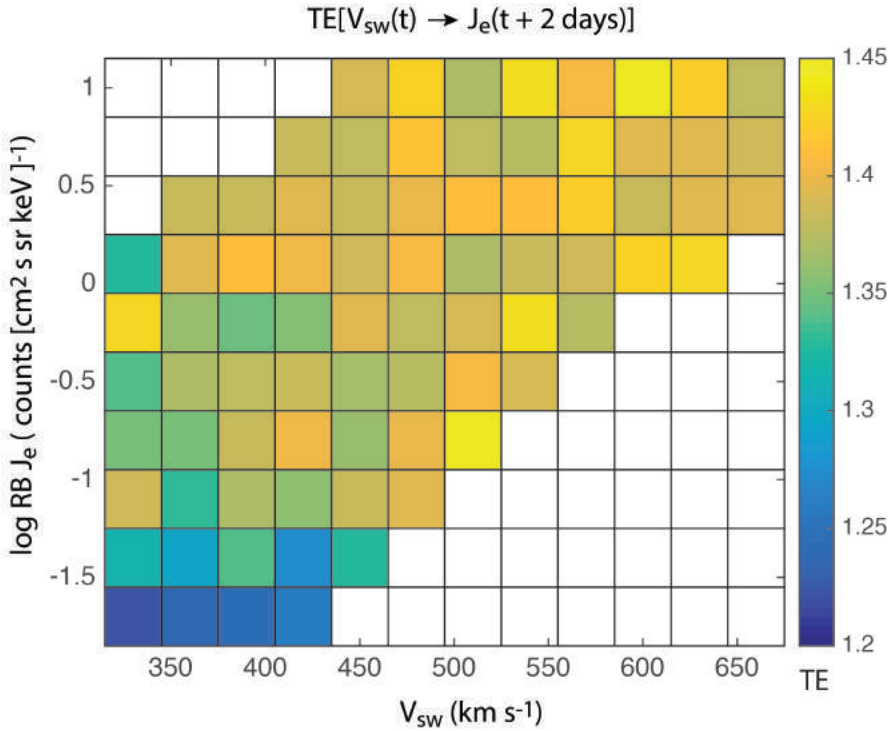


Figure 6.12. Mean $TE[V_{sw}(t) \rightarrow J_e(t + 2 \text{ days})]$ of each bin in $J_e(t + 2 \text{ days})$ vs. $V_{sw}(t)$ distribution shown in Figure 6.11a. The bin size is $0.3 \text{ counts (cm}^2 \text{ s sr keV)}^{-1} \times 30 \text{ km s}^{-1}$. Figure 6.11a shows that at $V_{sw} < 500 \text{ km s}^{-1}$, J_e has a large variance as previously shown, but it turns out that these points are well ordered by TE. Low J_e corresponds to low TE and vice versa.

Balikhin et al. [2011] suggests that the triangle distribution can be attributed to n_{sw} and *Kellerman and Shprits* [2012] suggests the saturation of J_e in the triangle distribution can be attributed to n_{sw} . Our analysis in Section 6.4.4 certainly supports the argument that n_{sw} has a significant effect on J_e . We investigate further the effect of n_{sw} on the triangle distribution. We assign $n_{sw}(t)$ for each point in the $\log J_e(t + 2 \text{ days})$ vs. $V_{sw}(t)$ scatter plot in Figure 6.11a. These points are then binned using the same bin size as in Figure 6.12. Figure 6.13a shows the mean n_{sw} of each bin. As in Figure 6.12, bins with fewer than 15 points are not displayed. The most prominent trend in Figure 6.13a is a strong

density gradient in the x direction because n_{sw} anticorrelates with V_{sw} .

However, our analysis and Figure 6.8a suggests that the maximum transfer of information from $n_{sw}(t)$ to $J_e(t + \tau)$ occurs at $\tau = 0$ day (< 24 hr). Hence, instead of assigning $n_{sw}(t)$ to each point in the $J_e(t + 2 \text{ days})$ vs. $V_{sw}(t)$ plot, we assign $n_{sw}(t + 2 \text{ days})$ so that J_e is not time shifted with respect to n_{sw} . We repeat the same procedure done for Figure 6.13a and the result is shown in Figure 6.13b. Now, there are density gradients in both x and y directions. As in Figure 6.13a, the density gradient in the x direction is due to the anticorrelation of n_{sw} with V_{sw} . Figure 6.13b clearly shows that for $V_{sw} < 500 \text{ km s}^{-1}$, larger n_{sw} hence larger P_{dyn} can be associated with lower J_e and vice versa. This density gradient in the y direction may be attributed to the magnetopause shadowing effect, which rapidly depletes radiation belt fluxes when solar wind pressure is increased, as discussed in Section 6.5.3.

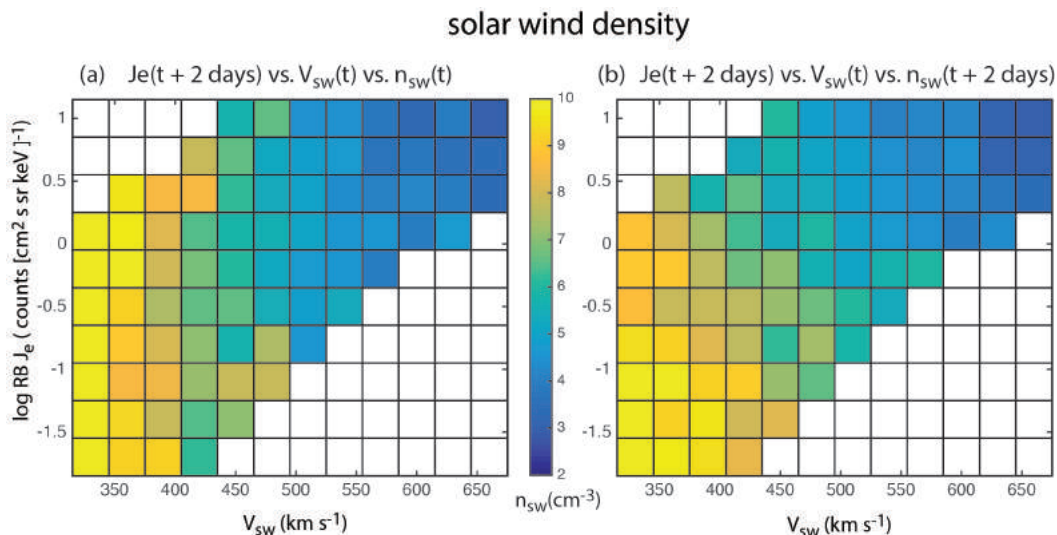


Figure 6.13. Points in $J_e(t + 2 \text{ days})$ vs. $V_{sw}(t)$ distribution in Figure 6.11a are binned in $0.3 \text{ counts } (\text{cm}^2 \text{ s sr keV})^{-1} \times 30 \text{ km s}^{-1}$ bins. Each point is assigned its $n_{sw}(t)$ and $n_{sw}(t + 2 \text{ days})$ values. The latter has no time shift with respect to J_e such that information transfer from n_{sw} to J_e maximizes. (a) shows the mean $n_{sw}(t)$ while (b) shows the mean $n_{sw}(t + 2 \text{ days})$ of each bin. In (a), the density gradient is mainly in the x direction due to the anticorrelation between n_{sw} and V_{sw} . However, in (b), there are density gradients in x and y direction. The latter can be attributed to P_{dyn} and magnetopause shadowing.

Figure 6.13b shows that large V_{sw} can be associated with large J_e and small n_{sw} . The latter can be mostly attributed to the anticorrelation of n_{sw} with V_{sw} .

Figure 6.13b also shows that large n_{sw} can decrease J_e , consistent with our analysis in Section 6.5.3, but it is not clear if n_{sw} alone can explain why small V_{sw} (< 500 km s⁻¹) can lead to high J_e and saturation of J_e for small n_{sw} . The high J_e and the saturation of J_e when $V_{sw} < 500$ km s⁻¹ can probably be attributed to the strong solar wind–radiation belt coupling as suggested by the high TE in Figure 6.12.

6.5.5 Improving models with information theory

Tools based on information theory can be used to improve modeling. Several ideas are discussed below.

6.5.5.1 Selecting input parameters

Often the first step in developing a parametric forecasting model is to decide which parameters should be used as inputs to the model. Using TE and CMI, one can determine the ranking of each parameter based on information transfer from the input to the output parameters. For example, Table 6.1 shows the ranking of solar wind parameters for solar wind–outer radiation belt system at daily resolution.

6.5.5.2 Detecting nonstationarity in system dynamics

As shown in Figure 6.10, TE can be used to detect changes in the system dynamics, e.g., nonstationarity of the system dynamics. Higher TE suggests that the solar wind–radiation belt system is more tightly coupled and vice versa. Figures 6.11b and 6.11c show visually the differences in the dynamics for low and high TE cases in J_e vs. V_{sw} . In this case, TE can help decompose the triangle distribution into something that can be more easily understood. This kind of information can help modelers. For example, modelers may want to create a model that varies the coupling function strength within the model, depending on the value of TE. Alternatively, two separate models may be developed: one for low TE and one for high TE.

6.5.5.3 Prediction horizon

TE shows how much information is transferred from the input time series x to output time series y . When TE is significantly above the noise level, it suggests that there is hope for the model to predict parameter y . Conversely,

when TE is at noise level, there is not much information transfer from x to y and hence it can be expected that x would not be able to predict y accurately.

For example, Figure 6.8a suggests that n_{sw} transfers the most information to J_e at $\tau_{max} = 0$ day, but the blue curve falls rapidly at $\tau > 2$ days, suggesting that little information is transferred from n_{sw} to J_e after 2 day lag time. Hence, the prediction horizon for using n_{sw} to predict J_e is about 1 day. Here we use mean noise + 3σ as the noise threshold, but using different threshold criterion would yield different prediction horizon. Likewise, Figure 6.8b suggests that the prediction horizon for using V_{sw} to predict J_e is about 7–10 days. Table 6.1 lists the prediction horizon for the parameters considered in the present study.

6.6 Summary

The present study applies information theoretical tools to investigate the solar wind drivers of the geosynchronous MeV electron fluxes. The following lists the summary of our results.

1. V_{sw} , n_{sw} , $|\mathbf{B}|$, P_{dyn} , $\sigma(B)$, E_{sw} , IMF B_x , IMF B_y , and IMF B_z (southward and northward) are causally related to J_e , but the amount of information transfer from each of this parameter to J_e differs. The ranking of these ten parameters in terms of information transfer is given in Table 6.1.
2. V_{sw} is the most dominant driver and the transfer of information from time series $V_{sw}(t)$ to $J_e(t + \tau)$ peaks at $\tau_{max} = 2$ days. V_{sw} transfers 2.7 times more information to J_e than n_{sw} .
3. Although the anticorrelation between n_{sw} and V_{sw} is perhaps well known, the large and persistent lag times for this anticorrelation is relatively unknown. $n_{sw}(t + \tau)$ anticorrelates with $V_{sw}(t)$ with $\tau_{max} = 14$ – 16 hr, but the exact τ_{max} has time dependence. It is not clear what causes τ_{max} of 14–16 hr. This may be due to the compression of the leading edge of the high speed stream when it encounters the denser background solar wind. Analyses of solar wind driving of the magnetosphere involving V_{sw} and n_{sw} should take into account this anticorrelation that can persist even at large lag times, up to 3–5 days. For example, the information transfer from n_{sw} to J_e drops 30% after the effects of V_{sw} are removed.
4. $J_e(t + 1 \text{ day})$ anticorrelates with $n_{sw}(t)$, but the 1 day lag and the anticorrelation

are mainly due to (1) $J_e(t + 2 \text{ days})$ correlation with $V_{sw}(t)$, and (2) $V_{sw}(t)$ anticorrelation with $n_{sw}(t + 1 \text{ day})$. Given V_{sw} , the transfer of information from $n_{sw}(t)$ to $J_e(t + \tau)$ peaks at $\tau_{max} = 0 \text{ day}$ ($< 24 \text{ hr}$), suggesting the loss mechanism due to n_{sw} or P_{dyn} has to operate in $< 24 \text{ hr}$.

5. The triangle distribution in J_e vs. V_{sw} plot, J_e shows a large variability for $V_{sw} < 500 \text{ km s}^{-1}$. However, these points are well ordered by their TE values: high TE corresponds to high J_e and vice versa. The triangle distribution can be decomposed to low and high TE cases. In the low TE case, the distribution looks more like a rectangle for $V_{sw} < 500 \text{ km s}^{-1}$, suggesting that V_{sw} has little influence on J_e in these conditions. In the high TE case, the lower and upper limits of J_e increase with V_{sw} for $V_{sw} < 600 \text{ km s}^{-1}$, but for $V_{sw} \geq 600 \text{ km s}^{-1}$, the higher limit of J_e saturates.
6. TE and CMI can be used effectively to improve modeling by (1) selecting model input parameters, (2) detecting changes in the dynamics of the system, and (3) determining prediction horizon. Table 6.1 gives this information for solar wind–outer radiation belt system.

The present study uses daily resolution LANL data. Reeves et al. [2013] investigated longer term relationships between J_e and V_{sw} . They found that longer-term, 1-month to 1-year, averages show much stronger correlations than 1-day averages. They showed that this is not just because there is more “noise” superposed on a linear distribution. The distribution of $\log J_e$ around the baseline (the yearly mean) is very stable throughout the solar cycle. It would be interesting to apply our information theoretical tools to this normalized (rebaselined) data. It would also be interesting to apply our tools to higher resolution data, e.g., hourly resolution data.

6.7 References

- Baker, D. N., R. L. McPherron, T. E. Cayton, and R. W. Klebesadel (1990), Linear prediction filter analysis of relativistic electron properties at $6.6 R_E$, *J. Geophys. Res.*, 95(A9), 15133–15140, doi:10.1029/JA095iA09p15133.
- Baker, D. N., X Li, J. B Blake, S. Kanekal (1998), Strong electron acceleration in the Earth's magnetosphere, *Adv. Space Res.*, 21, 609-613, doi:10.1016/S0273-1177(97)00970-8.
- Baker, D. N., and S. G. Kanekal (2008), Solar cycle changes, geomagnetic

- variations, and energetic particle properties in the inner magnetosphere, *J. Atmos. Sol. Terr. Phys.*, 70, 1950–206, doi:10.1016/j.jastp.2007.08.031.
- Balikhin, M. A., R. J. Boynton, S. A. Billings, M. Gedalin, N. Ganushkina, D. Coca, and H. Wei (2010), Data based quest for solar wind-magnetosphere coupling function, *Geophys. Res. Lett.*, 37, L24107, doi:10.1029/2010GL045733.
- Balikhin, M. A., R. J. Boynton, S. N. Walker, J. E. Borovsky, S. A. Billings, and H. L. Wei (2011), Using the NARMAX approach to model the evolution of energetic electrons fluxes at geostationary orbit, *Geophys. Res. Lett.*, 38, L18105, doi:10.1029/2011GL048980.
- Bale, S. D., J. C. Kasper, G. G. Howes, E. Quataert, C. Salem, and D. Sundkvist (2009), Magnetic fluctuation power near proton temperature anisotropy instability thresholds in the solar wind, *Phys. Rev. Lett.*, 103, 211101, doi:10.1103/PhysRevLett.103.211101.
- Belian, R. D., G. R. Gisler, T. Cayton, and R. Christensen (1992), High-Z energetic particles at geosynchronous orbit during the Great Solar Proton Event Series of October 1989, *J. Geophys. Res.*, 97(A11), 16897–16906, doi:10.1029/92JA01139
- Borovsky, J. E., M. F. Thomsen, and R. C. Elphic (1998), The driving of the plasma sheet by the solar wind, *J. Geophys. Res.*, 103, 17,617–17,640, doi:10.1029/97JA02986.
- Camporeale, E. (2015), Resonant and nonresonant whistlers-particle interaction in the radiation belts. *Geophys. Res. Lett.*, 42, 3114–3121, doi: 10.1002/2015GL063874.
- Camporeale, E., and G. Zimbardo (2015). Wave-particle interactions with parallel whistler waves: nonlinear and time-dependent effects revealed by Particle-in-Cell simulations. *Physics of Plasmas* 22, 092104, doi:http://dx.doi.org/10.1063/1.4929853.
- Claudepierre, S. G., M. K. Hudson, W. Lotko, J. G. Lyon, and R. E. Denton (2010), Solar wind driving of magnetospheric ULF waves: Field line resonances driven by dynamic pressure fluctuations, *J. Geophys. Res.*, 115, A11202, doi:10.1029/2010JA015399.
- Darbellay, G. A., and I. Vajda (1999), Estimation of the Information by an Adaptive Partitioning of the Observations Space, *IEEE Transactions on Information Theory*, 45, 1315–1321.
- De Michelis, P., G. Consolini, M. Materassi, and R. Tozzi (2011), An information theory approach to the storm-substorm relationship, *J. Geophys. Res.*, 116,

A08225, doi:10.1029/2011JA016535.

- Elkington, S. R., M. K. Hudson, and A. A. Chan (1999), Acceleration of relativistic electrons via drift-resonant interaction with toroidal-mode Pc-5 ULF oscillations, *Geophys. Res. Lett.*, 26, 3273.
- Engebretson, M., K.-H. Glassmeier, M. Stellmacher, W. J. Hughes, and H. Lühr (1998), The dependence of high-latitude PcS wave power on solar wind velocity and on the phase of high-speed solar wind streams, *J. Geophys. Res.*, 103(A11), 26271–26283, doi:10.1029/97JA03143.
- Fairfield, D. H., A. Otto, T. Mukai, S. Kokubun, R. P. Lepping, J. T. Steinberg, A. J. Lazarus, and T. Yamamoto (2000), Geotail observations of the Kelvin-Helmholtz instability at the equatorial magnetotail boundary for parallel northward fields, *J. Geophys. Res.*, 105(A9), 21159–21173, doi:10.1029/1999JA000316.
- Green, J. C., and M. G. Kivelson (2004), Relativistic electrons in the outer radiation belt: Differentiating between acceleration mechanisms, *J. Geophys. Res.*, 109, A03213, doi:10.1029/2003JA010153.
- Horne, R. B., R. M. Thorne, S. A. Glauert, J. M. Albert, N. P. Meredith, and R. R. Anderson (2005), Timescale for radiation belt electron acceleration by whistler mode chorus waves, *J. Geophys. Res.*, 110, A03225, doi:10.1029/2004JA010811
- Horne, R. B., R. M. Thorne, S. A. Glauert, N. P. Meredith, D. Pokhotelov, and O. Santolík (2007), Electron acceleration in the Van Allen radiation belts by fast magnetosonic waves, *Geophys. Res. Lett.*, 34, L17107, doi:10.1029/2007GL030267.
- Hundhausen, A. J., S. J. Bame, J. R. Asbridge, and S. J. Sydoriak (1970), Solar wind proton properties: Vela 3 observations from July 1965 to June 1967, *J. Geophys. Res.*, 75(25), 4643–4657, doi:10.1029/JA075i025p04643
- Jaynes, A. N., et al. (2015), Source and seed populations for relativistic electrons: Their roles in radiation belt changes, *J. Geophys. Res. Space Physics*, 120, 7240–7254, doi:10.1002/2015JA021234.
- Johnson, J. R., and S. Wing (2005), A solar cycle dependence of nonlinearity in magnetospheric activity, *J. Geophys. Res.*, 110, A04211, doi:10.1029/2004JA010638.
- Johnson, J. R., and S. Wing (2014), External versus internal triggering of substorms: An information-theoretical approach, *Geophys. Res. Lett.*, 41, 5748–5754, doi:10.1002/2014GL060928.
- Johnson, J. R., S. Wing, and P. A. Delamere (2014), Kelvin Helmholtz Instability

- in Planetary Magnetospheres, *Space Sci. Rev.*, 184, 1–31, doi:10.1007/s11214-014-0085-z.
- Kellerman, A. C., and Y. Y. Shprits (2012), On the influence of solar wind conditions on the outer-electron radiation belt, *J. Geophys. Res.*, 117, A05217, doi:10.1029/2011JA017253.
- Kennel, C. F., and H. E. Petschek (1966), Limit on stably trapped particle fluxes, *J. Geophys. Res.*, 71(1), 1–28, doi:10.1029/JZ071i001p00001.
- Kepko, L., and H. E. Spence (2003), Observations of discrete, global magnetospheric oscillations directly driven by solar wind density variations, *J. Geophys. Res.*, 108, 1257, doi:10.1029/2002JA009676
- Kissinger, J., R. L. McPherron, T.-S. Hsu, and V. Angelopoulos (2011), Steady magnetospheric convection and stream interfaces: Relationship over a solar cycle, *J. Geophys. Res.*, 116, A00I19, doi:10.1029/2010JA015763.
- Korotova, G. I., and D. G. Sibeck (1995), A case study of transient event motion in the magnetosphere and in the ionosphere, *J. Geophys. Res.*, 100(A1), 35–46, doi:10.1029/94JA02296.
- Li, W. (1990), Mutual Information Functions Versus Correlation Functions, *J. Stat. Phys.*, 60, 823–837.
- Li, X., and M. A. Temerin (2001), The electron radiation belt, *Space Sci. Rev.*, 95, 569 - 580.
- Li, X., M. Temerin, D. Baker, G. Reeves, and D. Larson (2001), Quantitative prediction of radiation belt electrons at geostationary orbit based on solar wind measurements, *Geophys. Res. Lett.*, **28**(9), 1887–1890.
- Li, X., D. N. Baker, M. Temerin, G. Reeves, R. Friedel, and C. Shen (2005), Energetic electrons, 50 keV to 6 MeV, at geosynchronous orbit: Their responses to solar wind variations, *Space Weather*, 3, S04001, doi:10.1029/2004SW000105.
- Lyatsky, W., and G. V. Khazanov (2008a), Effect of solar wind density on relativistic electrons at geosynchronous orbit, *Geophys. Res. Lett.*, 35, L03109, doi:10.1029/2007GL032524.
- Lyatsky, W., and G. V. Khazanov (2008b), Effect of geomagnetic disturbances and solar wind density on relativistic electrons at geostationary orbit, *J. Geophys. Res.*, 113, A08224, doi:10.1029/2008JA013048.
- Materassi, M., L. Ciruolo, G. Consolini, and N. Smith (2011), Predictive Space Weather: An information theory approach, *Adv. Space Res.*, 47, 877–885, doi:10/106/j.asr.2010.10.026.
- Mathie, R. A., and I. R. Mann (2000), A correlation between extended intervals of

ULF wave power and storm-time geosynchronous relativistic electron flux enhancements, *Geophys. Res. Lett.*, **27**, 3621–3264, doi:10.1029/2000GL003822.

- Mathie, R. A., and I. R. Mann (2001), On the solar wind control of Pc5 ULF pulsation power at mid-latitudes: Implications for MeV electron acceleration in the outer radiation belt, *J. Geophys. Res.*, **106**(A12), 29783–29796, doi:10.1029/2001JA000002.
- Meier, M. M., R. D. Belian, T. E. Cayton, R. A. Christensen, B. Garcia, K. M. Grace, J. C. Ingraham, J. G. Laros, and G. D. Reeves (1996), The energy spectrometer for particles (ESP): Instrument description and orbital performance, *AIP Conf. Proc.*, **383**, 203–210, Ameri. Inst. Phys., New York.
- Miyoshi, Y., and R. Kataoka (2008), Flux enhancement of the outer radiation belt electrons after the arrival of stream interaction regions, *J. Geophys. Res.*, **113**, A03S09, doi:10.1029/2007JA012506.
- Onsager, T. G., J. C. Green, G. D. Reeves, and H. J. Singer (2007), Solar wind and magnetospheric conditions leading to the abrupt loss of outer radiation belt electrons, *J. Geophys. Res.*, **112**, A01202, doi:10.1029/2006JA011708.
- Omura, Y., N. Furuya, and D. Summers (2007), Relativistic turning acceleration of resonant electrons by coherent whistler mode waves in a dipole magnetic field, *J. Geophys. Res.*, **112**, A06236, doi:10.1029/2006JA012243
- Paulikas, G. A., and J. B. Blake (1979), Effects of the solar wind on magnetospheric dynamics: Energetic electrons at the synchronous orbit, in *Quantitative Modeling of Magnetospheric Processes, Geophys. Monogr. Ser.*, Vol 21, pp. 180-202, AGU, Washington D.C.
- Prichard, D., and J. Theiler (1995), Generalized redundancies for time series analysis, *Physica D: Non-linear Phenomena*, **84**, 476–493, doi:10.1016/0167-2789(95)00041-2.
- Prokopenko, M., J. T. Lizier, and D. C. Price (2013), On thermodynamic interpretation of transfer entropy, *Entropy*, **15**(2), 524–543, doi:10.3390/e15020524.
- Reeves, G. D. (2007), Radiation Belt Storm Probes: A New Mission for Space Weather Forecasting. *Space Weather*, **5**: n/a. doi:10.1029/2007SW000341
- Reeves, G. D., S. K. Morley, R. H. W. Friedel, M. G. Henderson, T. E. Cayton, G. Cunningham, J. B. Blake, R. A. Christensen, and D. Thomsen (2011), On the relationship between relativistic electron flux and solar wind velocity: Paulikas and Blake revisited, *J. Geophys. Res.*, **116**, A02213, doi:10.1029/2010JA015735.

- Reeves, G., S. Morley, and G. Cunningham (2013), Long-term variations in solar wind velocity and radiation belt electrons, *J. Geophys. Res. Space Physics*, 118, 1040–1048, doi:10.1002/jgra.50126.
- Rigler, E. J., M. Wiltberger, and D. N. Baker (2007), Radiation belt electrons respond to multiple solar wind inputs, *J. Geophys. Res.*, 112, A06208, doi:10.1029/2006JA012181
- Roberts, D. A. (1991), Is there a strange attractor in the magnetosphere?, *J. Geophys. Res.*, 96(A9), 16031–16046, doi:10.1029/91JA01088.
- Roberts, D. A., D. N. Baker, A. J. Klimas, and L. F. Bargatze (1991), Indications of low dimensionality in magnetospheric dynamics, *Geophys. Res. Lett.*, 18, 151.
- Rostoker, G., S. Skone, and D. N. Baker (1998), On the origin of relativistic electrons in the magnetosphere associated with some geomagnetic storms, *Geophys. Res. Lett.*, 25, 3701–3704, doi:10.1029/98GL02801.
- Sharma, A. S., D. Vassiliadis, and K. Papadopoulos (1993), Reconstruction of low-dimensional magnetospheric dynamics by singular spectrum analysis, *Geophys. Res. Lett.*, 20, 335.
- Schreiber, T. (2000), Measuring Information Transfer, *Physical Review Letters*, 85, 461–464, doi: 10.1103/PhysRevLett.85.461.
- Simms, L. E., V. Pilipenko, M. J. Engebretson, G. D. Reeves, A. J. Smith, and M. Clilverd (2014), Prediction of relativistic electron flux at geostationary orbit following storms: Multiple regression analysis, *J. Geophys. Res. Space Physics*, 119, 7297–7318, doi:10.1002/2014JA019955.
- Simms, L. E., M. J. Engebretson, A. J. Smith, M. Clilverd, V. Pilipenko, and G. D. Reeves (2015), Analysis of the effectiveness of ground-based VLF wave observations for predicting or nowcasting relativistic electron flux at geostationary orbit. *J. Geophys. Res. Space Physics*, 120, 2052–2060. doi: 10.1002/2014JA020337.
- Shprits, Y. Y., R. M. Thorne, R. Friedel, G. D. Reeves, J. Fennell, D. N. Baker, and S. G. Kanekal (2006), Outward radial diffusion driven by losses at magnetopause, *J. Geophys. Res.*, 111, A11214, doi:10.1029/2006JA011657
- Shprits, Y. Y., D. A. Subbotin, N. P. Meredith, S. R. Elkington (2008), Review of modeling of losses and sources of relativistic electrons in the outer radiation belt II: Local acceleration and loss, *J. Atmos. Sol. Terr. Phys.*, 70, 1694–1713, doi:10.1016/j.jastp.2008.06.014.
- Shprits, Y. Y., D. Subbotin, and B. Ni (2009), Evolution of electron fluxes in the outer radiation belt computed with the VERB code, *J. Geophys. Res.*, 114,

A11209, doi:10.1029/2008JA013784.

- Summers, D., R. M. Thorne, and F. Xiao (1998), Relativistic theory of wave-particle resonant diffusion with application to electron acceleration in the magnetosphere, *J. Geophys. Res.*, 103(A9), 20487–20500, doi:10.1029/98JA01740.
- Summers, D., B. Ni, and N. P. Meredith (2007), Timescales for radiation belt electron acceleration and loss due to resonant wave-particle interactions: 1. Theory, *J. Geophys. Res.*, 112, A04206, doi:10.1029/2006JA011801.
- Tanskanen, E. I. (2009), A comprehensive high-throughput analysis of substorms observed by IMAGE magnetometer network: Years 1993–2003 examined, *J. Geophys. Res.*, 114, A05204, doi:10.1029/2008JA013682
- Thorne, R. M. (2010), Radiation belt dynamics: The importance of wave-particle interactions, *Geophys. Res. Lett.*, 37, L22107, doi:10.1029/2010GL044990
- Tsonis, A. A. (2001), Probing the linearity and nonlinearity in the transitions of the atmospheric circulation, *Nonlinear Processes in Geophysics*, 8, 341–345.
- Turner, D. L., Y. Shprits, M. Hartinger, and V. Angelopoulos (2012), Explaining sudden losses of outer radiation belt electrons during geomagnetic storms, *Nat. Phys.*, 8, 208–212, doi:10.1038/nphys2185.
- Ukhorskiy, A. Y., M. I. Sitnov, A. S. Sharma, B. J. Anderson, S. Ohtani, and A. T. Y. Lui (2004), Data-derived forecasting model for relativistic electron intensity at geosynchronous orbit, *Geophys. Res. Lett.*, 31, L09806, doi:10.1029/2004GL019616.
- Ukhorskiy, A. Y., K. Takahashi, B. J. Anderson, and H. Korth (2005), Impact of toroidal ULF waves on the outer radiation belt electrons, *J. Geophys. Res.*, 110, A10202, doi:10.1029/2005JA011017.
- Ukhorskiy, A. Y., B. J. Anderson, P. C. Brandt, and N. A. Tsyganenko (2006), Storm time evolution of the outer radiation belt: Transport and losses, *J. Geophys. Res.*, 111, A11S03, doi:10.1029/2006JA011690.
- Vassiliadis, D., S. F. Fung, and A. J. Klimas (2005), Solar, interplanetary, and magnetospheric parameters for the radiation belt energetic electron flux, *J. Geophys. Res.*, 110, A04201, doi:10.1029/2004JA010443.
- Vennerstrøm, S. (1999), Dayside magnetic ULF power at high latitudes: A possible long-term proxy for the solar wind velocity?, *J. Geophys. Res.*, 104(A5), 10145–10157, doi:10.1029/1999JA900015.
- Wing, S., J. R. Johnson, J. Jen, C.-I. Meng, D. G. Sibeck, K. Bechtold, J. Freeman, K. Costello, M. Balikhin, and K. Takahashi (2005a), Kp forecast

- models, *J. Geophys. Res.*, 110, A04203, doi:10.1029/2004JA010500
- Wing, S., J. R. Johnson, P. T. Newell, and C.-I. Meng (2005b), Dawn-dusk asymmetries, ion spectra, and sources in the northward interplanetary magnetic field plasma sheet, *J. Geophys. Res.*, 110, A08205, doi:10.1029/2005JA011086.
- Wyner, A. D. (1978), A definition of conditional mutual information for arbitrary ensembles, *Info. and Control*, 38, 51–59.

Chapter 7

Summary and discussion

7.1 Overview

As the solar wind ionized particles stream down from the Sun toward the Earth, they encounter an obstacle created by the Earth's magnetic field. For most of the solar wind particles, their encounter with the Earth is relatively uneventful. Once crossing the bow shock, in the magnetosheath, they slow down, their temperatures and densities increase, and they encounter some waves, as they approach the magnetopause. After they pass the subsolar magnetopause, nominally located at $\sim 10 R_E$ ($1 R_E \sim 6372$ km), as they flow around the Earth, they slowly speed up, their densities and temperatures decrease. Eventually, they regain the same properties they had before encountering the Earth as they leave the Earth behind on their journey to deep space. Unless they are captured by the outer planets, most of these particles will leave our solar system, perhaps never to see their parent (the Sun) again.

However, for a small fraction of the solar wind particles that do manage to enter the Earth's magnetosphere, they are in for a very interesting and exciting journey in which they will encounter more forces, more waves, and more turbulence than they have in the magnetosheath. Their fates are determined by where they enter the magnetosphere and which forces, waves, and turbulences they encounter along their trajectories in the magnetosphere.

In this thesis, we follow the improbable journey of these solar wind particles starting from the dayside magnetopause. They do not all follow the same path. Some enter the magnetosphere from the dayside through reconnection and its aftermath (region 1 in Figure 7.1 [same as Figure 1.2]). Some enter the magnetosphere further down, in the magnetotail, through a turbulence process involving Kelvin-Helmholtz waves or kinetic Alfvén waves at the low-latitude boundary layer (LLBL) (region 2 in Figure 7.1). Whether the entry point is

through the former (arrow 1*) or the latter (arrow 2*), many or most of the solar wind particles end up in the plasma reservoir called the plasma sheet (region 3 in Figure 7.1). Periodically, about once every few hours, substorms inject (arrow 4 in Figure 7.1) and energize the plasma sheet particles into the inner magnetosphere. Once, in the magnetosphere (region 5 in Figure 7.1), a fraction of the electrons, over a period of a couple days, get further energized, attaining energies > 1 MeV, to become part of the radiation belt population. So, this thesis follows the paths of these particles over the time scale of several days from the dayside magnetopause to the plasma sheet and to the radiation belt. Along the way, we investigate some interesting magnetospheric problems.

For the remainder of this chapter, we provide summary and discussion of each chapter in this thesis.

7.2 Chapter 2: Quantitative aspects of magnetospheric physics

The ions and electrons in the magnetosphere have finite nonzero velocities and temperatures and hence they rarely stand still. In Chapter 2, we review the physical properties of these particles, which exist in the state of plasma, and some of the physics that governs the motions of these particles once they are in the magnetosphere. Using these equations, we construct an APL open field line particle precipitation model (APL–OPM) that describes the entries of the solar wind ions and electrons in the aftermath of the dayside magnetic reconnection (region 1 in Figure 7.1). Satellite observations show that by the time the solar wind particles reach the ionosphere, they exhibit different properties at different locations, even though these particles all originate from the solar wind and hence start out with the same uniform properties. Solar wind particles that enter the magnetosphere and precipitate in the ionosphere have been classified into 4 categories based on their plasma properties: (1) open field line LLBL (open-LLBL), (2) cusp, (3) mantle, and (4) polar rain. Our model shows that the same physical processes can lead to all four different types of particle precipitation. Finally, we

Contribution statement:

S. Wing: contributed main ideas, wrote the chapter.

E. Camporeale: contributed useful comments and discussions.

U. Ebert: contributed useful comments and discussions.

show that our APL–OPM calculations agree well with DMSP satellite observations, including the energy-latitude dispersion in the cusp, which has been frequently cited as a signature of the dayside magnetic reconnection.

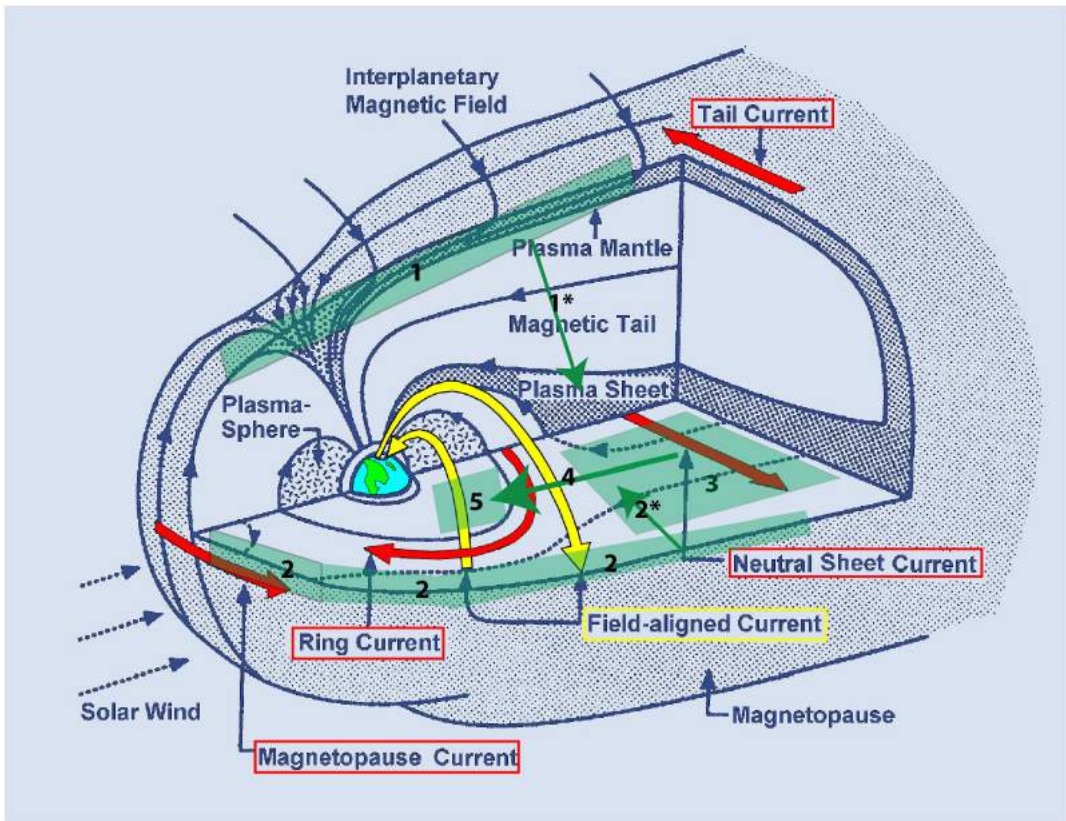


Figure 7.1. Schematic of the Earth's magnetosphere showing currents and plasma regions. (This figure is the same as Figure 1.2, but re-displayed here for convenience.) This dissertation covers the processes in the green shaded regions and green arrows. Except for 1 and 2, which can occur without any preferential order, the numbers give the **rough** sequence for solar wind plasma and energy transport from the dayside magnetopause to the plasma sheet and finally to the inner magnetosphere. The green arrows indicate plasma transport directions.

7.3 Chapter 3: Solar wind plasma and energy entry into the polar cap

In the aftermath of the dayside reconnection, the Earth's previously closed magnetic field line is open and solar wind can start entering the magnetosphere and some precipitate into the ionosphere (region 1 in Figure 7.1). Here, we explore

aspects of the solar wind electrons that precipitate in the ionosphere in the polar cap, which is the region in the ionosphere that is open. Most precipitating particles in the polar cap are electrons because ions have greater difficulty entering the magnetosphere, as described in Chapter 2. Based on the topics, Chapter 3 is naturally divided into two parts: (1) the dayside polar cap and (2) the nightside polar cap.

7.3.1 The dayside polar cap

Background and motivations: For the dayside polar cap, we explore the field-aligned electric field. The APL–OPM model predicts a downward electric field that arises from maintaining charge quasi-neutrality. Electrons can enter the magnetosphere more easily than ions due to their higher temperatures. As a result, a parallel electric field arises, which prevents more electrons from entering. This downward electric field has been confirmed observationally in two ways. First, spectral fitting of the DMSP electron data with potential drop as a free parameter confirms that electrons in the mantle and polar rain have gone through a retarding potential drop or an upward electric field. Second, comparisons of the solar wind electron distribution function with the DMSP electron distribution function obtained in the ionosphere reveal that indeed the solar wind electrons have gone through a retarding potential drop. However, this work found that there is an anomaly: the electric field is sometimes upward (accelerating potential drop) rather than downward (retarding potential drop). We investigate this anomalous electric field with DMSP satellite particle and magnetic field observations.

Results: It turns out that the upward electric field can be attributed to upward field-aligned current and Knight relation. In an upward field-aligned current region, when and where the electron density is not high enough to carry the current, an upward electric field, as evidenced by the downward electron acceleration, develops just above the ionosphere to draw more electrons downward. The probability of observing downward electron acceleration or upward electric field in an upward field-aligned current region is quite high, 0.82 to 0.96, depending on the magnetic local time (MLT). However, in the course of our investigation, we find another anomaly. Occasionally, a small scale upward electric field develops even in a downward current region. The probability of observing this anomaly is small, however, 0.03 to 0.11, depending on MLT.

Unresolved issues/caveats/future studies: The cause(s) of the small scale

upward electric field in a downward current region is unclear. This would be a topic of future studies.

7.3.2 The nightside polar cap

Background and motivations: On the nightside, the open field lines once again reconnect to form a closed field line (See Figure 3.1.) A signature of the nightside reconnection is the energy-latitude dispersion in the precipitating electrons in the polar cap, i.e., polar rain. An algorithm was developed to use this electron energy-latitude dispersion to estimate the magnetotail X-line distance. The accuracy of this algorithm had not been confirmed because of the difficulty of finding simultaneous observations of reconnection in the magnetotail and electron energy-latitude dispersion in the ionosphere. We investigate the accuracy of this algorithm using the APL–OPM model and DMSP particle observations.

Results: According to the model, the algorithm underestimates the electron path length from the magnetotail X-line to the ionosphere by at least 33%. The best estimate of the electron path length or X-line distance is obtained by using two of the highest energy electrons in the dispersion region. This study also raises the question of where the open–closed boundary is located. Many studies have assumed that the open–closed boundary is located at the poleward edge of the auroral oval, but our study suggests that the open–closed boundary can be located 0.7° – 1.5° poleward of the auroral oval.

Unresolved issues/caveats/future studies: The model assumes that there is no field-aligned potential drop, which would change the energies of the electrons. The algorithm gives an estimate of the electron path length from the magnetotail X-line to the ionosphere. However, to get an estimate of the X-line distance from the electron path length, we have used a factor of 0.78, which is obtained from our model for specific solar wind and magnetic field conditions. Therefore, this factor is somewhat crude and not accurate, if used for other conditions. The model boundary is limited by the magnetic field model boundary, which is at $x = -50 R_E$. Hence, we cannot model any events that have X-line locations $< -50 R_E$. One can improve on our methodology by using particle in a cell (PIC) simulation or by using test particles in an magnetohydrodynamic (MHD) simulation, both of which are computationally expensive and beyond the scope of the present study. The polar rain electron dispersion is not always observed. Although we have given some possible reasons, it would be interesting to determine conclusively how

frequently polar rain electrons exhibit dispersion and why dispersion is not observed all the time. The electron overhang needs to be further studied with modeling and simulations.

7.4 Chapter 4: Solar wind energy transfer at the low-latitude boundary layer

Background and motivations: We examine the energy transfer from the solar wind to the magnetosphere through LLBL (region 2 in Figure 7.1). This energy is used to drive upward field-aligned currents in the afternoon, which has the same polarity as the region-1 (R1) current. The source of the energy is the velocity shear between the tailward flowing solar wind and the nearly stagnant or moderately sunward flowing magnetospheric plasma. The velocity shear leads to an electric potential drop across the magnetopause boundary at low-latitude, which then drives the upward field-aligned currents from noon to dusk. An analytical theory for the afternoon upward field-aligned current generation is developed. However, in order for the theory to be trusted and useful, it needs to be validated with observations. Using simultaneous solar wind, DMSp particle precipitation and magnetometer observations, we validate the theory's predictions of field-aligned currents, current width, LLBL width, etc.

Results: We examine the scaling relations of the field-aligned current density (J_{\parallel}), current width (Λ), ionospheric Pedersen conductivity (Σ_p), LLBL width (Δ_m) with the solar wind parameters. The remarkable agreements between the theory and observations suggest that the theory captures the essential physics governing the solar wind interaction with the magnetosphere and the energy transfer to the magnetosphere–ionosphere system via field-aligned currents. The least square fit of calculated $J_{\parallel, \max}$ vs. observed J_{\parallel} returns $\log(J_{\parallel, \max, \text{cal}}) = (0.96 \pm 0.04) \log(J_{\parallel, \text{obs}}) + (0.03 \pm 0.01)$ for data points from 1100–1700 MLT, excluding data from noon. We show observationally that $\Lambda \sim n_{sw}^{-0.5}$ (n_{sw} = solar wind density), and $\Lambda \sim L$ (L = electrostatic auroral scale length) when $\Lambda/L < 5$, in agreement with the theoretical predictions. Up until this point, the width of the LLBL could only be determined by sending satellites to the magnetopause at distances $> 10 R_E$. One of the most amazing results from our work is that we show that we can estimate the width of the LLBL, which is about 3000 km (consistent with in situ observations), using just the commonly available solar wind and ionospheric observations.

Unresolved issues/caveats/future studies: Due to the unavailability of

observations at the LLBL and magnetosheath, we have to make some assumptions about their properties. For example, we assume that the magnetosheath velocity (V_0) = $0.15 V_{sw}$ (solar wind velocity). As a result there are rather huge uncertainties associated with these parameters. Σ_p is based on an old but popular empirical formula, which has an uncertainty. Because of these uncertainties, the scatters in some plots are rather large. In addition to the uncertainties in the observed parameters, the theory itself has some limitations. The theory does not take into account dynamic pressure driven current, which could be small but significant, near the subsolar magnetopause. The theory also assumes a linear current-voltage relationship based on the Knight relation, which ignores thermal current and nonlinear saturation as well as restricting the magnetospheric electron distribution function to be Maxwellian. Observations of intense localized peaks in current associated with energetic electron flux generally suggests that the current exceeds the thermal current, J_t (see Section 4.4.1). While most of the currents observed in this study exceed typical thermal currents in the boundary layer, the weaker currents may be comparable ($J_t \sim 0.1\text{--}1 \mu\text{A m}^{-2}$ for $n_e \sim 0.5\text{--}10 \text{ cm}^{-3}$ and $T_e \sim 100 \text{ eV}$); however, scaling relations may still apply even when the currents are comparable. However, most of the scaling relations shown in this chapter are tested with a subset of data with $\alpha < 1$ ($A/L < 5$), which have currents that are generally much larger than the thermal current. We have ignored the magnetopause reconnection and Kelvin-Helmholtz Instability (KHI), which would introduce small scale currents and scatters in our figures. The error sources for the observations and the limitations of the theory are discussed at length in Chapter 4 Section 4.4.4.

7.5 Chapter 5: Auroral particle precipitation

Background and motivations: Much of the solar wind that enters the magnetosphere ends up in the plasma sheet, which acts as the plasma reservoir for the Earth's magnetosphere (region 3 in Figure 7.1). However, it should be noted that not all plasma sheet particles originate from the solar wind. Some originate from the ionosphere. Periodically, substorms inject the plasma sheet plasma (arrow 4 in Figure 7.1) into the inner magnetosphere (region 5 in Figure 7.1). Substorms also release enormous amount of energy that is absorbed by the particles. How much energy is absorbed by these particles is a main topic of this chapter. During this process, the stretched magnetotail magnetic field lines become more dipolar. Thus, it can be said that substorms convert stored magnetic

energy to kinetic energy. The field-aligned plasma sheet and inner magnetospheric particles precipitate into the auroral oval in the ionosphere. In the magnetosphere, the field-aligned particles can be replenished through pitch-angle scattering. The electrons are pitch-angle scattered by waves, while the ions can be pitch-angle scattered by the neutral current sheet current at the equatorial plane of the magnetosphere. Hence, auroral particle precipitation provides a “window” into the magnetospheric plasma population and physical processes. Using almost 10 years of DMSP particle data, we statistically examine the characteristics of the auroral electron and ion precipitation as a function of substorm phase. We determine the duration of the substorm cycle as seen in the precipitating particles. Substorms release a huge amount of energy. How much of this energy is absorbed by the precipitating electrons and ions in the magnetosphere? The results of this study can help better understand the substorm process and place constraints on substorm theories. Electrons are classified into diffuse, broadband, and monoenergetic auroral electrons while the ions are not subclassified.

Results: The dawn-dusk asymmetry of each type of electrons over the entire substorm cycle is examined for the first time. The diffuse auroral electrons can be observed mainly in 2200–0900 MLT, which greatly coincides with the spatial distribution of the whistler-mode chorus waves that have been shown to be the predominant mechanism for pitch-angle scattering magnetospheric electrons into the loss cone. On the other hand, monoenergetic auroral electrons can be observed at the dusk-midnight sector. The monoenergetic electrons are magnetospheric electrons that have gone through a quasi-static parallel electric field in the upward field-aligned current regions. Broadband auroral electrons can be found mostly at 2200–0200 MLT where a peak in the Poynting flux of Alfvén waves is observed. Alfvén waves are known to cause broadband acceleration of electrons. The dawn-dusk asymmetry in the monoenergetic electrons increases after substorm onset. Substorms increase the monoenergetic electron power at dusk more than at dawn. In contrast, substorms do not appear to change much the dawn-dusk asymmetry in the broadband electrons. The substorms decrease the dawn-dusk asymmetry in the diffuse electrons 0–30 min after onset. Substorms increase the power of the diffuse, monoenergetic, and broadband electron aurorae by 310%, 71%, and 170%, respectively. These are higher than the previous estimates. The duration of the substorm cycle for monoenergetic and broadband auroral is ~5 hr, but it is longer than 5 hr for diffuse auroral electrons. This is longer than the previously reported substorm cycle

duration of 3 or 4 hr obtained from different sets of observations, which may partly explain the differences. There may be a link between monoenergetic and broadband electrons because both types of electrons appear to exhibit similar substorm cycle. Both types of electrons can be associated Alfvén waves. Broadband electrons can be associated with higher frequency Alfvén waves whereas monoenergetic electrons may be associated with lower frequency Alfvén waves, which would be consistent with the decay rates of their auroral electron powers.

Unresolved issues/caveats/future studies: This study uses substorms that are separated by at least 5 hr, but the duration of the diffuse electron substorm cycle is > 5 hr. Therefore, the durations of the growth and recovery phases and the total duration of the substorm cycle for the diffuse electrons are unresolved in this study. In order to resolve this, one would need a larger (probably by a factor of 2 or 3) substorm database, which is presently not available. The observations of the auroral diffuse, monoenergetic, and broadband electrons and ions are fairly solid and useful to substorm modelers, but this study does not establish the mechanisms conclusively. The reason is that this study uses only auroral particle precipitation data. For example, in order to link monoenergetic and broadband electrons to Alfvén waves, one would need simultaneous observations of precipitating electrons in the ionosphere and waves in the magnetosphere, the latter are not available for this study. Hence, the link between monoenergetic and broadband electrons cannot be established conclusively in this study. Another example is the link between fast flows in the magnetotail and the monoenergetic electrons cannot be established conclusively because we do not have simultaneous observations of precipitating electrons and plasma in the magnetotail. The mechanistic studies shall be conducted in the future.

7.6 Chapter 6: Solar wind drivers of the outer radiation belt

Background and motivations: After a long and arduous path, the solar wind particles finally end up in the inner magnetosphere (region 5 in Figure 7.1), which is also the last stop of our journey (though not necessarily the last stop of the particles' journey). Here, our study focuses on discovering the solar wind driver of the radiation belt electrons. Previous studies used the standard correlational analysis, but the solar wind–radiation belt system is highly nonlinear and hence

standard correlational analysis is inadequate or imprecise. Therefore, it is necessary to use information theoretical tools namely, mutual information, conditional mutual information, and transfer entropy, which can establish linear and nonlinear relationships. Some studies reported that solar wind velocity is the main driver of the radiation belt electron flux (J_e) with a two day response lag time, but others reported that solar wind density is the main driver of J_e with a one day response lag time. Additionally, studies have found that the scatter plot of radiation belt electron fluxes vs. solar wind velocity looks like a triangle. The mystifying part of the triangle distribution is that high values of radiation belt electron fluxes are observed for all solar wind velocity conditions. For the study described in Chapter 6, we use information theory to uncover this mystery and resolve conflicting findings.

Results: It is well known that solar wind velocity (V_{sw}) anticorrelates with solar wind density (n_{sw}), but our study reveals that this anticorrelation is long range, which has not been previously reported. This long range anticorrelation needs to be taken into account in any solar wind–magnetosphere coupling study involving V_{sw} and n_{sw} as drivers. Our study shows the previous finding of the solar wind density correlation with J_e with a one day lag can actually be attributed mainly to the anticorrelation between solar wind density and velocity and the correlation between solar wind velocity and J_e . If we remove the effects of solar wind velocity, the information transfer from the solar wind density to J_e peaks at 0 day (< 24 hr). We conclusively show that solar wind velocity is the main driver. Solar wind density transfers only about 36% as much information to J_e as the solar wind velocity does. We rank 10 solar wind parameters based on the amount of information transfer to J_e . We show that nonstationarity of the solar wind–radiation belt system dynamics can be determined with windowed transfer entropy. We also show that the triangle distribution in the radiation belt electron vs. solar wind velocity scatter plot can be understood better when we consider that V_{sw} and n_{sw} transfer information to radiation belt electrons with 2 days and 0 day (< 24 hr) lags, respectively.

Unresolved issues/caveats/future studies: The present study uses daily resolution data, which can provide information about solar wind driving of the radiation belt electrons on the time scale of days. However, solar wind–radiation belt system also exhibits dynamics at hours and minutes time scales. In order to investigate the solar wind driving of the radiation belt at smaller time scales, we need to use higher time resolution data from the recently launched Van Allen

Probe spacecraft. A previous study also found longer term, months to years time scale in the solar wind–radiation belt system. It would be interesting to repeat our study with longer time scales.

7.7 Practical applications: Space weather

A main goal of the study of space weather is to protect technological infrastructures and generally to improve lives. Space weather can adversely affect satellite health, satellite communication, Global Positioning Satellite (GPS) signals and navigation systems, cell phones, power grids, oil pipelines, commercial airline transpolar flights, space travels, etc. As our reliance on technology increases, so does our reliance on space weather forecast. In recognition of the importance of space weather, the President of the United States of America is briefed every morning on space weather conditions along with other essential information.

Although we have not mentioned space weather since Chapter 1, the pathways for the solar wind plasma and energy transfer to Earth's magnetosphere is generally central to the study of space weather. Obviously, if there were no pathway for solar wind to transfer plasma and energy to the magnetosphere, there would not be any space weather.

Some of the knowledge generated by this thesis work has direct applications to the study of space weather and space weather forecast. For example, in Chapter 6, the ranking of the solar wind parameters based on information transfer to the radiation belt can be useful to radiation belt modelers because the ranking can tell the modelers which solar wind input parameters to consider. Also, our ability to detect changes in the system dynamics based on the amount of information transfer from the drivers to the output parameters can help the modelers adjust (internal or external) parameters in their models accordingly. Radiation belt electrons are hazardous to satellites located at geosynchronous orbit (GEO $\sim 35,800$ km in altitude), which is within the outer radiation belt. However, because radiation belt electrons bounce from their mirror points in the ionosphere, satellites at low Earth orbit (LEO $< \sim 2000$ km in altitude) and medium Earth orbit (MEO with altitudes above LEO and below GEO) are also susceptible to radiation damages when the satellites intersect the footpoints of the magnetic field lines that trap radiation belt electrons. The radiation belt electrons with energies of a few MeVs or higher can penetrate deep into spacecraft components while those with

energies lower than one MeV can lodge on the surface of the spacecraft bodies, leading to devastating electrical discharges.

Other chapters are also relevant to space weather. The APL–OPM model described in Chapter 2 can help calculate the amount of plasma and energy transferred from the solar wind to the magnetosphere in open field lines. In Chapter 3, determining the X-line distance from Earth may also be useful in some substorm models. Our field-aligned current theory in Chapter 4 can help predict field-aligned currents, the magnetopause boundary layer thickness, and other useful parameters for space weather in the upward field-aligned current region located at the boundary layer and at open field lines. Chapter 5 gives an estimate of how much energy is gained by the precipitating particles during substorms.

Thus, although our research is driven by pure curiosity of the magnetosphere and solar wind–magnetosphere interactions and our motivation is to advance the state of magnetospheric physics, we also hope that we have produced something practical and useful for the inhabitants of the Earth.

Dankwoord

For this thesis, I studied the pathways for solar wind plasma and energy transfer to the Earth's magnetosphere. Because of the Earth's magnetic shielding, only a very small fraction of the solar wind particles manage to enter the magnetosphere. As I reflect back, I would like to think that my own journey to TU Eindhoven is perhaps just as improbable as the solar wind particles' journey into the Earth's magnetosphere.

I still remember fondly of the first western style public library in Makassar, Indonesia where I grew up. The library was funded by the Dutch government. It was there I found solace and refuge from all the noises, dings, and thumps of daily lives in a city with one of the highest population density in the world. The Dutch library fostered my love for books, perhaps the beginning of my academic career. From Indonesia, my journey took me to the United States of America, but I never imagined that my academic career would intersect the Netherlands once more. For this, I am eternally indebted to my Ph.D. promotor and copromotor Prof. Ute Ebert and Dr. Enrico Camporeale, respectively. They have given me the opportunity to fulfill a lifelong dream. Additionally, they have freely given me their time, guidance, and advice. They have graciously hosted my visits to Amsterdam and accompanied me on my visit to TU Eindhoven. I am most grateful for the freedom and trust they have given me in choosing the research topic for this thesis.

I would like to thank my long time collaborator, Dr. Jay Johnson, for providing the theoretical underpinnings for some of the works in this thesis, for allowing me to bounce off crazy ideas, and most importantly, for being a good friend. Working with Dr. Johnson does not feel like work as our physics discussions often move seamlessly from physics, to politics, to philosophy, etc., and back to physics. I would like to thank Dr. Kile Baker, who hired me at the Johns Hopkins University Applied Physics Laboratory (JHU/APL) and perhaps inadvertently and inevitably set me on the path to space physics (and to concert halls – in the darkest hours, confronted with the most challenging problems for this thesis, music came to the rescue – An die Musik). I would like to acknowledge

the JHU/APL Janney Fellowship that has partly funded some of the research for this thesis. I also would like to thank my wife Lisa and my son Benjamin for supporting and sharing my aspirations to fulfill my dream. Finally, I would like to acknowledge my parents, Daniel and Grace, without whose sacrifices, encouragements, and supports, my journey to TU Eindhoven would have been impossible.

Summary

Pathways for solar wind plasma and energy transfer to the Earth's magnetosphere

As the hot ionized particles (plasma) of the solar wind stream down from the Sun toward the Earth, the Earth's magnetic field deflects them around the Earth. As a result, most of these particles do not interact much with the Earth as they flow past the Earth to continue their journey to deep space. Unless they are captured by the outer planets, these particles will eventually leave the solar system. However, the Earth's magnetic shielding is not perfect and a small fraction of the solar wind particles do manage to enter the Earth's magnetosphere. Their fates are determined by where they enter the magnetosphere and which forces, waves, and turbulence they encounter along their trajectories in the magnetosphere.

In this thesis, we follow the improbable journey of these solar wind particles that enter the magnetosphere, starting from the dayside magnetopause (the outer boundary of the magnetosphere, which is nominally located at $\sim 10 R_E$ on the dayside [$R_E =$ earth radius ~ 6372 km]). They do not all follow the same path. Some enter the magnetosphere from the dayside through the magnetospheric magnetic field lines that have become open due to reconnection with the interplanetary magnetic field (IMF), which is the solar magnetic field that is "frozen in" the solar wind. Here, these particles may experience the downward field-aligned electric field that arises to keep most electrons out of the magnetosphere in order to maintain charge quasi-neutrality. Herein, field-aligned refers to aligned or parallel with magnetic field. However, if they enter the magnetospheric region where the field-aligned currents are upward, they sometimes experience upward field-aligned electric field located just above the ionosphere. On the nightside, near the boundary of open and closed magnetic field lines, the electrons that originate from the solar wind exhibit energy-latitude dispersion that can be used to estimate the location of the nightside reconnection region. (the open magnetic field line is the magnetic field line that has one end

connected to the Earth and the other connected to the solar wind; in contrast, the closed magnetic field line is the field line that has both ends connected to the Earth.) The accuracy of the algorithm is evaluated with a model. This work is presented in Chapter 3.

In Chapter 4, we explore the solar wind transfer of energy at the low-latitude boundary layer, which is the region near the magnetopause near the equatorial plane. The velocity shear between the solar wind and the magnetospheric plasma generates electric potential across the magnetopause boundary, which drives upward field-aligned currents in the afternoon. A theory for the field-aligned current generation is developed. We confirm the theory using ionospheric and solar wind observations. We confirm observationally that the theory allows us to estimate the magnetopause boundary layer thickness using commonly available solar wind and ionospheric observations.

The same velocity shear at the low-latitude boundary layer allows some solar wind particles to enter the magnetosphere through a turbulence process involving Kelvin-Helmholtz instability. Regardless of their entry points, most of the solar wind particles end up in the plasma sheet, which acts as the plasma reservoir for the magnetosphere. The plasma sheet is located on the nightside magnetosphere at altitudes $> \sim 6 R_E$. Periodically, about once every few hours, substorms inject and energize the plasma sheet particles into the inner magnetosphere, which is the region of the magnetosphere at altitudes of $\sim 1 - \sim 6 R_E$. The field-aligned particles from the plasma sheet precipitate in the auroral oval (nominally at geomagnetic latitudes of $\sim 60^\circ - \sim 70^\circ$) in the ionosphere. Hence, by monitoring the particle precipitation in the high-latitude ionosphere, we can study the plasma sheet particles. In Chapter 5, we study the characteristics of these precipitating ions and electrons as they are modulated by substorms. Substorms energize the precipitating electrons and ions. After substorm onsets, the precipitating electron energy fluxes remain elevated for a long time (> 3.5 hours).

Once in the inner magnetosphere, the electrons, over a period of 2–3 days, get energized further, attaining energies > 1 MeV, to become part of the radiation belt population. In Chapter 6, using information theoretical tools, we investigate the solar wind drivers of the radiation belt electrons. We rank the solar wind parameters based on the information transfer from the parameters to the radiation belt electrons. The ranking from the highest to lowest is as follows: solar wind velocity, magnitude of IMF, solar wind density, solar wind dynamic pressure, standard deviation of IMF (which gives a measure of IMF fluctuations), IMF $B_z <$

0, solar wind electric field, IMF B_y , IMF $B_z > 0$, and IMF B_x . We also show that the triangle distribution in the radiation belt electron vs. solar wind velocity plot can be understood better when we take into account the amount of information transfer from solar wind velocity to the radiation belt electrons.

Finally, Chapter 7 summarizes the main findings of this dissertation. It briefly describes the solar wind particle journey after these particles enter the magnetosphere from the dayside magnetopause to the plasma sheet and to the inner magnetosphere.

Curriculum Vitae

Simon Wing was born on 15-06-1963 in Makassar, Indonesia. After finishing his high school in 1981 at Catalina High School in Tucson, Arizona, USA, he received his Bachelor of Science degree in Physics at University of Arizona in 1984 (also in Tucson, Arizona). In 1988, he graduated with a Master of Science degree in Computer Science from The Johns Hopkins University in Baltimore, Maryland, USA. He is presently a Principal Professional Staff Physicist at The Johns Hopkins University Applied Physics Laboratory and an Adjunct Associate Professor at University of Maryland University College. His research interests include modeling the open field line particle precipitation; plasma sheet particle sources and transports; space weather; solar wind-magnetosphere interaction; and magnetosphere-ionosphere coupling. He pioneered a technique for inferring plasma sheet ion temperature, density, and pressure from ionospheric observations. His open field model predicted the existence of “double cusp” for B_y dominant IMF, which has been subsequently observed. He is an expert on DMSPP particle and magnetic field observations. His K_p forecast models have been adapted by national space weather centers, which broadcast his model K_p predictions (<http://www.swpc.noaa.gov/products/wing-kp>). In addition to research, he teaches graduate level computer and information science courses at University of Maryland. He has published over 70 papers and has given over 200 presentations at national/international scientific meetings, including more than 30 invited talks. His Google h-index is 24 and i10-index is 46. He has been recipient of numerous NASA and NSF grants. In 2015, he started a PhD project at the CWI (Centrum Wiskunde & Informatica) in Amsterdam, the results of which are presented in this dissertation.

Journal publications:

1. Baker, K. B., and S. Wing (1989), A New Magnetic System for Conjugate Studies at High Latitude, *J. Geophys. Res.*, 94, 9139-9143. (Over 450 citations).
2. Sigillito, V. G., S. P. Wing, L. Hutton, and K. B. Baker (1989), Classification of Radar Returns from the Ionosphere Using Neural Networks, *Johns Hopkins Technical Digest*, 10, 262-266.
3. Newell, P. T., S. Wing, C. I. Meng, and V. Sigillito (1990), A Neural Network Based System for Monitoring the Aurora, *Johns Hopkins Technical Digest*, 11, 291-299.
4. Newell, P. T., S. Wing, C. I. Meng, and V. Sigillito (1991), The Auroral Oval Position, Structure And Intensity of Precipitation From 1984 Onwards: An Automated On-Line Data Base, *J. Geophys. Res.*, 96, 5877-5882.
5. Wing, S., P. T. Newell, D. G. Sibeck, and K. B. Baker (1995), Large Statistical Study of the Entry of Interplanetary Magnetic Field Y-Component into the Magnetosphere, *Geophys. Res. Lett.*, 22, 2083-2086, 1995.

6. Wing, S., P. T. Newell, and T. G. Onsager (1996), Modeling the Entry of the Magnetosheath Electrons into the Dayside Ionosphere, *J. Geophys. Res.*, 101, 13155-13167.
7. Wing, S., and D. G. Sibeck (1997), The effects of Interplanetary Magnetic Field Z-Component and the Solar Wind Dynamic Pressure on the Magnetospheric Magnetic Field Line, *J. Geophys. Res.*, 102, 7207-7216.
8. Wing, S., and P. T. Newell (1998), Central Plasma Sheet Ion Properties as Inferred from Ionosphere Observations, *J. Geophys. Res.*, 103, 6785-6800.
9. Newell, P. T., and S. Wing (1998), Entry of Solar Wind Plasma Into the Magnetosphere: Observations Encounter Simulation, in *Geospace Mass and Energy Flow: Results From the International Space Physics Program*, *Geophys. Monog. Ser.*, vol. 104, edited by J. L. Horwitz, D. L. Gallagher, and W. K. Peterson, pp. 73-84, AGU, Washington D.C.
10. Newell, P. T., V. A. Sergeev, G. R. Bikkuzina, and S. Wing (1998), Characterizing the State of the Magnetosphere: Testing the Ion Precipitation Maxima Latitude (b2i) and the Ion Isotropy Boundary, *J. Geophys. Res.*, 103, 4739-4745.
11. Newell, P. T., Ching-I. Meng, and S. Wing (1998), Relation to Solar Activity of Intense Aurorae in Sunlight and Darkness, *Nature*, 393, 342-344.
12. Newell, P. T., Kan Liou, S. Wing, and Ching-I. Meng (1998), Ionospheric Conductivity and the Formation of Auroral Arcs: A Review with an Emphasis on Solar Cycle Effects, *Substorms-4*, edited by S. Kokubun and Y. Kamide, Terra Scientific Publishing Company/Kluwer Academic Publisher, pp. 41-46.
13. Wing, S., and Patrick T. Newell (2000), Quiet time plasma sheet ion pressure contribution to Birkeland currents, *J. Geophys. Res.*, 7793-7802.
14. Crowley, G., A. J. Ridley, D. Deist, S. Wing, D. J. Knipp, B. A. Emery, J. Foster, R. Heelis, M. Hairston, and B. W. Reinisch (2000), Transformation of high-latitude ionospheric F-region patches into blobs during the March 21, 1990 storm, *J. Geophys. Res.*, 105, 5215-5230.
15. Newell, P. T., and Simon Wing (2000), Remotely imaging the plasma sheet with low-altitude satellite clusters, *J. Atmos. and Solar-Terres. Phys.*, 62, 851-863.
16. Wing, S., Patrick T. Newell, and J. Michael Ruohoniemi (2001), Double cusp: Model prediction and Observational Verification, *Journal of Geophysical Research*, 106, 25,571-25,593.
17. Wing, S., D. G. Sibeck, M. Wiltberger, and H. Singer (2002), Geosynchronous magnetic field temporal response to the solar wind and IMF variations, *J. Geophys. Res.*, 107, 10.1029/2001JA009156.
18. Liou, K., C.-I. Meng, A. T. Y. Lui, P. T. Newell, and S. Wing (2002), Magnetic dipolarization with substorm expansion onset, *J. Geophys. Res.*, 107, 10.1029/2001JA000179.
19. Wing, S., and Patrick T. Newell (2002), 2D plasma sheet density profile for northward and southward IMF, *Geophys. Res. Lett.*, 29(9), 10.1029/2001GL013950.

20. Stenuit, H., M. Fujimoto, S. A. Fuselier, J.-A. Sauvaud, S. Wing, A. Fedorov, E. Budnik, S. P. Savin, K. J. Trattner, V. Angelopoulos, J. Bonnel, T. D. Phan, T. Mukai, and A. Pedersen (2002), Multi-spacecraft study oin the dynamics of the dusk-flank magnetosphere under northward IMF: January 10-11, 1997, *J. Geophys. Res.*, 107(A10), 1333, doi:10.1029/2002JA9009246.
21. Kubyshkina, M. V., V. A. Sergeev, S. V. Dubyagin, S. Wing, P. T. Newell, W. Baumjohann, and A. T. Y. Lui (2002), Constructing the magnetospheric model including pressure measurements, *J. Geophys. Res.*, 107(A6), 10.1029/2001JA900167.
22. Wing, S., and P. T. Newell (2003), LLBL contribution to the plasma sheet ions, in *Earth's low-latitude boundary layer*, *Geophys. Monog. Ser.*, vol. 133, edited by P. T. Newell and T. Onsager, pp. 273-282, AGU, Washington D.C.
23. Wing, S., R. A. Greenwald, C.-I. Meng, V. G. Sigillito, and L. V. Hutton (2003), Neural Networks for automated classification of ionospheric irregularities from HF radar backscattered signals, *Radio Sci.*, 38(4), 1063, doi:10.1029/2003RS002869.
24. Wing, S., P. T. Newell, and C.-I. Meng (2004), Cusp properties for By dominant IMF, in *Multiscale processes in the Earth's magnetosphere: From Interball to Cluster*, edited by J.-A. Sauvaud and Z. Nemecek, NATO science series, vol. 178, pp. 149-174, Kluwer Academic Publishers, The Netherlands.
25. Wing, S., P. T. Newell, C.-I. Meng (2005), Cusp Modeling and Observations at Low Altitude, *Surveys in Geophysics*, 26: 341-367, doi:10.1007/s10712-005-1886-0 (invited).
26. Johnson, J. R., and S. Wing (2005), A solar cycle dependence of nonlinearity in magnetospheric activity, *J. Geophys. Res.*, 110, A04211, doi:10.1029/2004JA010638.
27. Wing, S., J. R. Johnson, J. Jen, C.-I. Meng, D. G. Sibeck, K. Bechtold, J. Freeman, K. Costello, M. Balikhin, and K. Takahashi (2005), Kp forecast models, *J. Geophys. Res.*, 110, A04203, doi:10.1029/2004JA10500.
28. Wing, S., J. R. Johnson, P. T. Newell, and C.-I. Meng (2005), Dawn-dusk asymmetry in the northward IMF plasma sheet, *J. Geophys. Res.*, 110, A08205, doi:10.1029/2005JA011086.
29. Newell, P. T., S. Wing, T. Sotirelis, and C.-I. Meng (2005), Ion aurora and its seasonal variations, *J. Geophys. Res.*, 110, A01215, doi:10.1029/2004JA010743.
30. Zhang, Y., C.-I. Meng, L. J. Paxton, D. Morrison, B. Wolven, H. Kil, P. Newell, and S. Wing (2005), Far-ultraviolet signature of polar cusp during southward IMF Bz observed by TIMED/Global Ultraviolet Imager and DMSP, *J. Geophys. Res.*, 110, A01218, doi:10.1029/2004JA010707.
31. Zhang, Y., L. J. Paxton, Morrison, B. Wolven, H. Kil, and S. Wing (2005), Nightside detached auroras due to precipitating protons/ions during intense magnetic storms, *J. Geophys. Res.*, 110, A02206, doi:10.1029/2004JA010498.
32. Øieroset, M., J. Raeder, T. D. Phan, S. Wing, J. P. McFadden, W. Li, M. Fujimoto, H. Rème, and A. Balogh (2005), Global cooling and densification of the plasma sheet during an extended period of purely northward IMF on October 22-24, 2003, *Geophys. Res. Lett.*, 32, L12S07, doi:10.1029/2004GL021523.

33. Newell, P. T., S. Wing, C-I. Meng (2005), Spectral properties and source regions of dayside electron acceleration events, *J. Geophys. Res.*, 110, A11205, doi:10.1029/2005JA011264.
34. Wing, S., C-I. Meng, K. Takahashi, and S. Carr (2005), An Application for real-time magnetometer data: Space weather forecasting, in Proceedings of the XIth IAGA Workshop on Geomagnetic Observatory Instruments, Data Acquisition, and Processing, Nov 9-17 2004, Kakioka and Tsukuba, Japan.
35. Zhu, D., S. A. Billings, M. Balikhin, S. Wing, and D. Coca (2006), Data derived continuous time model for the Dst dynamics, *Geophys. Res. Lett.*, 33, L04101, doi:10.1029/2005GL025022.
36. Wing, S., J. R. Johnson, and M. Fujimoto (2006), Timescale for the formation of the cold-dense plasma sheet: A case study, *Geophys. Res. Lett.*, 33, L23106, doi:10.1029/2006GL027110.
37. Lavraud, B., M. F. Thomsen, S. Wing, M. Fujimoto, M. H. Denton, J. E. Borovsky, A. Aasnes, K. Seki, and J. Weygand (2006), Observations of two distinct cold, dense ion populations at geosynchronous orbit: local time asymmetry, solar wind dependence and origin, *Ann. Geophys.*, 24 (12), 3451-3465.
38. Wing, S., J. W. Gjerloev, J. R. Johnson, and R. A. Hoffman (2007), Substorm plasma sheet ion pressure profiles, *Geophys. Res. Lett.*, 34, L16110, doi:10.1029/2007GL030453.
39. Zhu, D., S. A. Billings, M. A. Balikhin, S. Wing, and H. Alleyne (2007), Multi-input data derived Dst model, *J. Geophys. Res.*, 112, A06205, doi:10.1029/2006JA012079.
40. Newell, P. T., S. Wing, and F. J. Rich (2007), Cusp for high and low merging rates, *J. Geophys. Res.*, 112, A09205, doi:10.1029/2007JA012353.
41. Zong, Q.-G., H. Zhang, T. A. Fritz, M. L. Goldstein, S. Wing, W. Keith, J. D. Winningham, R. Frahm, M. W. Dunlop, A. Korth, P. W. Daly, H. Reme, A. Balogh, and A. N. Fazakerley (2008), Multiple cusps during an extended northward IMF period with a significant By component, *J. Geophys. Res.*, 113, A01210, doi:10.1029/2006JA012188.
42. Fairfield, D. H., S. Wing, P. T. Newell, J. M. Ruohoniemi, J. T. Gosling, and R. M. Skoug (2008), Polar rain gradients and field-aligned polar cap potentials, *J. Geophys. Res.*, 113, A10203, doi:10.1029/2008JA013437.
43. Wing, S., and J. R. Johnson (2009), Substorm entropies, *J. Geophys. Res.*, 114, A00D07, doi:10.1029/2008JA013989.
44. Johnson, J. R., and S. Wing (2009), Northward interplanetary magnetic field plasma sheet entropies, *J. Geophys. Res.*, 114, A00D08, doi:10.1029/2008JA014017.
45. Newell, P. T., T. Sotirelis, and S. Wing (2009), Diffuse, monoenergetic, and broadband aurora: The global precipitation budget, *J. Geophys. Res.*, 114, A09207, doi:10.1029/2009JA014326.
46. Ohtani, S., S. Wing, G. Ueno, and T. Higuchi (2009), Dependence of pre-midnight field-aligned currents and particle precipitation on solar illumination, *J. Geophys. Res.*, 114, A12205, doi:10.1029/2009JA014115.

47. Wing, S., and J. R. Johnson (2010), Introduction to special section on Entropy Properties and Constraints Related to Space Plasma Transport, *J. Geophys. Res.*, 115, A00D00, doi:10.1029/2009JA014911.
48. Newell, P. T., T. Sotirelis, and S. Wing (2010), Seasonal variations in diffuse, monoenergetic, and broadband aurora, *J. Geophys. Res.*, 115, A03216, doi:10.1029/2009JA014805.
49. Newell, P. T., A. R. Lee, K. Liou, S.-I. Ohtani, T. Sotirelis, and S. Wing (2010), Substorm cycle dependence of various types of aurora, *J. Geophys. Res.*, 115, A09226, doi:10.1029/2010JA015331.
50. Ohtani, S., S. Wing, P. T. Newell, and T. Higuchi (2010), Locations of night-side precipitation boundaries relative to R2 and R1 currents, *J. Geophys. Res.*, 115, A10233, doi:10.1029/2010JA015444.
51. Newell, P. T., A. R. Lee, K. Liou, S. Ohtani, S. Wing, and M. Hairston (2010), Multisatellite low-altitude observations of a magnetopause merging burst, *J. Geophys. Res.*, 115, A11204, doi:10.1029/2010JA015438.
52. Wing, S., S. Ohtani, P. T. Newell, T. Higuchi, G. Ueno, and J. M. Weygand (2010), Dayside field-aligned current source regions, *J. Geophys. Res.*, 115, A12215, doi:10.1029/2010JA015837.
53. Newell, P. T., T. Sotirelis, K. Liou, A. R. Lee, S. Wing, J. Green, and R. Redmon (2010), Predictive ability of four auroral precipitation models as evaluated using Polar UVI global images, *Space Weather*, 8, S12004, doi:10.1029/2010SW000604.
54. Wei, H.-L., S.A. Billings, A. S. Sharma, S. Wing, R. J. Boynton, S. N. Walker (2011), Forecasting relativistic electron flux using dynamic multiple regression models, *Ann. Geophys.*, 29, 415 – 420, doi:10.5194/angeo-29-415-2011.
55. Wing, S., S. Ohtani, J. R. Johnson, M. Echim, P. T. Newell, T. Higuchi, G. Ueno, and G. R. Wilson (2011), Solar wind driving of dayside field-aligned currents, *J. Geophys. Res.*, 116, A08208, doi:10.1029/2011JA016579.
56. Wing, Simon (2012), "Mobile and Wireless Communication: Space Weather Threats, Forecasts, and Risk Management," *IT Professional*, 14, 40-46, 2012, doi:10.1109/MITP.2012.69.
57. Sanchez, E. R., S. Wing, E. Spanswick, and E. Donovan (2012), Entropy conservation and rate of propagation of bubbles in the Earth's magnetotail: A case study, *J. Geophys. Res.*, 117, A05226, doi:10.1029/2011JA017287.
58. Ohtani, S., H. Korth, S. Wing, E. R. Talaat, H. U. Frey, and J. W. Gjerloev (2012), The double auroral oval in the dusk-midnight sector: Formation, mapping and dynamics, *J. Geophys. Res.*, 117, A08203, doi:10.1029/2011JA017501.
59. Gkioulidou, M., C.-P. Wang, S. Wing, L. R. Lyons, R. A. Wolf, and T.-S. Hsu (2012), Effect of an MLT dependent electron loss rate on the magnetosphere-ionosphere coupling, *J. Geophys. Res.*, 117, A11218, doi:10.1029/2012JA018032.
60. Wing, S., M. Gkioulidou, J. R. Johnson, P. T. Newell, and C.-P. Wang (2013), Auroral particle precipitation characterized by the substorm cycle, *J. Geophys. Res. Space Physics*, 118, doi:10.1002/jgra.50160.

61. Clausen, L. B. N., J. B. H. Baker, J. M. Ruohoniemi, S. E. Milan, J. C. Coxon, S. Wing, S. Ohtani, and B. J. Anderson (2013), Temporal and spatial dynamics of the regions 1 and 2 Birkeland currents during substorms, *J. Geophys. Res. Space Physics*, 118, doi:10.1002/jgra.50288.
62. Wing, S., S. Ohtani, J. Johnson, G. R. Wilson, and T. Higuchi (2014), Field-aligned currents during the extreme solar minimum between the solar cycles 23 and 24, *J. Geophys. Res. Space Physics*, 119, 2466–2475, doi:10.1002/2013JA019452.
63. Berchem, J., R. Richard, P. Escoubet, S. Wing, and F. Pitout (2014), Dawn-dusk asymmetry in solar wind ion entry and dayside precipitation: Results from large-scale simulations, *J. Geophys. Res. Space Physics*, 119, 1549–1562, doi:10.1002/2013JA019427.
64. Ohtani, S., S. Wing, V. G. Merkin, and T. Higuchi (2014), Solar cycle dependence of nightside field-aligned currents: Effects of dayside ionospheric conductivity on the solar wind-magnetosphere-ionosphere coupling, *J. Geophys. Res. Space Physics*, 119, doi:10.1002/2013JA019410.
65. Walsh, A. P., Haaland, S., Forsyth, C., Keesee, A. M., Kissinger, J., Li, K., Runov, A., Soucek, J., Walsh, B. M., Wing, S., and Taylor, M. G. G. T. (2014): Dawn–dusk asymmetries in the coupled solar wind–magnetosphere–ionosphere system: a review, *Ann. Geophys.*, 32, 705–737, doi:10.5194/angeo-32-705-2014.
66. Johnson, J. R., and S. Wing (2014), External versus internal triggering of substorms: An information-theoretical approach, *Geophys. Res. Lett.*, 41, doi:10.1002/2014GL060928.
67. Johnson, J. R., S. Wing, and P. A. Delamere (2014), Kelvin Helmholtz Instability in Planetary Magnetospheres, *Space Sci. Rev.*, 184, 1 – 31, doi:10.1007/s11214-014-0085-z.
68. Wing, S., J. R. Johnson, C. C. Chaston, M. Echim, C. P. Escoubet, B. Lavraud, C. Lemon, K. Nykyri, A. Otto, J. Raeder, and C.-P. Wang (2014), Review of solar wind entry into and transport within the plasma sheet, *Space Science Reviews*, 184, 33 – 86, doi:10.1007/s11214-014-0108-9.
69. Carter, B. A., J. M. Retterer, E. Yizengaw, K. Wiens, S. Wing, K. Groves, R. Caton, C. Bridgwood, M. Francis, M. Terkildsen, R. Norman and K. Zhang (2014), Using solar wind data to predict daily GPS scintillation occurrence in the African and Asian low-latitude regions, *Geophys. Res. Lett.*, 41, doi:10.1002/2014GL062203.
70. Wing, S. and Zhang, Y. L. (2015), The nightside magnetic field line open–closed boundary and polar rain electron energy–latitude dispersion, *Ann. Geophys.*, 33, 39–46, doi:10.5194/angeo-33-39-2015.
71. Wing, S. and Johnson, J. R. (2015), Solar Wind Entry Into and Transport Within Planetary Magnetotails, in *Magnetotails in the Solar System* (eds A. Keiling, C. M. Jackman and P. A. Delamere), John Wiley & Sons, Inc, Hoboken, NJ. doi: 10.1002/9781118842324.ch14.
72. Johnson, J. R., and S. Wing (2015), The dependence of the strength and thickness of field-aligned currents on solar wind and ionospheric parameters. *J. Geophys. Res. Space Physics*, 120, 3987–4008. doi: 10.1002/2014JA020312.

73. Yongliang Zhang and Simon Wing (2015), Determining magnetotail reconnection location from polar rain energy dispersion, *J. Atmos. Sol. Terr. Phys.*, 130–131, 75–80, ISSN 1364-6826, doi:10.1016/j.jastp.2015.05.009.
74. Wing, S., D. H. Fairfield, J. R. Johnson, and S.-I. Ohtani (2015), On the field-aligned electric field in the polar cap, *Geophys. Res. Lett.*, 42, 5090–5099, doi:10.1002/2015GL064229.
75. Wing, S., and J. R. Johnson (2015), Theory and observations of upward field-aligned currents at the magnetopause boundary layer, *Geophys. Res. Lett.*, 42, 9149–9155, doi:10.1002/2015GL065464.
76. Berchem, J., R. L. Richard, C. P. Escoubet, S. Wing, and F. Pitout (2016), Asymmetrical response of dayside ion precipitation to a large rotation of the IMF, *J. Geophys. Res. Space Physics*, 121, 263–273, doi:10.1002/2015JA021969.
77. Weygand, J. M., and S. Wing (2016), Comparison of DMSP and SECS region-1 and region-2 ionospheric current boundary, *J. Atmos. Sol. Terr. Phys.*, 143, 8–13, doi:10.1016/j.jastp.2016.03.002.
78. Newell, P. T., K. Liou, J.W. Gjerloev, T. Sotirelis, S. Wing, E.J. Mitchell (2016), Substorm probabilities are best predicted from solar wind speed, *J. Atmos. Sol. Terr. Phys.*, 146, 28–37, doi:10.1016/j.jastp.2016.04.019.

Professional activities:

- Co-organizer/co-leader of GEM Global Interaction magnetotail campaign, June 25–30, 2006, Snowmass, CO.
- Co-organizer Isradynamics: Dynamical Processes in Space Plasma, 7–15 May 2006, Ein Bokek, Israel.
- Co-leader/co-organizer of GEM Plasma entry and transport into and within magnetotail (PET) focus group, 2007–2011.
- Guest editor of *Journal Geophys. Res.* special section "Entropy properties and constraints related to space plasma transport", 2009.
- Co-organizer PET09 workshop March 8–13, 2009, Fairbanks, Alaska.
- Member of NOAA advisory committee on space weather prediction testbed center (SWPT).
- Co-leader of ISSI International Team on Plasma Entry and Transport in the Plasma Sheet 2011 – 2012, Bern, Switzerland.
- Co-organizer, convener, and program committee member of a Chapman Conference entitled "Causes and consequences of the extended solar minimum between solar cycles 23 and 24 (4CESM)", Key Largo, Florida, 8 – 12 April, 2013.
- Guest editor of *JGR* special section entitled "Causes and consequences of the extended solar minimum between solar cycles 23 and 24 (4CESM)", 2013.
- Associate Editor of *JGR Space Physics* Jul 2013 – Dec 2014.
- The 2013 Editors' Citation for Excellence in Refereeing for *Journal of Geophysical Research- Space Physics*.
- Associate Editor of *IEEE Transactions on Cloud Computing (TCC)*, 2015–2017.
- The Johns Hopkins University Applied Physics Laboratory Janney Fellowship 2016.
- International Advisory Committee Member for 2015 International Conference on Space Science & Communication (ICONSPACE2015) 10 – 12 August 2015, Universiti Kebangsaan, Selangor Darul Ehsan, Malaysia.
- Co-Chair of International Association of Geomagnetism and Aeronomy (IAGA) Division III 2015 – 2019.